Ultrafast laser plasma doping of Er^{3+}-doped hybrid tellurite-silica thin films

Thomas Peter Mann

Submitted in accordance with the requirements for the degree of

Doctor of Philosophy

The University of Leeds
School of Chemical and Process Engineering

Feburary, 2019

To Mariana Amaral Garcia Avelino, I hope this helps to demystify the world of photonics!

The candidate confirms that the work submitted is his own, except where work which has formed part of jointly-authored publications has been included. The contribution of the candidate and the other authors to this work has been explicitly indicated below. The candidate confirms that appropriate credit has been given within the thesis where reference has been made to the work of others.

Jointly authored publications

The work in Chapter 5 of the thesis has appeared in the publication:

Thomas Mann et al. "Femtosecond laser ablation properties of Er3+ ion doped zinc-sodium tellurite glass". *Journal of Applied Physics* 124.4 (2018), p. 0440903

All of the work carried out in relation to this publications was conducted by the author of this thesis. The role of each of the co-authors for this publication was to provide guidance with respect to the development of the study investigation work, along with guidance on publication content and structure.

Publications involving works that do not appear in this thesis

The candidate was a co-author on the following publication, for which work from the publication was not included in this thesis:

Billy D. O. Richards et al. "Tm3+ Tellurite-Modified-Silica Glass Thin Films Fabricated Using Ultrafast Laser Plasma Doping". *IEEE Journal of Selected Topics in Quantum Electronics* 25.4 (2019), pp. 1-8

This copy has been supplied on the understanding that it is copyright material and that no quotation from the thesis may be published without proper acknowledgement.

The right of Thomas Peter Mann to be identified as Author of this work has been asserted by him in accordance with the Copyright, Designs and Patents Act 1988.

© 2018 The University of Leeds and Thomas Peter Mann.

Acknowledgements

First and foremost, I would like to express my sincere gratitude to my supervisor Gin Jose for his continuous support during my PhD study and research. From early morning teleconferences to impromptu discussions to even a late night in the laboratory, I could not have expected more in terms of input, guidance and patience. I admire his endless drive for innovation and would like to thank Gin for giving me the freedom to explore my own research interests and ideas. As a result of all this, the undertaking of my PhD has given me an invaluable learning experience.

I would also like to extend my thanks to my co-supervisor Zoran Iconic, without whom I would have likely been forever confused by the complex theoretical modelling! My colleagues deserves huge thanks for the experimental support and the many productive discussions. This includes Eric K. Barimah, Billy Richards, Matthew Murray, Robert Mathieson, Jayakrishnan Chandarappan, Suraya Kamil, Tarun Kakkar and Eduardo Henriques Dos Santos. Furthermore I would like to extend my gratitude to Christopher Russel and Paul Steenson for facilitating the use of equipment in the electrical engineering clean room, Stuart Micklethwaite and John Harrington at the Leeds Electron Microscopy and Spectroscopy (LEMAS) Centre for help in carrying out the SEM measurements, Christopher Hodges for support in atomic force microscopy measurements, Nick Kapur for help with setting up microfluidic experiments, Faith Bamiduro for support with X-ray diffraction measurements and, last but not least, Almut Beige and Nicholas Furtak-Wells for many enlightening discussions regarding quantum optics.

Finally, my biggest thanks is to my family, especially to my parents Marita and Nick, for their support throughout my entire education. My grandmother Elizabeth was always there to listen to what I had to say and I am very lucky to have my brother Michael standing by my side. My girlfriend Mariana Amaral Garcia Avelino has been a ray of light during what is usually a dark time of writing up the thesis. They have all collectively supported me right up until the final hour and have a special place in my heart!

Abstract

It has been a decade since the ultrafast laser plasma doping technique was first developed at The University of Leeds by Gin Jose. The capability of the technology to dope Er^{3+} ions into amorphous hybrid tellurite-silica glass thin films at the high concentrations required for Er^{3+}-doped waveguide amplifiers is unrivalled by other techniques. By avoiding clustering and crystallisation of the rare-earth ions, a long metastable photoluminescence lifetime of the first excited state required for population inversion is achieved. Despite the superior spectroscopic properties of this material, improvements to film homogeneity, quality and controlled growth rate are required. A fundamental understanding of the ultrafast laser plasma doping technique is lacking and is the aim of this thesis. The process is optimised sequentially, from the femtosecond laser ablation of the rare-earth doped tellurite target glass, to the ablation plume constituents to the film formation mechanism on silica substrates. Importantly, film formation in a vacuum is demonstrated for the first time and the sub-micron films are crack-free and highly uniform. Dehydroxylation of the silica surface during processing is also shown to eliminate quenching centres that typically reduce the metastable lifetime of Er^{3+} ions. The demonstration of high quality thin film growth, of the order of 100 nm, and capability to dope any rare-earth ion without a change in processing parameters, will allow for the application of this thin film technology to a variety of optical devices, such as sensors and lasers, alongside Er^{3+}-doped waveguide amplifiers.

Contents

1 Introduction **1**

1.1 Research Motivation . . . 1

1.2 Thesis Overview . . . 4

2 Light emission and energy transfer **8**

2.1 Introduction . . . 8

2.2 Spontaneous emission . . . 10

2.2.1 Homogeneous environment . . . 13

2.2.2 Inhomogeneous environment . . . 13

2.3 Fluorescence resonance energy transfer . . . 17

2.3.1 Förster theory . . . 18

2.3.2 Quantum Electrodynamics . . . 19

2.3.3 Multipoles . . . 21

3 Erbium ions in glass **22**

3.1 Basic properties . . . 22

3.2 Energy spectrum and optical transitions . . . 24

3.3 Transition rates . . . 25

3.3.1 Radiative decay . . . 25

3.3.2 Electron-phonon coupling . . . 27

3.3.3 980 nm pump wavelength band . . . 28

3.3.4 Excited state absorption . . . 29

3.4 Ion-ion interactions . . . 30

3.4.1 Energy migration . . . 31

3.4.2 Cooperative upconversion . . . 32

3.4.3 Cross relaxation . . . 33
3.4.4 Radiation trapping . . . 34

4 Ultrafast Laser Plasma Doping 35
4.1 Introduction and background . . . 35
4.2 Theoretical background . . . 39
4.2.1 Ultrafast laser ablation . . . 40
4.2.2 Plume expansion and transport . . . 46
4.2.3 Film growth . . . 50
4.3 Experimental Setup . . . 50
4.3.1 Laser delivery . . . 52
4.3.2 Target . . . 54
4.3.3 Substrate/heater stage . . . 55
4.3.4 Substrate heater . . . 56
4.3.5 Chamber atmosphere . . . 57
4.4 Optimisation procedure . . . 57
4.4.1 Femtosecond laser ablation . . . 58
4.4.2 Plume expansion . . . 60
4.4.3 Film growth . . . 61

5 Femtosecond laser ablation properties of Er^{3+}-doped zinc-sodium tellurite glass 64
5.1 Introduction . . . 64
5.2 Theoretical background . . . 66
5.2.1 Ablation threshold determination . . . 66
5.3 Experimental setup . . . 69
5.3.1 Sample preparation . . . 69
5.3.2 Characterisation . . . 69
5.3.3 Ablation experiments . . . 70
5.4 Results and discussion . . . 71
5.4.1 Characterisation . . . 71
5.4.2 Ultrafast laser ablation . . . 75
5.5 Conclusion . . . 82

6 Femtosecond laser deposited Er^{3+}-doped zinc-sodium tellurite glass films 85

6.1 Introduction . . . 85
6.2 Theoretical background . . . 87
6.2.1 Non-radiative de-excitation processes between Er^{3+} and silicon . 87
6.2.2 Atomic number density . . . 89
6.3 Experimental setup . . . 89
6.3.1 Sample Fabrication . . . 89
6.3.2 Characterisation . . . 90
6.4 Results and Discussion . . . 92
6.4.1 Physical and structural properties . . . 92
6.4.2 Target surface quality . . . 99
6.4.3 Optical properties . . . 101
6.5 Conclusion . . . 107

7 Thin film formation with the ultrafast laser plasma doping technique 109

7.1 Introduction . . . 109
7.2 Theoretical background . . . 110
7.2.1 Cracking of thin films . . . 110
7.3 Experimental setup . . . 112
7.3.1 Fabrication . . . 112
7.3.2 Characterisation . . . 114
7.4 Results and Discussion . . . 116
7.4.1 RT deposition followed by post heating . . . 116
7.4.2 Laser fluence optimisation . . . 128
7.4.3 Oxygen atmosphere depositions . . . 155
7.5 Conclusion . . . 163

8 Surface dehydroxylation during the ultrafast laser plasma doping technique 164

8.1 Introduction . . . 164
8.2 Theoretical background . . . 167
8.2.1 Measuring the OH content in silicate glass . . . 167
8.2.2 Surface dehydroxylation by annealing in silica glass . . . 168

8.3 Experimental setup 170
8.4 Results and discussion 171
8.4.1 Substrate hydroxyl impurities 171
8.4.2 Film characterisation 173
8.4.3 Concentration quenching 178
8.5 Conclusion 184

9 Conclusion and outlook **186**
9.1 Key findings 186
9.2 Further investigations 188

Appendices **210**

A Field amplitudes **211**
A.1 Radiative modes 211
A.2 Guided modes 213

B Transfer matrix method **216**
B.1 Maxwell's equations 217
B.2 Reflection and transmission 220
B.2.1 Transverse Electric Waves (TE or s-polarised) 222
B.2.2 Transverse Magnetic Waves (TM or p-polarised) 223
B.2.3 Summary 225
B.3 Transfer Matrix Method 226
B.3.1 Interference Matrix 227
B.3.2 Layer matrix 228
B.3.3 System transfer matrix 228
B.3.4 Internal Layer Field 229
B.3.5 Guided Modes 230

C Emission spectrum of heating elements **233**

D Tellurite glass polishing procedure **235**

E VASE measurements and fitting procedure **239**
E.1 Target glass 240
E.2 Glass Substrates 244
E.3 Thin films 247
E.3.1 Chapter 6 section 4.2 247
E.3.2 Chapter 7 248

F Post anneal **250**

List of Figures

1.1 Schematic representation of waveguide structures that can be used to fabricate a planar optical waveguide amplifier. Light is confined in the high refractive index waveguide core (medium grey) by total internal reflection. The Er doped core material is embedded in a low refractive index cladding layer (light grey). The device rests on a silicon substrate (dark grey). The waveguide structures are (a) a channel waveguide, (b) a ridge waveguide, (c) a strip loaded waveguide and (d) a diffused waveguide. Figure replicated from [2]. 2

2.1 (a) Energy-level diagram depicting spontaneous emission. The spontaneous emission rate Γ_{rad} is the rate of radiative energy transfer to any location in the environment. The acceptor is not considered as part of the environment. (b) Energy-level diagram depicting energy transfer between two neighbouring atoms or molecules, denoted as donor (D) and acceptor (A), due to a Coulombic interaction (virtual photon exchange, non-radiative) or real photon exchange (radiative). The donor and acceptor must have overlapping emission and absorption spectra, respectively, and the rate of transfer to the acceptor is denoted Γ_{DA}. Figure adapted from [27]. 9

2.2 Schematic view of the multilayer dielectric structure. The lower (layer 0) and the upper (layer M + 1) claddings with dielectric constants ε_0 and ε_{M+1}, respectively, are taken to be semi-infinite and surround the M dielectric layers, each characterised by a thickness d_j and dielectric constant ε_j for $j = 1, \ldots,$ M. Figure reproduced from [36]. 15

3.1 The energy levels of Er^{3+}. Leftmost scale shows the energy relative to the g.s. in 10^3 cm^{-1} and the inner scale shows the energy levels of each transition in Russel-Saunders notation. The thickness of the lines represents the broadening of the energy levels. Arrows indicate radiative transitions with the PL wavelength explicitly stated. 26
3.2 Schematic representation of the Er^{3+} intra-4f energy levels; (a) shows the 980 nm pump band excitation leading to 1.54 μm emission, (b) and (c) show the excited state absorption of a 1480 nm pump/1540 nm emission and a 980 nm pump photon, respectively, and the non-radiative ion-ion interactions in (d) and (e) show energy migration and cooperative upconversion, respectively. 29

4.1 The fs-PLD system used to fabricate hybrid tellurite-silica films. Mirror (M), partially reflective mirror (PRM), power meter (PM), shutter (SH), linear polariser (LP), half-wave plate ($\lambda/2$). The Ti-sapphire femtosecond pulsed laser (Libra, Coherent), operating at a central 800 nm wavelength with 100 fs pulse width, is indecent on the target surface at an angle of incidence of 45° and focused to a spot area of $\sim 3.24 \times 10^{-5}$ cm^2 ($\sim$ 27 μm radius spot normal to the beam). 38
4.2 Overview of the stages for fs-PLD/ULPD, indicated by number. Stage (1) light absorption in the solid target. Stage (2) one-dimensional expansion after the laser pulse. Stage (3) free three-dimensional expansion. Stage (4) expansion in the background gas. Stage (5) film growth on substrate. Figure adapted from [131]. 40
4.3 Typical timescales and intensity ranges of several phenomena and processes occurring during and after irradiation of a solid with an ultrashort laser pulse of about 100 fs duration. Excitation takes place in the range of femtoseconds (duration of the laser pulse). The timescale of melting may vary for different processes and lies roughly in the picosecond regime. Material removal, i.e. ablation, lasts up to the nanosecond regime. Figure reproduced from [132]. 41

4.4 Snapshots of molecular dynamic simulations of (a) heterogeneous and (b) homogeneous melting. A 50 nm Nickel film was assumed to be heated with an ultrashort laser pulse of 200 fs duration. The red atoms indicate crystal surroundings while blue regions are molten. In (a) the crystal is heated slightly above melting temperature and the melt front due to heterogeneous melting propagates from the front and rear side of the samples where the energy barrier is zero at the solid-vapor interface. In (b) strong overheating results in the procession of ultrafast melting due to homogeneous nucleation. Images reproduced from [145]. 45
4.5 CCD camera plume images recorded from the laser ablation of $BaTiO_3$ 100 μs after the 620 nm laser pulse in (a) the nanosecond regime (5 ns and 0.5 J/cm^2) and (b) in the femtosecond regime (90 fs and 1 J/cm^2). The size of each image is around 3 cm $\times$ 5 cm and the grey intensities are on a log scale. Image reproduced from [151]. 46
4.6 Optical emission spectra of plasma plumes generated by fs laser ablation; (a) Time-resolved intensity of a MgO plume ablated at various beam energies with a laser beam spot size of 9.4 $\times$ 10^{-5} cm^2 and (b) spectra of a gold plume for different time delays τ, at d = 1 mm for a laser fluence F = 0.6 J/cm^2. Reproduced from [124] and [152], respectively. . 48
4.7 CCD images of the evolution of a brass fs-laser ablation (800 nm, 40 fs, F = 1.77 J/cm^2) plume at a delay of 300 ns after the onset of plasma as a function of ambient argon pressure. Images are aquired with an exposure time of 30 ns and are normalised to the maximum intensity. Reproduced from [156]. 49
4.8 A photograph of the upgraded ULPD system used in this thesis. 51
4.9 Schematic of the experimental setup used to fabricate thin films using the upgraded ULPD system. Mirror (M), partially reflective mirror (PRM), power meter (PM), shutter (SH), linear polariser (LP), half-wave plate (λ/2). 51
4.10 The femtosecond laser optics. Image reproduced from the manufacture's user manual. 53
4.11 A 3D schematic of the target manipulator. Image reproduced from the manufacture's user manual. 55

4.12 Substrate holders for 10 mm by 10 mm sized substrates; (a) 1 by 1, (b) 2 by 2 and (c) 3 by 3. 56
4.13 The heating procedure used for the fabrication of hybrid tellurite-silica films with the ULPD technique. (RT) room temperature, (T) processing temperature. 57
4.14 (a) Inhomogeneous surface and (b) cracking in thin films fabricated via the ULPD technique. Reproduced from [163] and [25], respectively. . . . 58
4.15 Photographs of the erbium doped TZN target glass used in the ULPD technique; (a) polished with P320 SiC prior to processing, (b) catastrophic melting and reaction with the brass baseplate after processing at 650°C in a vacuum, (c) heat polished surface after processing at 750°C in an oxygen atmosphere (70 mTorr, 15 sccm). 61

5.1 Schematic of laser-induced ablation on a material (top) and the corresponding Gaussian fluence profile along the x-axis (bottom). D marks the diameter of the ablated area. The pulse number dependence of F_{th} is implicit. 67
5.2 Various stages of erbium doped TZN glass fabrication; (a) grinding the raw constituents into a fine powder with a pestle and mortar, (b) transferring the powder into a gold crucible before placing in an electric furnace, (c) removing the glass from the mould post annealing, (d) an optically polished glass. 69
5.3 A schematic of the experimental setup used to determine the ablation threshold of target glasses. The laser beam path is depicted with a red line. Mirror (M), flip mirror (FM), power meter (PM), shutter (SH), linear polariser (LP), half-wave plate ($\lambda/2$). 71
5.4 X-ray diffraction patterns of the two highest and lowest erbium target glass doping concentrations used. The intermediate doped glasses showed a similar spectra. Only a broad halo in the range $20^\circ < 2\theta < 40^\circ$ is observed indicating amorphous structure. 72

5.5 Optical absorption spectra for TZN and 0.75ErTZN glasses. Text shows the Er^{3+} ion transitions from the ground state ($^4I_{15/2}$) giving rise to the peaks (only the prominent transitions are displayed for clarity, refer to text for all transitions). 73
5.6 Tauc plots to determine the (a) direct band gap, (b) indirect band gaps and (c) Urbach energy of TZN glass. 74
5.7 Optical microscopy image of the array of craters ablated with increasing laser fluence F (going from left to right) and pulse numbers N (bottom to top) on TZN. The grid spacing of the crater array was 0.3 mm. Note that the pen marking on the left hand side was for location of the array under the microscope. 75
5.8 (a) AFM profiles of craters produced on TZN by a single laser pulse at several energies and a spot size of 32.0 μm. On the cross sectional profiles it is depicted how the crater diameter and height was determined, from which the 'effective optical penetration depth' and volume were calculated. (b) DIC micrographs of laser produced craters at a pulse energy of 45.8 μJ and spot size of 13.9 μm with different numbers of applied pulses. 77
5.9 SEM images (15 kV electron accelerating voltage) of multi-pulse ablation craters in TZN glass at a spot size of $w_0 = 32$ μm. Top row 10 pulses per site (a, b, c) and bottom row 32 pulses per site (d, e, f). $E_{\text{pulse}} =$ 23.4 μJ, $F_0^{\text{av}} = 0.73$ J/cm^2 (a, d), $E_{\text{pulse}} = 36.4$ μJ, $F_0^{\text{av}} = 1.13$ J/cm^2 (b, e) and $E_{\text{pulse}} = 137.8$ μJ, $F_0^{\text{av}} = 4.29$ J/cm^2 (c, f). 78
5.10 (a) The multipulse threshold fluence dependence of TZN. Data is fitted with eq. (5.12) with the parameters $F_{\text{th}}(1) = 0.51$, $F_{\text{th}}(\infty) = 0.18$ and $k = 0.074$ $F_{\text{th}}(\infty)$ for $w_0 = 13.9$ μm (solid line) and $F_{\text{th}}(1) = 0.32$, $F_{\text{th}}(\infty) = 0.14$ and $k = 0.051$ for $w_0 = 32.0$ μm (dashed line). (b) The multipulse ablation threshold measurements of TZN glass as determined from the single pulse crater depth. The legend is the same as for (a). The plots presents the logarithmic dependence of the ablation rate h_a on the laser fluence F_0^{avg}. Extrapolation of eq. (5.13) to zero gives a limiting multipulse threshold fluence of $F_{\text{th}}^{\infty} = 0.17 \pm 0.03$ J/cm^2 and the gradient gives an effective optical penetration depth $\alpha_{\text{eff}}^{-1} = 187 \pm 15$. 79

5.11 The fitted parameters to the accumulation model in eq. (5.12) for the TZN glasses doped with varying concentrations of Er^{3+}. The ablation threshold F_{th} values are given in J/cm^2. 81

5.12 (a) The volume of the ablated craters as a function of the logarithm of the laser fluence. A linear fit through the first three data points of single pulse craters and extrapolation to zero gives $F_{\text{th}}(1) = 0.38$ and 0.621 J/cm^2 for $w_0 = 32.0$ and 13.8 μm, respectively. (b) Volume per pulse per unit of energy as a function of the logarithm of the laser fluence. . . 84

6.1 Schematic diagrams of non-radiative de-excitation energy transfer processes from Er^{3+} (right) to Si (left); (a) Auger quenching with free electrons, (b) Auger quenching with holes, (c) energy backtransfer. The Si conduction band is denoted C, the valence band is denoted V and E_F denotes the Fermi level. Schematic reproduced from [201]. 88

6.2 SEM images of depositions at a spot size of $A = 8.57 \times 10^{-5}$ cm^2 and varying laser fluences; (a) $F = 0.20$ J/cm^2, (b) $F = 0.73$ J/cm^2, (c) $F = 1.25$ J/cm^2, (d) $F = 2.05$ J/cm^2, (e) $F = 3.32$ J/cm^2, (f) $F = 5.31$ J/cm^2. 92

6.3 Particle size distribution for a deposition at 0.2 J/cm^2. Bin sizes were 5 nm. The fitted log-normal distribution (black line) had an average radius of 12 nm and a standard deviation of 8.6 nm. 94

6.4 The maximum particle sizes (dashed line) and corresponding film thickness (solid line) against laser fluence. Values are measured from SEM images of several locations on the sample. 94

6.5 Cross section SEM images of depositions at a spot size of $A = 8.6 \times 10^{-5}$ cm^2 and varying laser fluences; (a) $F = 1.25$ J/cm^2, (b) $F = 2.05$ J/cm^2, (c) $F = 3.32$ J/cm^2 and (d) 5.13 J/cm^2. Note that (d) has a different scale bar to the other images. The Si substrate is indicated with text and the NP deposited films with arrows. 95

6.6 Grazing incidence X-ray diffraction patterns for the film deposited at a laser fluence of 3.32 J/cm^2 with (a) linear and (b) logarithmic intensity scales. The peaks correspond to γ-TeO_2 and $Zn_2Te_3O_8$, and are identified in the text. 96

6.7 SEM images of depositions at different laser fluences F and two target surface roughnesses. Ablation using the target polished to a lower surface roughness of $R_a \sim 5$ nm requires a much higher F to give an equivalent deposited volume as with a rougher, $R_a \sim 108$ nm, target. 100
6.8 Photoluminescence (a) spectra and (b) decay of the particulate depositions at varying fluences. Shaded blue region in (a) shows the spectra of the 1ErTZN target glass for reference. 103
6.9 The radiative decay rate of perpendicular $\perp$, parallel $\parallel$ and randomly Avg $= (2/3) \parallel + (1/3)\perp$ orientated dipole compared to the free space decay rate at $\lambda = 1540$ nm as a function of position in a multilayer structure; Si substrate at $z \to -\infty$, (a) 50 nm or (b) 1540 nm thick tellurite film, air superstrate at $z \to \infty$. Light blue shaded region indicates the refractive index of the layer and vertical black lines indicate the boundaries of the layers. 105
6.10 Lifetime measured from the NP depositions at varying fluences compared to theoretical simulation of the average dipole decay rate within the film. Left scale shows the lifetime normalised to the bulk value (Purcell factor), which for experimental measurements is chosen to be 3.45 ms and theoretical calculations is $(1/n_{bulk})$ ms. Right scale shows the measured lifetime of the depositions. The 1ErTZN target had a lifetime of 4.34 ms. 106

7.1 Photographs of room temperature depositions (a, b, c, d) and post heat treatment (e, f, g, h) on silica (a, c, e, g) and silicon (b, f, d, h) substrates. 117
7.2 UV-VIS transmission measurement of deposited nanoparticle films on silica at two fluences. Measurements performed using a pristine silica substrate in reference beam path. Rayleigh scattering by the nanoparticle depositions results in the reduction in transmittance. 118
7.3 Optical microscopy of room temperature depositions on silicon pre (a, b) and post heat treatment (c, d). 119
7.4 SEM images of room temperature depositions on silicon post heat treatment at two different laser fluences. The features in (a) were measured by EDX and identified as fluorine contamination. The crystalline features seen in (b) grew with heating. 120

7.5 EDX images of room temperature depositions at $F = 2.08$ J/cm^2 on Si post heat treatment, fig. 7.4(b). The large crystalline features are composed of elements in the erbium doped TZN target glass. Oxygen appears over the entire surface and indicates that a it has formed a silica with the silicon substrate while the remainder of the target glass elements have evaporated off. 121
7.6 Photoluminescence (a) spectra and (b) decay of $F = 2.08$ J/cm^2 depositions on Si substrates. Light blue shaded region in (a) shows the spectra of the 1ErTZN target glass for reference. The narrowing in spectra and shift in peak wavelength upon heat treatment indicates that the Er^{3+} ions transition from a tellurite to a silica environment. 122
7.7 Optical microscopy of room temperature depositions on silica pre (a, b) and post heat treatment (c, d). 124
7.8 SEM images of room temperature depositions on silica post heat treatment at two laser fluences. The crystalline features in (a) were crystabolites as EDX only detected the elements Si and O and result from stress induced in the substrate by the high energy electrons and ions in the plume. 125
7.9 EDX images of room temperature depositions at $F = 2.08$ J/cm^2 on silica post heat treatment, fig. 7.8(b). The crystalline features correspond to the regions concentrated in Te. 125
7.10 Photoluminescence (a) spectra and (b) decay of $F = 2.08$ J/cm^2 depositions on silica substrates. Light blue shaded region in (a) shows the spectra of the 1ErTZN target glass for reference. The decrease in lifetime after annealing, due to the appearance of a second shorter exponential component is due to the Er^{3+} ions forming clusters. 127
7.11 Photographs of heated depositions at varying fluences on different substrates. Left column (a, c, f, i) Si substrate, middle column (d, g, j) SOS, right column (b, e, h, k) SiO_2 substrate. 130
7.12 Optical microscopy images of heated depositions on Si substrates. Note (d) has a different scale bar to the other images. 132

7.13 SEM images of heated depositions at two laser fluences on Si substrates. Inset in (a) shows a higher magnification image of gold nanoparticle clusters. Note that the black spots seen in (a) are not physical and are due to charging effects. 133
7.14 EDX images of heated depositions at $F = 1.04$ J/cm^2 on Si substrate corresponding to the SEM image in fig. 7.13(a). The spots on the target surface are droplets of target glass that have not evaporated. 133
7.15 The size distribution of the 23 Au clusters shown in the inset of fig. 7.13(a) fitted with a log-normal distribution of mean 13.6 nm and standard deviation of 4.3 nm. 134
7.16 EDX images of the transition between the ring structured and the smooth cracked film in the heated deposition at $F = 4.27$ J/cm^2 on Si substrate in fig. 7.13(b). 135
7.17 EDX images of the feature surrounded by a circular crack in the heated deposition at $F = 4.27$ J/cm^2 on Si substrate in fig. 7.13(b). 135
7.18 Photoluminescence (a) spectra and (b) decay of the films on Si substrates. Light blue shaded region in (a) shows the spectra of the 1ErTZN target glass, which had a FWHM of 68.0 nm, for reference. 137
7.19 Optical microscopy images of films on SOS substrates. Cracking occurs only for the highest fluence due to the increase in film thickness and density. Images (c) and (d) are the same sample but at different magnifications. 139
7.20 SEM images of films fabricated at $F = 4.27$ J/cm^2 on SOS substrates. Inset in (a) shows a higher magnification of one of the islands of Au clusters. The cracking occurred upon cooling due to the the high thickness of the film an the mismatch in CTE and the substrate. 140
7.21 The size distribution of the Au clusters shown in the inset of fig. 7.20(a) fitted with a log-normal distribution of mean 72.4 nm and standard deviation of 31.1 nm. 141
7.22 EDX images of a film fabricated at $F = 4.27$ J/cm^2 on SOS substrates, corresponding to the SEM image in fig. 7.20(b). Note that the Er signal is not shown due to low signal to noise. 141

7.23 Photoluminescence (a) spectra and (b) decay of films fabricated on SOS substrates. Light blue shaded region in (a) shows the spectra of the 1ErTZN target glass, which had a FWHM of 68.0 nm, for reference. . . 142
7.24 Optical microscopy images of films fabricated on SiO_2 substrates at different laser fluences. 144
7.25 SEM image of a droplet on a film fabricated at $F = 1.04$ J/cm^2 on SiO_2 substrate. Droplets appear as dark spots in the optical microscopy images in fig. 7.24(a). 144
7.26 EDX images of a droplet on a film fabricated at $F = 1.04$ J/cm^2 on a SiO_2 substrate. The region corresponds to the SEM image in fig. 7.25. . 145
7.27 Photoluminescence (a) spectra and (b) decay of films fabricated on SiO_2 substrates at different laser fluences. Light blue shaded region in (a) shows the spectra of the 1ErTZN target glass for reference. 146
7.28 AFM images of films fabricated at $F = 1.56$ J/cm^2 on (a) Si, (b) SOS and (c) SiO_2 substrates. 148
7.29 Backscattered electron SEM cross-sectional images of films fabricated at $F = 1.56$ J/cm^2 on Si, SOS and SiO_2 substrates. The features seen in the substrates are due to slight variations in the polish. Inset in (a) shows a higher resolution image of the crystalline structures. 149
7.30 Optical model fitted to the ellipsometry data for the thin film fabricated at $F = 1.56$ J/cm^2 on SiO_2 (Spectrosil 2000). The transparent film has a slight linear index grading resulting from the dissolution process during film formation. The raw data is given in appendix E.3.1. 151
7.31 Photoluminescence (a) spectra and (b) decay of films fabricated at 1.56 J/cm^2 on various substrates; Silicon (Si), fused silica (SiO_2) and 10 μm silica-on-silicon. Light blue shaded region in (a) shows the spectra of the 1ErTZN target glass for reference. 154

7.32 The radiative decay rate of perpendicular $\perp$, parallel $\parallel$ and randomly Avg $= (2/3) \parallel + (1/3) \perp$ orientated dipole compared to the free space decay rate at $\lambda = 1540$ nm as a function of position in a multilayer structure; SiO_2 substrate at $z \to -\infty$, hybrid tellurite-silica film of ($n = 1.611$, $d = 297$ nm), air superstrate at $z \to \infty$. The parameters are the same as measured in table 7.6. Light blue shaded regions indicate the refractive index of each layer and vertical black lines indicate the boundaries of the layers. The average purcell factor $F_p = \Gamma/\Gamma_0$ within the film was 1.31. . 155
7.33 Photographs of the Er^{3+}-doped target at various stages of processing; (a) Polished with P320 SiC paper prior to processing, (b) post processing with $F = 1.56$ J/cm^2 at 600°C in vacuum and (c) post processing with $F = 1.56$ J/cm^2 at 700°C in an O_2 atmosphere of 100 mTorr. In (b) and (c), the laser raster area on the target can be seen, however the increased heating in (c) causes the target surface to melt and become shiny (i.e. smoother). 156
7.34 Optical microscopy images of films fabricated at different temperatures in an oxygen atmosphere on SOS substrates. 157
7.35 Photoluminescence (a) spectra and (b) lifetime of SOS substrates at varying deposition temperatures in an oxygen atmosphere. 159
7.36 Optical microscopy images of films fabricated on SiO_2 substrates at different temperatures in an oxygen atmosphere. 161
7.37 Photoluminescence (a) spectra and (b) lifetime of films on silica substrates fabricated at varying deposition temperatures in an oxygen atmosphere. 162

8.1 Relative concentration of OH-groups at a depth H from the surface of a KU-1 (type III silica) glass plate after annealing for 1.5 hours at varying temperatures T. The entire modified surface layer is shown in (a) and the region 1 μm below the surface is shown in (b). 169
8.2 Transmission measurements of 1.1 mm thick glass substrates. Data from UV-vis-NIR and FT-IR is joined at 2.5 μm. The strong absorption below 2400 cm^{-1} is attributed to the excitation of Si-O vibrations. 172

8.3 Transmission spectra near the free OH absorption peak at $\sim$3670 cm^{-1} with cubic spline baseline (dashed) evaluated from the points marked with filled circles. The peak location is denoted with a vertical red line and the height from the baseline is evaluated at this location. 174
8.4 Optical microscopy of the thin films on different glass substrates. 175
8.5 Ellipsometry fits of a graded wavelength independent refractive index thin film on different glass substrates. 176
8.6 Photoluminescence (a) spectra and (b) lifetime of different glass substrates. Shadowed fill plot in (a) shows the spectra of the 1ErTZN target glass for reference. 177
8.7 The radiative decay rate of perpendicular $\perp$, parallel $\|$ and randomly Avg = $(2/3)\,\| + (1/3)\perp$ orientated dipole compared to the free space decay rate at $\lambda = 1540$ nm as a function of position in the film; Glass substrate is at $z \to -\infty$ and the air superstrate is at $z \to \infty$ and the film in between is plotted. The values for the film thickness, (average) film and substrate refractive index are given in table 8.3. Shaded light blue region indicates the refractive index of the layer. $\mathrm{F_p}$ gives the average Purcell factor (Γ/Γ_0) for randomly orientated dipoles at all locations within the film. 181
8.8 PL decay rate for thin films fabricated on four different glasses as a function of OH concentration in the bulk glass. The borosilicate glass has a PL higher decay rate to the silica glasses due to boron related defects caused by the high energy ions and electrons in the plume. The PL decay rates of the silica glasses show no/slight decreasing dependence with an increase in OH content, which is because the surface layer is dehydroxylated during processing. 182
8.9 PL decay rate for films fabricated on SiO_2 glass substrates (Infrasil 301, Corning 7980 and Spectrosil 2000) as a function of the film inhomogenity (index grading from top to bottom of the film). The films with lower inhomogenity have improved dissolution and surface dissolution, due to increased radiative heating, and therefore have lower PL decay rates. Radiative heating of the bulk in these substrates was determined by the impurity OH content. 184

B.1 Schematic of a multilayered structure consisting of M layers between a semi-infinite transparent ambient medium ($j = 0$) and a semi-infinite substrate ($j =$ M+1). Each layer j ($j = 1, 2, ..., $M) has a thickness d_j and is described by its complex index of refraction n_j. 217
B.2 Monochromatic electromagnetic plane wave incident on an dielectric interface. 221
B.3 Schematic of a multilayered structure consisting of M layers between a semi-infinite transparent ambient medium ($j = 0$) and a semi-infinite substrate ($j =$ M+1). Each layer j ($j = 1, 2, ..., $M) has a thickness d_j and is described by its complex index of refraction n_j. The electric (shown) and magnetic field within each layer is described by the superposition of a forward and a backward propagating field. 226

C.1 Typical emission spectra of (a) an infrared heating lamp [248] and (b) a SiC heating element [249]. The quartz infrared heating lamps in the system described in section 4.3 correspond to the medium wave spectra in section 4.3(a). 234

D.1 Optical microscopy images of the various stages of lapping and polishing the zinc-sodium tellurite glass. 236

E.1 VASE measurements of psi and delta with the fitted optical model (black dashed line). 242
E.2 Refractive index of the targets at a function of wavelength. 243
E.3 VASE measurements of psi and delta with the fitted optical model (black dashed line). 245
E.4 Refractive index of the glass substrate at a function of wavelength. . . . 246
E.5 VASE measurements of psi and delta for thin film fabricated at $F = 1.56$ J/cm^2 on Spectrosil 2000 with the fitted optical model (black dashed line).248
E.6 VASE measurements of psi and delta for thin films fabricated on different glass substrates with the fitted optical model (black dashed line). 249

F.1 SiO_2 substrate sample processed at $F = 1.56$ J/cm^2 (a) pre and (b) post heat treatment. The cutout in the sample in (b) is where a section was taken for cross-sectional SEM analysis. 251

F.2 Photoluminescence (a) spectra and (b) decay of SiO_2 substrate samples. Shadowed fill plot in (a) shows the spectra of the 1ErTZN target glass for reference. 252

Abbreviations

A	Acceptor
AFM	Atomic force microscopy
BSE	Backscattered electron
CTE	Coefficient of Thermal Expansion
D	Donor
DDI	Dipole-dipole interaction
DIC	Differential interference contrast
EDFA	Erbium doped fiber amplifier
EDWA	Erbium doped waveguide amplifier
FIB	Focused ion beam
fs	Femtosecond
FT-IR	Fourier-transform infrared spectroscopy
FWHM	Full width half maximum
GIXRD	Grazing incidence X-ray diffraction
HAADF	High angle angular dark field
IR	Infrared
LDoS	Local density of states
MSE	Mean square error
NIR	Near-infrared
NP	Nanoparticles
ns	Nanosecond
PES	Potential energy surface
PIC	Photonic integrated circuit
PIQ	Pair-induced quenching
PL	Photoluminescence
PLD	Pulsed laser deposition
ps	Picosecond
QE	Quantum efficiency
RBS	Rutherford backscattering spectrometry

RE	Rare-earth
RPM	Revolutions per minute
SAED	Selected area electron diffraction
SE	Spontaneous emission
SEM	Scanning electron microscopy
Si	Silicon
SiO_2	Silica
SOS	Silica-on-silicon
TZN	Zinc-sodium tellurite
TEM	Transmission electron microscopy
ULPD	Ultrafast laser plasma doping
UV	Ultraviolet
VASE	Variable angle spectroscopic ellipsometry
XRD	X-ray diffraction

Symbols

at. %	Atomic percent
α	Absorption coefficient [cm^{-1}]
λ	Wavelength [nm or μm]
σ_{em}	Stimulated emission cross-section [cm^2]
ω	Angular frequency [rad/s]
$\hbar$	Reduced Planck's constant $h/2\pi$
Γ	Decay rate [s^{-1}]
Γ_{rad}	Radiative decay rate [s^{-1}]
Γ_{nrad}	Non-radiative decay rate [s^{-1}]
$\hat{H}$	Hamiltonian
C_{up}	Upconversion coefficient [cm^6 s^{-1}]
E_p	Pulse energy [μJ]
F	Laser fluence [J/cm^2]
$\mathrm{F_p}$	Purcell factor, $= \Gamma/\Gamma_0$
k	Extinction coefficient of the medium
n	Refractive index of the medium
R_0	Förster distance [Å]
Ra	Average surface roughness [nm]
Rms	Root mean square surface roughness [nm]
T	Temperature [°C or K]
T_g	Glass transition temperature [°C or K]
T_x	Glass onset of crystallisation temperature [°C or K]
T_m	Glass onset of melting temperature [°C or K]
τ	Photoluminescent lifetime [ms]
τ_{rad}	Radiative lifetime [ms]
τ_{nrad}	Non-radiative lifetime [ms]

Chapter 1

Introduction

1.1 Research Motivation

Thin film coatings provide unique electrical, mechanical, thermal, chemical and optical properties to the surface of a bulk material. The typical thicknesses range from several nanometers to tens of microns. The ability to functionalise a surface without modifying the bulk properties has widespread uses in modern technology ranging from display to biomedical to energy fields. For example, coating crown glass with approximately 100 nm of magnesium fluoride (MGF_2) provides a cheap and simple means to achieve anti-reflective properties. Alternatively, an aluminium coating can make the glass highly reflecting [1].

In the field of photonics there is great interest in doping rare-earth ions into thin films and bulk materials to provide the unique spectroscopic properties required for optical devices, such as miniature sensors, lasers and waveguide amplifiers. In particular, the development of photonic integrated circuits (PICs) is seen as a solution to cope with the surge in demand for high speed data. The functional photonic components that make up PICs include optical filters, lasers, waveguide arrays, splitters, modulators, and photodetectors. With an increasing number of components, propagation and interconnect losses become evermore significant and an optical waveguide amplifier is required to compensate for the optical losses in the circuits [2]. The waveguide structure consists of a high dielectric index core surrounded by a lower dielectric index cladding on top of the PIC substrate. Electromagnetic waves can be confined and transmitted within the core through total internal reflection. Silicon based PICs

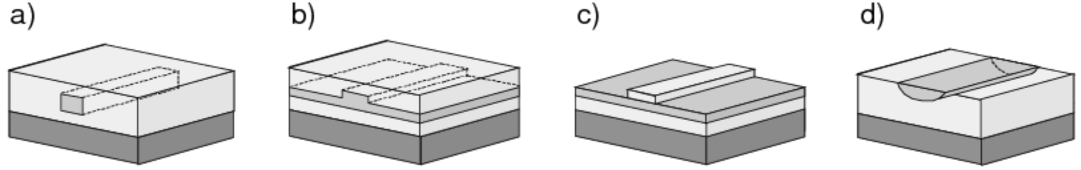

Figure 1.1: Schematic representation of waveguide structures that can be used to fabricate a planar optical waveguide amplifier. Light is confined in the high refractive index waveguide core (medium grey) by total internal reflection. The Er doped core material is embedded in a low refractive index cladding layer (light grey). The device rests on a silicon substrate (dark grey). The waveguide structures are (a) a channel waveguide, (b) a ridge waveguide, (c) a strip loaded waveguide and (d) a diffused waveguide. Figure replicated from [2].

allow for co-integration with transistor based electronics and, as silica-on-silicon (SOS) substrates are readily available, the cladding layer below the core is typically thermally grown silica. The most commonly reported waveguide structures are depicted in fig. 1.1 and include channel/buried, strip-loaded, rib, diffused and ridge waveguides [2, 3]. Light amplification is achieved through stimulated emission of ions doped in the core that have been excited with an external pump laser.

In optical fibre technology, erbium-doped fibre amplifiers (EDFAs) are already in widespread use for long distance communication links [4]. The success of using the optical transition of Er^{3+} ions at 1.54 μm, which lies in the low-loss C band window of silica (1530 to 1565 nm), has set a standard for optical telecommunications. Similar in principle, the development of a compact planar erbium-doped waveguide amplifier (EDWA) for PICs is of interest. To provide sufficient gain over several centimetres in the EDWA, optically active Er^{3+}-doping concentrations in the range of 10^{19} - 10^{20} cm^{-3} (0.1 - 1 at.%), without significant shortening of the photoluminescence lifetime, are required as the emission cross-section σ_{em} of Er^{3+} in silica is typically only 10^{-21} - 10^{-20} cm^2 [2, 5, 6]. At such high doping densities, the distance between ions becomes small enough so that electric dipole-dipole interactions between Er^{3+} ions become significant, which can lead to an increase in non-radiative decay. These interactions are termed concentration quenching effects as they depend on the doping concentration and act to reduce the quantum efficiency and, often, the photoluminescence lifetime. Silica based EDWAs are preferred for compatibility with well-developed silica based

fibre optics (matching the refractive index reduces coupling losses) and complementary metal–oxide–semiconductor (CMOS) processing. The rare-earth ion solubility of pure silica is, however, limited at 0.7×10^{18} cm^{-3} [7]. To overcome this barrier, the addition of network modifiers, such as phosphourous and aluminium [8], has proven effective.

Pan et al. [9] fabricated a 20 cm long aluminosilicate buried channel waveguide (1.2 μm thick by 4.2 μm wide) with an Er^{3+}-doping concentration of 2.9×10^{20} cm^{-3}, using physical vapour deposition (PVD) followed by standard photolithographic and reactive ion etch processes. The waveguide was pumped with 176 mW at 976nm producing a net gain of $\sim$ 1 dB/cm. Critical to the waveguide gain performance is the propagation loss, which occurs due to scattering by roughness at the core/cladding interfaces or by defects/impurities within the core. Owing to the low film roughnesses of the PVD technique combined with the well established etch process for aluminosilicate, the waveguides had an exceptionally low loss of 0.05 dB/cm. Nonetheless, the long length of the waveguide limits its use. Shuto et al. [10] fabricated a 7.5 cm long buried phosphosilicate EDWA using plasma enhanced chemical vapour deposition (PECDV) for the core and flame hydrolysis deposition (FHD) for the silica cladding. The Er^{3+}-doping concentration was 0.4×10^{20} cm^{-3} and the waveguide loss was 0.17 dB/cm. They achieved a net gain of 0.67 dB/cm by pumping with 420 mW at 980 nm. Other sililca based glasses that have been used for EDWAs include soda lime silicate (0.76 dB/cm net gain, 0.1 dB/cm loss) [11], SiO_2-GeO_2 (0.16 dB/cm net gain, 0.06 dB/cm loss) [12], oxyfluoride-silicate (0.92 dB/cm net gain, 1.0 dB/cm loss) [13] and SiO_2-HfO_2 (net gain not reported, 0.8 dB/cm loss) [14].

Standard thin film and doping fabrication techniques such as PECVD, ion implantation, sputtering, FHD and ion exchange all exhibit concentration quenching in silica based glasses at modest doping levels of $\sim 10^{20}$ cm^{-3} due to clustering of the rare-earth ions that reduces the ion-ion separation distances [6]. The fabrication of shorter waveguides that provide an equivalent gain requires greater doping concentrations. As such, the use of non-silica glasses (tellurite [15], phosphate [16] and bismuthate [17, 18]), ceramics (Al_2O_3 [19], zirconia [20]) and polymers (PMMA [21]) for EDWAs have also been explored. Tellurite glasses are attractive hosts as they exhibit high rare-earth ion solubility, wide bandwidth and high refractive index (which leads to improved waveguide mode confinement and rare-earth ion absorption/emission cross-sections). A 5 cm

long ridge EDWAs in tellurite glass doped at a concentration of 2.2×10^{20} cm^{-3} produced an optical gain of 2.8 dB/cm and a loss of 0.6 dB/cm when pumped at 1480 nm with 250 mW [15]. Tellurite glasses are however limited by their low thermal stability [22] and, without the presence of stabilising oxides, low chemical stability that renders them impractical. To overcome this limitation, a novel thin film fabrication technique developed at The University of Leeds termed ultrafast laser plasma doping (ULPD), has proven capable of forming hybrid tellurite-silica films with the high Er^{3+}-doping level required without clustering and significant shortening of the metastable photoluminescence lifetime [6, 23, 24]. The best ever lifetime-density product of 0.96×10^{19} s·cm^{-3} was achieved on a silica platform at an Er^{3+}-doping concentration of 0.91×10^{21} cm^{-3} (1.4 at.%) [6]. The technique shares similarities with pulsed laser deposition techniques in that a femtosecond laser is used to ablate a rare-earth doped tellurite target glass and the resulting plume is collected on substrate to form a film. The ULPD technique is unique in that the silica or silica-on-silicon substrate is heated at hundreds of degrees so that a metastable hybrid tellurite-silica glass material is formed within the glass. The ULPD technique has also been proven for doping and co-doping other rare-earth ions Tm^{3+} and Yb^{3+} [23, 25]. Despite the superior spectroscopic proprieties of the material, and the macroscopic properties of the thin films typically suffer from a combination of inhomogeneous refractive index distributions, high surface roughness, cracking and batch to batch variation. These limitations must be overcome before the technology may be exploited for optical devices such as sensors, lasers and waveguide amplifiers, which require a high film quality. Due to the novelty of the ULPD technique, previous experiments have mostly been single attempts and lack systematic work based on the underlying physics to optimise the experimental parameters. The goal of this research is to define the parameter space from first principles such that high quality films with a controllable growth rate can be fabricated reliably, thus paving the way for direct implementation of the technology for photonics devices.

1.2 Thesis Overview

This thesis describes the research and development in characterising and optimising the ULPD technique for the fabrication of Er^{3+}-doped hybrid tellurite-silica thin glass films. In particular, the thesis covers the following achievements (I) characterisation of

femtosecond laser ablation of tellurite glass in dependence of pulse number and laser fluence, (II) characterisation of the nanoparticles in the femtosecond laser ablation plume in dependence of laser fluence, (III) demonstration of sub-micron film formation in a vacuum with the ULPD technique (IV) identification of dehydroxylation at the silica surface during processing with the ULPD technique and its role on film formation and photoluminescence.

The thesis is structured as follows:

Chapter 2 provides an overview of environmental and atomic interactions that lead to the transfer of energy from an excited atom and forms the theoretical basis for photoluminescence characterisation of the films fabricated with the ULPD technique. Radiative decay by spontaneous emission results in the emission of a photon. The rate at which this occurs is dependent on the photonic environment and the special case of an atom inside a multilayer dielectric structure is considered. Next, the radiative and non-radiative energy transfer processes that result in the transfer of an excitation to another atom are described.

Chapter 3 presents the properties of trivalent erbium (Er^{3+}) in glasses relating to optical applications utilising the photoluminescence emission at 1540 nm. It contains detailed information on the electron configuration, the ionic energy spectrum and erbium specific dipole-dipole interactions (expanding on the discussion in the preceding chapter). Particular attention is given to undesirable concentration quenching effects that manifest as a reduction in the quantum efficiency and a reduction of the photoluminescent lifetime.

Chapter 4 summarises the development of the ULPD technique and key results of the rare-earth doped hybrid tellurite-silica thin glass films fabricated. A description of ultrafast laser ablation of dielectrics and film formation based on theoretical and experimental findings are then presented. The experimental setup of the system, which has superseded an older system, is detailed next and finally the optimisation methodology used in this research is presented.

The next 4 chapters concern the scientific results of this thesis. These chapters all follow the same structure with a brief introduction of the relevant literature at the start followed by the theoretical background specific to the chapter. The experimental procedure is then detailed followed by the results and discussion. The conclusion at the end of the chapter summarises the key findings of the research.

Chapter 5 contains our publication on the femtosecond laser ablation threshold of Er^{3+}-doped zinc-sodium tellurite glass:

Thomas Mann et al. “Femtosecond laser ablation properties of Er3+ ion doped zinc-sodium tellurite glass”. *Journal of Applied Physics* 124.4 (2018), p. 044903

It presents detailed information on the ablation threshold, material incubation and crater size of zinc-sodium tellurite glass irradiated with 800 nm, 100 fs pulse width laser light at two focal spot sizes. Importantly it is found that the ablation properties do not change significantly for low rare-earth ion doping concentrations.

Chapter 6 presents fundamental research characterising the physical, structural and photoluminescence properties of femtosecond pulsed laser deposited thin films on silicon substrates. From this, the laser fluence regime corresponding to an ablation plume predominantly composed of nanoparticles is inferred. Photoluminescence studies of the Er^{3+}-doped films reveal non-radiative energy transfer processes to silicon that act to shorten the metastable lifetime and reduce the quantum efficiency.

Chapter 7 analyses the film formation with the ULPD technique for silicon, silica and silica-on-silicon substrates. The role of heat treatment, laser fluence, substrate temperature, deposition rate and background oxygen gas are systematically investigated to find the optimum processing parameters.

Chapter 8 investigates the role of surface dehydroxylation that occurs due to the high processing temperature used during the ULPD technique on film formation and concentration quenching by energy migration. The substrate surface dehydroxylation

is found to play an important role during dissolution and manifests itself in the refractive index grading of the thin film. Photoluminescence studies show that despite the high concentration of Er^{3+} ions the low measured decay rates result from the lack of OH-group quenching sites in the dehydroxylated surface layer, which mitigates the effect of energy migration. It is concluded that the substrate OH-group content actually serves to improve heating of the silica substrates by radiative absorption thus producing higher quality films.

Finally, chapter 9 concludes the thesis with an outlook on possible future directions for the ULPD technique with a focus on developing photonic devices.

Chapter 2

Light emission and energy transfer

The scope of this chapter is to review radiative emission of an excited atom and electrodynamic energy transfer between atoms. First section 2.1 gives an introduction to the chapter. Section 2.2 presents the spontaneous emission rate of independent atoms with respect to the environment. Next, in section 2.3 the electrodynamic energy transfer between atoms is discussed, with particular attention given to the dipole-dipole interactions.

2.1 Introduction

The energetic interaction of atoms and molecules with their environment or other atoms and molecules resulting in modified fluorescence intensities and decay rates are widely researched for both fundamental and practical interest. An excited atom or molecule interacts with its environment by emitting a photon into the electromagnetic field and transitioning to a lower energy state. The process is described by the quantum mechanical process spontaneous emission (SE) and is illustrated in fig. 2.1a. The SE rate is proportional to the density of photonic modes of the environment, which can be controlled using engineered photonic structures. Enhancing the SE rate is particularly of interest for single photon sources [28, 29], while suppression is beneficial for applications where population inversion is desired, such as waveguide amplifiers and lasers. The position dependence of such effects has also led to the demonstration of optical

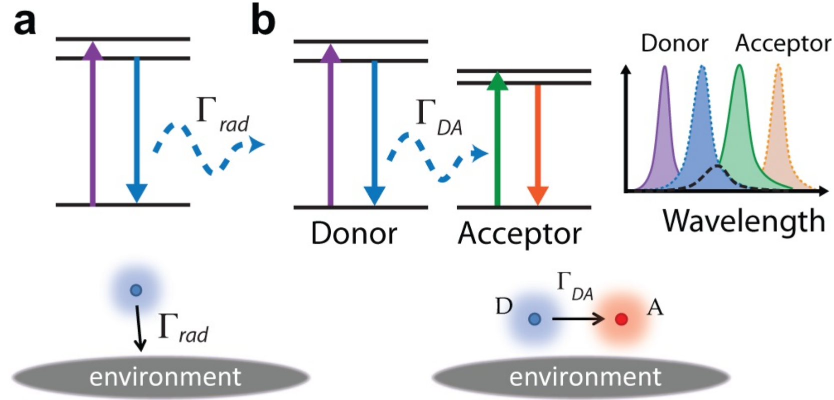

Figure 2.1: (a) Energy-level diagram depicting spontaneous emission. The spontaneous emission rate Γ_{rad} is the rate of radiative energy transfer to any location in the environment. The acceptor is not considered as part of the environment. (b) Energy-level diagram depicting energy transfer between two neighbouring atoms or molecules, denoted as donor (D) and acceptor (A), due to a Coulombic interaction (virtual photon exchange, non-radiative) or real photon exchange (radiative). The donor and acceptor must have overlapping emission and absorption spectra, respectively, and the rate of transfer to the acceptor is denoted Γ_{DA}. Figure adapted from [27].

distance rulers capable of measuring from the sub-nanometer to 100 nm range [30].

The electrodynamic interactions between two neighbouring atoms or molecules denoted as donor (D) and acceptor (A) with overlapping emission and absorption spectra, respectively, occurs through non-radiative (virtual photon exchange) and radiative (real photon exchange) means depending on their separation distance. The incoherent and irreversible process is illustrated in fig. 2.1b. The atom-atom interactions in homogeneous media are mediated by a propagating field with an expanding wavefront. As such, the amplitude of the radiated field decays inversely with distance and so the short ranged interactions are typically only significant for a separation of less than a few wavelengths [31]. In particular, the non-radiative dipole-dipole energy transfer, Förster resonance energy transfer (FRET), that is inversely proportional to the sixth power of the D-A separation distance, typically has a range between 1 and 10 nm and manifests itself in the quenching of the donor's fluorescence intensity and lifetime.

The range of dipole-dipole interactions are the strongest and longest compared to higher order multipolar interactions and so FRET is widely used across all of the sciences. The range of FRET is particularly suited to biological systems as it is of a similar

scale to the diameter of many proteins, the thickness of biological membranes and the distance between sites on multisubunit proteins [32]. It is for this reason that FRET is often called a 'spectroscopic ruler' [33]. Other applications range from imaging cellular processes to energy harvesting to molecular sensing [27, 32, 34]. In rare-earth doped media, the dipole-dipole interactions become significant and detrimental at lower ion-ion distances (i.e. high doping concentrations) as they act to reduce the quantum efficiency and photoluminescence lifetime of optical devices through concentration quenching effects. FRET interactions can lead to upconversion, a process in which the acceptor is multiply excited and radiatively decays by emission of a photon with a higher frequency than the excitation frequency (anti-Stokes emission). This phenomenon has been used in optical devices such as infrared quantum counter detectors, temperature sensors and compact solid state lasers [34]. The interactions between erbium ions will be discussed further in chapter 3.

Improvements in our understanding of FRET paves the way for ever more innovative ways to engineer the dipolar interactions between atoms for novel atomic-based technologies. A notable recent example is the research by Solano et al. [31], in which the interaction range of FRET was increased to atom-atom separations of hundreds of resonant wavelengths by confining the field in a one-dimensional optical fibre to create super-radiance atomic states. The theoretical work by Cortes and Jacob [27] has revealed the strong dependence of FRET on the photonic environment and that through a suppression of the SE rate it is possible to enhance the efficiency of the FRET process by more than 300 %.

2.2 Spontaneous emission

Spontaneous emission (SE) is the process in which a quantum mechanical system, such as an atom, transitions from an excited state to a lower energy state, e.g. the ground state, through the emission of a photon into the electromagnetic field (radiative decay), as shown in fig. 2.1a. Luminescence is a special case of SE in which the excitation does not result from heat and photoluminescence is SE following the absorption of photons.

So long as the coupling between the atom and the electromagnetic field is weak, the SE rate can be explained by both classical electromagnetism and in the framework of quantum electrodynamics. Classically, the SE rate is proportional to the power

dissipated by a self-driven dipole interfering with it's reflected field emitted at a previous time and is proportional to the square of the electric field strength at the origin of the dipole [35]. In the framework of quantum electrodynamics, SE is stimulated by zero-point fluctuations of the electromagnetic field [36]. The description of the SE rate in this section follows the quantum-electrodynamical formalism by Creatore and Andreani [36] (in Gaussian units) and assumes a non-uniform isotropic dielectric medium with a unit magnetic permeability and the absence of external charges.

The total Hamiltonian for a two-level atom initially in the excited state $|x\rangle$ of energy $\hbar\omega_x$ that undergoes spontaneous dipole transition to its ground state $|g\rangle$ of energy $\hbar\omega_g$ through the emission of a photon into the electromagnetic field with energy $\hbar\omega_0 = \hbar\omega_x - \hbar\omega_g$ can be written as

$$\hat{H} = \hat{H}_\gamma + \hat{H}_A + \hat{H}_{\gamma-A}, \tag{2.1}$$

where $\hat{H}_\gamma$ is the free-field Hamiltonian, $\hat{H}_A$ is the free-atom Hamiltonian and $\hat{H}_{\gamma-A}$ is the atom-field interaction term. Following the canonical quantization of the electromagnetic field in a non-uniform isotropic dielectric media, the second-quantized form for the free photon field is

$$\hat{H}_\gamma = \sum_{\mathbf{k},n} \hbar\omega_{\mathbf{k},n} \left(\hat{a}^\dagger_{\mathbf{k}n} \hat{a}_{\mathbf{k}n} + \frac{1}{2} \right), \tag{2.2}$$

where $\hat{a}^\dagger_{\mathbf{k}n}$ and $\hat{a}_{\mathbf{k}n}$ are the Bose creation and destruction operators of field quanta with energies $\hbar\omega_{\mathbf{k}n}$, respectively, satisfying the usual commutation relations

$$\left[\hat{a}_{\mathbf{k}n}, \hat{a}^\dagger_{\mathbf{k}n} \right] = \delta_{\mathbf{k},\mathbf{k}'} \delta_{n,n'}, \quad \left[\hat{a}_{\mathbf{k}n}, \hat{a}_{\mathbf{k}'n'} \right] = \left[\hat{a}^\dagger_{\mathbf{k}n}, \hat{a}^\dagger_{\mathbf{k}'n'} \right] = 0, \tag{2.3}$$

and n is the index labeling the corresponding eigenmode characterised by the wavevector $\mathbf{k}$.

The free-atom Hamiltonian $\hat{H}_A$ is given by,

$$\hat{H}_A = \hbar\omega_x \left| x \right\rangle \left\langle x \right| + \hbar\omega_g \left| g \right\rangle \left\langle g \right|, \tag{2.4}$$

and finally the atom-field interaction term near the atomic resonance $\omega \approx \omega_0$ and in the dipole-approximation, is given by [36, 37]

$$\hat{H}_{\gamma-A} \approx (\hat{\sigma}_{+}\mathbf{d} + \hat{\sigma}_{-}\mathbf{d}^{*}) \cdot \hat{\mathbf{E}}(\mathbf{r}, t), \tag{2.5}$$

where $\hat{\sigma}_{-} = |g\rangle\langle x|$ and $\hat{\sigma}_{+} = |x\rangle\langle g|$ are the atomic down and atomic up- transition operators, respectively, and the dipole matrix element $\mathbf{d} = \langle x|\hat{\mathbf{d}}|g\rangle = |\mathbf{d}|\hat{\varepsilon}_d$ with the atomic dipole operator of the atom located at $\mathbf{r}$ being $\hat{\mathbf{d}} = e\hat{\mathbf{r}}$. The orientation of the dipole is given by $\hat{\varepsilon}_d$. The electric field operator $\hat{\mathbf{E}}(\mathbf{r})$ is derived from the quantized field vector potential and given by [36]

$$\hat{\mathbf{E}}(\mathbf{r}, t) = i \sum_{\mathbf{k},n} (2\pi\hbar\omega_{\mathbf{k},n})^{1/2} [\hat{a}_{\mathbf{k}n}\mathbf{E}_{\mathbf{k}n}(\mathbf{r})e^{-i\omega_{\mathbf{k}n}t} - \hat{a}^{\dagger}_{\mathbf{k}n}\mathbf{E}_{\mathbf{k}n}(\mathbf{r})e^{i\omega_{\mathbf{k}n}t}]. \tag{2.6}$$

The spontaneous emission rate $\Gamma_{\text{rad}} = \Gamma_{\text{rad}}(\mathbf{r})$ of an atom located at position $\mathbf{r}$ is given by Fermi's Golden Rule [38]

$$\Gamma_{\text{rad}}(\mathbf{r}) = \frac{2\pi}{\hbar^2} \left| \langle f| \hat{H}_{\gamma-A} |i\rangle \right|^2 \delta(\omega_i - \omega_f), \tag{2.7}$$

where $|i\rangle$ and $|f\rangle$ are the initial and final states with energies $\hbar\omega_i$ and $\hbar\omega_f$, respectively. By considering the atom-radiation system, the initial state has no photons in the electromagnetic field and the atom in the excited level $|i\rangle = |0\rangle \otimes |x\rangle$ and the final state has a photon of frequency $\omega_{\mathbf{k}n}$ emitted into the electromagnetic field with the atom in the ground state $|f\rangle = |1_{\mathbf{k}n}\rangle \otimes |g\rangle$. Using eq. (2.5) in eq. (2.7) and the standard bosonic commutation rules, the SE rate can be written as [36]

$$\Gamma_{\text{rad}}(\mathbf{r}) = \frac{4\pi^2|\mathbf{d}|^2}{\hbar} \sum_{\mathbf{k},n} |\mathbf{E}_{\mathbf{k}n}(\mathbf{r}) \cdot \hat{\varepsilon}_d|^2 \omega_{\mathbf{k}n} \delta(\omega_i - \omega_f). \tag{2.8}$$

In this form, it is apparent that the decay rate of a dipole is proportional to the square of the electric field amplitude parallel to and at the origin of the dipole once the contribution to the electric field strength from all modes in the system are included. This dependence on the states that can be occupied by a photon, known as the local density of states (LDoS), allows control over the atomic SE rates through modification of the environment (electromagnetic boundary conditions). I.e. when the LDoS is increased or decreased the SE rate is enhanced or suppressed, respectively.

Evaluating the SE rate of a dipole is therefore a matter of first decomposing the electromagnetic field into the normal modes supported by the structure under consideration. The SE rate is then directly retrieved from Fermi's Golden Rule. In the following

subsections, the SE rate for a dipole in a homogeneous dielectric media (homogeneous environment) is presented and then the results of this procedure for the specific case of a multilayer dielectric structure (inhomogeneous environment) is given.

2.2.1 Homogeneous environment

In a vacuum the spontaneous emission rate of a randomly orientated dipole is given by [36]

$$\Gamma_{\text{rad}} = \Gamma_0 = \frac{4\,|\mathbf{d}|\,\omega_0^3}{3\hbar c^3}. \tag{2.9}$$

In a homogeneous dielectric media the SE rate scales with the refractive index $n = \varepsilon^{1/2}$ as [39–41]

$$\Gamma_{\text{rad}} = \varepsilon^{1/2}\Gamma_0. \tag{2.10}$$

It has been shown experimentally by Yablonovitch, Gmitter, and Bhat [42] that the rate of SE is enhanced for $\varepsilon > 1$ and suppressed for $\varepsilon < 1$.

According to the semi-classical theory of radiation, the SE rate (quantum mechanical in origin) is related to the classical dissipated power P by

$$\Gamma_{\text{rad}} = \frac{P}{\hbar\omega} = \frac{|\boldsymbol{\mu}|^2\varepsilon^{1/2}\omega_0^3}{3\hbar c^3}, \tag{2.11}$$

where the dipole moment $\boldsymbol{\mu}$ is taken to be twice the quantum mechanical transition dipole moment $\mathbf{d}$ for the radiative transition and P is given by the Lamor formula [35]. Both derivations lead to the same result.

2.2.2 Inhomogeneous environment

The control of the SE rate of a dipole through modification of the LDoS has been investigated for various photonic structures both theoretically and experimentally. Purcell [43] was the first to show an enhancement in the SE for atoms inside a cavity and an inhibition in the SE rate was later shown by Kleppner [44]. Other researchers have investigated a myriad of other systems; Dielectric half-spaces [39, 40, 45], periodic structures [46, 47], slot waveguides [28, 48, 49], dielectric cylindrical waveguides [50], metallic interfaces [35], metallic cavities [51, 52], scattering nanocrystals [53], photonic crystals [54–56]. It is not within the scope of this chapter to review all these methods

and so only the relevant situation of a dipole situated inside a multilayer dielectric structure is considered.

Spontaneous emission in multilayer dielectric media

The derivation of the SE rate of a dipole inside a multilayer dielectric structure as a function of position continues to follow the quantum-electrodynamical formalism by Creatore and Andreani [36] described before. Note that while the derivations are given in Gaussian units, the final results of the SE rates are normalised to the vacuum SE emission rate Γ_0 of a randomly orientated dipole (eq. (2.9)) to give the Purcell factor Γ/Γ_0, which is the figure of merit when analysing SE rates [27].

A schematic of the multilayer dielectric structure under consideration is shown in fig. 2.2. In total, it comprises M + 2 dielectric layers that are parallel to the xy plane and infinite in the x and y axis. The lower (layer 0) and upper (layer M + 1) cladding layers are taken to be semi-infinite and surround the inner M dielectric layers, which each have a thickness of d_j ($j = 1, \ldots, \mathrm{M}$). Each of the M + 2 media is assumed to be lossless, isotropic, and homogeneous along the vertical z direction so that the dielectric constant $\varepsilon(\mathbf{r}) = \varepsilon(\boldsymbol{\rho}, z)$ is a piecewise constant function in the z direction and can be denoted $\varepsilon_j = \varepsilon_j(z)$ in each of the M + 2 dielectric media.

The electromagnetic modes supported by the structure are found as solutions to the eigenvalue problem

$$\nabla \times \left[\frac{1}{\varepsilon(\mathbf{r})} \nabla \times \mathbf{H}\right] = \frac{\omega^2}{c^2}\mathbf{H}, \tag{2.12}$$

which is derived from the homogeneous Maxwell equations for the electric $\mathbf{E}$ and magnetic $\mathbf{H}$ fields having harmonic time dependence $\exp(-i\omega t)$ and the condition $\nabla \cdot \mathbf{H} = 0$. The set of fundamental modes is complete and orthonormal [36]

$$\mathbf{H}(\mathbf{r}) = \sum_\mu c_\mu \mathbf{H}_\mu(\mathbf{r}) \tag{2.13}$$

$$\int \mathbf{H}^*_\mu(\mathbf{r}) \cdot \mathbf{H}_\nu(\mathbf{r}) \mathrm{d}\mathbf{r} = \delta_{\mu\nu}. \tag{2.14}$$

and the electric field eigenmodes are found by application of the Maxwell equation

$$\mathbf{E}(\mathbf{r}) = i\frac{c}{\omega\varepsilon(\mathbf{r})} \nabla \times \mathbf{H}(\mathbf{r}) \tag{2.15}$$

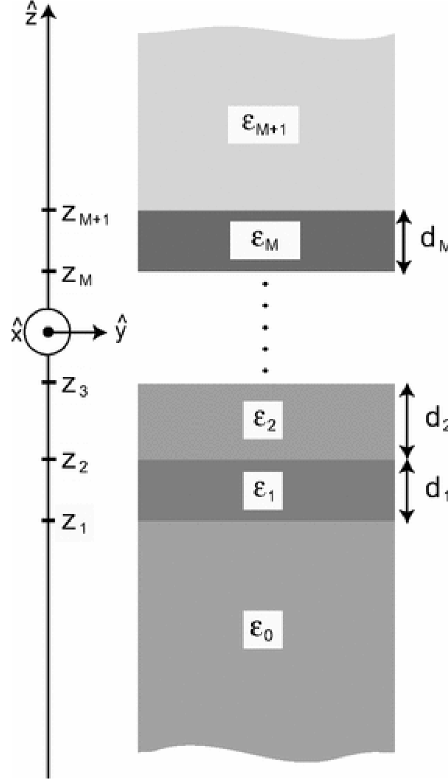

Figure 2.2: Schematic view of the multilayer dielectric structure. The lower (layer 0) and the upper (layer M + 1) claddings with dielectric constants ε_0 and ε_{M+1}, respectively, are taken to be semi-infinite and surround the M dielectric layers, each characterised by a thickness d_j and dielectric constant ε_j for $j = 1, \ldots,$ M. Figure reproduced from [36].

and are orthonormal according to [57]

$$\int \varepsilon(\mathbf{r})\mathbf{E}^*_\mu(\mathbf{r}) \cdot \mathbf{E}_\nu(\mathbf{r})\mathrm{d}\mathbf{r} = \delta_{\mu\nu}. \tag{2.16}$$

In a lossless multilayer dielectric structure, the complete set of orthonormal modes consists of an infinite number of radiative (leaky) modes and a finite number of guided modes. As the structure is homogeneous in the xy plane, field modes are labelled by the in-plane (parallel) component of the wave vector $\mathbf{k}_\parallel = k_\parallel \hat{k}_\parallel = (k_x, k_y)$ and, for guided modes, by a mode index α. Leaky modes either radiate in both the upper and lower cladding or radiate in the cladding with the higher refractive index and are evanescent decreasing in the lower index cladding. The guided modes exist if one of the inner

layers has a dielectric constant higher than either cladding (i.e. $\varepsilon_j = \varepsilon_{\max} > \varepsilon_0, \varepsilon_{M+1}$) and propagate along the dielectric planes in this layer. They have an evanescent field profile in the cladding layers. The radiative decay rate Γ_{rad} inside multilayer dielectric structures is therefore due to the contribution of emission into leaky and guided modes

$$\Gamma_{\text{rad}} = \Gamma_{\text{rad}}^{\text{leaky}} = \Gamma_{\text{rad}}^{\text{gui}}. \tag{2.17}$$

Analytical expressions $\Gamma_{\text{rad}} = \Gamma_\alpha^p(z)$ are derived as functions of emitter position z and transverse electric (TE)/transverse magnetic (TM) polarisations ($p =$ TE, TM) and for both in-plane (horizontal) and perpendicular (vertical) orientated dipoles ($\alpha_\parallel$) lying along the dielectric planes and perpendicular (or vertical) ones ($\alpha_\perp$) oriented along the vertical z-direction. The SE rate into leaky modes are evaluated according to [36]

$$\Gamma_\alpha^p = g_\alpha^p \sum_{j=U,L} \varepsilon_j^{3/2} \int_0^{\pi/2} \left| E_\alpha^p(k_\parallel = k_j \sin\theta, z)\right|^2 \sin\theta d\theta, \tag{2.18}$$

$$g_\parallel^{\text{TE}} = \frac{|\mathbf{d}|^2 \omega_0^3}{2\hbar c^3}, \quad g_\parallel^{\text{TM}} = g_\parallel^{\text{TE}} \frac{c^2}{\omega_0^2[\varepsilon(z)]^2}, \quad g_\perp^{\text{TM}} = 2g_\parallel^{\text{TM}},$$

where $\mathbf{d}$ is the dipole matrix element for a dipole located at z, ω_0 is it's frequency, $\varepsilon(z)$ is the dielectric constant of the dielectric layer in which the dipole is situated. The electric field amplitude $E_\alpha^p(k_\parallel, z)$ is given in appendix A and evaluated with the transfer-matrix method (described in appendix B). The emission into lower ($j = L$) and upper ($j = U$) cladding layers with dielectric constants ε_L and ε_U, respectively, through leaky modes occurs when the relation

$$k_\parallel < k_j = \frac{\sqrt{\varepsilon_j}\omega_0}{c}, \tag{2.19}$$

for the in-plane wave vector $k_\parallel$ is satisfied.

The SE rate into guided modes are given by [36]

$$\Gamma_\alpha^p = \tilde{g}_\alpha^p \sum_\lambda \left| E_\alpha^p (k_\parallel = k_{0_\lambda} \sin\theta, z \right|^2 \frac{k_{0_\lambda}}{v}, \tag{2.20}$$

$$\tilde{g}_\parallel^{\mathrm{TE}} = \frac{|\mathbf{d}|^2 \pi \omega_0^3}{\hbar c^2}, \quad \tilde{g}_\parallel^{\mathrm{TM}} = \tilde{g}_\parallel^{\mathrm{TE}} \frac{c^4}{\omega_0^4}, \quad \tilde{g}_\perp^{\mathrm{TM}} = 2\tilde{g}_\parallel^{\mathrm{TM}},$$

where the sum is over all the guided modes supported by the structure, indexed by α, the in-plane wave vector $k_{0_\alpha} = k_\parallel^\alpha(\omega = \omega_0)$ and the group velocity of the αth guided mode evaluated at the dipole emission frequency ω_0 is given by v_{0_α}. The electric field amplitudes are given in appendix A and evaluated with the transfer matrix method (described in appendix B).

For a randomly orientated dipole, the contributions of $\Gamma_{\mathrm{rad}}^{\mathrm{leaky}}$ and $\Gamma_{\mathrm{rad}}^{\mathrm{gui}}$ to the total SE rate in eq. (2.17) are given by the averaged rates

$$\Gamma_{\mathrm{rad}} = \frac{2}{3}\Gamma_\parallel + \frac{1}{3}\Gamma_\perp, \tag{2.21}$$

where $\Gamma_\parallel = \Gamma_\parallel^{\mathrm{TE}} + \Gamma_\parallel^{\mathrm{TM}}$ is the sum over the two polarisations for a planar (horizontal) dipole and the vertical dipole only couples to TM modes $\Gamma_\perp = \Gamma_\perp^{\mathrm{TM}}$ for a vertical dipole.

2.3 Fluorescence resonance energy transfer

Fluorescence resonance energy transfer (FRET), Förster resonance energy transfer (FRET), resonance energy transfer (RET) and electronic energy transfer (EET) are all terms used for processes that involve the transfer of energy from a donor (D) initially in an electronically excited state to an acceptor (A) providing there is an overlap between the donor emission and acceptor absorption spectra, as shown in fig. 2.1b.

While the equations for FRET are based on the interaction of non-overlapping transition dipoles, other forms of interaction are possible. For example, when the wavefunctions of particles significantly overlap the energy transfer process that exponentially decays with distance can be described by Dexter theory [58]. In this case, the system of coupled chromophores (light absorbing atomic or molecular components) lose their electronic and optical integrity [59]. A description of the FRET processes,

that operate most efficiently at small distances, between two coupled chromophores (an excited donor and an acceptor) will be the focus of this section.

2.3.1 Förster theory

A theory describing the non-radiative Coulombic energy transfer process of inverse sixth power distance dependence that was observed in fluorescence quenching experiments was first detailed by Förster [60]. The theory is based upon weak interactions between donor (D) and acceptor (A) meaning that the spectroscopic properties are not altered by direct interaction of the presence of one another. In the weak coupling regime, typically satisfied for donor-acceptor separations greater than 5 Å, Förster treated the electronic coupling between donor and acceptor with an equilibrium Fermi's Golden Rule approach with second-order perturbation theory [61]. To ensure that FRET is incoherent (Markovian) and irreversible, the theory assumes that the coupling to the bath is much greater than the electronic coupling between donor and acceptor. A second assumption is that the bath equilibrates subsequent to electronic excitation of the donor on a timescale that is considerably faster than that of FRET [61]. Restricting the donor-acceptor separations R to be substantially smaller than the radiation wavelength, the Förster theory expresses the rate of energy transfer Γ_{DA} from an excited donor to an acceptor in a dielectric medium with refractive index n as

$$\Gamma_{DA} = \frac{1}{\tau_D}\left(\frac{R_0}{R}\right)^6, \quad R_0^6 = \frac{9000(\ln 10)\kappa^2 Q_D}{128\pi^5 N n^4} J(\lambda), \tag{2.22}$$

where τ_D is the fluorescence decay time of the donor in the absence of any acceptors, Q_D is the quantum yield of the donor in the absence of the acceptor, N is Avogadro's number, κ^2 is a factor describing the relative orientation in space of the transition dipoles of the donor and acceptor and $J(\lambda)$ is the overlap integral, defined as

$$J(\lambda) = \int_0^\infty F_D(\lambda)\varepsilon_A(\lambda)\lambda^4 d\lambda = \frac{\int_0^\infty F_D(\lambda)\varepsilon_A(\lambda)\lambda^4 d\lambda}{\int_0^\infty F_D(\lambda) d\lambda}, \tag{2.23}$$

where $F_D(\lambda)$ is the corrected fluorescence intensity of the donor in the wavelength range λ to $\lambda + \delta\lambda$, with the total intensity (area under the curve) normalised to unity, $\varepsilon_a(\lambda)$ is the extinction coefficient of the acceptor at λ [32, 33].

The κ orientation factor depends on the orientations of the donor and acceptor, with respect to one another, and the displacement unit vector $\hat{\mathbf{r}}$ by

$$\kappa = \hat{\boldsymbol{\mu}}_D \cdot \hat{\boldsymbol{\mu}}_A - 3(\hat{\mathbf{r}} \cdot \hat{\boldsymbol{\mu}}_D)(\hat{\mathbf{r}} \cdot \hat{\boldsymbol{\mu}}_A) \tag{2.24}$$

$$= 2\cos\theta_D \cos\theta_A + \sin\theta_D \sin\theta_A \cos\varphi, \tag{2.25}$$

where $\hat{\boldsymbol{\mu}}$ is the unit vector in the direction of the considered transition dipole moment, the magnitude of the centre-to-centre separation of the chromophores is R, the angles θ_D and θ_A are between the dipoles and the vector joining the donor and the acceptor and φ is the angle between the planes [59, 61]. For dynamic random averaging of the donor and acceptor it is usually assumed that $\kappa = 2/3$. This is the case for triplet state decays of trivalent rare-earth ions that exhibit long-lived photoluminescence [33]. The Förster distance encapsulates all dependence upon the extent of spectral overlap of the emission spectrum of the donor with the absorption spectrum of the acceptor, the quantum yield of the donor and the relative orientation of the donor and acceptor transition dipoles. When the D-A distance is equal to the Förster distance $R = R_0$ then the transfer efficiency is 50% and the donor emission intensity is reduced to half of what it would be in the absence of the acceptor. The scaling constant is set so that when ε_A is given in units of M^{-1} cm^{-1} and the wavelength λ in nm, the Förster distance is in units of Å [32]:

$$R_0 = 0.211[\kappa^2 n^{-4} Q_D J(\lambda)]^{1/6}. \tag{2.26}$$

The efficiency of energy transfer E of the process is the fraction of photons absorbed by the donor that are transferred to the acceptor, given by

$$E = \frac{\Gamma_{DA}}{\tau_D^{-1} + \Gamma_{DA}} = \frac{1}{1 + (R/R_0)^6} \tag{2.27}$$

where the $\tau_D^{-1} = \Gamma_D$ is the spontaneous emission rate [32]. The Förster radius is typically in the range of a few nm. As a result, when the D-A separation is greater than R_0, spontaneous emission is the primary de-excitation pathway.

2.3.2 Quantum Electrodynamics

A unified theory for chromophore interactions is derived in the framework of quantum electrodynamics to include photon mediated (radiative) transitions [61]. I.e. where

Förster theory only considers non-radiative electronic transitions (virtual photon exchange), the radiative process where a photon emitted by the donor travels through the medium and is absorbed by an acceptor (photon exchange) occurs for larger chromophore separations.

In the Förster theory, the Coulombic coupling was approximated as a dipole-dipole interaction between transition dipole moments μ of the donor and acceptor chromophores

$$V_{\text{dip}}(\mathbf{r}) = \frac{1}{4\pi\varepsilon_0}\frac{\kappa\mu_D\mu_A}{R^3}, \tag{2.28}$$

where the κ orientation factor is defined as before in eq. (2.24) [61]. The decay rate is given by Fermi's golden rule and is therefore proportional to the square of this potential, which gives the $1/R^6$ distance dependence. The QED treatment takes into account the interaction of a transition dipole at A with a retarded electric field produced by a transition dipole source at D, i.e the time taken for the donor and acceptor to interact [59]. The result is that for randomly orientated chromophores a substitution in eq. (2.28) is made by [61]

$$\frac{\kappa^2}{R^6} \rightarrow \frac{2(3 + k^2R^2 + k^4R^4)}{9R^6}, \tag{2.29}$$

where $\mathbf{k}$ is the wavevector of the exchanged photon, $k = \omega/c$. For short range distances where $kR \ll 1$ converges to the classical $1/R^6$ separation dependence. However at longer distances where $kR \gg 1$, the time taken for the interaction (and hence the additional terms) becomes more important and the interaction scales as k^4/R^2. The latter corresponds to real photon exchange and is typically operative for separations of ~ 1 μm [61]. It can also be seen that an intermediate regime exists where $kR \sim 1$ (on the order of hundreds of nanometers) and both radiative and nonradiative process are at play [59]. It is because of this revelation that both Förster non-radiative (the short-range asymptote) and radiative (long-range asymptote) coupling are components to a single process that operates over all separations (beyond wavefunction overlap) that QED theory is described as a unified theory [59].

Table 2.1: Equation for energy transfer governed by Coulomb interaction as a function of the type of electric multipolar interaction. The range gives the typical interaction distances for spin allowed transitions. Table reproduced from [62, pg. 390].

Interaction type	Equation form	Range (nm)
Dipole-dipole	$\Gamma_{DA} = (1/\tau_D)(\mathrm{R}_0/R)^6$	3.5
Dipole-quadrupole	$\Gamma_{DA} = (1/\tau_D)(\mathrm{R}_0/R)^8$	0.8
Quadrupole-quadrupole	$\Gamma_{DA} = (1/\tau_D)(\mathrm{R}_0/R)^{10}$	0.2

2.3.3 Multipoles

The Förster formula pertains to the interaction between transition dipoles, a first-order multipole approximation of the chromophore potential. The influence of multipoles has since then been derived. In the Förster range, the separation dependence in the potential eq. (2.28) scales as $1/R^{(\mathrm{P}+\mathrm{Q}+\beta)}$, where the index P and Q refer to the order of the electric or magnetic multipole for the transition between the donor and acceptor, respectively, and $\beta = 1$ for similar transitions (i.e. two transition electric multipoles or two magnetic monopoles) or $\beta = 0$ for the coupling of an electric multipole with a magnetic multipole [59]. For example, the coupling between an electric dipole ($\mathrm{P} = 1$) and a magnetic quadrupole ($\mathrm{P} = 2$) ($\beta = 0$) has a R^3 distance dependence within the Förster range. Therefore with increasing order multipole interactions and recalling that Γ_{DA} is proportional to the square of the separation distance dependence R in the potential from Fermi's golden rule, the interaction decreases to subnanometer ranges, as summarised in table 2.1. In general the coupling between the considered transition is described by the lowest order of multipole as each unit increase in multipolar order and the substitution of an electric transition with a magnetic counterpart, lowers the strength of the interaction by a factor of the order 10^{-2} to 10^{-3} [59]. The reduction of efficiency of successive multipole orders limits their use in the analysis of FRET when compared to other decay mechanisms [59, 61]. Furthermore the shape of molecules becomes important at the subnanometer scales and must be taken into account as the approximation of a point-form multipoles breaks down [61].

Chapter 3

Erbium ions in glass

This chapter introduces the optical properties of trivalent erbium (Er^{3+}), the preferred bonding state in condensed matter of the lanthanide series element. A wide range of optical absorption and emission lines result from intra-$4f$ electronic transitions and the discussion here focuses on the transition from the first excited state centred at 1.54 μm, which falls in the low loss C-band of silica and is an important wavelength in telecommunications. The basic properties of erbium and Er^{3+} are given in section 3.1. Following this, the energy spectrum and optical transitions are described in more detail in section 3.2. This includes the radiative and non-radiative transition rates, excitation with the 980 nm laser pump wavelength band and the upconversion process excited state absorption. Lastly, section 3.4 describes the Er^{3+} ion-ion energy transfer interactions (energy migration, cooperative upconversion and radiation trapping) that become more efficient at high doping concentrations.

3.1 Basic properties

The rare-earth metal erbium (Er) belongs to the lanthanide series of the periodic table[1]. Erbium is termed a rare-earth element as it occurs in low concentrations of about 2.8 ppm in the Earth's crust [63]. It has an atomic number of $Z = 68$, an atomic mass of 167.26 amu (1 amu $= 1.6605402 \times 10^{-27}$ kg) and metallic radius of 1.758 Å [63]. Pure solid erbium is a silvery-white metal and must be artificially isolated from natural erbium that occurs in chemical combination with other elements. It has a high melting

[1]Lanthanides have atomic numbers 57 through to 71

point of 1529 °C and boiling point of 2868 °C, which is usual for lanthanides. Erbium metal tarnishes slowly in air and burns readily to form pink erbium(III) oxide:

$$4\ \mathrm{Er} + 3\ \mathrm{O_2} \rightarrow 2\ \mathrm{Er_2O_3} \tag{3.1}$$

According to the Aufbau principle ground-state erbium has an electron configuration, which is often referred to as a *submerged-shell* configuration. Electrons are distributed among electron orbitals[1] simply as

$$(1s^2 2s^2 2p^6 3s^2 3p^6 3d^{10} 4s^2 4p^6 4d^{10} 5s^2 5p^6) 4f^{12} 5d^0 6s^2. \tag{3.2}$$

The order in which the subshells are filled with electrons, known as the Madelung rule, results in the $6s$ orbital filling before all of the $4f$ orbitals. The bracketed part of the electron configuration is usually abbreviated as [Xe] as it is equal to the electron configuration of xenon. The seven $4f$ orbitals can take a maximum of 14 electrons.

As is usual for lanthanides, the preferred bonding state of erbium in condensed matter is the trivalent level of ionisation ($\mathrm{Er^{3+}}$), which removes the $6s^2$ and one of the $4f$ electrons [64]. $\mathrm{Er^{3+}}$ has an ionic radius of 0.96 Å [65] and the electron configuration is

$$[\mathrm{Xe}]4f^{11}. \tag{3.3}$$

$\mathrm{Er^{3+}}$ in the ground state (g.s.) is in an I-state with an orbital angular momentum quantum number of $L = 6$ due to LS-coupling of all electrons. Using the spin and total electronic angular momentum quantum numbers S and J, respectively, the ground state of $\mathrm{Er^{3+}}$ is written as[2]

$$g.s.:\ {}^4\mathrm{I}_{15/2}$$
$$L = 6,\ S = 3/2,\ J = 15/2.$$

[1] Using the standard spectroscopic notation, $n\ell^e$, with n the principal quantum number, followed by the orbital quantum number, ℓ (denoted by $s = 0$, $p = 1$, $d = 2$, $f = 3$, . . .), and the number of electrons, e, in each orbital as superscript.

[2] The Russell-Saunders notation is used; ${}^{2S+1}L_J$, where S is the total spin quantum number, $2S+1$ is the spin multiplicity, L is the total orbital quantum number in spectroscopic notation (S=0, P=1, D=2, F=3, G=4, H=5, I=6...) and J is the total angular momentum quantum number.

3.2 Energy spectrum and optical transitions

As with almost all transition lines in lanthanide ions, the wide range of optical absorption and emission spectra of the Er^{3+} ion result from electric-dipole transitions within the manifold of the $4f$ electrons[1] [65, 66]. It is these transitions that are referred to when referring to energy levels herein, unless otherwise stated.

Free ions exhibit sharp transitions, however in a glass or crystal host the energy levels are broadened by the interaction between the ions and the local electric field in the lattice (known as Stark splitting) and dynamical perturbation (homogeneous or 'thermal' broadening) [64, 67]. Each level within the stark level manifold is occupied populated according to a Boltzmann distribution. For amorphous materials, such as glass, an additional inhomogeneous broadening occurs due to the structural disorder resulting in position dependent electric field of a dopant ion. Nonetheless, the outer lying $5s$ and $5p$ orbitals shield the inner $4f$ orbitals resulting in relatively narrow absorption and emission lines (almost free ion like) that are only weakly dependent on the host [64, 65].

An energy level diagram with the corresponding photoluminescent (PL) emission from the transitions of Er^{3+} in a host is shown in fig. 3.1. The thickness of the lines represent the broadening of the energy levels. For the meta-stable $^4I_{13/2}$ state and $^4I_{15/2}$ ground state of Er^{3+} ions doped in silica, the splitting of the J manifold into $(2J + 1)/2$ Stark levels results in 56 possible transitions [68, 69]. At temperatures close to 0 K only the lowest level of each manifold is occupied and as for crystalline hosts, which exhibit a high point symmetry, sharp transition lines are observed [67, 68]. At room temperature even the highest energy levels have some Boltzmann-distributed population and so the emission and absorption spectra produce a broadened spectra [69].

Several of the optical transitions have important uses for technological applications. The prominent transition at 2940 nm is suited to laser surgery due to the very high absorption of water in tissues. The transition centred at 1540 nm falls in the low loss C-band window of silica, which is used in optical telecommunications and so the doping of Er^{3+} ions in silica fibres and planar waveguides for amplifiers and lasers are active

[1] Eu^{3+} being an exception as it is a magnetic-dipole transition [66].

areas of research. The 1540 nm optical transition of Er^{3+} will be the focus of this chapter.

3.3 Transition rates

The total decay rate for an excited state population $\Gamma = 1/\tau$, where τ is the corresponding measured lifetime, is given by

$$\Gamma = \Gamma_{\text{rad}} + \Gamma_{\text{nrad}} = \frac{1}{\tau_{\text{rad}}} + \frac{1}{\tau_{\text{nrad}}}, \tag{3.4}$$

where Γ_{rad} is the intrinsic radiative decay rate and Γ_{nrad} is the non-radiative decay rate. The radiative decay rate is a result of the rare earth site local crystal field symmetry and therefore depends on the host matrix. The local vibrational density of states of the host depopulates the excited state non-radiatively as heat through electron-phonon coupling. Other non-radiative loss mechanisms include concentration quenching effects, which may be enhanced by clustering and involve the transfer of excited state energy between rare earth ions until an defect or trap is encountered, and excited state absorption, which acts to depopulate an excitation through the conversion to a higher energy photon [70]. For low dopant ion concentrations, concentration quenching processes is negligible. The effect of excited state absorption depends on the energy level structure of the dopant ion, the excitation wavelength and excitation intensity.

The quantum efficiency (QE) of a transition determines the fraction of excitations converted to photons and depends on the radiative efficiency as

$$\text{QE} = \frac{\Gamma_{\text{rad}}}{\Gamma_{\text{rad}} + \Gamma_{\text{nrad}}}. \tag{3.5}$$

Reductions in QE therefore not only affect the PL intensity but also the measured PL lifetime.

3.3.1 Radiative decay

The intra-$4f$ transition rates of rare-earth ions doped in glasses and crystals are difficult to measure directly and are typically calculated for bulk glasses with the semiempirical Judd-Ofelt theory [71, 72]. The oscillator strength for the transition between two states ${}^{2S+1}\text{L}_J$ (described by the wavefunction Ψ_i, specified by the f^N configuration for

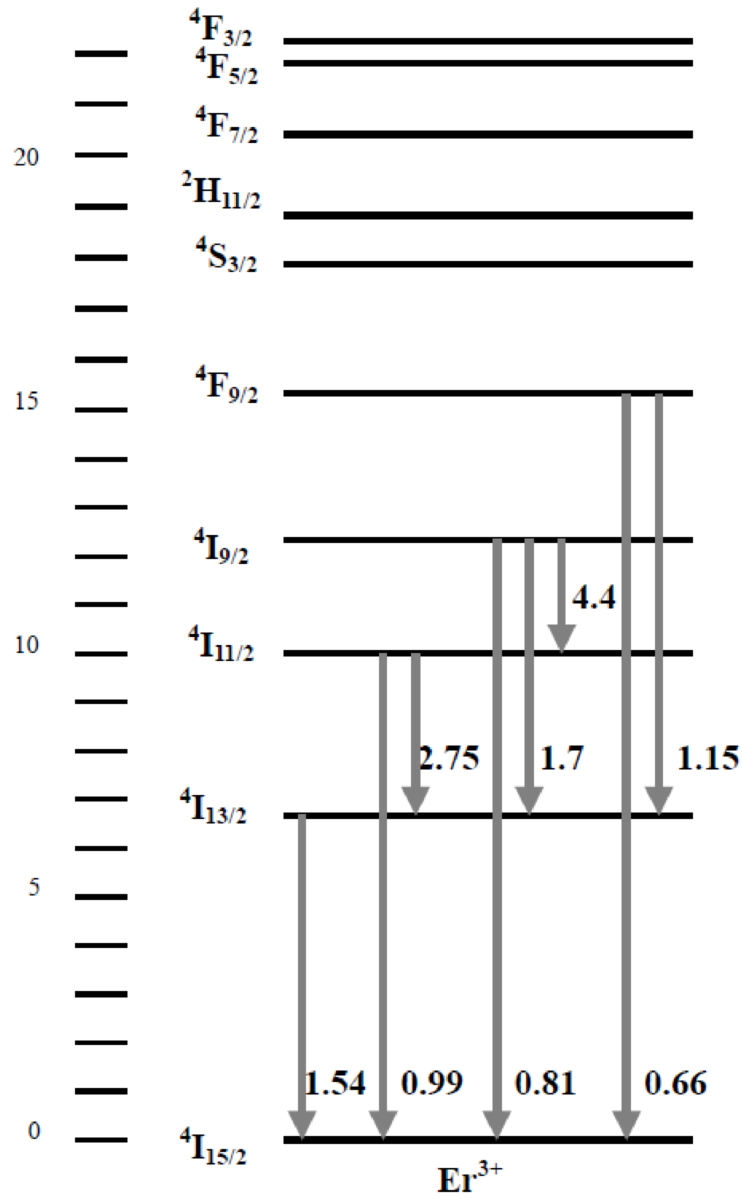

Figure 3.1: The energy levels of Er^{3+}. Leftmost scale shows the energy relative to the g.s. in 10^3 cm^{-1} and the inner scale shows the energy levels of each transition in Russel-Saunders notation. The thickness of the lines represents the broadening of the energy levels. Arrows indicate radiative transitions with the PL wavelength explicitly stated.

a partially filled f shell, the quantum numbers S, L, J and a factor γ to distinguish electronic states that share the same values of S and L) and ${}^{2S+1}\mathrm{L}_{J'}$ (described by Ψ_f and specified in a similar way) is given by [68]

$$S = \frac{1}{e^2}\left|\langle\Psi_f|\, H\, |\Psi_i\rangle\right| = \sum_{k=2,4,6} \Omega_k \left|\left\langle f^N \gamma S' L' J' \right| U^{(k)} \left| f^N \gamma S L J \right\rangle\right|^2, \tag{3.6}$$

where H is the electric-dipole Hamiltonian, expressed in tensor form as $U^{(k)}$, and the Ω_k coefficients are the Judd-Ofelt parameters, which describe the influence of the external crystal field on the radiative transition probabilities of the intra-4f transitions. The transition matrix elements $\left|\langle|\, U^{(k)}\, |\rangle\right|$ do not differ significantly from host to host and the free-ion values calculated by Morrison and Leavitt [73, 74] are often used [75, 76]. The three Judd-Ofelt intensity parameters are typically determined by measuring the absorption oscillator strengths for at least five or six ground state transitions and then using the chi-square method to minimise the difference between the calculated and measured oscillator strengths [77]. The accuracy of the Judd-Ofelt analysis is typically 10 - 15 %. Other methods to calculate the radiative lifetime in bulk glasses include the Einstein model, which approximates the transition as a two level system and uses the absorption spectrum, and McCumber theory, which relates the absorption and emission cross-sections [78]. For thin films, where measurement of the emission and absorption spectra is more difficult, the local density of states within the doped film can be modified by varying the index of external layers and then comparisons of the measured and theoretically calculated lifetimes yields the radiative decay rate [45].

3.3.2 Electron-phonon coupling

Non-radiative relaxation from the excited state back to the ground state can occur due to the interaction between the electrons and the lattice in which optical phonons (lattice vibrations) are produced (thermal quenching) [79]. The rate of multiphonon emission Γ_{nrad} for 4f levels of lanthanide ions is inversely proportional to the exponential of the energy gap ΔE to the next lowest available electronic energy level and described by

$$\Gamma_{\mathrm{nrad}} = C \exp\left(-\frac{\Delta E}{a\hbar\omega}\right), \tag{3.7}$$

where $\hbar\omega$ is the maximum phonon energy of the host, C and a are phenomological host dependent constants[1] [80–84]. The highest energy phonons dominate the de-excitation process [70]. To a good approximation, if the energy gap between the excited and next lowest-lying level is greater than ten times the phonon frequency then the transition is temperature independent (i.e. radiative recombination dominates and the branching ratio is unity). Alternatively, if the gap is less than four times the phonon energy the luminescence is completely quenched (i.e. all excitations are converted into heat) [79].

The energy gap between the $^4I_{13/2}$ first excited meta-stable level and the $^4I_{15/2}$ ground level of the Er^{3+} ion is 6500 cm^{-1}. Silicate (1000 - 1100 cm^{-1}), phosphate (1100 - 1350 cm^{-1}) and borate (1350 - 1480 cm^{-1}) glasses typically have high phonon energies which can lead to a slightly reduced QE. Alternative hosts with low phonon energies include, tellurite (600 - 850 cm^{-1}), fluoride (500 - 600 cm^{-1}), germanate (800 - 975 cm^{-1}) and chalcogenide (200 - 350 cm^{-1}) glasses [85, 86].

3.3.3 980 nm pump wavelength band

The emission at 1540 nm of Er^{3+} corresponds to the $^4I_{13/2} \rightarrow ^4I_{15/2}$ electronic transition. To excite ions to the $^4I_{13/2}$ level, laser pump wavelengths bands at the four longest wavelength bands, 1480 nm, 980 nm, 800 nm and 654 nm, have been used for waveguide amplifiers [64, 69]. Longer wavelengths are typically preferred as scattering losses are reduced [2]. The 1480 nm pump band, depicted in fig. 3.2(a), induces stimulated emission (due to the spectral overlap with the pump wavelength and $^4I_{13/2} \rightarrow ^4I_{15/2}$ emission) and has significant excited state absorption (discussed in section 3.3.4), which limits the population inversion of the first excited state [2].

The 980 nm pump band excites the $^4I_{15/2} \rightarrow ^4I_{11/2}$ transition of Er^{3+} and corresponds to a 3-level system as depicted in fig. 3.2(a). Following excitation, fast non-radiative relaxation ($\sim$1 μs [87]) corresponding to an energy gap of $\sim$0.45 eV occurs from $^4I_{11/2} \rightarrow ^4I_{13/2}$ via multiphonon emission (heat). It has proven to have a high efficiency due to the relatively large absorption cross-section combined with weak excited state absorption and limited pump induced stimulated emission [2, 69]. The absorption cross-section peaks between 970 - 980 nm and varies with glass composition [69]. The availability of high power laser diodes at this wavelength band has lead to widespread use and a 976 nm laser excitation wavelength is used in this research.

[1] The position of the energy levels for rare earths is only weakly dependent on the host [79].

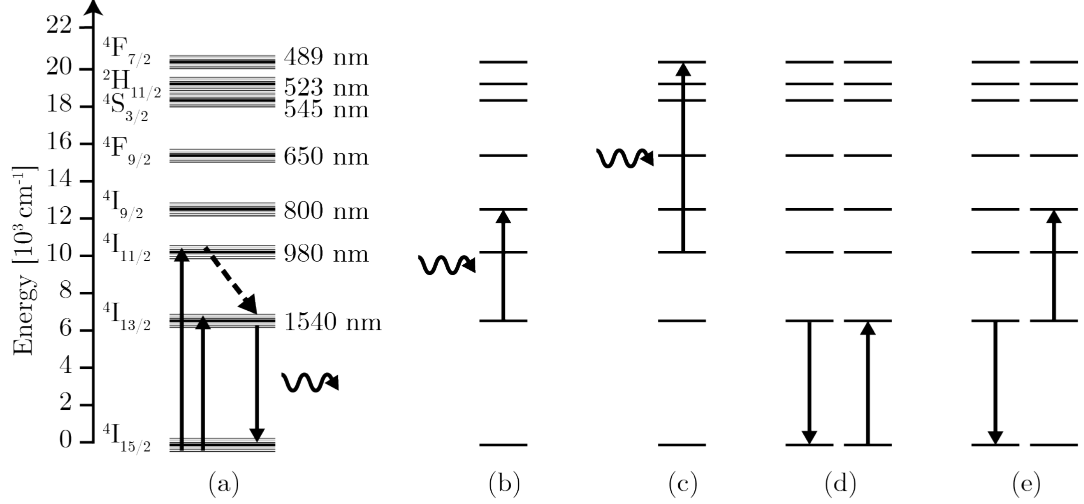

Figure 3.2: Schematic representation of the Er^{3+} intra-4f energy levels; (a) shows the 980 nm pump band excitation leading to 1.54 μm emission, (b) and (c) show the excited state absorption of a 1480 nm pump/1540 nm emission and a 980 nm pump photon, respectively, and the non-radiative ion-ion interactions in (d) and (e) show energy migration and cooperative upconversion, respectively.

3.3.4 Excited state absorption

Excited state absorption is where an ion in the excited metastable level absorbs a second photon and is promoted to a higher lying excited state that resonates with the photon energy. The step-wise absorption of lower-energy photons into a higher-energy photon via the metastable level makes this an upconversion process and not a multiphoton process where the absorption of photons occurs simultaneously. Excited state absorption is more efficient than the two photon upconversion process that involve virtual states, but less efficient than cooperative upconversion (to be discussed in section 3.4.2) [34, 88].

For Er^{3+} ions pumped at 1480 nm or excited by a 1540 μm photon emitted by another ion, excited state absorption corresponds to the $^4I_{13/2} \rightarrow ^4I_{9/2}$ transition, as illustrated in fig. 3.2(b). The doubly excited ion may return to the metastable state through radiative or non-radiative multiphonon decay. As the radiative decay emits a photon at a different wavelength to the pump photon the process is described as a loss mechanism (two pump photons absorbed and one emitted).

Under laser excitation in the 980 nm wavelength band, excited state absorption corresponding to the $^4I_{11/2} \rightarrow ^4F_{7/2}$ transition is also possible, as depicted in fig. 3.2(c). Fast non-radiative decay occurs via multiphonon emission either ending at the $^2H_{11/2}$ level or the $^4S_{3/2}$ level and results in the emission of green photoluminesence at 523nm and 545 nm, respectively. The $^4I_{11/2}$ state is however short lived and so excited state absorption by the 980 nm pump is relatively inefficient.

3.4 Ion-ion interactions

The electrodynamic interaction between two ions can result in numerous energy transfer processes. These processes have been reviewed extensively for ion activated solids in [64, 88, 89]. The discussion presented here is restricted to the resonant interaction between two Er^{3+} ions that have, equal energy level structures, and in particular the interactions involving the first excited energy level $^4I_{13/2}$ are considered.

Energy transfer from the excited Er^{3+} ion can occur either to an unexcited or already excited Er^{3+} ion. The former case includes the radiative transfer process *radiation trapping* and the non-radiative transfer process *energy migration*. The latter situation is described by the non-radiative *cooperative upconversion* process.

Radiation trapping occurs through the exchange of real photons and manifests itself as an increase the measured lifetime from a population of ions. Energy transfer effects tend to be more pronounced in rare-earth ions with forbidden transitions due to the long metastable levels [34]. The non-radiative processes occur via the exchange of virtual photons due to dipole-dipole Förster-Dexter interactions mediated by the electric field [7, 90]. The efficiency of interactions depend on the average separation between neighbouring ions and are therefore enhanced with increasing concentrations. The term concentration quenching effects is used to describe these interactions when they result in a loss of the excited-state population to non-radiative means and result in a reduction of the quantum efficiency [64, 77]. An accompanying reduction in the photoluminescence lifetime is often but not always observed, for example in some cases of cooperative upconversion [64].

While concentration quenching effects can be minimised through the use of low doping concentrations in long erbium doped fibre amplifiers, these undesirable effects are important for compact devices that require high doping concentrations, such as planar

waveguide amplifiers and lasers [77]. In addition to these physical limitations at high levels of doping concentrations, the rare-earth solubility in the host material, a chemical limitation, becomes important. Precipitation occurs at different levels depending on the host glass. Chemical clustering results in ions separated by distances less than a few Å, which greatly enhances the ion-ion interaction by a form of upconversion called pair induced quenching [7, 34, 77]. Alternatively, ions can form non-optically active compounds with the host network [68]. These will not be detected in lifetime data, which only probes optically active ions [5]. In one-constituent glass, such as pure silica, the large rare-earth ions (~ 1Å) are rejected by the host resulting in a doping concentration limited to about 0.7×10^{18} cm^{-3} (100 ppm) [7]. Multi-component glasses typically have a larger lattice spacing, which results in a higher solubility limit. Another possibility is that at high concentrations the rare-earth network modifiers devitrify glasses [7]. The various inter-ionic interactions for Er^{3+} are described in the following.

3.4.1 Energy migration

Energy migration, involves the non-radiative energy transfer from an Er^{3+} ion excited in the $^4I_{13/2}$ energy level to a nearby unexcited ion, as depicted in fig. 3.2d [89]. Following the energy transfer, the originally excited ion is left in the ground state. The resonant diffusion of energy between the identical Er^{3+} ion levels only results in the loss of the excitation if an Er^{3+} ion strongly coupled to a non-radiative quenching or defect site is reached. A well known quenching site in glasses are impurity OH-groups (water vapour) [90–93]. The energy of the $^4I_{13/2} \rightarrow {}^4I_{15/2}$ transition (1.54 μm) corresponds almost exactly to twice that of the second harmonic of the OH-group stretching vibration (2.7 - 2.9 μm) and therefore non-radiative decay may occur through a two phonon decay mechanism [90].

The Förster type energy transfer interaction is more efficient at higher Er^{3+}-doping concentrations as the ionic separation distances are smaller. With each successive energy transfer, the probability of coupling to a quenching site increases and the non-radiative decay results in a reduced lifetime of the excited state. A simple model for the decay rate Γ as a function of optically active Er^{3+} ion concentration N_{Er} resulting from energy migration is given by [5, 91]

$$\Gamma(\mathrm{Er}) = \Gamma_{\mathrm{rad}} + \Gamma_{\mathrm{int}} + 8\pi C_{\text{Er-Er}} N_{\mathrm{Er}} N_{\mathrm{Q}}, \tag{3.8}$$

where Γ_{rad} is the radiative decay rate, Γ_{int} is the internal non-radiative recombination rate (due to the emission of phonons), N_Q the density of quenching centres coupled to a small fraction of the Er^{3+} ions and $C_{Er\text{-}Er}$ the interaction constant between ions. The decay rate in the absence of migration is given by $\Gamma_{rad} + \Gamma_{int}$. The increase in decay rate is therefore linear with the optically active Er^{3+} ion concentration. It is typically assumed that all the OH-groups in glass couple optically active ions and obtaining longer lifetimes at higher doping concentrations is therefore achieved through reducing the OH-group content in the glass. Furthermore, derivation of the equation approximates that the overlap between the absorption spectra of the quenching sites and that of the Er^{3+} are equal as the OH-groups that are closely bound to a few of the Er^{3+} quench via excitation of vibrations [91].

3.4.2 Cooperative upconversion

The energy transfer or *cooperative upconversion* process relies on the interaction between two excited ions [64, 88]. For two Er^{3+} ions in the first excited state $^4I_{13/2}$, one ion can transfer its excitation to the other promoting it to the higher $^4I_{9/2}$ energy level while decaying to the ground state in the process, as is illustrated in fig. 3.2e. The doubly excited ion may then quickly and non-radiatively decay to the ground state or back to the metastable state. In the latter case, radiative recombination is possible. The process therefore results in the loss of either one or two excitations. In the case of oxide glasses, fast non-radiative relaxation back to the metastable energy level through multiphonon relaxation ($^4I_{9/2} \rightarrow {}^4I_{11/2} \rightarrow {}^4I_{13/2}$) occurs [69]. A second order upconversion process that populates the $^4S_{3/2}$ level also exists and results in green photoluminescence at 545 nm and is typically observed for highly Er^{3+}-doped materials that exhibit large cooperative upconversion interactions during excitation [94].

Cooperative upconversion has a major role in limiting gain in Er^{3+}-doped devices operating at 1540 nm for Er^{3+}-doping concentrations above 10^{19} - 10^{20} cm^{-3} [2, 64, 94, 95]. The interaction depends on the excited fraction of ions and therefore leads to non-exponential decay that is dependend on the excitation intensity. The Er^{3+}-ion decay can be modelled using a two-level rate equation by assuming that the lifetime of the higher $^4I_{9/2}$ level is short compared to that of the metastable $^4I_{15/2}$ level. This approximation is valid in silica as the $^4I_{9/2}$ level has a sub-microsecond lifetime and the

${}^4I_{13/2}$ level has a lifetime of ∼10 ms [68]. The fraction of Er^{3+} ions in the ${}^4I_{13/2}$ level n_2 is given by

$$\frac{dn_2}{dt} = W_{1,2}n_1 - W_{2,1}n_2 - \Gamma_{2,1}n_2 - [\mathrm{Er}]C_{\mathrm{up}}n_2^2, \tag{3.9}$$

where the subscripts 1 and 2 refer the ground ${}^4I_{15/2}$ and metastable ${}^4I_{13/2}$ energy levels, respectively. The rates of pump photon absorption and stimulated emission are given by $W_{1,2}$ and $W_{2,1}$, respectively, the spontaneous emission rate is given by $\Gamma_{2,1} = 1/\tau$ and C_{up} is the cooperative upconversion coefficient. The upconversion term is quadratic as it involves two excited ions and due to the short lifetime of the ${}^4I_{9/2}$ level, excited state absorption is neglected and the following approximation for the concentration of optically active ions $[\mathrm{Er}] = n_1 + n_2$ can be made.

As the interaction efficiency depends on the ion-ion spacing, the microscopic distribution of the ions within the host material is also an important consideration. At high doping concentrations approaching or exceeding the rare earth solubility limit of the host, ions can form pairs and large clusters, which result in much shorter inter-ionic separations (in the order of the ion diameter of 0.2 nm) [7, 69, 96]. Alternatively, the formation of clusters or molecules may be a direct consequence of the fabrication technique, for example co-sputtering of Er_2O_3 [2]. Two types of upconversion processes are therefore identified. Homogeneous cooperative upconversion (HUC) describes the process in a homogeneous media and pair induced quenching (PIQ) occurs when ions form pairs and large clusters. The energy transfer rate is much more efficient in PIQ due to the smaller inter-ionic separations and occurs on a sub-millisecond timescale while HUC typically occurs in the millisecond range [97].

3.4.3 Cross relaxation

Cross relaxation is an interaction where an ion decays from a higher energy level to an intermediate level through partial energy transfer to an unexcited neighbouring ion [89]. The interaction is the inverse of the cooperative upconversion process and therefore also depends on the energy level structure of the ion along with the doping concentration. The Er^{3+} ion has no states between the metastable first excited and ground state and so cross relaxation cannot occur between these levels [69]. Additionally, the energy level structure state favours the cooperative upconversion process rather than cross relaxation of the higher lying ${}^4I_{9/2}$ level.

3.4.4 Radiation trapping

Radiation trapping is a resonant radiative energy transfer process between ions. The energy is emitted via real photons and then absorbed by any other ions within a photon travel distance. As real photons are emitted in this process, the lifetime of the excited ion that spontaneously emits the photon is unaffected [88]. The sequential spontaneous emission and reabsorption events between ions that have a large spectral overlap between the fluorescence and absorption spectra, results in trapped excitations and an increase in the measured lifetime of the sample. The scale of the effect depends on the measurement technique, sample doping concentration and geometry. In a homogeneous medium this interaction scales as R^{-2}, where R is the distance between donor and acceptor [76]. However, in thin films emission into a wave-guiding mode causes the effective optical thickness of the medium to be increased making it possible for radiation tapping to be observed. The usual condition of optical thinness is therefore not always sufficient to eliminate the effect of radiation trapping [98]. The process can occur at macroscopic (millimetre and centimetre) distances [7]. Depending on the symmetry between the metastable level emission and ground-state absorption spectra and number of emission-reabsorption events, the photoluminescence spectra may also change.

For Er^{3+} radiative recombination dominates the relaxation, as the branching ratio for the $^4I_{13/2} \rightarrow ^4I_{15/2}$ transition is equal to unity, and results in efficient radiation trapping [99]. Quantification of the level of radiation trapping is typically performed with the pin-hole method [98].

Chapter 4

Ultrafast Laser Plasma Doping

This chapter focuses on the ultrafast laser plasma doping (ULPD) technique used to fabricate rare-earth doped hybrid tellurite-silica thin films. The ULPD system used in this work was custom made by PVD Products to supersede an older femtosecond pulsed laser deposition (fs-PLD) system and installed at the University of Leeds in 2017. As the physical processes involved in film formation via the ULPD technique are not well understood, the aim of this chapter is to devise an optimisation procedure for this new system so that repeatable and high quality thin films can be fabricated for optical applications.

The chapter is structured in four sections: Section 4.1 presents a literature review of the novel ULPD technique, developed at the University of Leeds. The key findings of research leading to the development of the ULPD technique are discussed and the experimental setup of the previous fs-PLD system is also given. Next, in section 4.2 the well-known physical processes from femtosecond laser ablation to film deposition are described and the experimental findings of hybrid tellurite-silica film formation, specific to the ULPD technique, are summarised. Section 4.3 presents an overview of the ULPD system used in this research. Lastly, section 4.4 details the optimisation methodology for the system that will be used in this thesis.

4.1 Introduction and background

The doping of optically active rare earth (RE) ions as thin films and waveguides is a lively area of research. The unique spectroscopic properties may be utilised for a

variety of photonic applications, such as sensors, lasers and optical amplifiers [67, 100–107]. For example, the amplification of optical signals in the third telecommunications window (C and L bands) is achieved with erbium-doped fibre amplifiers (EDFA) as the $^4I_{13/2} \rightarrow ^4I_{15/2}$ transition of Er^{3+} ions is centred at 1.54 μm. Driven by the increased consumption of data, the development of compact erbium doped waveguide amplifiers (EDWA) that are compatible with photonic integrated circuits is necessary. In order to achieve scaling down the device dimensions from long EDFAs (typically 40 m) to the centimetre long EDWAs, the doping concentration of Er^{3+} ions that are optically active must be greatly increased so that an equivalent optical gain can be achieved [2]. Typical values for the stimulated emission cross-section σ_{em} of Er^{3+} are around 10^{-20} - 10^{-21} cm^2 and so doping concentration of at least 10^{19} - 10^{20} cm^{-3} without significant decrease in the metastable lifetime are required for gain over several centimetres [2].

In pure silica glass, the Er^{3+} ion chemical solubility is limited to about 0.7×10^{18} cm^{-3} (0.1 at.%) after which clustering of ions occurs due to a lack of space in the one-constituent glass network to accommodate the large RE ions [7]. The reduced spacing between ions in clusters enhances unwanted dipole-dipole interactions that quench the luminescence through non-radiative relaxation and increases the photoluminescence (PL) decay rate of the metastable $^4I_{13/2}$ state (previously discussed in chapter 3) [91]. These effects are undesirable for optical applications such as lasers and amplifiers that require high population inversion and efficiency. To overcome this limitation, other multi-component glasses to either replace or compliment the currently used silica-based host matrix have been investigated. Tellurite glasses are of interest due to their unique properties, such as high RE ion solubility, wide transmission range in the visible and near-infrared (0.35 - 5 μm), high non-linear and linear refractive index, low phonon energy (600 - 850 cm^{-1}), good chemical stability and low melting temperature compared with other oxide glasses [85, 108]. Furthermore, the $^4I_{13/2} \rightarrow ^4I_{15/2}$ emission bandwidth of Er^{3+} ions in a tellurite host is broader ($>$ 60 nm) than in a silica host ($\sim$ 20 nm) and extends up to 1630 nm, which is desirable for broadband optical amplifier applications [69, 108, 109].

Fabrication of tellurite EDWAs has been achieved by several groups with sol-gel [110], ion-exchange [111–113], sputtering [114, 115] and pulsed laser deposition (PLD) [116–118] techniques. However, high optical losses resulting from poor film quality and

limitations in doping concentrations of all these techniques have proved difficult to overcome [113]. Thin films deposited in 2007 via the PLD technique using a nanosecond (ns) ultraviolet ArF excimer laser to ablate a tungsten tellurite glass target (ns-PLD) in a reactive oxygen atmosphere appeared promising as they had a good optical transparency [117]. However the presence of micrometer sized droplets is a characteristic of ns-PLD that limits the capability of this technique for waveguiding type applications where a high film homogenity and low scattering is required [119–122]. The formation of droplets occurs during plume expansion through gas phase condensation and is a direct result of the large volume of material evaporated by the high energy pulse [123].

The formation of droplets may be avoided or considerably reduced in femtosecond laser ablation regime, where individual pulse energies are several orders of magnitude lower (microjoules rather than joules) [123–126]. To this end, in 2009 Jose et al. [127] coupled a femtosecond (fs) laser to a PLD system (Dual PLD, PVD Products, USA) and ablated zinc-sodium tellurite glasses onto a heated silica substrate (fs-PLD). A schematic of the fs-PLD experimental setup is shown in Figure 4.1. In this work, the process parameters (in this order) oxygen pressure, laser pulse energy, target to substrate distance and processing temperature were optimised for film transparency. There were two key findings from this optimisation procedure. Firstly it was found that a processing temperature of < 500 °C produced opaque films and highly transparent films were achieved with a deposition temperature greater than or equal to 650 °C. Secondly, a lower laser fluence closer to the (unknown) ablation threshold of the target glass produced more transparent films with no microparticles. While the authors believed they had deposited erbium-doped tellurite glass films, PL spectra of the films was much narrower than that of the tellurite target glass and the peak was red shifted from 1531 nm in the tellurite target to 1540 nm, which is indicative of Er^{3+} ions in a silicate host [5, 91].

In 2012, Jose et al. [128] studied cross-sections of the films using transmission electron microscopy (TEM) and high angle angular dark field (HAADF) elemental mapping. While the TEM images showed well defined and homogeneous films on a pristine silica substrate, the HAADF profiles revealed that the films were a mixture of the silica and tellurite glass. At the boundary between the ∼800 nm film and pristine silica substrate there was a transition region of ∼100 nm in which the target elements tailed

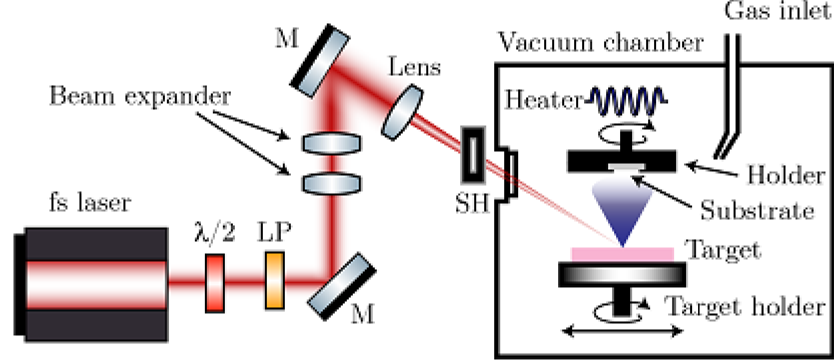

Figure 4.1: The fs-PLD system used to fabricate hybrid tellurite-silica films. Mirror (M), partially reflective mirror (PRM), power meter (PM), shutter (SH), linear polariser (LP), half-wave plate ($\lambda/2$). The Ti-sapphire femtosecond pulsed laser (Libra, Coherent), operating at a central 800 nm wavelength with 100 fs pulse width, is indecent on the target surface at an angle of incidence of 45° and focused to a spot area of $\sim 3.24 \times 10^{-5}$ cm^2 (~ 27 μm radius spot normal to the beam).

off and the silicon from the silica substrate increased to the bulk value. The oxygen remained constant throughout. It was therefore apparent that the fabrication procedure was not simply fs-PLD as the film was a modified substrate surface layer arising from a diffusion process of the plume species mediated by temperature. It was concluded that the high energy ions in the ablation plume colliding with the silica produced defect species, which were successfully transported when the substrate temperature was sufficient. What the authors neglected to consider, was that ions only constitute a small fraction of the total matter in the ablation plume (few %) with the majority being nanoparticle (NP) clusters [1, 129]. The low thermal stability of tellurite glass is problematic for practical applications and so a hybrid tellurite-silica glass was an additional promising feature to the films [109].

The potential of the technology was realised in 2015 whereby films were doped with a maximum Er^{3+} ion concentration of 0.91×10^{21} cm^{-3} (1.4 at. %) without clustering, which is the highest ever reported for a pure silica platform (note that these films are a hybrid tellurite-silica material) [23]. Furthermore, the record high lifetime-density product of 0.96×10^{19} s·cm^{-3} demonstrated that the concentration quenching effects were reduced in this multicomponent glass film and thus a high optical gain should be achievable in EDWAs. The amorphous state of the film was confirmed via selected

area electron diffraction (SAED) on a cross-section prepared by focused ion beam (FIB) lithography. Rutherford backscattering spectrometry (RBS) analysis showed a transition thickness typically ∼30 % of film thickness and a much reduced Te content from ∼ 26 at.% in the target to 2 - 3 at.% in the film. Chandrappan et al. [23] concluded that the reduced concentration quenching compared to other fabrication techniques at similar doping concentrations arose from increased inter-ionic separation distances in the multi-component modified silica by lack of clustering. Chandrappan et al. [130] have shown that the evolution of irreversible crystalline phases (devitrification) in the Er^{3+}-doped hybrid tellurite-silica films occurs when annealed at temperatures above 600°C and the total evaporation of TeO_2 at 800°C. In 2016, Kamil et al. [24] fabricated erbium-doped hybrid tellurite-silica films on silica-on-silicon substrates, which are compatible with integrated optics platforms. It was from hereon that the technique was termed *ultrafast laser plasma doping* (ULPD).

Investigations into doping with other or combinations of RE elements have also been reported. The co-doping of Er/Yb is attractive for waveguide amplifiers as Yb^{3+} has a larger and broader absorption cross-section and transfers the energy to Er^{3+} to improve the pumping efficiency while mitigating concentration quenching effects. This was demonstrated with the ULPD technique in 2015 by Chandrappan et al. [23], who co-doped Er^{3+} and Yb^{3+} to a concentration of 1.63×10^{21} cm^{-3} (2.8 at.%) without clustering and a PL lifetime of 9.1 ms. This concentration is approximately an order of magnitude higher than what is achievable by other methods. Recently, using the upgraded ULPD system that will be described in section 4.3, Richards et al. [25] fabricated Tm^{3+}-doped hybrid tellurite-silica films. From these results it may be expected that any RE ion may be doped into hybrid tellurite-silica thin films.

4.2 Theoretical background

The basic stages of fs-PLD/ULPD, depicted in fig. 4.2, from the ultrafast laser ablation mechanisms of subpicosecond pulses to expansion of the plume to interfacial reactions with the substrate are considered in this section. The theoretical background presented here will form the basis for the optimisation procedure of the ULPD technique that will be carried out with the upgraded system in this thesis.

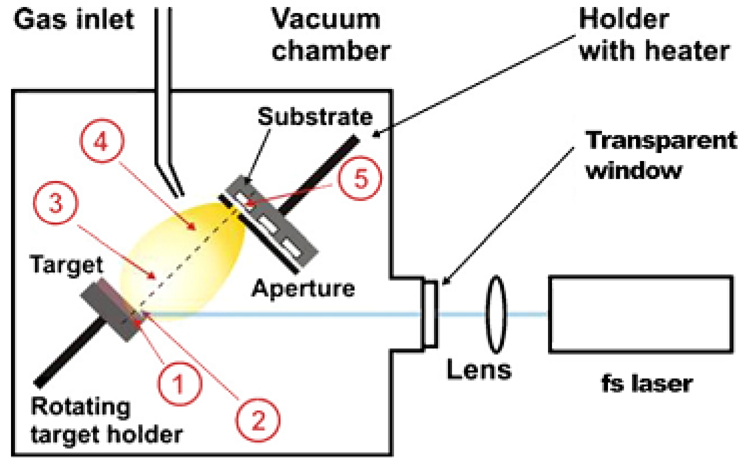

Figure 4.2: Overview of the stages for fs-PLD/ULPD, indicated by number. Stage (1) light absorption in the solid target. Stage (2) one-dimensional expansion after the laser pulse. Stage (3) free three-dimensional expansion. Stage (4) expansion in the background gas. Stage (5) film growth on substrate. Figure adapted from [131].

4.2.1 Ultrafast laser ablation

Laser ablation is the removal of matter from a solid or bulk following sufficient energy deposition by a laser pulse and is represented by (1) in fig. 4.2. Ultrafast lasers emit ultrashort pulses of femtosecond or picosecond (typically below 100 ps) duration. For sub-picosecond pulses, the ultrashort time of excitation allows the processes of absorption or excitation, melting and material removal to be separated in time and analysed sequentially [132]. The typical processes leading to ultrafast laser ablation of metals, semiconductors and dielectrics by a ~100 fs duration and 10^{10} W cm^{-2} - 10^{14} W cm^{-2} intensity pulse are depicted in fig. 4.3. In the ULPD technique, ultrafast laser ablation of dielectrics occurs by sub-picosecond laser pulses and this will therefore be the focus of this section.

Absorption of ultrashort pulses in dielectrics

In dielectrics, where the band gap is larger than the laser photon energy, absorption of the ultrafast pulse energy occurs in the skin layer through non-linear ionisation effects (multiphoton, tunneling, impact) that are made possible by the high peak intensity [123, 132, 133]. The conduction band of a dielectric is empty and so initial electronic

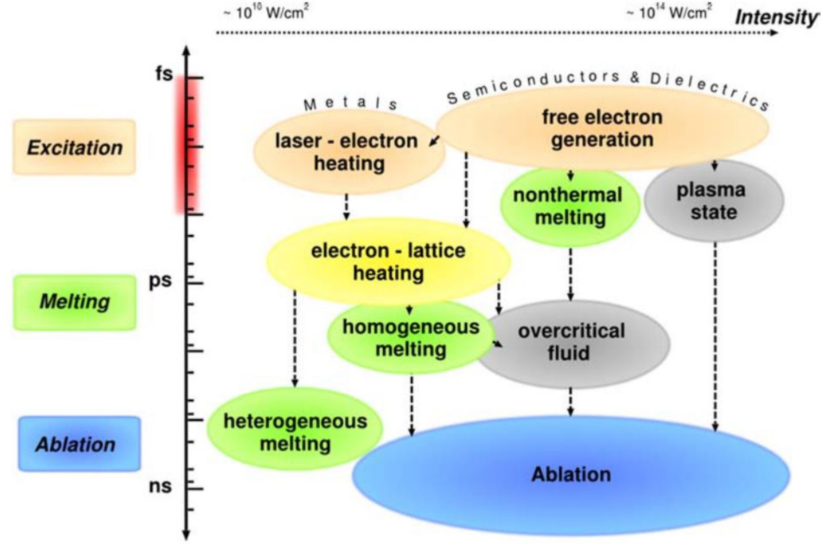

Figure 4.3: Typical timescales and intensity ranges of several phenomena and processes occurring during and after irradiation of a solid with an ultrashort laser pulse of about 100 fs duration. Excitation takes place in the range of femtoseconds (duration of the laser pulse). The timescale of melting may vary for different processes and lies roughly in the picosecond regime. Material removal, i.e. ablation, lasts up to the nanosecond regime. Figure reproduced from [132].

excitation begins via multiphoton ionisation, where multiple photons are absorbed in one step, and tunneling ionisation, where the potentials are bent by the electric laser field. The contribution of each process is described by the Keldysh parameter $\gamma_{\mathrm{K}} = \omega_{\mathrm{L}}\sqrt{m_{\mathrm{red}}\epsilon_{\mathrm{gap}}}/eE_{\mathrm{L}}$, where m_{red} is the reduced mass of electrons and holes, ϵ_{gap} is the band gap, ω_{L} is the frequency of the laser and E_{L} is the electric field amplitude of the laser [134]. The multiphoton process dominates when $\gamma_{\mathrm{K}} \gg 1$ and tunnelling ionisation dominates for very high intensities when $\gamma_{\mathrm{K}} \ll 1$.

Photoionisation excites electrons at the lowest energy in the conduction band. The free electrons are able to gain further kinetic energy in the high frequency electric field of the laser light through intraband absorption (i.e. inverse bremsstrahlung) [132, 135]. When free electrons exceed a certain critical energy ϵ_{crit}, which is on the order of the band gap energy, they are able to partially transfer their kinetic energy to an electron in the valence band and promote it into the conduction band [135, 136]. It is assumed that the rate of impact ionisation directly depends on the free electron density and

for timescales longer than the timescale of intraband absorption, the electron energy distribution is static and free electron generation is dominated by avalanche ionisation [132]. The percentiles of collisional avalanche ionisation to multiphoton ionisation for silica in dependence of laser intensity and pulse duration have been calculated by Rethfeld [137]. As the free electron density increases during the pulse, the laser-irradiated dielectric exhibits strong metallic-like absorption due to the transition to an imaginary dielectric function (negative refractive index) [132].

Electron-phonon relaxation

Following the heating of the electrons in the skin layer of the dielectric through ultrafast laser irradiation, thermalisation between the electrons and phonons to an equilibrium takes place. Thermalisation (dephasing of the polarization) of electrons occurs first through electron-electron collisions that take place over a timescale of femtoseconds [138]. While individual electron-phonon collisions that cause the heating of the lattice only take a few femtoseconds, the relaxation time to equilibrium occurs in a time scale of picoseconds as only a small energy transfer from electron to phonon occurs in each of the incoherent interactions [132, 139]. The electron-phonon coupling strength in dielectrics depends on the properties of the conduction band electrons and their density. Once thermal equilibrium is achieved, the energy distribution is characterised by the, now defined, temperature of the laser-excited material.

Ultrafast phase transitions

So long as there is a sufficient deposition of energy into the laser irradiated dielectric, phase transitions occur. The heating of the electrons on the subpicosecond timescale results in highly nonequilibrium states that are not accessible by other means. Structural modification through the nonequilibrium processes *Coulomb explosion* and *nonthermal melting* take place first. The electron-lattice thermalisation that occurs through incoherent electron-phonon interactions and the electron wave mediated transport of energy through the material, which typically takes a few ps for an equilibrium temperature gradient to be reached [132, 139]. Providing the melting temperature is surpassed, *thermal (homogeneous and heterogeneous) melting* takes place. The various ablation mechanisms occur on different timescales, as shown in fig. 4.3, and will be considered in the following.

Coulomb explosion is the term used for the direct emission of surface atoms through strong repulsive forces of positively charged ions. In this process, the electrons in the skin layer accumulate enough energy during laser irradiation to be directly ejected from the target. The space charge separation between the highly energetic electrons in the plasma and the remaining positive ions creates a strong electric field. The magnitude of the field depends on the electron kinetic energy $E_e \sim (T_e - E_{\text{esc}})$, where E_{esc} is the work function and T_e is the electron temperature, and the electron density gradient normal to the target (assuming one-dimensional expansion) [123]. If the electron energy is larger than the binding energy E_b of ions in the lattice, the ions are pulled out of the lattice with a maximum energy $E_i(t) \approx Z(T_e - T_{\text{esc}} - E_b)$ as all energy losses due to electron-ion Coulomb collisions and heat conduction are negligible. The emitted ions of different mass therefore all have equal momenta. Coulomb explosion is not reliant on the thermalisation of electrons and has a characteristic time comparable to subpicosecond pulse duration, lasting ~100 fs, and is therefore the only ablation process that occurs during the laser pulse [123]. In dielectrics, Coulomb explosion is made possible as the strong transient electric fields at the surface cannot be neutralised quickly by mobile conduction band electrons of the bulk material (as is the case in metals) [140, 141]. The contribution to total ablated material mass by this process is small [1, 129, 132]. Experiments on sapphire have shown that this type of ablation is dominant only in the low fluence 'gentle' ablation regime and allows the control of ablation depth to nanometer scale [142].

Nonthermal melting is characterised by high temperature electrons surrounded by a cold lattice. The highly nonequilibrium state that can live for a couple of picoseconds arises due to the fact that, following laser excitation, electron thermalisation through electron-electron collisions occurs on timescales generally much shorter than lattice heating through incoherent electron-phonon collisions. The effective potential acting on the ions (binding energy) is dependant on the electronic state and represented by the potential energy surface (PES). Excitation of a large number of electron-hole pairs by the laser pulse creates a sudden change in potential resulting in a movement of the ions. The motion is typically cooperative (ions do not move independantly) and can also be coherent [143, 144]. The order of the lattice is affected leading to instabilities if the forces due to the PES are strong enough. The fast material disorder occurring before electron-phonon heating is interpreted as melting and the new phase change post

recombination of electron-hole pairs and/or electron cooling is permanent [132]. It is important to mention that it is experimentally very difficult to characterise nonthermal melting and to distinguish it from ultrafast thermal melting.

Thermal melting exists in two forms, heterogeneous and homogeneous nucleation. Heterogeneous nucleation of the molten phase begins at the surface as there is no energy barrier at the solid-vapour interface [132]. The melt front proceeds into the heated layer of the material with a velocity ultimately limited by the speed of sound (typically hundreds of m/s) taking approximately 100 ps [132]. The molecular dynamic simulation in fig. 4.4a shows 20 ps separated snapshots of the melt front proceeding from both surfaces of a Nickel film heated slightly above melting point by an ultrashort laser pulse of 200 fs duration [145]. Homogeneous nucleation of the molten phase occurs if a sufficient ratio T/T_m of overheating is achieved. The total time of lattice melting is characterised by the electron-lattice heating time, which typically occurs on a timescale of a few picoseconds. Figure 4.4b shows a strongly overheated area with the same material and laser parameters as before [145]. The snapshots begin at 14 ps after the laser pulse and it is seen that small nuclei of molten phase grow within several picoseconds until the entire region is molten. In the case of strong overheating, molten nuclei grow homogeneously due to fluctuations and are superimposed upon the slower melt front propagation due to heterogeneous melting. This melt front continues to proceed into regions of lower overheating with temperatures around melting temperature.

Hydrodynamic expansion

Despite having undergone phase transformations, the ultrafast heating of the matter is isochoric as the change in density at the relevant time scales is not significant. The state of the solid matter is called warm dense matter [132]. Rapid thermal expansion of the heated skin layer proceeds from this point on leading to nanoparticle formation. Numerous phenomena may occur including fragmentation (either through decomposition by homogeneous nucleation or mechanical stress) [146], evaporation (resulting in an atomic plume) [123], vapour condensation into droplets [123, 147], droplet formation through violent sub-surface thermal effects [121, 148], spinodal decomposition (the development of inhomogeneous structures as a result of thermodynamic instabilities[1])

[1] This occurs when cooling and adiabatic expansion (pressure and temperature decrease without the gain or loss of heat) of the material that is heated above the vapour-liquid critical temperature

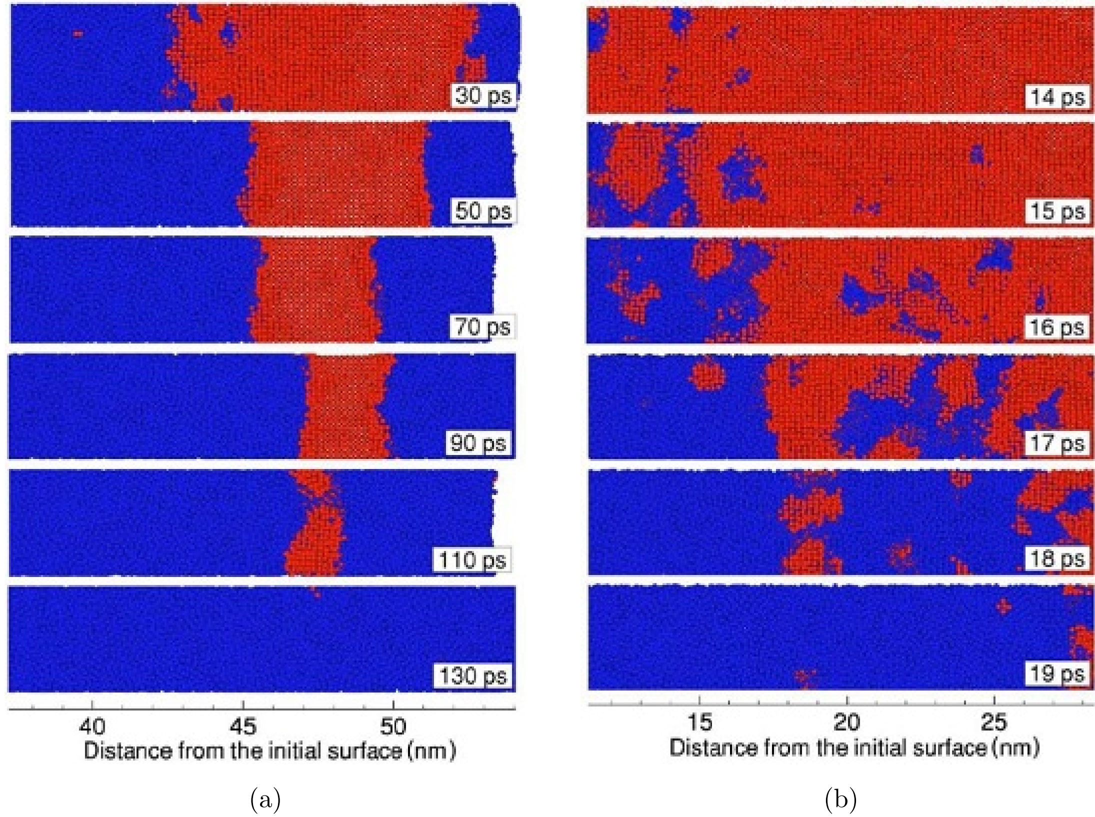

Figure 4.4: Snapshots of molecular dynamic simulations of (a) heterogeneous and (b) homogeneous melting. A 50 nm Nickel film was assumed to be heated with an ultrashort laser pulse of 200 fs duration. The red atoms indicate crystal surroundings while blue regions are molten. In (a) the crystal is heated slightly above melting temperature and the melt front due to heterogeneous melting propagates from the front and rear side of the samples where the energy barrier is zero at the solid-vapor interface. In (b) strong overheating results in the procession of ultrafast melting due to homogeneous nucleation. Images reproduced from [145].

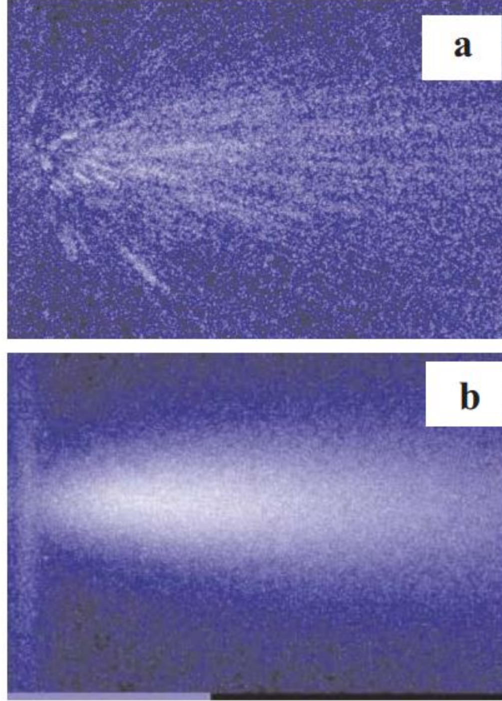

Figure 4.5: CCD camera plume images recorded from the laser ablation of $BaTiO_3$ 100 μs after the 620 nm laser pulse in (a) the nanosecond regime (5 ns and 0.5 J/cm^2) and (b) in the femtosecond regime (90 fs and 1 J/cm^2). The size of each image is around 3 cm $\times$ 5 cm and the grey intensities are on a log scale. Image reproduced from [151].

[149] and spallation (pressure wave into the target) [150]. Except for spallation, all these processes lead to ejection of material [1].

4.2.2 Plume expansion and transport

The expansion of the ablation plume occurs in three stages. One-dimensional expansion is followed by three-dimensional expansion in the vacuum and finally the expansion in the background gas. Each stage is depicted by (2), (3) and (4) in fig. 4.2, respectively. Individual femtosecond pulses do not interact with the ejected material and so the complicated secondary laser interactions of plume expansion with the tails of ns and ps pulses does not occur [146].

arrives close to the critical point so that phase separation results in participates.

One-dimensional vacuum expansion

The initial thermal and pressure gradients are predominantly one-dimensional and so the initial sub-nanosecond plume expansion (the time in which the ejected material has travelled less than a laser focal diameter from the residual surface) into the vacuum may be approximated as one-dimensional [147]. Nanoparticle formation due to the adiabatic expansion and rapid temperature quenching (one to three orders of magnitude faster than the irradiated surface material) of the highly energetic and pressurised fluid occurs during this phase [147].

Three-dimensional vacuum expansion

Three-dimensional expansion ensues at a later time. The femtosecond laser ablation plume is highly directional pointing away and normal to the target surface, more so than for nanosecond pulses as shown in fig. 4.5. Time-resolved optical emission spectroscopy studies of the laser induced plasma resulting from fs ablation, when the laser intensity is of the order of the plasma formation threshold, typically show three distinct features separated in time regardless of target material, as shown in fig. 4.6 [121, 124, 152, 153]. Immediately after the fs pulse (< 0.5 μs), sharp emission lines are observed due to ions/atoms travelling at 10^6 - 10^7 cm/s [129, 153]. For low conductivity dielectrics these ions are formed via coulomb explosion [140]. While the emission is intense, ions/atoms only make up only a small fraction of the matter in the plume (few %) [124]. Molecular species of TiO have also been observed during this time and travel at slightly lower velocity of $\approx 2 \times 10^5$ cm/s [129]. At longer delay times (5 - 100 μs) the plume luminescence is characterised by a structureless broad continuum due to the blackbody-like radiation from hot (of the order of several thousand K) NPs and, at later times providing the laser fluence is sufficient, droplets travelling at $\approx 10^4$ cm/s [121, 124, 152, 153]. Radiative cooling ensures rapid cooling during plume transport [152]. The presence and size of droplets increases with laser fluence [121].

The most volatile component from the high temperature aggregated NPs and droplets is known to preferentially evaporate during initial plume transport for multi-component targets [154]. It has also been experimentally observed that a variation in composition may occur with angle (isotopic content [155] and stoichiometry for multi-component targets [151, 154]) that is not explained by the current understanding of femtosecond

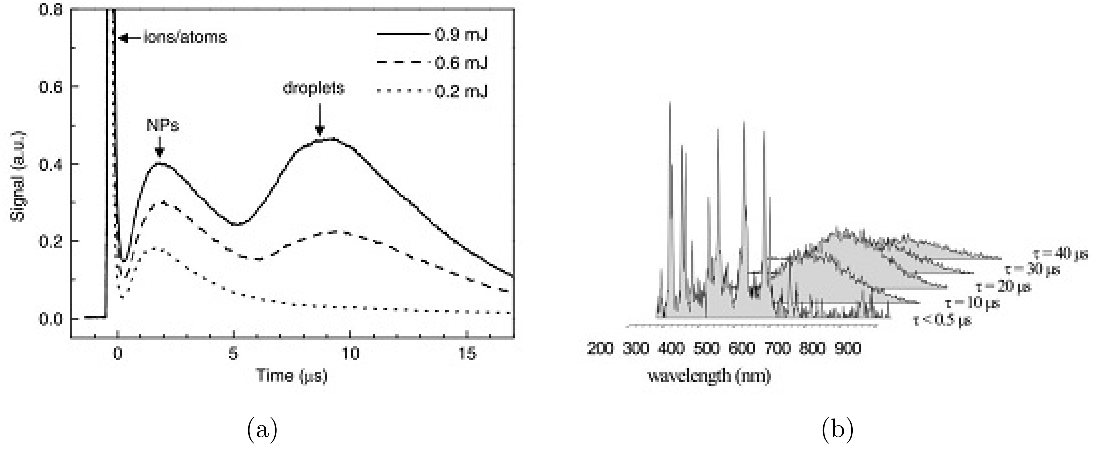

(a) (b)

Figure 4.6: Optical emission spectra of plasma plumes generated by fs laser ablation; (a) Time-resolved intensity of a MgO plume ablated at various beam energies with a laser beam spot size of 9.4×10^{-5} cm^2 and (b) spectra of a gold plume for different time delays τ, at $d = 1$ mm for a laser fluence $F = 0.6$ J/cm^2. Reproduced from [124] and [152], respectively.

laser ablation. A further consideration for Gaussian shaped intensity profiles of the focused laser beam on the target surface results in varying levels of heating on the target surface and therefore different species of plume constituents may be present within a single pulse irradiated area [123].

Background gas expansion

The nanoparticle formation directly at the target surface without the requirement of a background gas is a unique feature of fs laser ablation that is advantageous for film formation [1, 123, 129]. Nonetheless, a background gas may be introduced in the chamber for numerous reasons. In experimental setups where the laser focus on the target is fixed under the substrate, such as in fig. 4.1 and fig. 4.2, the pressure from a background gas is used to disperse the highly directional femtosecond laser ablation plume to give a more uniform deposition on the target surface. The expansion of a brass plume generated by femtosecond laser ablation at varying ambient argon pressures is shown in fig. 4.7. Collisions of the plume species with the ambient gas were significant for pressures $\gtrsim$200 mTorr and almost negligible for lower pressures [156, 157]. Collisions with the ambient gas confined the plasma and increases inter-species

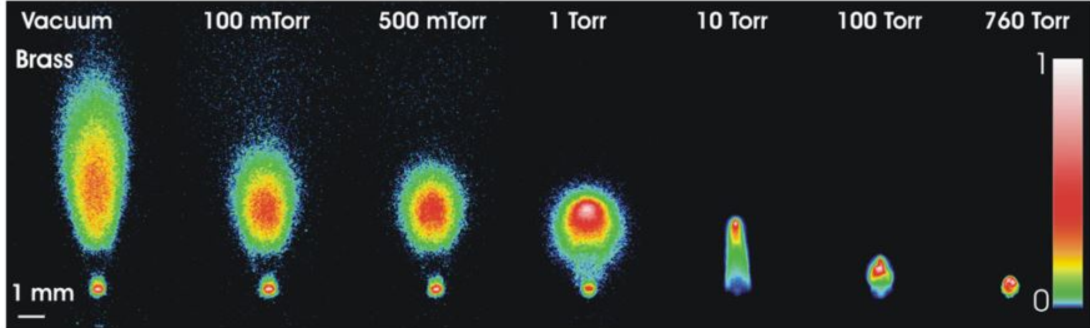

Figure 4.7: CCD images of the evolution of a brass fs-laser ablation (800 nm, 40 fs, F = 1.77 J/cm^2) plume at a delay of 300 ns after the onset of plasma as a function of ambient argon pressure. Images are aquired with an exposure time of 30 ns and are normalised to the maximum intensity. Reproduced from [156].

collisions [157]. Furthermore, at moderate pressure levels between 1 and 10 Torr, a reduction in temperature of the now jet-like plume occurred.

The high energy ions and nanoparticles in the ablation plume may collide with background gas particles at a rate dependent on pressure. Collisions may reduce the energy of ions and thus reduce sputtering of the film [158]. Nucleation of both ions and nanoparticles may also occur if a high enough pressure is used. Gamaly et al. [159] ablated graphite targets with 12 picosecond 532 nm laser pulses in various ambient gasses (He, Ar, Kr and Xe) and found that there was only a noticeable increase in nanoparticle size for pressures above 50 Torr, ranging from around 4 nm at 100 Torr to 8 nm at 1000 Torr. Below this pressure, the hydrodynamic expansion of the plume determined the nanoparticle size. Teghil et al. [154] attempted to compensate for the loss of oxygen in the NPs during plume transport by collisions with the background oxygen gas molecules but found that the oxygen uptake by the hot NPs was ineffective as the plume is not primarily atomised, as for ns-PLD, and NP formation does not occur through gas phase condensation. Nonetheless, it has also been found that for some target materials combinations of laser fluence and background pressure result in a film of significantly different composition to the target or the recovery of the stoichiometric composition of the target [1].

4.2.3 Film growth

The growth of the film occurs as the ablation plume impacts the, possibly heated, substrate, as shown by stage (5) in fig. 4.2. The majority of films formed via the fs-PLD technique occurs through the random stacking of deposited NPs [1]. The impact of ions with a high kinetic energy has been found to produce defects resulting in crystalline phases in ZnO films [160]. Millon et al. [151] found that the choice of substrate affected whether $BaToO_3$ deposited films were amorphous or crystalline.

Er^{3+}-doped zinc-sodium tellurite glass NPs have been incorporated in polymer films through fs-PLD by Kumi-Barimah et al. [161]. Similarly, the ULPD technique collects the ablation plume on a heated silica substrate to form amorphous hybrid tellurite-silica thin films. Film formation using the ULPD technique has only ever been reported in a $\approx$ 70 mTorr oxygen atmosphere [6, 23, 24, 162, 163]. For silica substrates, Chandrappan [162] found that processing at room temperature (25°C) produced a deposited film without dissolution. Selected area electron diffraction (SAED) patterns of the film showed discrete reflections and it was hypothesised that it was due to the the crystallisation of tellurite components at high temperatures in the plume. High processing temperature optical microscopy studies between 650°C and 700°C showed the evolution of a rough island like film at low temperatures into a smooth surface layer at high temperatures. The narrow 1.54 μm photoluminescence spectra of the 700°C film was characteristic for Er^{3+} in silicate and showed that dissolution had been achieved. The films processed at 650°C contained large droplets, tens of micron in diameter, presumably due to the high laser fluence and resulted in rough films surfaces. Similar observations on processing temperature for silica-on-silicon substrates was shown by Kamil [163]. A processing temperature of 400°C resulted in a deposited nanoparticle layer. Increasing the deposition temperature to 570°C produced amorphous films. Further increments to the processing temperature up to 700°C resulted in thicker films believed to be due to the weakening of Si-O bonds.

4.3 Experimental Setup

A photograph of the ULPD system is shown in fig. 4.8 and a schematic is given in fig. 4.9. The femtosecond laser is focused onto a target surface inside a stainless steel vacuum chamber with gas ports (deposition chamber). Inside, a substrate is mounted

in a rotating holder situated above the target and beneath the quartz infrared heating lamps. While the experimental setup appears similar to that shown in fig. 4.1, key differences exist between the two systems. The following section details the system components and procedures.

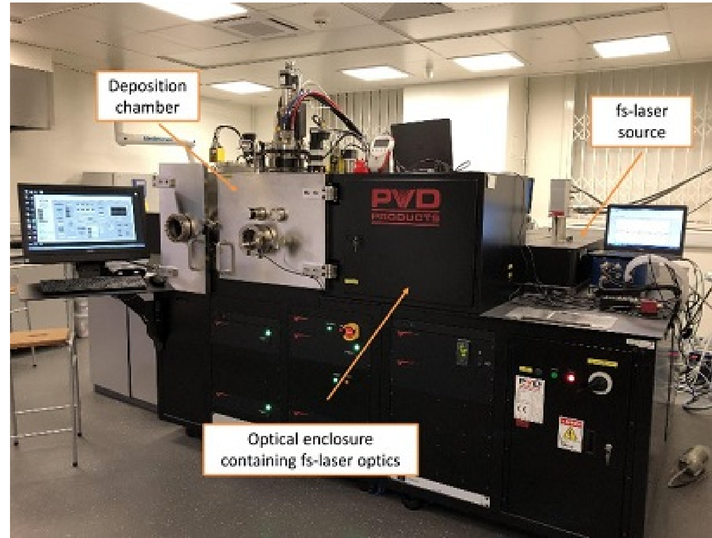

Figure 4.8: A photograph of the upgraded ULPD system used in this thesis.

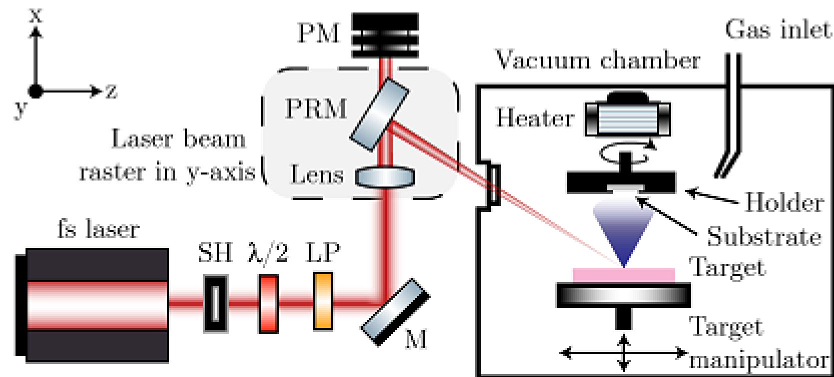

Figure 4.9: Schematic of the experimental setup used to fabricate thin films using the upgraded ULPD system. Mirror (M), partially reflective mirror (PRM), power meter (PM), shutter (SH), linear polariser (LP), half-wave plate ($\lambda/2$).

4.3.1 Laser delivery

Laser source

The laser source is a variable repetition rate ultrafast Ti:sapphire amplifier (Wyvern 1000-10, KMLabs) producing a horizontal p-polarised beam with a central wavelength of 800 nm ($\sim$ 53 nm full width half maximum). For the research in this thesis the repetition rate is however fixed at 1 kHz as the cryogenic cooling of the laser amplification crystal was not able to operate at the, manufacturer specified, maximum 10 kHz. The almost diffraction limited beam is near TEM_{00} with an $M^2 < 1.3$. The pulse duration is $\sim$ 40 fs and can be measured using a FROG system (FROGscan, MesaPhotonics)[1]. The maximum pulse energy at a 1 kHz repetition rate is $\sim$ 4 mJ. The pre-pulse and post-pulse contrast on the ns scale is >250:1 and >100:1, respectively.

Beam steering and power control

A shutter controlled by the computer software is used to allow the laser into the optics box and then the vacuum chamber. The femtosecond laser optics are shown in fig. 4.10. The laser pulse energy is controlled with a variable attenuator/beam splitter that is also software controlled. It consists of a quartz half-wave plate housed in a motorised translation stage and two thin film Brewster type polarisers, which reflect s-polarised light while transmitting p-polarised light. The setup allows the intensity of the two differently polarised beams to be varied without alteration of other beam parameters just by rotating the wave plate.

The laser is then directed via reflective coated mirrors held in kinematic mounts to a linear stage mounted focal lens and turning mirror. The laser beam is focused with a 56.5 cm focal length plano-convex lens and then directed into the vacuum chamber at a 60° angle of incidence onto the target surface by a partially reflective (99%) mirror. A pyroelectric detector and energy meter (PE50-DIF-C and Starlite Energy Meter, Ophir) placed behind a partially reflective (99%) mirror provides a real-time measurement of the laser energy during processing. The loss in pulse energy due to reflection from the vacuum chamber window is accounted for by calibrating with a second energy

[1] The pulse width inside the chamber will be considerably longer and closer to ~100 fs due to dispersion when passing through the glass windows.

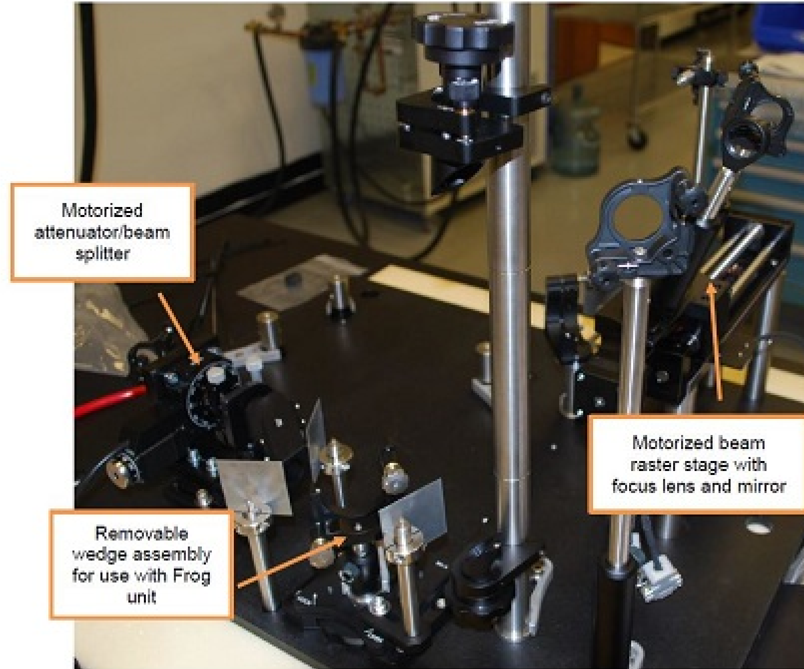

Figure 4.10: The femtosecond laser optics. Image reproduced from the manufacture's user manual.

measurement inside the chamber. Both the focusing lens and partially reflective mirror are mounted on a linear translation stage for laser rastering.

Focal spot measurement

From theoretical calculations using the collimated fs-laser output beam and the focusing lens focal length, the focused spot size normal to the beam is approximately 75 μm in diameter and the Rayleigh length was of the order of mm. The elliptical laser spot on the target surface therefore has Gaussian beam waists ($1/e^2$ of the intensity profile) of approximately 32.5 μm and 65 μm, giving an area of 6.64×10^{-5} cm^{-2}.

A direct measurement of the beam area is necessary to account for daily variation as small uncertainties lead to large errors in fluence calculations. Prior to ablation, the elliptical laser spot at the target surface is measured on a diffuse white card with a USB microscope.

Laser rastering

One-axis laser rastering on the target surface is achieved with the linear translation stage upon which the focusing lens and partially reflective mirror are mounted. Two positions on the translation stage that place the spot close to the edges of the target are found empirically. The stage is then translated between these two positions at the maximum speed of 10 mm/s by the computer software. To give a uniform ablation on the substrate it was ensured that the raster length on the target was much larger than the substrate width.

4.3.2 Target

Target manipulator

The targets are mounted in a three position target manipulator, shown in fig. 4.11. The maximum size of the targets is 170 mm long and 50 mm wide. The Z stage is used to raise or lower the height of the target so that the surface is at the focus of the laser spot. The X stage, mounted beneath the Z stage, allows for target indexing and provides motion for rastering over the target width. The stages both contain encoders with a 0.1 millimeter accuracy.

Following each line that the laser rasters across the length of the target, translation of the X stage provides a new target surface for rastering. Each target translation used in this work was 0.1 mm. Alternating steps of laser raster and target raster are performed forwards and backwards over the entire target surface.

Surface preparation

The target surface is prepared first by rough polishing the target surface with P320 grit SiC sand paper. The laser is then rastered twice over the target surface at the set deposition laser fluence. This involved 10 - 15 pulses/unit area being applied to the target surface. After this preparation, the material incubation and surface roughness reached a steady state, giving a constant ablation threshold. A pneumatically controlled substrate shutter prevented the ablation plume from reaching the substrate during this procedure.

It is known that the target surface quality (roughness and material incubation from previous irradiation) has a strong effect on the material ablation threshold (will be

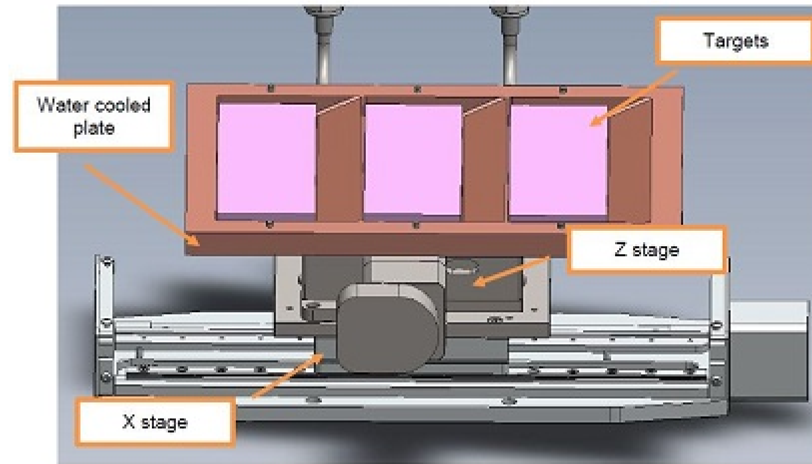

Figure 4.11: A 3D schematic of the target manipulator. Image reproduced from the manufacture's user manual.

discussed in chapter 5 and chapter 6). The variation in ablation plume during the first laser raster profiles was clearly seen at high fluence ablation on a polished target. The first raster gives no visible albation plume but by the third raster, where the target had roughened significantly and material incubation from previous pulses occurs, results in a large (several cm) jet like ablation plume. Reaching a steady state ablation threshold prior to sample fabrication is especially critical for thin film production where the laser may only be rastered over the target several times.

4.3.3 Substrate/heater stage

The substrate and heater stage is located above the target stage. The entire assembly is mounted to a motorised vertical stage allowing a variable target-to-substrate distance of 35 to 105 mm.

Substrate Holders

Substrates all had surface areas of 10 mm by 10 mm and are held in stainless steel holders. The holders used depended on the number of substrates being processed and are shown in fig. 4.12.

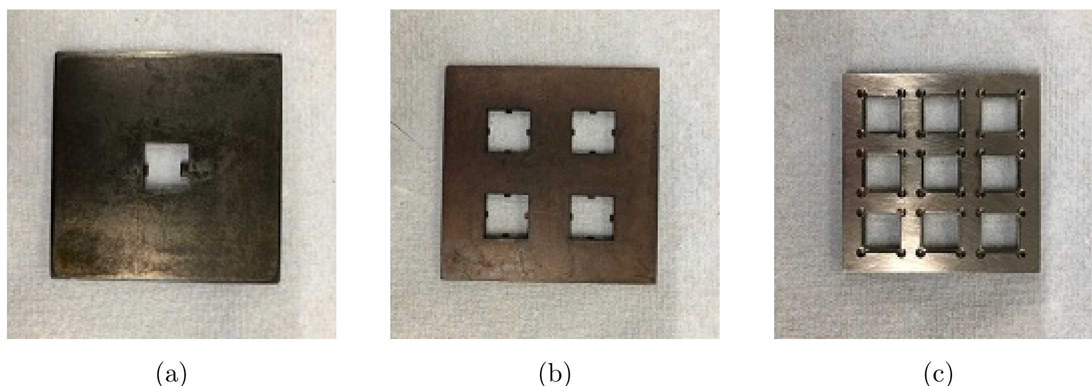

(a) (b) (c)

Figure 4.12: Substrate holders for 10 mm by 10 mm sized substrates; (a) 1 by 1, (b) 2 by 2 and (c) 3 by 3.

4.3.4 Substrate heater

Backside substrate heating is achieved by a bank of quartz infrared heating lamps (QH1200T3/CL/HT MIH, General Electric) housed inside a reflective, water-cooled block. A type K thermocouple mounted inside the stage provides a closed feedback loop to a Eurotherm controller for substrate temperature control. The calibration for substrate temperatures was performed by the manufacturer using a second thermocouple attached to the inocel substrate holder. Appendix C provides the emission spectra of the quartz infrared heating lamps in comparison to a SiC heating element (used in the previous system).

The heat treatment procedure is depicted in Figure 4.13 and was only initiated once the processing atmosphere was set. The room temperature was typically 22°C. The initial hold time at the processing temperature is to allow for the temperature inside the deposition chamber to stabilise. The post processing hold time is to allow for dissolution of the most recently deposited NPs with the silica substrate. It has been shown by [130] that holding hybrid tellurite-silica thin films fabricated via the ULPD technique for extended periods of time ($\gtrsim$ 30 minutes) at elevated temperatures ($>$ 600°C) causes undesired phase separation and crystallisation. It may be possible and even preferable to reduce this post deposition hold time depending on the rate of material dissolution, however this has not been characterised. The fastest ramp down rate possible is used to avoid crystallisation in the metastable films.

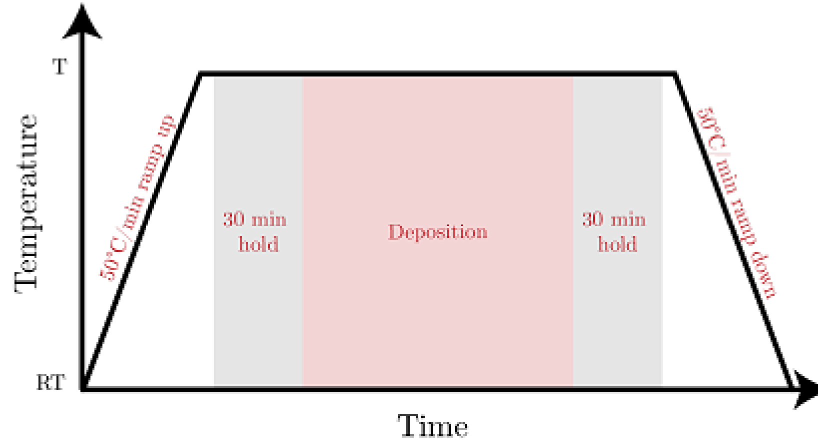

Figure 4.13: The heating procedure used for the fabrication of hybrid tellurite-silica films with the ULPD technique. (RT) room temperature, (T) processing temperature.

4.3.5 Chamber atmosphere

A dry pump (EV-A03, Ebara) is used to evacuate the deposition chamber during an initial roughing cycle and then a turbo drag pump (HiPace 700 l/s, Pfeiffer), backed by the dry pump is used to reach a chamber base pressure of $<1\times10^{-4}$ Torr. Oxygen, nitrogen and argon gasses may be introduced to the chamber at varying pressures via three 20 sccm full scale mass flow controllers. Venting of the chamber back to atmospheric pressure post processing was performed with nitrogen gas.

4.4 Optimisation procedure

It is known that film formation through ultrafast laser pulsed laser deposition is dependent on numerous parameters, such as the laser parameters (intensity distribution of the laser on the target, pulse energy, wavelength, pulse width), the pre-pulse and post-pulse laser energies, the pressure of the reactive gas in the deposition chamber and the substrate temperature [123]. Despite an incomplete understanding of these processes, the fabrication of high concentration RE-doped hybrid tellurite-silica thin films with desirable material optical properties has been achieved [6, 23–25]. The fabrication of sub-micron thin films and films suitable for optical applications requires excellent film homogeneity. Films fabricated with the ULPD technique so far have typically suffered from macroscopic surface roughness (most likely resulting from droplets) and cracking

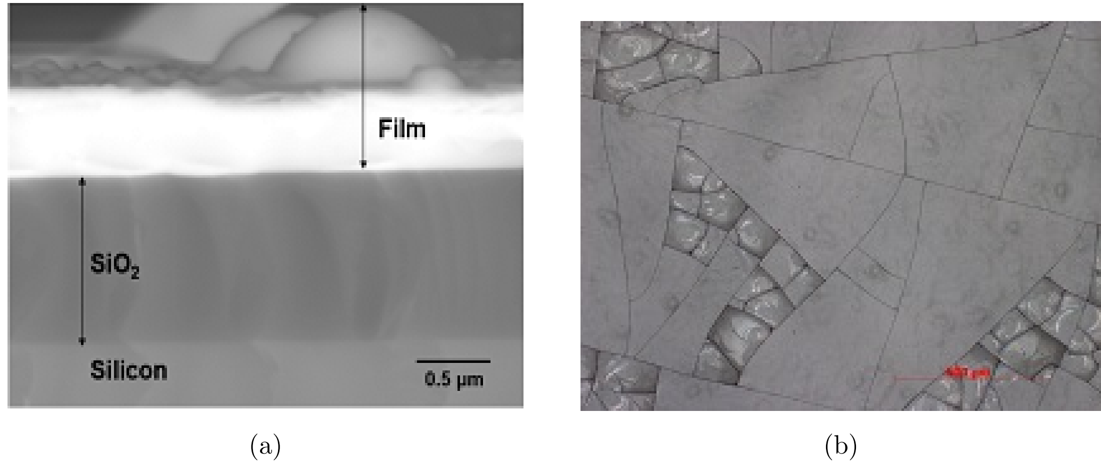

(a) (b)

Figure 4.14: (a) Inhomogeneous surface and (b) cracking in thin films fabricated via the ULPD technique. Reproduced from [163] and [25], respectively.

of thick films, as shown in fig. 4.14. The need to improve the quality of the thin films for optical applications through a better understanding of the processes involved in the ULPD technique is often stated [127, 128, 162, 163]. Furthermore it is questionable as to whether the parameters reported in the literature to fabricate micron thin films are optimal.

There are several key differences between the system that is used in this work and described in section 4.3 with the older system that was used for most of the previous research (reviewed in section 4.1). Namely, the shorter pulse width (45 fs rather than 100 fs) [164, 165], the increase in spot size (due to a larger angle of incidence and longer focal length lens) [124] and the rastering procedure (area scan compared to static) may all affect the process. An optimisation of the process parameters is therefore required. The optimisation procedure in this thesis follows the sequential order of events that occur during film formation through femtosecond laser ablation, which were described in section 4.2 and are depicted in fig. 4.2.

4.4.1 Femtosecond laser ablation

The plume formation is a direct consequence of the femtosecond laser-matter interaction and can therefore be controlled by considering the laser parameters (pulse duration, pulse energy, wavelength, intensity distribution) in relation to the target parameters (density, thermal diffusivity, binding energy, etc.). Characterisation is performed in a

two step process. First the ablation threshold and rate of tellurite glass is determined and then the plume species in dependence of laser fluence relative to target ablation threshold is investigated.

Ablation threshold

The cascade of laser-matter interactions at the short time scales of femtosecond laser pulses are complex. A phenomenological approach is typically used to quantify the morphological changes to the material [166]. The ablation threshold represents the minimum laser fluence required to remove material upon irradiation of a target and is routinely measured to characterise this interaction. A measurement of the ablation threshold of tellurite glass under femtosecond laser irradiation is lacking in the literature. Evaluation of this quantity may be performed via measurements of optical breakdown, surface light-scattering of a coherent laser, extrapolation of ablated volume to zero and the extrapolation to zero of logarithmic dependence of the damage crater area on the energy/fluence of a Gaussian laser pulse [167]. The use of latter methodology is the most widely reported in the literature due to it's simplicity and is used in this thesis. This stage of the optimisation procedure is detailed in chapter 5.

Plume species

The plume species (nanoparticles and droplets) is investigated through room temperature vacuum depositions on silicon substrates at varying laser fluences. The goal of this optimisation step is to identify the experimental conditions that do not produce droplets. Measurements of the film thicknesses allow for an evaluation of the deposition rate. Further insight into the nature of the ablated material is achieved by studying the composition, crystalline state and photoluminescence properties of the deposited films. While compositional changes may occur during plume transport, such as evaporation of volatile components, the target-substrate distance used is similar to what has been used in previous research and the results therefore directly correlate to what may be expected in ULPD fabrication. This stage of the optimisation procedure is detailed in chapter 6.

4.4.2 Plume expansion

The effects of three-dimensional vacuum plume expansion are not investigated as only the centimetre order target-substrate distance used in the previous study of the plume species is relevant for the ULPD technique. In addition to this, time- and space-resolved optical emission spectroscopy would be required for analysis of the plume species and their temperature and velocity, which the system does not currently have. Langmuir probe studies may provide insight into the energetic ions, however ablation of the multicomponent target glass results in ions of different charges and so the analysis would not be clear.

The use of a background atmosphere to control the energy of the ions to avoid sputtering could be investigated with Langmuir probe studies, but, as the sputtering is not observed in ULPD films it was not deemed critical to and within the scope of the optimisation procedure in this research. The expansion of the NPs in the plume within a reactive oxygen background gas is also not investigated for several reasons. Most importantly, the rastering of the laser over the target surface in the new ULPD system negates the need for plume shaping to improve deposition homogeneity on the substrate. In addition to this, the need for a reactive gas in the chamber that has been used in previous research is unclear as the possibility of film formation in a vacuum using ULPD has not been reported. Previous research states that the background oxygen gas is required for the replenishment of lost oxygen during plume transport. However, as previously mentioned, the uptake of oxygen by hot nanoparticles is ineffective. This suggests that any effect of oxygen in the atmosphere will occur during the dissolution film formation stage and should therefore be investigated last. Chandrappan et al. [6] reasoned that 'a significant amount of Te, most volatile and structurally unstable component in the target glass, could deplete in the absence of proper oxygenation during the transport and results in the reduced concentrations of Te' in the erbium-doped hybrid tellurite-silica film, however based on the literature in section 4.2.2 this seems unlikely at the low (∼100 mTorr) oxygen pressures used. Furthermore, evaporation of the Te out of the films at the elevated substrate temperatures used during fabrication has since been shown [130]. Instead, it may either be a remnant of the ns-PLD technique where nanoparticle formation through gas phase condensation is required for the highly

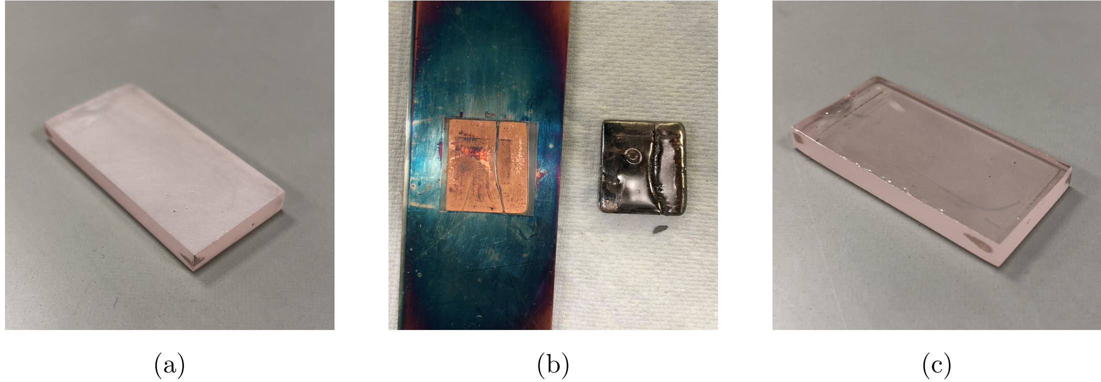

(a) (b) (c)

Figure 4.15: Photographs of the erbium doped TZN target glass used in the ULPD technique; (a) polished with P320 SiC prior to processing, (b) catastrophic melting and reaction with the brass baseplate after processing at 650°C in a vacuum, (c) heat polished surface after processing at 750°C in an oxygen atmosphere (70 mTorr, 15 sccm).

atomised plume or simply a tool to spread the plume for a more homogeneous and slower deposition.

4.4.3 Film growth

The rate of growth and optical properties of films produced through fs-PLD is characterised as a result of the previous plume species optimisation stage. For the ULPD technique, the interfacial dissolution between the plume and the substrate resulting in the formation of hybrid tellurite-silica films by is investigated by applying heat to the substrates post and during depositions.

Previous research has shown that a certain threshold processing temperature must be surpassed for material dissolution to occur and that further increasing temperature beyond this improves the dissolution rate without any negative effects [127, 162, 163]. Therefore in this work, the highest possible temperature was used for the fabrication of all films with the ULPD technique. Practically, this upper limit turned out to be 600°C, which is lower than the ideal case of over 700°C used in previous research. It was observed through various trials that processing at higher temperatures in a vacuum atmosphere resulted in catastrophic melting of the target glass and reaction with the metallic holder at random time intervals into the experiment. An photograph of a target

before and after catastrophic melting is shown in fig. 4.15(a) and (b), respectively. In an oxygen atmosphere (70 mTorr) temperatures of up to 750°C could be used, however, melting of the target surface occurred resulting in a heat polished surface, as shown in fig. 4.15(c). The oxygen flow inside the chamber cools the metal inside the chamber so that melting and reaction does not occur for the target faces in contact with the metal holder. This was deemed unsuitable for several reasons. Firstly, the smooth heat polished melted target surface has a different ablation threshold to a rough surface (as will be shown in chapter 5 and chapter 6) and the effect on plume constituents of ablating a semi-molten surface compared to a solid target are not known. Secondly, the high temperature target surface may result in the evaporation of tellurium resulting in a target that changes in composition with deposition time. This will introduce uncertainties in experiments that reuse old targets. Finally, a chemical reaction between the molten tellurite target glass and the metal holder occurs and contaminates the target, as shown in fig. 4.15(b). Melting was not seen with the previous system and is attributed to the different emission spectra between the heating elements (shown in appendix C) that results in a weaker absorption by the substrates and so a higher power is required to reach similar temperatures. The result of this, however is that the metallic chamber increases in temperature and the tellurite target is heated to higher temperatures (above melting point) through increased absorption of the radiant flux emitted by the heater.

The mechanism to film growth via the ULPD technique is characterised for silicon, silica and silica-on-silicon substrates through a series of experiments in chapter 7. Firstly the possibility of forming hybrid tellurite-silica films through (room temperature) fs-PLD deposited films followed by heat treatment is investigated. Previous research has not investigated whether the activation energy for dissolution must be applied during the deposition process. If thin film can be made in a two step process, the ULPD technique will be vastly simplified. Next, high processing temperature depositions at varying laser fluences are performed to find the optimum fluence for film growth rate and quality. Direct comparisons between the different substrates is performed as all were processed in the same run, which has not been carried out previously and is necessary to eliminate uncertainties from experimental results. Finally, oxygen is introduced into the chamber to investigate whether higher processing temperatures

improve the film properties. Following the reasoning before, it is assumed that the effect of the low oxygen pressure on the plume species is negligible.

Finally, in chapter 8, the film formation on varying silica/silicate substrates is investigated with the goal of improving photoluminescence properties of the RE-doped ions. While Richards et al. [25] have recently shown a difference between silica and quartz substrates, the samples were fabricated in different runs and with different processing parameters, which obscures the physical interpretation of the results.

Chapter 5

Femtosecond laser ablation properties of Er^{3+}-doped zinc-sodium tellurite glass

This chapter presents the femtosecond laser (100 fs, 800 nm) ablation properties of Er^{3+} ion doped zinc-sodium tellurite glass. The work in this chapter was published in the *Journal of Applied Physics* [26] and featured by the *American Institute of Physics* [168]. An introduction is given in section 5.1 and the theoretical description of the ablation threshold determination method is described in section 5.2. The experimental setup for the ablation experiments and characterisation is detailed in section 5.3. The results are presented in section 5.4 and a conclusion to the chapter is given in section 5.5.

5.1 Introduction

For the continued development and miniaturisation of integrated optics, transitioning from long optical fibres to planar waveguides is a necessary step [169]. Out of the various optical materials investigated, tellurite-based glasses have proven to be particularly promising due to their high refractive index, low phonon energy, high rare earth solubility and large emission bandwidth [170, 171]. Rare-earth ions are often doped into the host glass to provide the unique spectroscopic properties required for photonic applications. For example, the superbroadband luminescence obtained in tellurite glasses is utilised by optical amplifiers and tunable lasers [172, 173]. The fabrication of er-

bium doped waveguide amplifiers (EDWA) is a particularly active area of research. This is due to the transition of erbium in its preferred trivalent bonding state from the ground state to the metastable first excited state ($^4I_{15/2} \rightarrow {}^4I_{13/2}$) occurring at 1.54 μm, which is a standard wavelength for telecommunications as it coincides with the low loss C-band window of silica [5].

A variety of glass optical waveguide fabrication techniques have been explored and can be classified into two primary categories; index modification and thin film deposition [169]. Ultrafast lasers are used in several of these fabrication techniques. Laser inscription forms waveguides in a bulk or thin film glass by modifying the local refractive index with femtosecond laser irradiation [174–178]. The type of modification depends on both the laser and glass parameters and can be classified as either a smooth refractive index change, a birefringent refractive index modification or voids due to microexplosions [170]. The ultrafast laser plasma doping (ULPD) technique has been used to incorporate a record high lifetime-density product of Er^{3+} ions as thin films into silica glass substrates without clustering, thus overcoming a key limitation of the other EDWA fabrication techniques [6]. This technique has also been proven for silica-on-silicon (SOS) substrates, which is particularly promising as it enables the use of technology developed for microelectronics [24]. In brief, ULPD forms thin films onto a substrate by ablating an Er^{3+} ion doped zinc-sodium tellurite glass with femtosecond laser irradiation. The plume resulting from the ablated volume reacts with a substrate forming a superficial rare earth doped tellurite modified silica layer [6]. The laser fluence in relation to the target properties is a critical parameter as it must be above ablation threshold but not too high so that the plume consists of ions and nano-particles with an absence of micro-particles (droplets) [1, 124].

For controlled material processing, a detailed characterisation of the femtosecond laser-matter interaction is therefore of key importance. A characterisation of the ablation threshold and rate for Er^{3+} ion doped zinc-sodium tellurite (TZN) glass is lacking in the literature and is the focus of this research. A basic optical and physical characterisation of the Er^{3+} ion doped TZN glass is presented first. Following this we investigate the laser ablated crater morphology, ablation threshold and ablation rate of the Er^{3+} ion doped TZN glass.

5.2 Theoretical background

5.2.1 Ablation threshold determination

The ablation threshold $F_{\mathrm{th}}(N)$ (or threshold fluence) represents the minimum laser fluence required for material ablation (removal), where N is the number of pulses applied to the material. The ablation threshold is a function of the applied number of pulses and, in general, becomes lower with increasing pulse numbers due to material incubation effects that will be discussed later in this chapter. The determination of the ablation threshold is performed via measurements of the crater diameter D for different average laser fluences F_0^{av} (at fixed pulse numbers) and using the linear relationship between D^2 and $\ln(F_0^{\mathrm{av}})$, which is derived as follows.

The laser fluence F of a Gaussian spatial beam profile with a $1/e^2$ laser beam radius w_0 has a radial distribution given by

$$F(r) = F_0^{\mathrm{peak}} \exp\left(-\frac{2r^2}{w_0^2}\right), \tag{5.1}$$

where F_0^{peak} is the peak laser fluence. Ablation will occur above a certain threshold fluence $F_{\mathrm{th}}(N)$ resulting in an ablation crater of diameter $D = 2r$ as depicted in fig. 5.1. Realising that below the threshold there will be no material ablation, so that $D = 0$ at $F_0^{\mathrm{peak}} = F_{\mathrm{th}}(N)$, allows one to obtain the linear relation between the squared diameter and the logarithm of the peak laser fluence [167]

$$D^2 = 2w_0^2 \ln\left(\frac{F_0^{\mathrm{peak}}}{F_{\mathrm{th}}(N)}\right). \tag{5.2}$$

The relationship between the total pulse energy E_{pulse} the peak laser fluence F_0^{peak} is found through integration of the laser fluence over an irradiated area with radius w_0 [133]

$$F_0^{\mathrm{peak}} = \frac{2E_{\mathrm{pulse}}}{\pi w_0^2}. \tag{5.3}$$

It is common in the literature to report threshold fluences in terms of the average fluence, which for a Gaussian beam is given by

$$F_0^{\mathrm{av}} = \frac{F_0^{\mathrm{peak}}}{2} \tag{5.4}$$

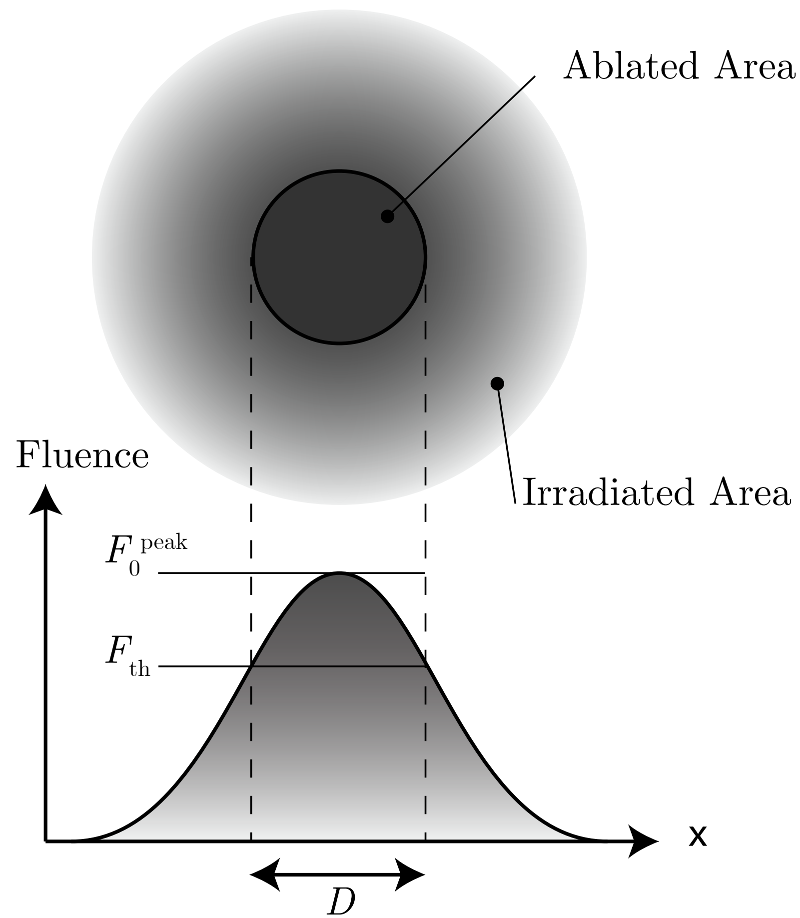

Figure 5.1: Schematic of laser-induced ablation on a material (top) and the corresponding Gaussian fluence profile along the x-axis (bottom). D marks the diameter of the ablated area. The pulse number dependence of F_{th} is implicit.

and this is the convention used in this thesis. The gradient of eq. (5.2) is not affected by the use of the average fluence and hence we arrive at

$$D^2 = 2w_0^2 \ln\left(\frac{F_0^{\mathrm{av}}}{F_{\mathrm{th}}(N)}\right). \tag{5.5}$$

Precise knowledge of w_0 (at the material surface) is required for the conversion of the, experimentally measured, pulse energy to fluence. This is retrieved directly from the measurements by realising that the energy and fluence are proportional and recasting the right-hand side of eq. (5.5) in term of pulse energy as

$$D^2 = 2w_0^2 \ln\left(\frac{E_{\mathrm{pulse}}}{E_{\mathrm{th}}(N)}\right), \tag{5.6}$$

which gives a linear relationship between the squared diameter and the logarithm of the pulse energy. The beam waist, w_0, is therefore extracted from the gradient of a linear fit[1].

The decrease in ablation threshold with pulse number is attributed to material incubation. For this work we assume that the <10 Hz femtosecond laser repetition rate is low enough so that heat accumulation does not occur between pulses [181]. Incubation has been observed in various materials irradiated with ultrafast pulsed lasers including metals, insulators, polymers and semiconductors and so the accumulation models are material dependent [182]. For dielectrics, incubation results from laser-induced point defects. Multi-photon excitation generates electron-hole pairs that then go on to form self-trapped excitons and Frenkel pairs, and a small fraction of the latter go on to form colour centers by direct trapping of conduction band electrons [183, 184]. After numerous incubating pulses the creation of defect sites reaches a steady state and so the ablation threshold reaches a limiting value. The accumulation dependence is described by a phenomenological model [185]:

$$F_{\mathrm{th}}(N) = F_{\mathrm{th}}(\infty) + \left[F_{\mathrm{th}}(1) - F_{\mathrm{th}}(\infty)\right] e^{-k(N-1)}, \tag{5.7}$$

where the parameter k describes the rate at which the ablation threshold approaches the infinite pulse value.

[1] Note that for high band-gap materials care must be taken when doing such an in-situ determination of the spot size [179, 180].

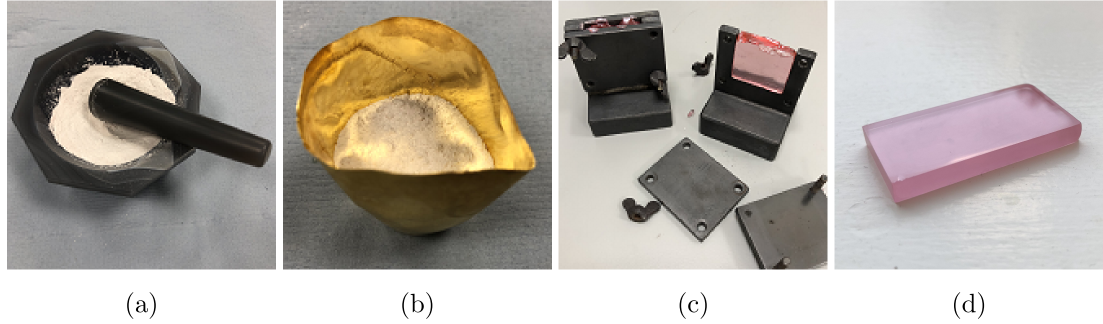

(a) (b) (c) (d)

Figure 5.2: Various stages of erbium doped TZN glass fabrication; (a) grinding the raw constituents into a fine powder with a pestle and mortar, (b) transferring the powder into a gold crucible before placing in an electric furnace, (c) removing the glass from the mould post annealing, (d) an optically polished glass.

5.3 Experimental setup

5.3.1 Sample preparation

Glasses with compositions of (80-x)TeO_2-10ZnO-10Na_2O-xEr_2O_3 (x=0.00, 0.25, 0.50 0.75, 1.00, 1.25, 1.50) mol.%, denoted TZN for x=0 and xErTZN otherwise, were prepared using analytical grade chemicals (TeO_2, ZnO, Na_2O and Er_2O_3) of purity $>$ 99.99 % and synthesised using a conventional melt-quenching procedure. After the chemicals were weighed out in their molar masses, they were ground into a fine powder using a marble pestle and mortar. A gold crucible containing the glass constituents was placed in a furnace at 875 °C for 3 hours with a low oxygen flow rate (1-2 l/min) to drag vapour from within the chamber and keep the OH^- content of the glass low. The melt was then cast into a preheated brass mould, transferred into an annealing furnace and kept at 295 °C for 4 hours to remove redisual thermal and mechanical strains. The samples were then cooled down to room temperature by 0.5 °C/min. Finally the samples were cut and polished until they reached optical quality for characterisation (procedure described in appendix D) with dimensions of $\sim 30 \times 30 \times 3$ mm^3. Several stages of the process are shown in fig. 5.2.

5.3.2 Characterisation

The amorphous nature of the glasses were examined by a X-ray diffractometer (D8, Bruker) using Cu-Kα radiation ($\lambda = 1.54$ Å) 40 kV and 40 mA, with scanning angle 2θ

ranges between 10° and 100°. The density was measured using a helium pycnometer (Pycnomatic ATC, Thermofisher Scientific). The refractive index was obtained from the critical angle using a prism coupler (2010/M, Metricon) fitted with a 633 nm laser. The absorption spectra from 380 - 1800 nm was measured using a computer aided two-beam spectrophotometer at a resolution of 0.25 nm (LAMBDA 950 UV/Vis/NIR, PerkinElmer). All measurements were performed at room temperature ($\sim$ 20°C).

5.3.3 Ablation experiments

The experimental setup is shown in fig. 5.3. Laser ablation was performed in ambient (21°C, ~750 Torr) conditions using a Ti-sapphire laser (Libra series, Coherent) with a central wavelength of 800 nm, pulse duration of 100 fs and maximum repetition rate of 1 kHz. The laser energy was determined with a pyroelectric detector and energy meter (PE50-DIF-C and Starlite Energy Meter, Ophir), and controlled with a half-wave plate and beam splitting polariser. The desired number of pulses were applied using an optical shutter (SH05, ThorLabs) with the laser operating at a reduced frequency of 20 Hz. Prior to irradiation the samples were cleaned in an ultrasonic bath with acetone and isopropanol. Sample positioning was performed on an XYZ motorised translation stage (A3200 Npaq controller and ABL1000 Air-Bearing Direct-Drive Linear Stages, Aerotech). Testing sites were separated by 0.3 mm to avoid overlap and ablation debris from neighbouring sites from interfering with measurements. The linearly polarised output beam of 6 mm was diaphragmed through a 5.5 mm aperture to avoid edge defects and then focussed at normal incidence onto the sample surface using a f = 100 mm achromatic doublet lens. Different spot sizes at the sample surface were achieved by positioning the sample before the focal plane. A long focal length lens was chosen for an easier characterisation of laser produced craters and a less critical sample positioning.

The pulse energies were measured from the average of 50 pulses prior to ablation and ranged from 11.4 to 137.8 μJ after the focussing lens. According to the manufacturer the pre-pulse and post-pulse contrast ratio of the laser was >1000:1 and >100:1, respectively. Even at the maximum applied energies, the pre- and post-pulse fluence at the sample surface was well below ablation threshold and so had no effect on the measurements.

Beam spot sizes and threshold fluences were evaluated via the D2-lnF method [167], using data measured ex-situ by differential interference contrast (DIC) microscopy

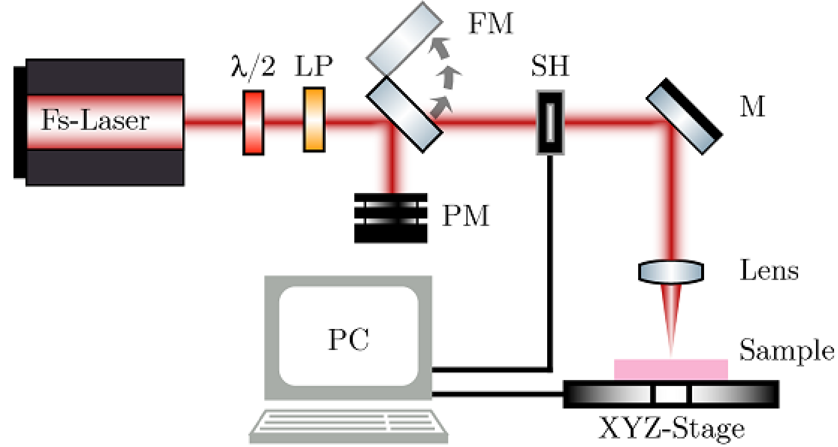

Figure 5.3: A schematic of the experimental setup used to determine the ablation threshold of target glasses. The laser beam path is depicted with a red line. Mirror (M), flip mirror (FM), power meter (PM), shutter (SH), linear polariser (LP), half-wave plate ($\lambda/2$).

(Axio Imager A1m, Zeiss). More detailed characterisation of the morphological changes of the laser irradiated areas was undertaken via scanning electron microscopy (SEM) (Hitachi TM3030 operating at 15 kV) and atomic force microscopy (AFM) operating in tapping mode (D3100 Atomic force microscope, Veeco Digital Instruments, with a nanoscope IVa controller and 14 nm nominal tip diameter). AFM data was analysed with the open source software Gwyddion [186, 187].

5.4 Results and discussion

5.4.1 Characterisation

The X-ray diffraction patterns of the glass samples presented in fig. 5.4 did not show any sharp peaks but a broad halo in the range $20° < 2\theta < 40°$, confirming the amorphous nature of the samples. The introduction of 1.5 mol. % Er_2O_3 into the host TZN glass raised the density of the glass from 5.18 to 5.27 g/cm^3. The increase in density is a result of the replacement of TeO_2 by Er_2O_3, which has a higher molecular weight. Furthermore the linear increase in density with Er^{3+} ion concentration indicates that the glass network resists the formation of non-bridging oxygens at the low doping

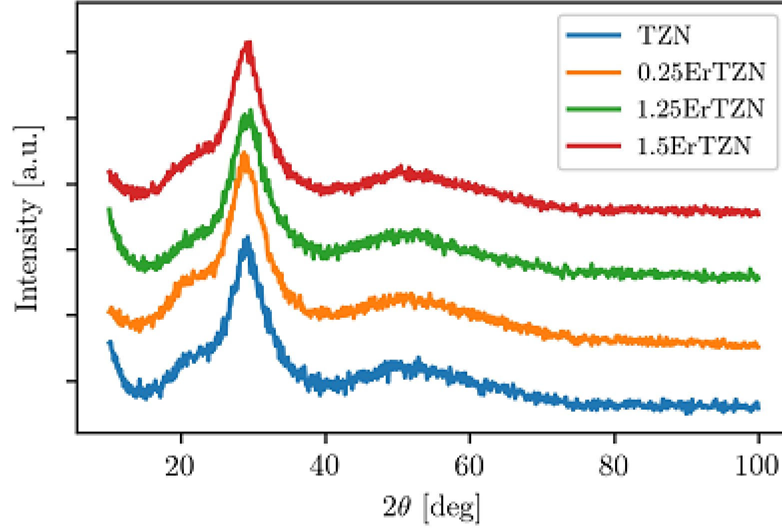

Figure 5.4: X-ray diffraction patterns of the two highest and lowest erbium target glass doping concentrations used. The intermediate doped glasses showed a similar spectra. Only a broad halo in the range $20° < 2\theta < 40°$ is observed indicating amorphous structure.

concentrations of Er_2O_3 used. The refractive index of TZN was 2.048.

The increase in Er^{3+} ion content caused a change in the colour of the glass samples from clear to a deep pink. The colour variation is a consequence of the Er^{3+} ion having electronic excited states in the visible region. The optical absorption coefficients of the glasses as a function of the photon frequency ν were calculated by

$$\alpha(\nu) = \frac{A}{L}, \tag{5.8}$$

where L is the thickness of the sample and A is the absorbance measured using the spectrometer. The absorption spectra of TZN and 0.75ErTZN in the range of 380 - 1800 nm are shown in fig. 5.5. TZN exhibits featureless absorption with an absorption baseline of approximately 0.11 cm^{-1} after the UV absorption edge at 387 nm (3.2 eV). The addition of Er^{3+} dopant ions gives rise to eleven prominent transitions from the ground state ($^4I_{15/2}$) to the different excited states, $^4I_{13/2}$, $^4I_{11/2}$, $^4I_{9/2}$, $^4F_{9/2}$, $^4S_{3/2}$, $^2H_{11/2}$, $^4F_{7/2}$, $^4F_{5/2}$, $^4F_{3/2}$, $^2H_{9/2}$, $^4G_{11/2}$ centred at the wavelengths 1531 (with a smaller peak at 1497), 976, 800, 653, 545, 522, 489, 452, 444, 407 and 380 nm. The

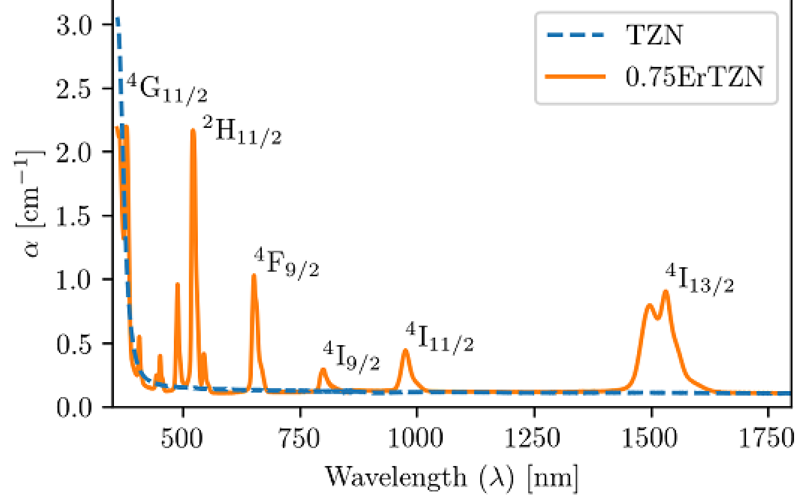

Figure 5.5: Optical absorption spectra for TZN and 0.75ErTZN glasses. Text shows the Er^{3+} ion transitions from the ground state ($^4I_{15/2}$) giving rise to the peaks (only the prominent transitions are displayed for clarity, refer to text for all transitions).

energy levels of the Er^{3+} ion in the host are split due to the Stark effect, resulting in broadened transitions [5]. The other doping concentrations showed similar spectra, with the height of the peaks increasing with the concentration of Er^{3+} ion in the glass.

Optical transition and electronic band structure are examined by the absorption edge in the UV region. For direct and indirect transitions, electromagnetic waves excite the electrons in the valence band across the fundamental gap to the conduction band. According to Davis *et al.* [188], the absorption coefficient, $\alpha(\nu)$, of amorphous materials can be expressed as a function of photon energy, $h\nu$, for the direct and indirect allowed transition by

$$\alpha(\nu) = B\frac{(h\nu - E_g)^n}{h\nu}, \tag{5.9}$$

where B is a constant, E_g is the band gap (direct or indirect), and n is the index number; $n = 1/2$ for direct allowed transitions and $n = 2$ for indirect allowed transitions. Both band gaps are interband transitions, but the later involves a phonon interaction. The optical band gap values were obtained from the linear part of the curves and extrapolating to $(\alpha h\nu)^2 = 0$ and $(\alpha h\nu)^{1/2} = 0$ for direct and indirect transitions, respectively. fig. 5.6a and b show the Tuac plots and fitting procedure for TZN,

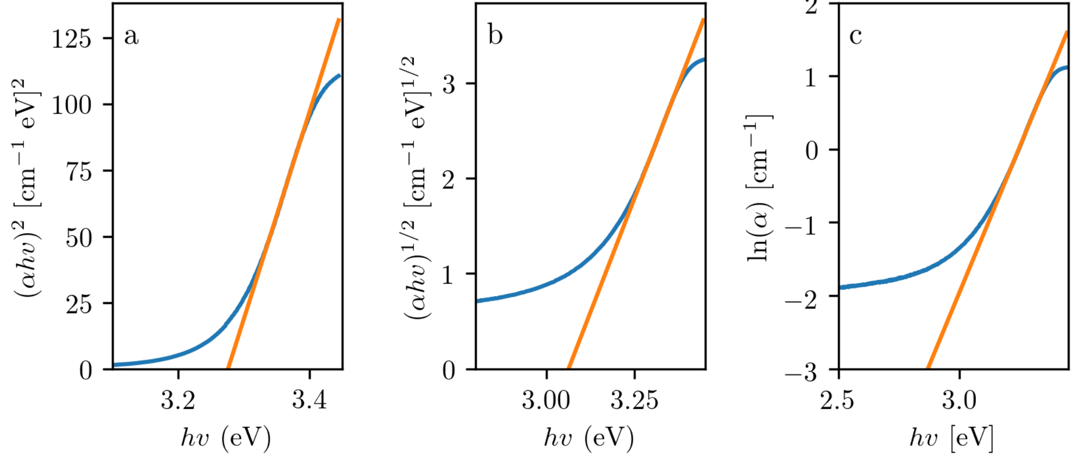

Figure 5.6: Tauc plots to determine the (a) direct band gap, (b) indirect band gaps and (c) Urbach energy of TZN glass.

giving a direct band gap value of 3.28 ± 0.02 eV and an indirect band gap value of 3.06 ± 0.01 eV.

Amorphous materials do not have long range order and so the valence and conduction bands do not have a sharp cut off but rather tails of localised states. As a result the absorption coefficient, $\alpha(\nu)$, near the optical band edge exhibits an exponential behaviour on the photon energy, $h\nu$, due localised states extending into the band gap. The dependence is known as Urbach empirical rule, which is given by [189]

$$\alpha(\nu) = \alpha_0 \exp(h\nu/\Delta E), \tag{5.10}$$

where α_0 is a constant and ΔE is the Urbach energy. The exponential behaviour is a result of the valence and conduction band tails extending into the band gap. The values of Urbach energy were calculated by taking the reciprocals of slopes of the linear portion of the high photon energy regions, as shown in fig. 5.6c. The Urbach energy was 0.1252 ± 0.0003 eV. The effect on the band gap and Urbach energy values due to the addition of Er^{3+} ions (if any) was within the error of measurement as the Er^{3+} ion transition $^4I_{15/2} \rightarrow {}^4G_{11/2}$ reduced the accuracy of the fitting procedure.

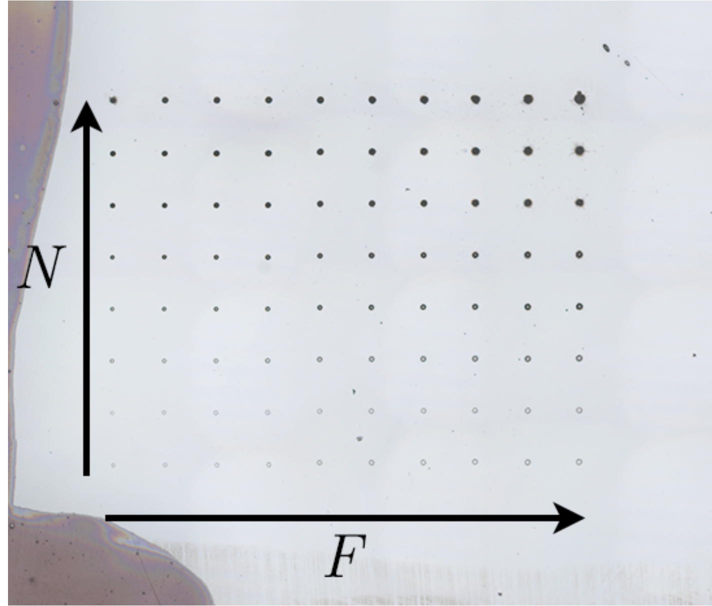

Figure 5.7: Optical microscopy image of the array of craters ablated with increasing laser fluence F (going from left to right) and pulse numbers N (bottom to top) on TZN. The grid spacing of the crater array was 0.3 mm. Note that the pen marking on the left hand side was for location of the array under the microscope.

5.4.2 Ultrafast laser ablation

An optical microscope image of the array of craters on the TZN glass is shown in fig. 5.7. The craters are well separated, even at the highest pulse numbers and fluences. Therefore interference between neighbouring sites is not an issue.

Crater Morphology

Figure 5.8a presents AFM images and their respective cross-sectional profiles of craters ablated with a single laser pulse at energies 36.4, 56.8 and 88.4 μJ and a spot size of 32.0 μm. The single pulse craters had a shallow profile with an aspect ratio (depth divided by diameter) of $\sim$0.02 and 0.01 for $w_0 = 13.9$ and 32.0 μm, respectively. At low energies, where the fluence was $\lessapprox 2$ J/cm^2, the craters take on a cylindrical profile. With increasing fluence the craters transitioned to a Gaussian profile. A rim surrounding the craters, typically 20 to 50 nm in height, that extends upwards and increases in height with laser fluence is observed. Craters were also accompanied by radial splashes, seen

clearly in the crater produced by an 88.4 μJ laser pulse in fig. 5.8a. These features are due to the formation of a thin molten zone below the ablated area and the pressure-driven flow generated by the plasma [148]. It could be the case that at low fluences the plasma pressure is not sufficient to eject the molten material from the crater and hence re-solidification of the melt results in a flat bottomed crater. This effect would be greater for TZN glasses as the volume of molten material would be greater due to the low glass transition temperature (280°C) when compared to other glasses (fused silica 1050°C and borosilicate 593°C [190]).

The crater morphologies for several different fluences and irradiation with 10 or 32 pulses is shown in fig. 5.9. Irradiation with 32 pulses close to the ablation threshold resulted in a ripple surface structure that is not seen with irradiation of 10 pulses (for example compare fig. 5.9a and d). The ripples were most pronounced and homogeneous across the crater surface for fluences exceeding the multipulse ablation threshold by less than a factor of 5 ($\sim$0.85 J/cm^2). The ripple periodicity was $\sim$1.4 μm, which is larger than the incident wavelength. Coarse ripples such as these are less commonly observed than fine ripples on transparent media [191]. Above this fluence a peripheral nano-roughness is observed on the fringes of the craters (see fig. 5.9e and f), where the Gaussian beam has a lower fluence. This is accompanied by a smooth melt feature central to the crater. At even higher fluences, a pillar-like macro feature that extends upward is observed, as shown in fig. 5.9f (and confirmed via AFM). A similar crater profile was observed via SEM in fused silica after irradiation with 80, 220 fs duration pulses centred at a wavelength of 780 nm and fluence of 10.7 J/cm^2 by Lenzer *et al.* [190]. This may be attributed to the inability of the molten material to escape the crater due to the increase in crater aspect ratio and solidifying as a 'splash' in the centre [190].

Threshold fluence

The ablation threshold F_{th} (also known as damage threshold or threshold fluence) was determined from the linear relationship between the square of the crater diameter D and the logarithm of the average laser fluence F_0^{avg} (D2-LnF method) [167]

$$D^2(N) = 2w_0^2 \ln\left(\frac{F_0^{\mathrm{avg}}}{F_{\mathrm{th}}(N)}\right), \tag{5.11}$$

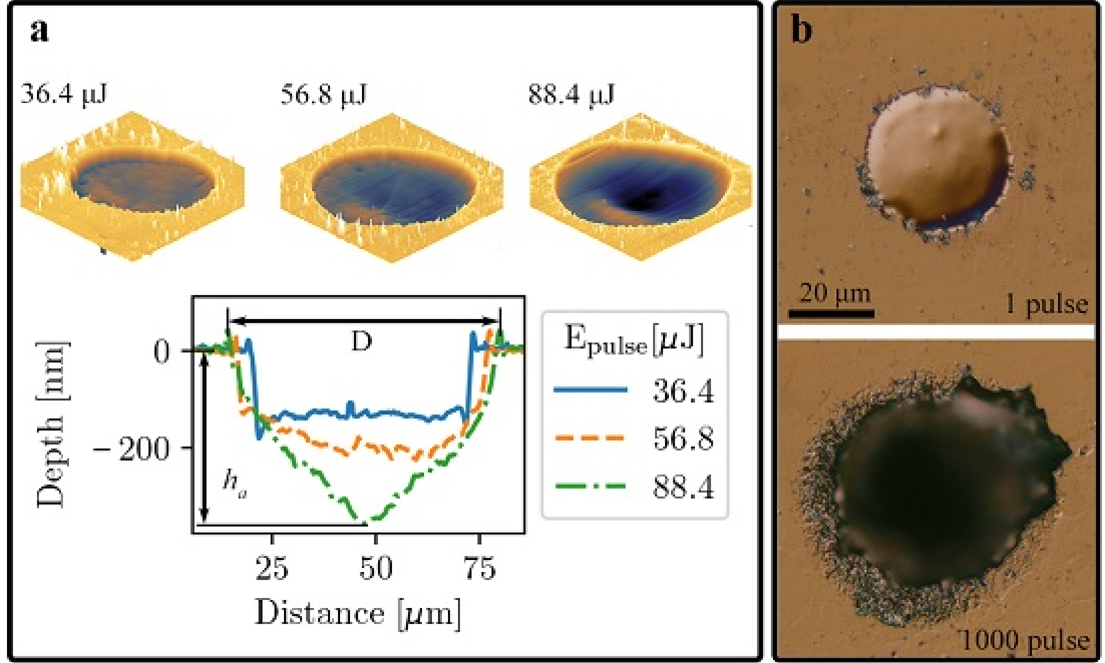

Figure 5.8: (a) AFM profiles of craters produced on TZN by a single laser pulse at several energies and a spot size of 32.0 μm. On the cross sectional profiles it is depicted how the crater diameter and height was determined, from which the 'effective optical penetration depth' and volume were calculated. (b) DIC micrographs of laser produced craters at a pulse energy of 45.8 μJ and spot size of 13.9 μm with different numbers of applied pulses.

where w_0 is the $1/e^2$ laser beam radius for a Gaussian spatial beam profile and N is the number of pulses applied per sampling position. The average laser fluence of a Gaussian laser beam is related to the total pulse energy E_{pulse} through the relation $F_0^{\text{avg}} = E_{\text{pulse}}/(\pi w_0^2)$. Additionally, due to the linear dependence of the laser fluence on the pulse energy, w_0 may be calculated from the plot of the crater diameter squared against the logarithm of the pulse energy.

The ablation threshold is dependent on N due to the 'incubation effect', which occurs when the low fluence region of the laser beam, below the single shot ablation threshold, deposits energy into the material causing mechanical and/or chemical modifications [192, 193]. As a result defects, are generated which lead to a lower ablation threshold. The generation of defects in dielectrics, such as F-centres, is experimentally found to saturate after a certain number of pulses causing the ablation threshold to

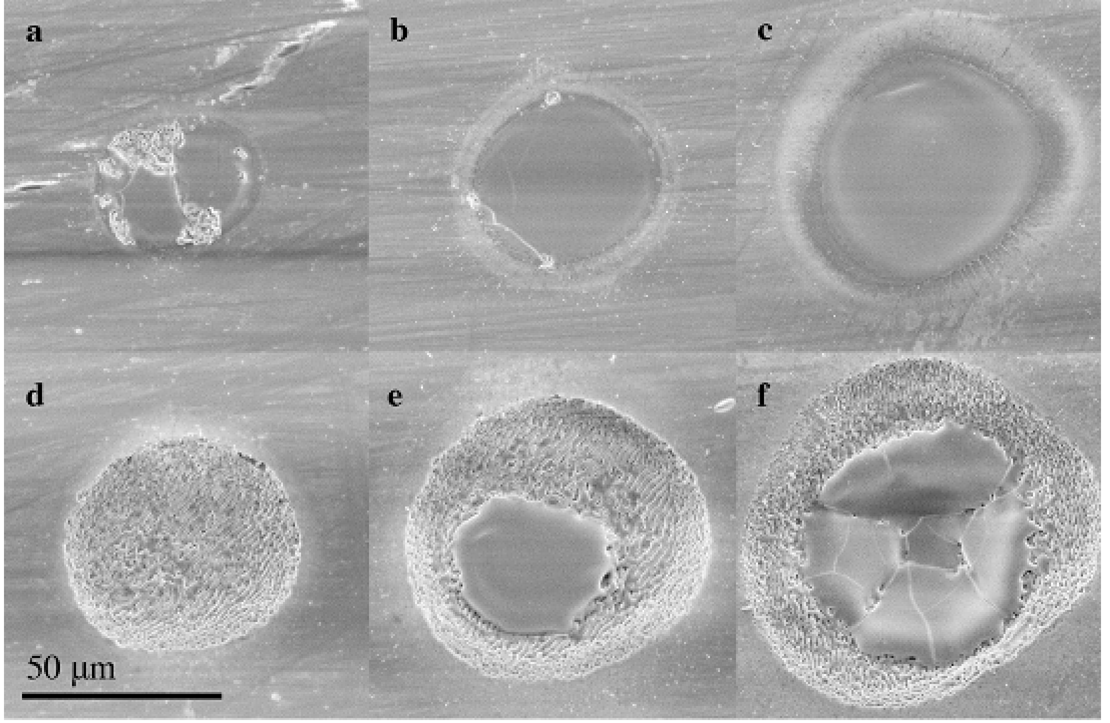

Figure 5.9: SEM images (15 kV electron accelerating voltage) of multi-pulse ablation craters in TZN glass at a spot size of $w_0 = 32$ μm. Top row 10 pulses per site (a, b, c) and bottom row 32 pulses per site (d, e, f). $E_{\mathrm{pulse}} = 23.4$ μJ, $F_0^{\mathrm{av}} = 0.73$ J/cm^2 (a, d), $E_{\mathrm{pulse}} = 36.4$ μJ, $F_0^{\mathrm{av}} = 1.13$ J/cm^2 (b, e) and $E_{\mathrm{pulse}} = 137.8$ μJ, $F_0^{\mathrm{av}} = 4.29$ J/cm^2 (c, f).

remain constant with increasing pulse numbers. To quantify this, an accumulation model was proposed by Ashkenasi *et al.* [185]

$$F_{\mathrm{th}}(N) = F_{\mathrm{th}}(\infty) + [F_{\mathrm{th}}(1) - F_{\mathrm{th}}(\infty)]\, e^{-k(N-1)}, \tag{5.12}$$

where k is a parameter defining the rate at which the threshold fluence approaches the infinite pulse value. In our measurements the linear relationship of eq. (5.11) was observed up to ~10 times the ablation fluence. Above this fluence D^2 showed an exponentially increasing dependence upon the logarithm of the fluence and data was therefore not included in the analysis. The deviation at high fluences is due to a combination of excessive cracking in the glass, as shown in fig. 5.8b, due to mechanical modification by previous incubating pulses [194] and a deviation from the ideal Gaussian

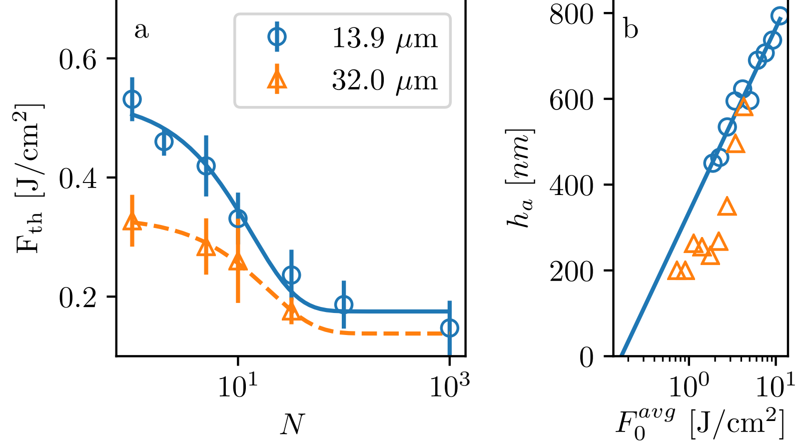

Figure 5.10: (a) The multipulse threshold fluence dependence of TZN. Data is fitted with eq. (5.12) with the parameters $F_{\mathrm{th}}(1) = 0.51$, $F_{\mathrm{th}}(\infty) = 0.18$ and $k = 0.074$ $F_{\mathrm{th}}(\infty)$ for $w_0 = 13.9$ μm (solid line) and $F_{\mathrm{th}}(1) = 0.32$, $F_{\mathrm{th}}(\infty) = 0.14$ and $k = 0.051$ for $w_0 = 32.0$ μm (dashed line). (b) The multipulse ablation threshold measurements of TZN glass as determined from the single pulse crater depth. The legend is the same as for (a). The plots presents the logarithmic dependence of the ablation rate h_a on the laser fluence F_0^{avg}. Extrapolation of eq. (5.13) to zero gives a limiting multipulse threshold fluence of $F_{\mathrm{th}}^{\infty} = 0.17 \pm 0.03$ J/cm^2 and the gradient gives an effective optical penetration depth $\alpha_{\mathrm{eff}}^{-1} = 187 \pm 15$.

profile in the beam tails [195], as shown in fig. 5.9f. Extrapolating the linear regression for each number of applied pulses using eq. (5.11) yields the pulse dependent ablation threshold, as shown in fig. 5.10a. For both spot sizes the ablation threshold drops within the first 50 pulses to a limiting value that is approximately 40% of the single shot value and is well described by eq. (5.12). This reduction is less than for αSiO_2 where a 75% reduction in threshold fluence was observed from 3.7 J/cm^2 reduced to 0.9 J/cm^2 after 20 applied pulses [192] and borosilicate (in air) where a 76 % reduction from 2.6 J/cm^2 to 1.74 J/cm^2 was measured [133]. The dependence of ablation threshold on spot size has been observed in dielectric thin films [196] and barium borosilicate glass [197] and is explained by realising that the ablation threshold is composed of two components; an intrinsic material ablation threshold and a defect ablation threshold component. The probability of the latter increases with beam size leading to an overall lower ablation threshold.

The limiting multipulse ablation threshold $F_{\text{th}}(\infty)$ may also be evaluated from the single pulse crater depth h_a so long as the fluences are well above ablation threshold, so that steady state material removal occurs, by using the relation proposed by Ben-Yakar *et al.* [133]

$$h_a = \alpha_{\text{eff}}^{-1} \ln \left(\frac{F_0^{\text{avg}}}{F_{\text{th}}(\infty)} \right), \tag{5.13}$$

where α_{eff}^{-1} is interpreted as the 'effective optical penetration depth' as expected from Beer-Lambert law. This parameter primarily determines the volume in which the non-thermal femtosecond ablation processes take place. Extrapolation to zero for TZN glass at a spot size of 13.9 μm, as shown in fig. 5.10b, gives $F_{\text{th}}(\infty) = 0.17 \pm 0.03$ J/cm^2, which agrees well with the D2-LnF measurements. The effective optical penetration depth $\alpha_{\text{eff}}^{-1} = 187 \pm 15$ nm corresponds to an effective absorption coefficient of $\alpha_{\text{eff}} = 5.4 \pm 0.4 \times 10^4$ cm^{-1}. The measured absorption coefficients are slightly higher than that for borosilicate glass exposed to 780 nm 200 fs laser pulses ($\alpha_{\text{eff}} = 4.2 \times 10^4$ cm^{-1}, $\alpha_{\text{eff}}^{-1} = 238$ nm) [133].

Er^{3+} ion dopant

D2-LnF ablation threshold measurements of the Er^{3+} ion doped glass samples at a spot size of ~13.9 μm had no trend with dopant concentration, as shown in fig. 5.11. The mean and standard deviation of the parameters to the fits of eq. (5.12) for all glass samples was $F_{\text{th}}(1) = 0.51 \pm 0.03$ J/cm^2, $F_{\text{th}}(\infty) = 0.18 \pm 0.01$ J/cm^2 and k = 0.053 ± 0.009. This is to be expected at low doping concentrations for the following reasons. Firstly, femtosecond laser ablation is a non-linear process owing to the highly intense laser field of the short pulse duration [198]. The band gap value is therefore one of the main parameters characterising this process and did not vary to any significant degree with Er^{3+} ion concentration. Secondly, at the highest 1.5 mol.% doping concentration the linear absorption at 800 nm was increased from 0.11 cm^{-1} for TZN to 0.85 cm^{-1}. The 'effective optical absorption coefficient' for the non-linear process had a value of 5.4 $\times 10^4$ cm^{-1} for TZN, which is five orders of magnitude larger than the linear absorption coefficient, and it is therefore clear that the linear absorption is of no relevance. Finally, physical changes to the glass parameters such as density, refractive index and melting

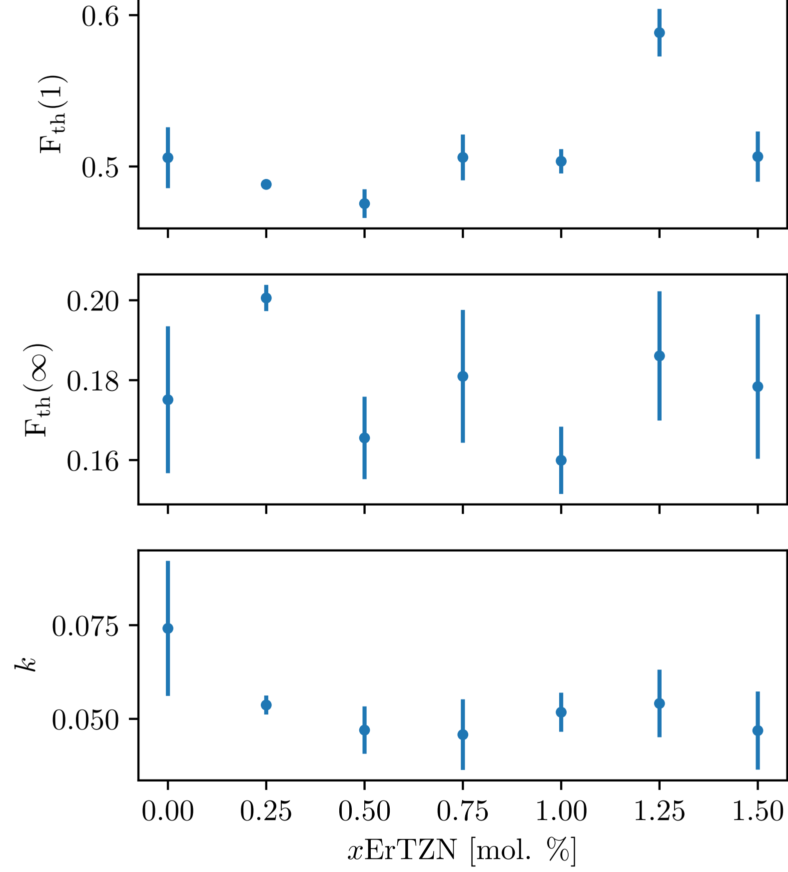

Figure 5.11: The fitted parameters to the accumulation model in eq. (5.12) for the TZN glasses doped with varying concentrations of Er^{3+}. The ablation threshold F_{th} values are given in J/cm^2.

point are small at low doping concentrations and are therefore not expected to modify the ablation threshold.

Ablation volume

As shown in fig. 5.8a, the profiles of the laser ablated craters depends on the applied fluence. In the Gaussian profile regime ($\gtrapprox 2$ J/cm^2) both D^2 and h_a each depend on the logarithm of the fluence and therefore the volume is linear in the squared logarithm of the fluence. In the low fluence cylindrical regime h_a was roughly constant at 210 nm ($\sim \alpha_{\text{eff}}^{-1}$) and the volume is therefore dependent on the logarithm of the fluence. The

ablated volume is plotted as a function of the logarithm of the laser fluence in fig. 5.12a. A linear fit through the first three data points (low fluence cylindrical profile regime for $w_0 = 32.0$ μm) of single pulse craters and extrapolation to zero gives $F_{\text{th}}(1) = 0.38$ and 0.621 J/cm^2 for $w_0 = 32.0$ and 13.8 μm, respectively. The values are overestimations of the values found via the D2-LnF method. This highlights why the ablation threshold determination via volume measurements can be less accurate as knowledge of the profile shape is required, which can change depending on the fluence regime. Coincidently, the ablation with single pulses at $w_0 = 32.0$ μm gave equivalent material removal rates with $N = 5$ at $w_0 = 13.9$ μm.

For micromachining and ULPD type applications, knowledge of the volume per unit input energy of ablated material is of great importance. Figure 5.12b shows that below $\sim$2 J/cm^2, or $\sim 5 \times F_{\text{th}}(1)$, the ablation rate is approximately flat at 6.8 ± 0.3 μm^3/μJ at a spot size of 32 μm. Between the range 2 - 11.5 J/cm^2 the ablation volume per unit input energy decreases with fluence from $\sim$7.3 to 4.5 μm^3/μJ. A reduction in ablation efficiency was observed by Perry *et al.* [199] for glass exposed to high fluences ($F_0 > 5 - 10 \times F_{\text{th}}$) due to a large portion of the incident energy being reflected back off the sample caused by an increase in the reflectivity of dielectrics at high laser fluences. The metallic behaviour of dielectrics under damage-threshold fluence irradiation has also been reported by Buividas, Mikutis, and Juodkazis [191]. The ablation rates are far higher than the 1.5 μm^3/μJ observed for borosilicate glass irradiated with 200 fs laser pulses at 780 nm between $10 < F_0^{\text{avg}} < 40$ J/cm^2.

5.5 Conclusion

The femtosecond laser ablation properties of Er^{3+} ion doped TZN glass was investigated. The direct band gap of TZN was 3.276 eV, which is just over twice the femtosecond laser photon energy (1.55 eV or 800 nm). The laser ablated crater profile depended on the applied fluence and pulse number. Below an average fluence of $\sim$2 J/cm^2 the craters had a cylindrical profile and above this fluence the craters had a Gaussian profile. The laser fluence and number of applied pulses determines whether nano- micro- or macro-structuring takes place. Ripples with a periodicity of $\sim$1.4 μm were observed with multiple pulses close to the ablation threshold.

Measurements of the crater diameter at varying fluences yielded a single shot ablation threshold of 0.51 and 0.32 J/cm^2 at a spot size of 13.9 and 32.0 μm, respectively. The multipulse ablation threshold was found after approximately 50 applied pulses and was ~40% of the single pulse value. The ablation threshold was found to decrease with an increase in the laser spot size at the surface due to an increase in the probability of the laser beam striking a defect in the glass. The ablation threshold did not change with the addition of up to 1.5 mol.% Er_2O_3 dopant concentration.

The amount of material removal per unit input energy is about 6.8 μm^3/μJ up to a fluence of 2 J/cm^2 and linearly decreasing from 7.3 - 4.5 μm^3/μJ in an intermediate fluence regime. The decrease in ablated volume with increasing laser fluence indicates a reduced ablation efficiency at higher fluences, which may be attributed to an increased surface reflectivity.

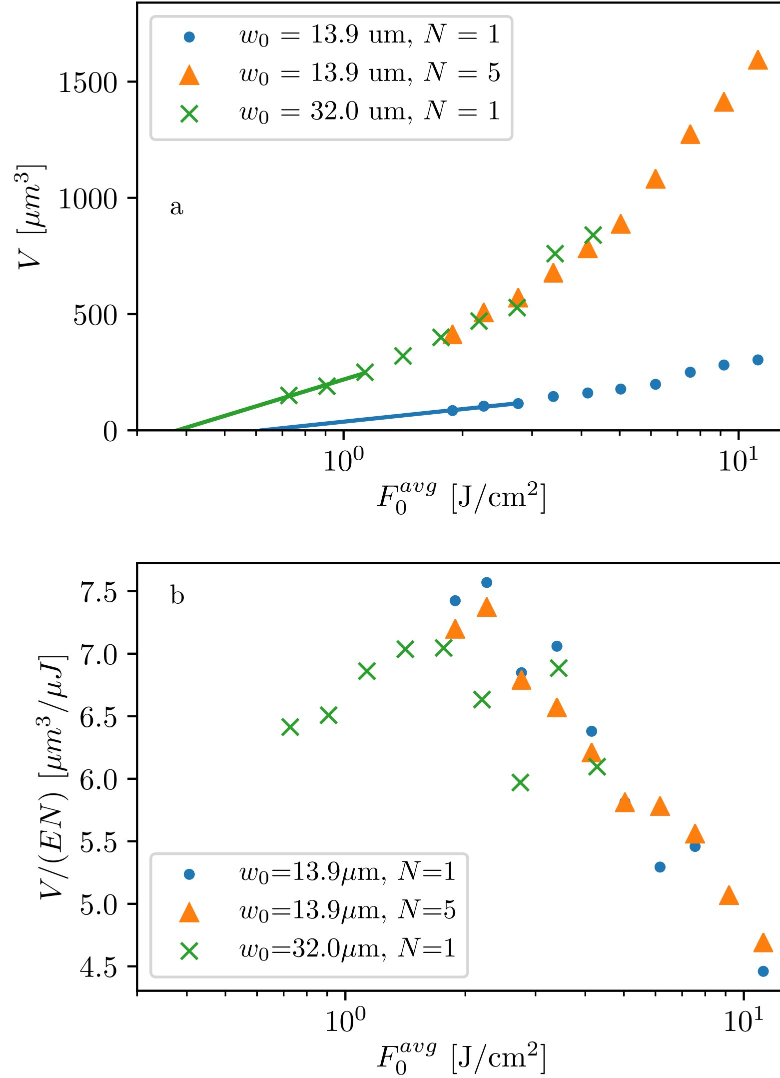

Figure 5.12: (a) The volume of the ablated craters as a function of the logarithm of the laser fluence. A linear fit through the first three data points of single pulse craters and extrapolation to zero gives $F_{\mathrm{th}}(1) = 0.38$ and 0.621 J/cm^2 for $w_0 = 32.0$ and 13.8 μm, respectively. (b) Volume per pulse per unit of energy as a function of the logarithm of the laser fluence.

Chapter 6

Femtosecond laser deposited Er^{3+}-doped zinc-sodium tellurite glass films

This chapter characterises the physical and optical properties of fluorescent films deposited on silicon substrates via femtosecond laser (40 fs, 800 nm) ablation of Er^{3+} ion doped zinc-sodium tellurite glass as a function of laser fluence. An introduction to the chapter is given in section 6.1. Following this, the theoretical background in section 6.2 describes the non-radiative de-excitation processes between Er^{3+} and Si and the calculation used to convert atomic percent to atomic number density. The experimental setup for sample fabrication and characterisation is described in section 6.3. The results are presented in section 6.4, in which the laser fluence regime required for the formation of films composed of nanoparticles without droplets is found, the composition and crystallinity of the deposited material is reported and the photoluminescence of the films is characterised in dependence of film thickness. A conclusion to the chapter is given in section 6.5.

6.1 Introduction

Tellurite glasses are good hosts for rare-earth ions due to the high rare-earth solubility and low phonon energy [170, 171]. The fabrication of Er^{3+}-doped tellurite-based glass thin films is of interest for optical sensors, waveguide amplifiers and lasers [171, 178].

Pulsed laser deposition (PLD) has proven to be a valid and efficient technique for the stoichiometric transfer of material from target to a film on a substrate, which is not possible with the growth of films from atomic species [131].

Nanosecond (ns) PLD has been used by several research groups to form erbium doped tellurite thin films [116–118, 200]. However, micrometer sized droplet formation resulting from violent subsurface heating effects during vaporisation of the target and gas phase condensation of the large volume of ablated material by the high energy pulses is a characteristic of ns-PLD that limits the capability of this technique [120, 121, 123]. Due to the non-thermal energy deposition and lower pulse energies required for femtosecond (fs) laser ablation, the formation of droplets can be avoided providing that the laser fluence is not too high [123, 124]. The formation of nanoparticles in ns-PLD occurs during gas phase condensation of an atomised plasma plume confined in a pressurised atmosphere. This is significantly different in fs-PLD, where nanoparticle generation occurs in vacuum and is thought to be due to mechanical fragmentation of the highly pressurised fluid undergoing rapid quenching during the hydrodynamic expansion [124, 132]. The majority of fs-PLD fabricated nanostructured films result from the random stacking of NPs, typically in the 10 - 60 nm range [1, 121, 124, 125, 153]. Er^{3+}-doped zinc-sodium tellurite glass NPs have recently been incorporated into polymers for low-cost integrated optical amplifiers using the fs-PLD technique [161]. In a similar fashion, the ultrafast laser plasma doping (ULPD) technique ablates a rare-earth (RE) doped zinc-sodium tellurite target onto a heated silica based substrate such that the subsequent interfacial dissolution forms RE-doped hybrid tellurite-silica thin films [6, 23–25].

The species (ions, nanoparticles and droplets) in the ablation plume are a direct consequence of the fs laser and target properties. The high energy ions and electrons (atomic species) typically only make up a few percent of the total ablated matter [124]. At a fixed fs laser wavelength, pulse width, spot size and repetition rate, the laser fluence relative to the target ablation threshold is the key parameter dictating the particle size distribution in the ablation plume [123, 124]. The ablation threshold of Er^{3+}-doped zinc-sodium tellurite glass in atmosphere irradiated with a fs laser of pulse duration 100 fs and central wavelength of 800 nm has been characterised in chapter 5 [26]. It was found that the single shot ablation threshold was 0.32 J/cm^2 and dropped to a multipulse value of 0.14 J/cm^2 at a spot size of 32 μm. A characterisation of the

nanoparticles and droplets in the fs ablation plume for tellurite glass does not exist in the literature and is the purpose of this work.

Structural characterisation is achieved through scanning electron microscopy studies of vacuum depositions on silicon substrates at varying laser fluences. The composition of the depositions and the crystalline structure are studied with energy dispersive X-ray spectroscopy and grazing incidence X-ray diffraction, respectively. The effect of target polish on plume species is also investigated. The radiative spontaneous emission (SE) rate of the Er^{3+}-doped films are measured using time-resolved photoluminescence spectroscopy and compared with a quantum-electrodynamical model for the average SE rate for ions inside multilayer dielectric structures. An increase in decay rate for very thin films is observed due to the electric field confinement within the film and an increase in the fraction of ions coupled non-radiative recombination processes. The latter is due to a combination of Auger quenching and energy backtransfer, which are known to limit the efficiency of room temperature Er^{3+} ion doped/deposited silicon based light sources [28, 68, 201, 202].

6.2 Theoretical background

6.2.1 Non-radiative de-excitation processes between Er^{3+} and silicon

The fabrication of silicon based light emitting devices is desirable for integration with optoelectronics [201]. Particular interest has been paid to the 1.54 μm emission from Er^{3+} ions doped in silicon as this is a standard telecommunications wavelength. Low temperature photoluminescence (PL) from Er^{3+} ions doped in silicon was first achieved in 1983 by Ennen et al. [203]. Room temperature PL has however proven to be more problematic as quenching, due to the non-radiative de-excitation processes (Auger quenching and phonon assisted energy backtransfer) that are made possible by the long radiative lifetime ($\sim$2 ms) and enhanced for temperatures above 150 K [201, 202]. A reduction in the quantum efficiency of 20 nm thick Er^{3+}-doped SiO_2 (concentration $7.6 \times 10^{19}cm^{-3}$) deposited thin films and slot waveguides on polycrystaline silicon has also been shown [28]. The radiative efficiency was estimated to be $\sim$0.65 for these structures and was attributed to the interaction of Er^{3+} transition with surface defect states at the SiO_2/Si interfaces and to Auger quenching with free and bound carriers

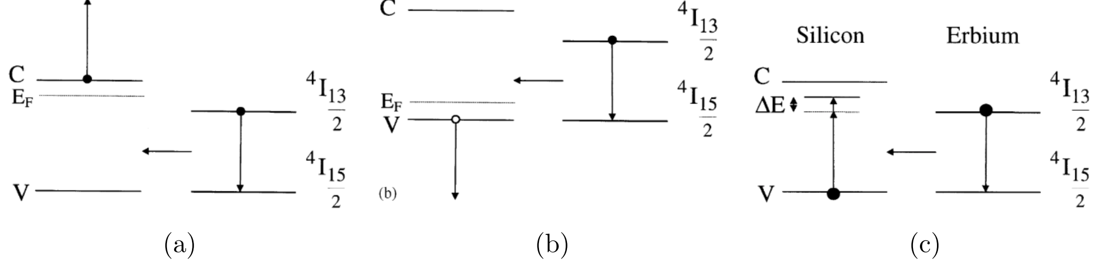

Figure 6.1: Schematic diagrams of non-radiative de-excitation energy transfer processes from Er^{3+} (right) to Si (left); (a) Auger quenching with free electrons, (b) Auger quenching with holes, (c) energy backtransfer. The Si conduction band is denoted C, the valence band is denoted V and E_F denotes the Fermi level. Schematic reproduced from [201].

in silicon. The reduction of de-excitation processes through a better theoretical understanding has been the subject of much research in order to improve electroluminescence efficiencies [68, 201, 202]. A schematic of the two de-excitation processes resulting in the non-radiative transition ${}^4I_{13/2} \rightarrow {}^4I_{15/2}$ of the Er^{3+} ion, *Auger quenching* and *energy backtransfer*, are shown in fig. 6.1 and briefly summarised in the following.

De-excitation of the $4f$ shell electron in the Er^{3+} ion by *Auger quenching* occurs either through excitation of a free electron to a higher state in the conduction band or excitation of a free hole to a lower state in the valence band in the Si matrix [201]. The former is depicted in fig. 6.1(a) and the latter in fig. 6.1(b). The process is important at temperatures above 30 K and, because it is related to the concentration of free carriers in the silicon host, proportional to the doping level.

Energy backtransfer to silicon, schematically depicted in fig. 6.1(c), dominates at temperatures above 130 K. The Er^{3+} ion excitation is transferred to an electron in the valence band of the silicon located 0.15 eV below the conduction band [201]. Additional energy to complete the process is supplied by phonons and so the efficiency of the process increases with temperature. The additional energy ΔE required is given by

$$\Delta E = E_{\mathrm{G}} - E_{\mathrm{T}} - E_{\mathrm{Er}} = 0.15 \text{ eV}, \tag{6.1}$$

where E_{G} is the Si bandgap, $E_{\mathrm{Er}} = 0.8$ eV is the energy of the excited Er^{3+} ion and the location of the excited Er^{3+} level from the bottom of the Si conduction band $E_{\mathrm{T}} = 0.15$ eV.

For an Er^{3+} ion in silicon at room temperature, the probability of non-radiative recombination through *energy backtransfer* has been estimated to be as high a 70% and found to exceed the *Auger quenching* rate by three orders of magnitude, while at 15K, the rate of both processes was almost zero [202]. While the direct non-radiative interaction only occurs between Er^{3+} close to silicon, energy migration between Er^{3+} ions acts to couple the Si quenching centres to ions that are too far away for a direct interaction.

6.2.2 Atomic number density

The calculation used to convert atomic percentage *at.*%, the percent of atoms or molecules in a material, measured via energy-dispersive X-ray spectroscopy to atomic number density is detailed. The number of atoms or molecules n in a mass of a pure material m [g], having an atomic or molecular weight M [g/mol] is given by

$$n = \frac{mN_A}{M}, \tag{6.2}$$

where Avogadro's number $N_A = 6.022 \times 10^{23}$ [at./mol]. The atomic number density N [at./cm^3] is the number of atoms or molecules per unit volume V [cm^3] can be calculated when the material density ρ [g/cm^3] is known by

$$N = \frac{n}{V} = \frac{\rho N_A}{M}. \tag{6.3}$$

The molecular weight M [u $\equiv$ g/mol] is calculated by

$$M = \sum_{\text{elements}} u \cdot \frac{at.\%}{100}. \tag{6.4}$$

6.3 Experimental setup

6.3.1 Sample Fabrication

The depositions were performed using the ULPD system described in section 4.3. The elliptical laser spot on the sample surface was measured with a microscope (Maozua 5MP USB Microscope calibrated with Thorlabs R1L3S2P Stage Micrometer) prior to ablation and had an area of $A = 8.57 \times 10^{-5}$ cm^2 (Gaussian beam waists of $\sim$ 82 and 32 μm). The pulse energies E_p ranged from 17 to 440 μJ, corresponding to an average

laser fluence F from 0.20 to 5.13 J/cm^2. Each deposition constituted the application of 180k pulses per cm^2 to the target surface directly below the substrate. Specifically, the laser rastering involved scanning 180 lines at a speed of 10 mm/s over a length larger than the substrate (22 mm) and moving the target in 0.1 mm steps perpendicular to the laser raster axis after each line (18 mm length in total). The experiments were carried out in a vacuum ($<1\times10^{-4}$ Torr) and at room temperature (23°C).

The target was an Er^{3+}-doped zinc-sodium tellurite glass of composition 79TeO_2-10ZnO-10Na_2O-1Er_2O_3 mol.% (1ErTZN). Fabrication and characterisation of the target glass has been presented in chapter 5 [26]. The glass was wet polished with P1200 grit silicon carbide (SiC) sandpaper to the dimensions of $\sim$ 30 $\times$ 30 $\times$ 3 mm. The resulting surface roughness $R_a \approx 108$ nm (measured on a 100 $\times$ 100 μm region). For investigations into the effect of target surface quality on the ablation plume, the glass was given an optical polish to $R_a \approx 5$ nm using the same procedure detailed in appendix D.

The constituents of the ablation plume were collected on a polished silicon wafer substrate (P<100>B doped, resistivity of 1-20 ohm·cm, diced into 10 mm by 10 mm squares, $R_a < 0.3$ nm) placed parallel to and 40 mm above the target surface. Each substrate was cleaned for 5 minutes in an ultrasonic bath with acetone and then isopropanol prior to depositions. The Si substrate was rotated at 5 RPM around its centre to give a uniform deposition.

6.3.2 Characterisation

Characterisation of the deposited films was studied by using high resolution scanning electron microscopy (SEM, Hitachi SU8230). In order to determine the size distribution of the particles, several SEM images were processed using Fiji [204, 205]. Deposition thicknesses d were evaluated on cross-sections after snapping the substrate from the rear. Elemental identification of the depositions was performed using energy-dispersive X-ray spectroscopy (EDX) coupled to the SEM (80mm^2 X-Max detector, Oxford Instruments). Point measurements were taken at the centre of droplets to minimise the effect of surface geometry on the results (the analysis assumes a flat surface). The strongest peak signal in the spectra corresponding to the Si substrate was not included in the analysis. Sodium and zinc both exhibit their L emission lines very close to each other and could not be resolved in the spectra. As a result the relative ratio of Zn

to Na are inaccurate and this also quantification of the weight % other elements as the normalisation to 100 % is not accurate. As a result of all of these limitations, the compositional results with the EDX technique are semi-quantative.

The average surface roughness R_a and the root mean square roughness R_{RMS} was characterised via an atomic force microscope (AFM) operating in tapping mode (Innova Atomic Force Microscope, Bruker with a μmasch AFM probe of 8 nm nominal tip radius) and averaging over areas at least several times larger than the largest features. The data was analysed with the open source software Gwyddion [186, 187]. AFM measurements were made on the polished target, the substrate and for all samples bar the highest fluence deposition, which was too rough to measure.

The crystallinity of the 3.32 J/cm^2 deposition was studied by grazing incidence X-ray diffraction (GIXRD). This was preferred over the standard $\theta/2\theta$ XRD configuration to avoid the signal from the silicon substrate that would otherwise swamp the spectral features of the thin film. GIXRD measurements were performed on an X-ray diffractometer (X'Pert, Phillips) using Cu-Kα radiation (1.5406 Å) across the 2θ range 10 - 80° at a angle of incidence of 2° and a scan rate of 0.005°/second. The peaks in the measured diffraction patterns were identified and indexed using the X'pert High Score Plus software package. The spectral shift in the GXID spectra was -0.29° and evaluated prior to fitting using a $\theta/2\theta$ XRD scan on the same sample[1].

PL measurements were performed using a fluorescence spectrometer (FLS 920, Edinburgh Instruments) at room temperature. A 976 nm excitation laser source (BL976-PAG500976, Thorlabs), which resonates with the ${}^4I_{15/2} \rightarrow {}^4I_{11/2}$ transition of Er^{3+}, with a power of 375 mW was was focused to a spot size of approximately 1 mm at an angle of 45° to the sample normal (the target was excited on the edge at 0° to avoid radiation trapping effects). The 1.54 μm centred PL, corresponding to the ${}^4I_{13/2} \rightarrow {}^4I_{15/2}$ transition of Er^{3+} was also collected at 45° (90° for the target) and initially spectrally analysed with a single grating monochromator, detected with a liquid-nitrogen cooled photomultiplier tube (Hamamatsu) and then analysed with a photon counting multichannel scaler (PMS-400A, Becker and Hickl) with an overall time resolution of 10 μs. The steady state emission PL spectra of the samples was acquired in 0.5 nm steps from 1400 to 1700 nm with a 0.2 ms dwell time. For the time-resolved PL measurement a 0.1

[1] The spectral shift becomes more significant in GXID as the shallower angle results in a longer path length through the crystal planes.

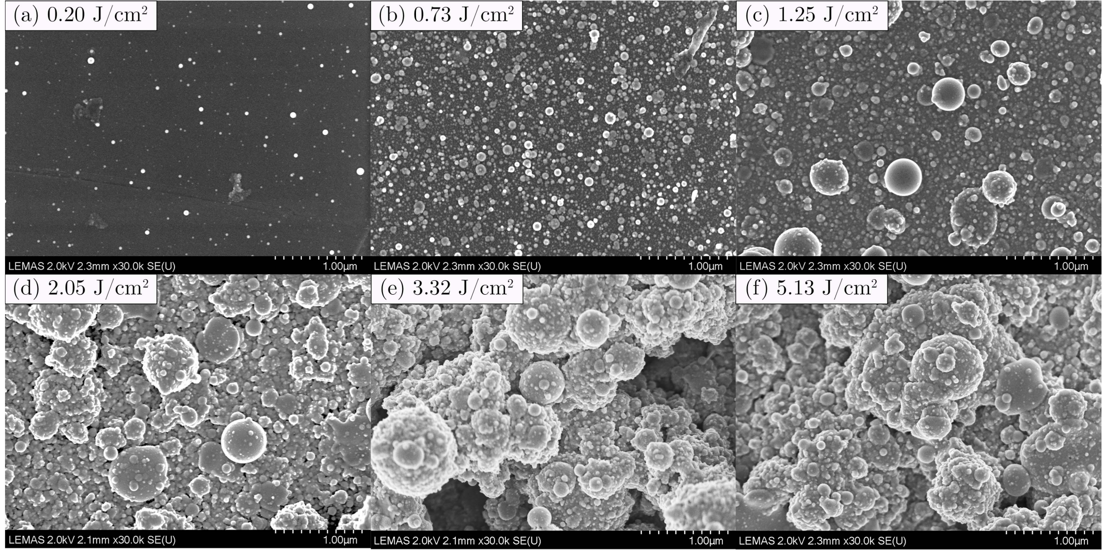

Figure 6.2: SEM images of depositions at a spot size of $A = 8.57 \times 10^{-5}$ cm^2 and varying laser fluences; (a) $F = 0.20$ J/cm^2, (b) $F = 0.73$ J/cm^2, (c) $F = 1.25$ J/cm^2, (d) $F = 2.05$ J/cm^2, (e) $F = 3.32$ J/cm^2, (f) $F = 5.31$ J/cm^2.

ms excitation pulse, modulated electronically at a frequency of 10 Hz, was accumulated over 400 sweeps and fitted with a single exponential curve. Due to the reduced signal to noise ratio of the two lowest fluence depositions, a pump time of 5 ms (to steady state) was used to maximise the signal and 2000 sweeps were collected. The fits to the decays all had a chi-squared value of less than 1.1 and flat residuals indicating a good fit.

6.4 Results and Discussion

6.4.1 Physical and structural properties

SEM images for depositions at six fluences increasing from close to the predicted ablation threshold (the multipulse value $F_{\mathrm{th}}(\infty) = 0.14$ J/cm^2 chapter 5 [26]) are shown in fig. 6.2. It is apparent that with increasing fluence, the deposition rate increases along with the particle size. At the lowest fluence of 0.2 J/cm^2, the particles are in the nanometer size range and well dispersed with an area coverage on the substrate of only ∼1.65%. The size distribution of the nanoparticles (NP) is shown in fig. 6.3 and followed a log-normal distribution with an average radius of 12 nm and a standard

Table 6.1: Physical and optical properties of depositions at varying laser fluences.

F [J/cm^2]	d [nm]	R_a [nm]	R_{RMS} [nm]	τ [ms]	FWHM [nm]
0.20	20 ± 20	7.5	12.5	2.35 ± 0.08	-
0.73	240 ± 150	13.8	18.1	2.69 ± 0.03	-
1.25	500 ± 200	81.5	123.5	3.49 ± 0.03	37.8
2.05	700 ± 250	226.9	308.8	3.50 ± 0.01	37.4
3.32	4000 ± 1500	577.3	700.0	3.45 ± 0.01	38.7
5.13	24000 ± 1500	-	-	3.36 ± 0.05	37.4

deviation of 8.6 nm. No particles had a radius of more than 65 nm.

It is seen in fig. 6.2 that for ablations at and above 1.25 J/cm^2 a second distribution of much larger particles, droplets, that increase in size with laser fluence appear. Figure 6.4 shows that the maximum sizes of the droplets increase with laser fluence and they are typically a micron in diameter at a fluence of ~1 J/cm^2. While droplets occur at a relatively low frequency they are most important to characterise for thin film fabrication techniques (if it is not possible to avoid them by using a lower fluence) as they dictate the film homogenity and affect the growth rate. The increase in film surface roughness with laser fluence, given in table 6.1, correlates with the observed increase in particle size as expected. Note that the deposition at 0.20 J/cm^2 was not sufficient to form a coverage of the substrate and so the measured value is an underestimate for a longer deposited thin film fabricated at this fluence.

Comparing fig. 6.5 with the cross-sections in fig. 6.2 it is clear that the films are formed through the random stacking of NPs and droplets, as is typical for fs-PLD [1]. The thickness of the films is given in fig. 6.4 and showed an exponential increase with laser fluence. This is due to the exponential dependence in ablated volume with fluence that was measured in chapter 5.

The composition of the target glass and the deposited droplets are reported in table 6.2. The depositions had a reduced tellurium content compared to the target of ~9%, which is likely due to the fact that the most volatile element in the ablated species, namely tellurium (heat of vaporization, 52.55 kJ/mol), preferentially evaporates off during early transport in the plume [1]. There may also be some loss of tellurium from the target glass melt in the furnace during fabrication. The reduction in tellurium was

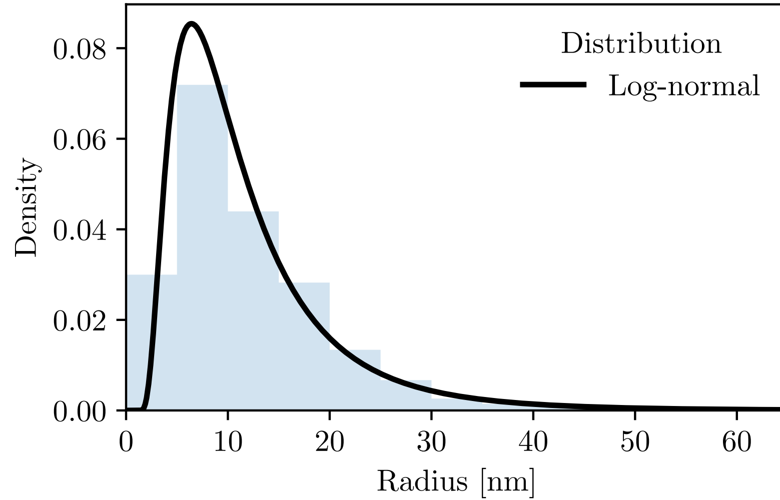

Figure 6.3: Particle size distribution for a deposition at 0.2 J/cm^2. Bin sizes were 5 nm. The fitted log-normal distribution (black line) had an average radius of 12 nm and a standard deviation of 8.6 nm.

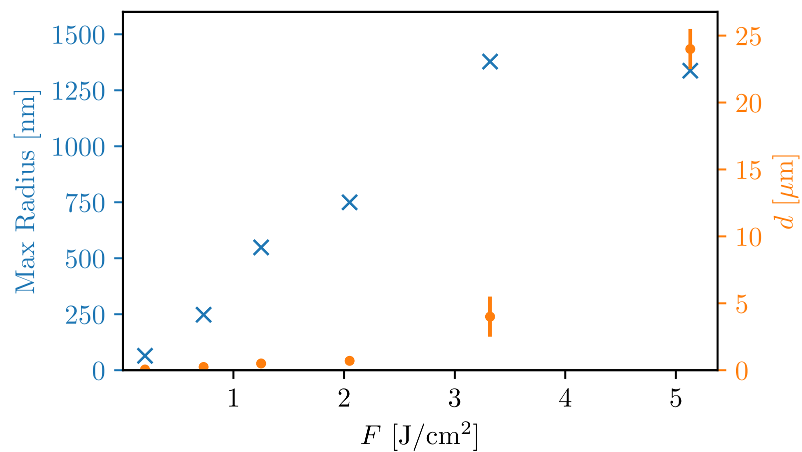

Figure 6.4: The maximum particle sizes (dashed line) and corresponding film thickness (solid line) against laser fluence. Values are measured from SEM images of several locations on the sample.

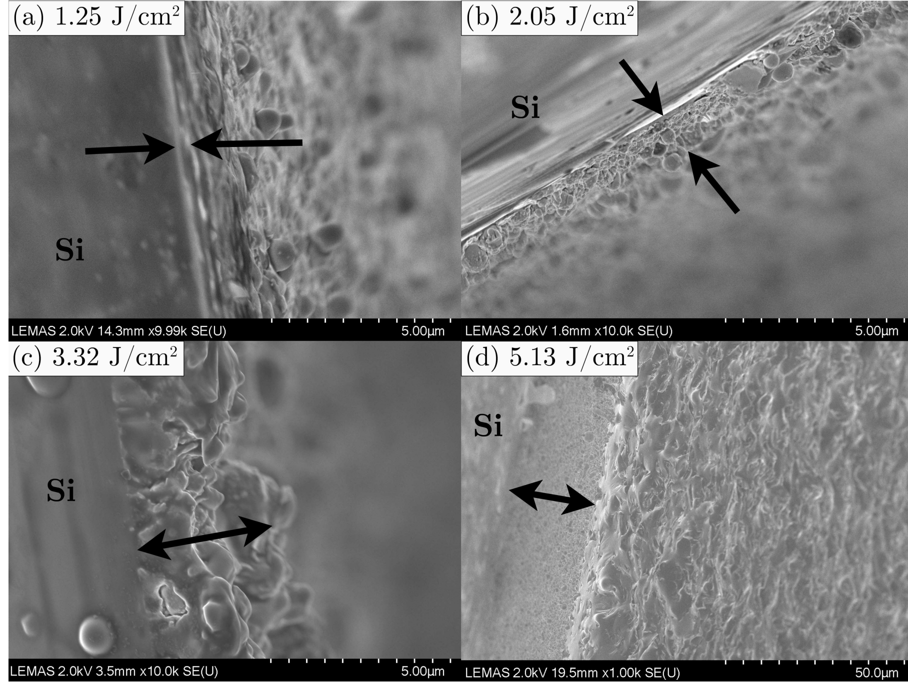

Figure 6.5: Cross section SEM images of depositions at a spot size of $A = 8.6 \times 10^{-5}$ cm^2 and varying laser fluences; (a) $F = 1.25$ J/cm^2, (b) $F = 2.05$ J/cm^2, (c) $F = 3.32$ J/cm^2 and (d) 5.13 J/cm^2. Note that (d) has a different scale bar to the other images. The Si substrate is indicated with text and the NP deposited films with arrows.

responsible for the increase in concentration of all other elements (note that the total concentration of Zn and Na must be compared). The small variations in composition with laser fluence were not significant enough for any further conclusions to be made from the semi-quantitative EDX data. The Er^{3+}-doping concentration in the deposited material, assuming the density of the target $\rho_{1\text{ErTZN}} = 5.24$ g/cm^3 (chapter 5), was 8.78×10^{20}cm^{-3}. This is 3.4 times higher than in the target which had a Er^{3+}-doping concentration of 2.58×10^{20} cm^{-3}. Changes in composition between the NPs and droplets may be possible due to the different formation processes but this can not be measured reliably with EDX.

The GIXRD pattern of the film deposited at a laser fluence of 3.32 J/cm^2 is presented in fig. 6.6. The peak of the Si(100) substrate at $2\theta = 69.8°$ is not observed, confirming that all peaks are from the deposited material. The diffraction peaks indicate that the material exhibits crystalline phases and is not amorphous like the target

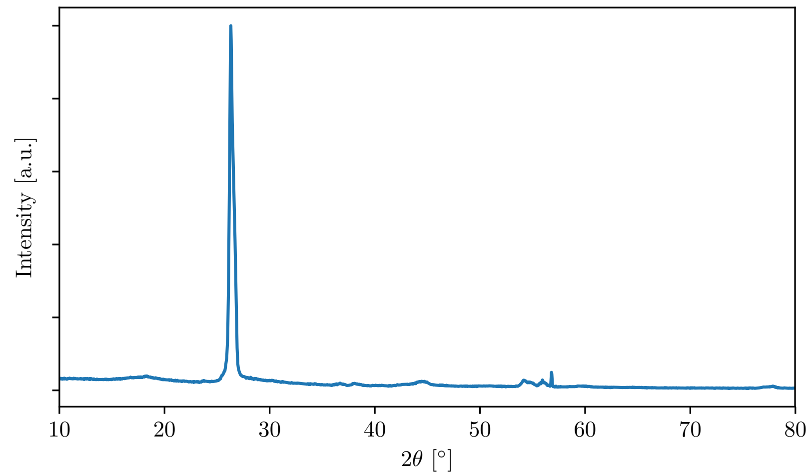

(a)

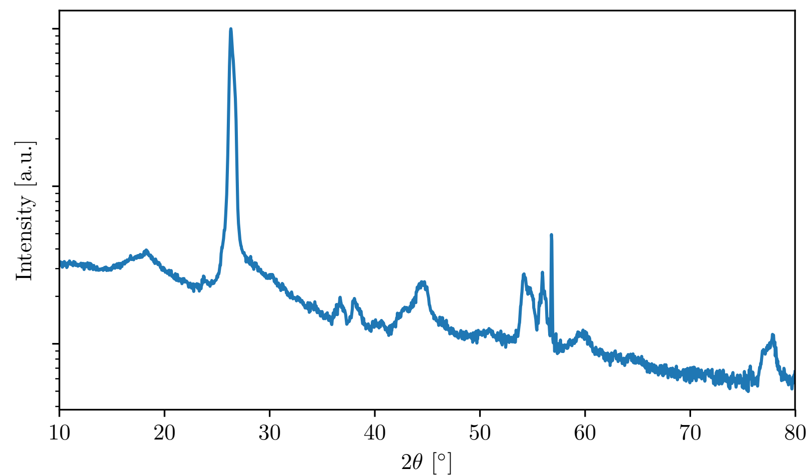

(b)

Figure 6.6: Grazing incidence X-ray diffraction patterns for the film deposited at a laser fluence of 3.32 J/cm^2 with (a) linear and (b) logarithmic intensity scales. The peaks correspond to γ-TeO_2 and $Zn_2Te_3O_8$, and are identified in the text.

Table 6.2: The atomic composition of the target glass and the deposited particulate films. The target glass composition was calculated from the molecular formula of the glass and so the evaporation of Te during melting is not taken into account. The composition of the depositions was measured by EDX and are semi-quantitative as the accuracy is reduced for rough surfaces and the Zn/Na spectral peaks overlap.

	Element [at. %]				
	Te	O	Zn	Na	Er
Target					
1ErTZN	26.3	61.6	5.0	6.7	0.4
Deposition [J/cm^2]					
1.25	17.0	66.1	5.3	10.6	1.1
2.05	16.4	69.6	4.3	8.7	1.1
3.32	17.6	69.1	3.8	8.5	1.1
5.13	17.2	67.1	4.5	10.1	1.1
Mean	17.0	68.0	4.5	9.5	1.1
Std.*	0.5	1.6	0.6	1.0	0.0

* Standard error on the mean.

(compare to the broad halo in fig. 5.4 [26]). Finding an exact match to the broad overlapping peaks of the multiple crystalline phases with the existing ICDD database was not possible and so the approach used here was to identify the known crystal structures and compare them to the measured GIXRD pattern [206]. The spectra is dominated by peaks centred at $2\theta = 26.28°$ and $26.58°$. The broad nature of the high intensity spike indicates that it contained more peaks but it was not possible to spectrally resolve them. These peaks were indexed to tellurium oxide (γ-TeO_2 (101) and (120), ICCD reference code: 04-014-3924) and zinc tellurium oxide ($Zn_2Te_3O_8$ (-311)/(310), ICCD reference code: 04-012-2189). All other peaks were much smaller with a relative intensity of <4 %. A sharp peak with the next highest intensity at $2\theta = 56.80°$ corresponded to $Zn_2Te_3O_8$ (-331)/(-117). The rest of the spectra contained broad and weak peaks corresponding to multiple crystalline planes. The broad peaks at 18.10°, 38.15°,

44.43°, 54.77° and 56.80° were indexed to $Zn_2Te_3O_8$, while the peaks at 54.14° and 55.94° were indexed to γ-TeO_2. The remaining peaks at 29.09°, 36.66°, 42.70°, 59.65°, 76.91°, 77.38° and 77.83° resulted from combinations of the various crystalline planes of $Zn_2Te_3O_8$ and γ-TeO_2. Tellurium was present in both the crystalline structures due to it being the highest concentration element in the ablated material.

A comparison with previous research shows that the formation of crystalline phases is not surprising. Kumi-Barimah et al. [161] observed crystallisation for NP implanted in polymer from the selected area electron diffraction (SAED) patterns, however they were unable to identify the crystals as no peaks were observed in the XRD patterns. This was likely due to the fact that the polymer had a large background signal and the GIXRD method was not used. SAED patterns in room temperature deposited films have also shown unidentified crystalline phases [162]. XRD analysis of films fabricated at 400°C on silica using the ULPD technique, below the temperature required for dissolution, has shown the presence of $Zn_2Te_3O_8$ with miller indices of (111) and (332) and Na_2TeO_3 with miller indices of (022) and (242) crystals [163]. XRD studies of amorphous hybrid tellurite-silica films fabricated with the ULPD, show the formation of TeO_2, ZnO, $Na_2Si_2O_5$ and SiO_2 crystalline structures during annealing above 650°C [130].

The NPs and droplets have a similar composition to the target glass, which has a melting temperature $T_m \approx 850$ K (measured for 75TeO_2-20ZnO-2.25Na_2O-2.25Li_2O-0.5NaF (mol%) glass [207]), crystallisation temperature $T_x = 694$ K and transition temperature $T_g = 565$ K (measured for 80TeO_2-10ZnO-10Na_2O (mol%) glass [208]). Initial NP temperatures (1 mm distance from the target) depend on the critical point and are typically of the order ≈2000 K for gold and silicon [152]. Assuming a similar heating regime, the NPs and droplets have a temperature $T > T_m$ and are in a molten state. Amoruso et al. [146] have shown that radiative cooling dominates during late stage plume expansion and occurs at rates of 28 K/μs, 6.5 K/μs and 0.9 K/μs for NPs at T of 2000 K, 1500 K and 1000 K, respectively. Impact and deposition on the substrate with a temperature $< T_x$ will result in a much more rapid quenching that would not favour crystallisation. The formation of crystalline phases must therefore occur during plume transport and depends on the speed of the species and the target-substrate distance. This conclusion is supported by the previously mentioned research that has found crystalline films for all substrate temperatures that are not $\gg T_x$,

(i.e. outside the ultrafast laser plasma doping regime). Boulmer-Leborgne et al. [121] found that NPs travelled at a few 10^4 cm/s while droplets travelled with slightly slower velocities of several 10^3 cm/s, regardless of the ablated material (metal, semiconductor and insulator). As a result the droplets undergo longer periods of radiative cooling and are deposited in a colder and less compliant state. This is seen in fig. 6.5a and b, where the droplets have a highly spherical shape compared to the hemispherical NPs. It is therefore likely that the fast NPs arrive at the substrate with $T > T_x$ and so are deposited in an amorphous state while the slower droplets have crystallised and cooled sufficiently to $T < T_x$ before deposition. This raises the possibility of forming amorphous tellurite films through the use of low laser fluences to eliminate the presence of droplets.

6.4.2 Target surface quality

SEM images comparing a deposition at $F = 1.67$ J/cm^2 using an optically polished target of $R_a \approx 5$ nm with depositions at $F = 0.20$ and 0.73 J/cm^2 using a rough target of $R_a \approx 108$ nm (as characterised in section 6.4.1) are shown in fig. 6.7. The volume of material ablated using an optically polished target is much lower than that of a rough target. Surface roughness can trap light and enhances near-field effects leading to an improved light-matter coupling and hence a reduction in ablation threshold. A second clear observation is the increased fraction of droplets to NP in the ablated matter. This is an important consideration for fs-PLD type applications and, as far as we are aware, this effect has not been reported in the literature.

As reported in chapter 5 and [26], that the change in ablation threshold in atmosphere of a tellurite glass that is optically polished to one that has had numerous incubating pulses, which cause roughening, is $F_{\text{th}}(1)/F_{\text{th}}(\infty) = 0.32/0.14 = 2.29$ [26]. Additionally, Ben-Yakar and Byer [133] observed that for borosilicate glass the change in single pulse ablation threshold $F_{\text{th}}(1)$ from vacuum ($<7.5\times10^{-5}$ Torr) to air was $4.1/2.6 = 1.58 \approx 1.6$ and the corresponding multipulse $F_{\text{th}}(\infty)$ change was $1.68/1.74 = 0.97 \approx 1$. The effect of reduced ablation threshold in atmosphere is attributed to an increase in the efficiency of plasma-surface coupling (i.e. heating) due to a decreased plume expansion [133, 157, 209]. It may therefore be expected that the increase in ablation threshold of the optically polished compared to the rough polished tellurite glass in vacuum is $2.29 \times 1.6 \approx 3.7$. Hence, the ablation at $F = 1.67$ J/cm^2

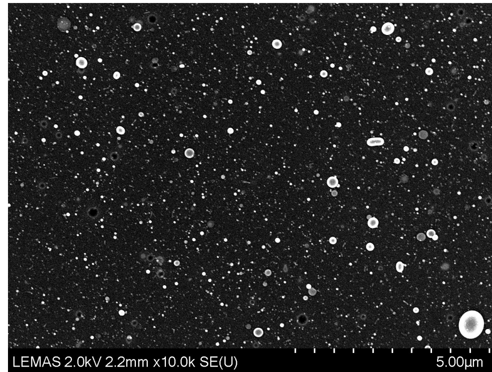

(a) $F = 1.67$ J/cm^2, target $R_a \sim 5$ nm.

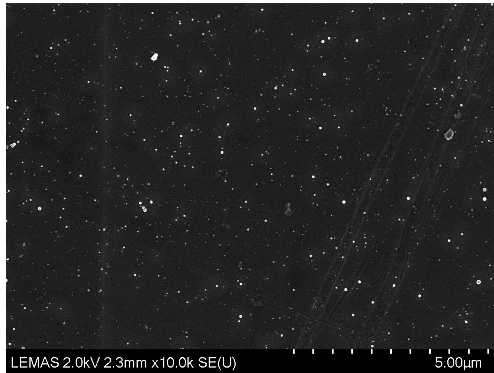

(b) $F = 0.20$ J/cm^2, target $R_a \sim 108$ nm.

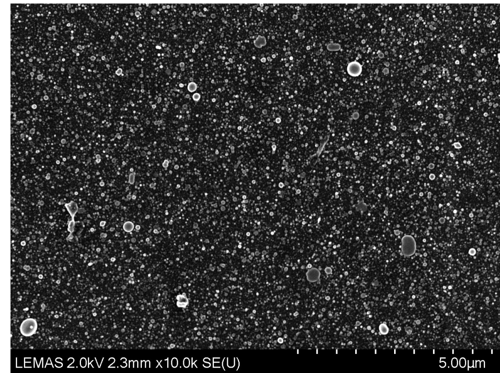

(c) $F = 0.73$ J/cm^2, target $R_a \sim 108$ nm.

Figure 6.7: SEM images of depositions at different laser fluences F and two target surface roughnesses. Ablation using the target polished to a lower surface roughness of $R_a \sim 5$ nm requires a much higher F to give an equivalent deposited volume as with a rougher, $R_a \sim 108$ nm, target.

in fig. 6.7(a) should give a similar deposition using a rough polished target using $F \approx 0.45$ J/cm^2. This agrees well with a visual comparison of fig. 6.7(b) and (c).

We conclude that for fs-PLD type applications the higher surface roughness is not only beneficial in terms of having a smaller particle size but also results in a reduced laser energy requirement. In addition to this, the damage that typically occurs to the surface during ablation typically results in a rough surface and should therefore be maintained from the very start of the deposition by using an unpolished target. The increased droplet fraction from smooth surfaces are also relevant for the more unique cases involving the ablation of liquids and requires more fundamental research to explain this phenomenon.

6.4.3 Optical properties

The PL spectra of the 1ErTZN target glass and depositions are shown in fig. 6.8a. It was not possible to characterise the PL spectra for the depositions at $F = 0.20$ J/cm^2 and 0.73 J/cm^2 as the PL emission was too weak due to the small volume of deposited material and low quantum efficiency (discussed later in this section). The spectra of all the depositions was similar, showing a Stark broadened peak centred at 1533 nm, like the target glass. There are no sharp spectral lines in the PL spectra, confirming that the Er^{3+} ions remain in amorphous tellurite host. This is expected as the crystalline structures measured via GIXRD do not correspond to crystalline phases of erbium. The full width half maximum (FWHM) of the target was 68.0 nm and the FWHM of the depositions, reported in table 6.1, had an average of 37.8 ± 0.6 nm. Tellurite glass is known to exhibit broadened Er^{3+} ion fluorescence band and so the narrower FWHM of the deposition is a result of the decrease in Te concentration that was measured with EDX in table 6.2. The reduction in tellurium concentration resulted in lower sidebands at 1503, 1555 and 1597 nm. The shoulder at 1503 nm decreased in intensity from 0.43 to 0.39 with an increase in laser fluence of 1.25 J/cm^2 to 5.13 J/cm^2, which may be due to increased evaporation of Te during plume transport caused by the higher heating of the material by the laser.

The 1.54 μm centred PL lifetime τ of the depositions, shown in fig. 6.8(b) and presented in table 6.1, were all shorter than that of the target $\tau_{\text{target}} = 4.34 \pm 0.02$ ms. It is worth noting that pin hole measurements of the lifetime on the bulk glass showed no evidence of radiation trapping [98]. For depositions at $F \geqslant 1.25$ J/cm^2

where the average film thickness d was greater than ~500 nm, τ was stable at 3.45 ± 0.07 ms. The decrease in lifetime from the target to the deposited films is due to the increased erbium concentration giving rise to more efficient concentration quenching. For lower fluence depositions, which had a lower film thickness, τ continued to decrease (along with a decrease in PL intensity). The shortest lifetime measured was 69% of the thicker film high fluence depositions, where the lifetime was constant. NPs implanted in polymers generated through fs laser ablation of Er^{3+}-doped TZN glass in a 70 mTorr oxygen atmosphere (spot size is not reported but it is estimated that $F \approx 1$ J/cm^2) exhibited identical spectra (FWHM of 39.2 nm) and a similar lifetime (~4 ms) [161]. The role of low pressure oxygen background is therefore not important in determining the PL of ablated material, which is to be expected at such low pressures as collisions of the plume species with the background gas atoms is almost negligible [156, 157].

A decrease in PL lifetime with a decrease in laser fluence was observed for $F <$ 1.25 J/cm^2. As all the lifetimes were monoexponential is may be expected that the compositional differences between the NPs and the droplets are small. The decrease in lifetime can therefore not be attributed solely to the lack of droplets for these low fluence depositions. Furthermore, the similarity in the PL spectra confirms this conclusion. The difference in the PL lifetime τ is therefore attributed to the film thickness as explained in the remainder of this section.

The decay rate $\Gamma = 1/\tau$ of an ion is composed of a radiative decay rate Γ_{rad} and a non-radiative decay rate Γ_{nrad} by

$$\Gamma = \Gamma_{\text{rad}} + \Gamma_{\text{nrad}}, \tag{6.5}$$

where the non-radiative decay rate is composed of the internal non-radiative recombination rate Γ_{int} and the concentration quenching rate due to ion-ion interactions Γ_{q} by $\Gamma_{\text{nrad}} = \Gamma_{\text{int}} + \Gamma_{\text{q}}$.

The spontaneous emission (SE) rate Γ_{rad} of an dipole is given by Fermi's golden rule and is proportional to the refractive index in a homogeneous dielectric media (see chapter 2). Inside stratified dielectric media, electric field confinement effects due to the index contrast at the interfaces results in a position dependent $\Gamma_{\text{rad}}(z)$, where z is the position of the dipole in the axis perpendicular to the interfaces. These effects become particularly important for thin films where all dipoles are close to interfaces as the experimentally measured Γ_{rad} represents an ensemble average of dipoles at all positions

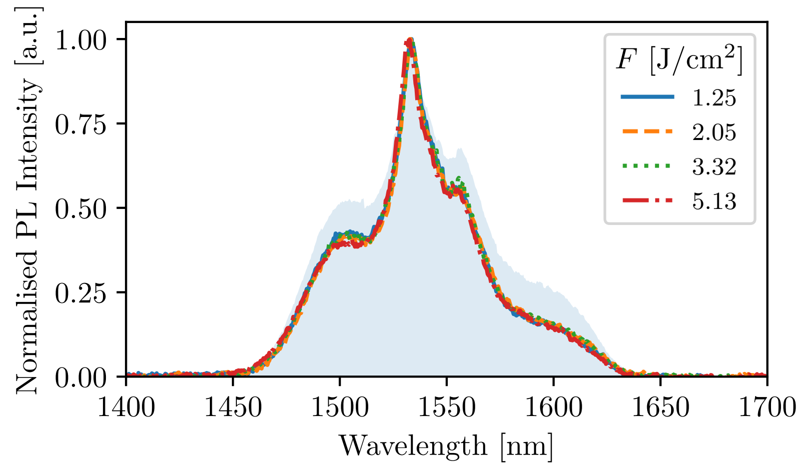

(a)

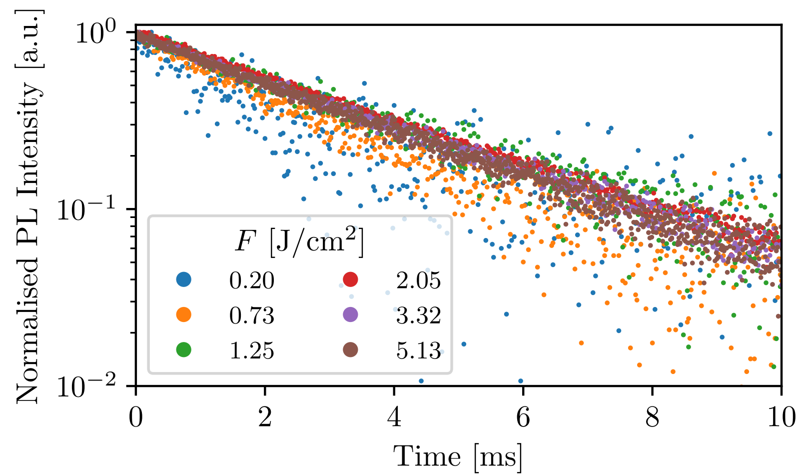

(b)

Figure 6.8: Photoluminescence (a) spectra and (b) decay of the particulate depositions at varying fluences. Shaded blue region in (a) shows the spectra of the 1ErTZN target glass for reference.

within the film. To investigate this effect, simulations were performed using a quantum-electrodynamical formalism suited to the analysis of the radiative SE rate in multilayer dielectric structures (model is described in chapter 2) [36]. The multilayer dielectric structures consisted of a variable thickness Er^{3+}-doped TZN layer (approximated to be the same as the 1ErTZN target $n_{1\text{ErTZN}} = 2.048$, measured in chapter 5 [26]) bounded by an infinite Si (n_{Si}=3.48) substrate ($z \to -\infty$) and air (n_{air}=1) superstrate ($z \to \infty$) layers. The structures did not support emission into waveguiding modes as the Si substrate had the highest index. The radiative SE rates normalised to the free space value (Purcell factor, F_p) for a dipole emitting at $\lambda = 1.54$ μm as a function of position for two multilayer structures having film thickness of 50 nm and 1540 nm is shown in fig. 6.9. The decay rates for dipoles orientated perpendicular $\perp$, parallel $\parallel$ and randomly Avg $= (2/3) \parallel + (1/3)\perp$ are shown. For Er^{3+} ions the randomly orientated dipole decay rate is relevant.

Dipoles in the thinner 50 nm film have an enhanced decay rate at most positions within the film originating from the parallel component that couples to TE modes. For the thicker 1540 nm film, the SE rate of randomly orientated dipoles is enhanced at the Si/ErTZN interface and suppressed at the air/ErTZN interface. For the majority of dipole positions in the film, which are far from the interfaces, the SE rate is unaffected by the interfaces and equals what would be measured in a bulk medium. The SE rate for dipoles located deep in the substrate/superstrate and far from the interfaces, the Purcell factor tends to the dielectric index as expected [39, 41, 50].

The theoretical average decay rate for randomly orientated dipoles averaged over all positions within a film, corresponding to the experimentally measured τ, for thicknesses ranging from 5 to 4000 nm is plotted alongside the experimental data in fig. 6.10. The theoretical and experimental trends are similar in that τ tends to the bulk value after a film thickness of ~500 nm. This is in agreement with the experimental measurements of Er^{3+} ions implanted in sodalime silicate glass showing that films thicker than 1 μm had an average lifetime close to that of a bulk system [45]. It is not expected for the experimental measurements to show the oscillations seen in the simulations as the surface roughness of the films results in a poorly defined film thickness. For thin films the experimentally measured τ drops like the theoretical predictions, however the decrease is greater for the experimental results.

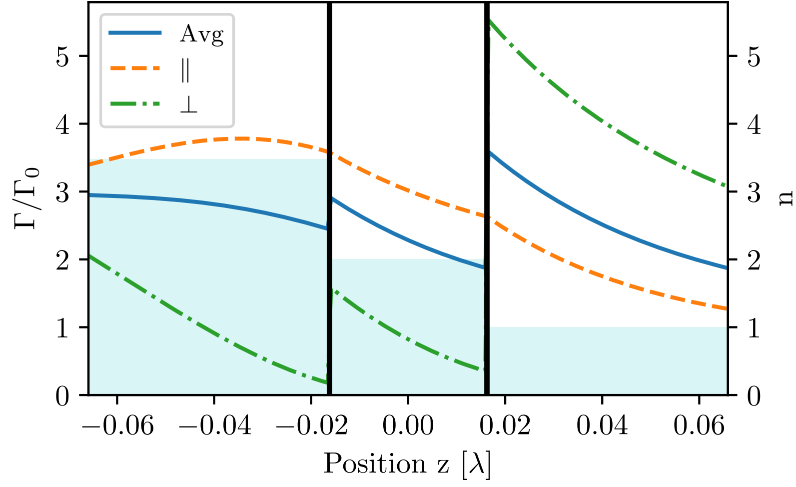

(a)

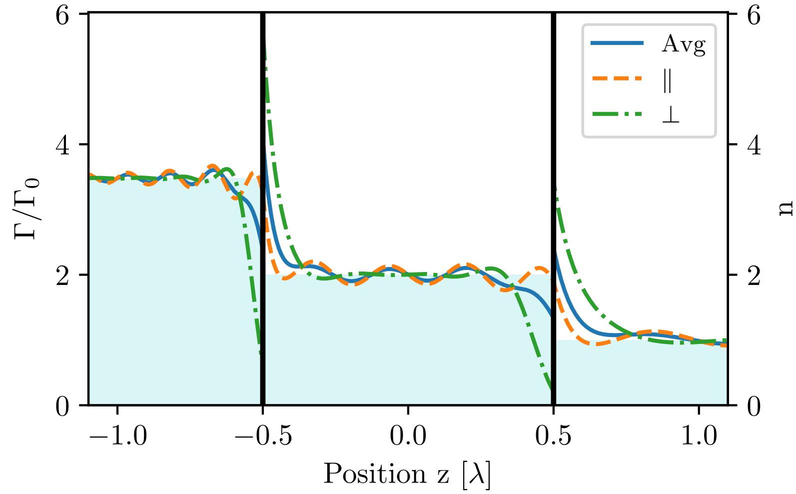

(b)

Figure 6.9: The radiative decay rate of perpendicular $\perp$, parallel $\parallel$ and randomly Avg $= (2/3) \parallel + (1/3)\perp$ orientated dipole compared to the free space decay rate at $\lambda = 1540$ nm as a function of position in a multilayer structure; Si substrate at $z \to -\infty$, (a) 50 nm or (b) 1540 nm thick tellurite film, air superstrate at $z \to \infty$. Light blue shaded region indicates the refractive index of the layer and vertical black lines indicate the boundaries of the layers.

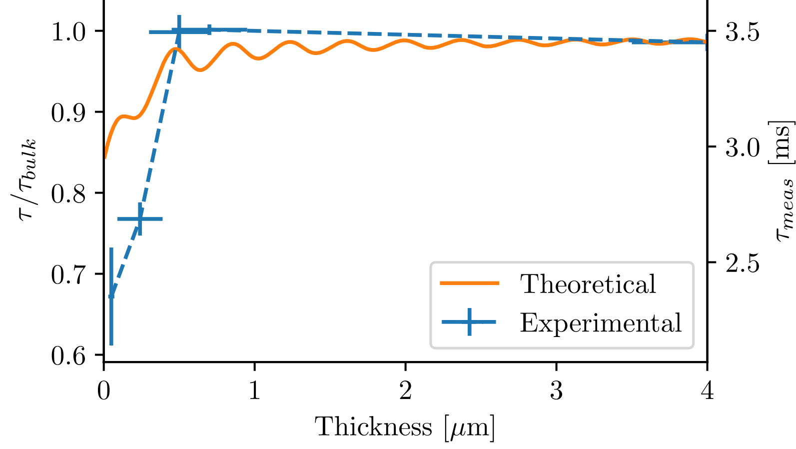

Figure 6.10: Lifetime measured from the NP depositions at varying fluences compared to theoretical simulation of the average dipole decay rate within the film. Left scale shows the lifetime normalised to the bulk value (Purcell factor), which for experimental measurements is chosen to be 3.45 ms and theoretical calculations is $(1/n_{bulk})$ ms. Right scale shows the measured lifetime of the depositions. The 1ErTZN target had a lifetime of 4.34 ms.

For Er^{3+} ion implanted silicates doped to a similar concentration of 2×10^{20} cm^{-3}, in which no clustering occurs, it has been shown that 100% of the Er^{3+} ions are in optically active states (i.e. 100% quantum efficiency) [5]. Furthermore, the low phonon energy of tellurite glass ensures that internal non-radiative recombination of Er^{3+} ions from the first excited state does not occur through multiphonon emission [64]. It is therefore assumed that $\Gamma_{\text{int}} = 0$ in this case. The Er^{3+} ions are assumed to always be within the same tellurite dielectric material and so local field effects are not considered [210].

At high doping concentrations energy migration, due to non-radiative short-range Förster energy transfer between ions, becomes more efficient and each transfer increases the probability that an ion coupled to a quenching centre is met. This non-radiative decay rate is characterised by Γ_{q} [5]. For Er^{3+}-doped silica glasses, OH-groups are known to be resonant quenching centres [91]. In this case, non-radiative decay processes are enhanced for ions close to the Si interface due to energy backtransfer and Auger quenching with free and bound charge carriers in silicon [28]. These effects are known to be

significant in silica deposited slot waveguides on silicon, where an increased fraction of Er^{3+} ions are close to Si interfaces and limits both the possible gain of the structure and maximum Purcell factor enhancement possible [28, 211]. Energy migration effectively couples ions further from the interface to the Si quenching centres. As the films get thicker, increasing numbers of ion transfer processes are required to reach the Si quenching centres for the furthest ions and so the probability of non-radiative decay decreases. Thus for PL measurements of thicker films, where a greater fraction of Er^{3+} ions are far from the Si interface, the probability of non-radiative recombination through energy migration becomes negligible and so the average decay rate from the ensemble of ions $\Gamma = \Gamma_{\mathrm{rad}}$. The radiative quantum efficiency $\Gamma_{\mathrm{rad}}/(\Gamma_{\mathrm{rad}} + \Gamma_{\mathrm{nrad}}) = \Gamma_{\mathrm{rad}}/\Gamma_{\mathrm{meas}}$ for the thinnest 20 nm film (actually composed of disperse NPs) is 80% and so radiative recombination is still the dominant process. This value is larger compared to the 67% quantum efficiency measured for a reactive cosputtered 20 nm Er-doped SiO_2 layer on Si (concentration $7.6 \times 10^{19}\mathrm{cm}^{-3}$). The difference is attributed to a combination of doping concentration and increase in thickness.

6.5 Conclusion

Er^{3+}-doped zinc-sodium tellurite glass films formed through the random stacking of nanoparticles and droplets were deposited in vacuum on Si at varying femtosecond laser fluences. For $F < 1.25$ J/cm^2 the films were solely composed of nanoparticles with an average radius of 12 nm. The film thicknesses ranged from 20 nm to 24 μm at $F = 0.20$ J/cm^2 and 5.13 J/cm^2, respectively. The surface roughness of the films increased with laser fluence due to the formation of larger droplets in the ablation plume. The depositions had tellurium oxide and zinc tellurium oxide crystalline phases that either formed by thermal quenching during the hydrodynamic expansion and plume transport or upon impact with the cool substrate. There was a slight ~9% loss in Te content during plume transport due to evaporation and resulted in the increase in Er^{3+} concentration. The lifetime of the films was reduced compared to the target as a result of the compositional changes. For films below ~500 nm, the increase in the local density of states combined with an increase in the non-radiative recombination rate due to Auger quenching and energy backtransfer resulted in shorter photoluminescence lifetimes and a reduction in quantum efficiency to 80%.

To summarise, the results presented here characterise the structural and optical properties of fluorescent films generated through fs-laser ablation of a tellurite-based glass target in vacuum. Doping the target glass with rare-earth elements other than erbium is trivial and not expected to change the findings. This is because the target ablation threshold, which is the critical parameter to NP fabrication, does not vary for typical doping concentrations and the material linear absorption is not relevant in the highly non-linear femtosecond laser ablation process [26] (see chapter 5). As such films or nanoparticles can be produced that have a wide range of fluorescent bands, providing suitable rare-earth ion transitions exists.

Chapter 7

Thin film formation with the ultrafast laser plasma doping technique

This chapter presents a systematic study of the film formation mechanism that takes place in the ultrafast laser plasma doping technique. An introduction to the chapter is given in section 7.1 and then the theoretical background behind cracking in thin films is described in section 7.2. Section 7.3 details the experimental setup. This includes a description of the processing parameters used for each sample and the analysis techniques employed for characterisation. The results are presented in section 7.4; Section 7.4.1 employs a two step fabrication process of room temperature deposition followed by sequential heating for film fabrication, section 7.4.2 investigates the optimum laser fluence at a high ULPD processing temperature and an oxygen atmosphere during processing is introduced in section 7.4.3 for even higher processing temperatures. Section 7.5 gives a conclusion to the chapter.

7.1 Introduction

Amorphous Er^{3+}-doped hybrid tellurite-silica thin films have been formed on silica and silica-on-silicon substrates with the ultrafast laser plasma doping (ULPD) technique. The superior spectroscopic properties (long metastable lifetime) at high doping concentrations compared to other techniques is particularly promising for optical applications,

such as waveguide amplifiers and thin disk lasers [6, 171, 178]. Doping into or on silicon is also of interest for electronically pumped light sources or detectors [29, 212]. Kamil [163] found that for silica-on-silicon substrates, tellurite crystallisation occurred at the silicon interface when the deposited volume great enough to saturate the silica layer. Direct film formation on silicon has not been studied.

For the superior spectroscopic properties of films to be realised in photonic devices, the film quality must be sufficiently high. The formation of films with the ULPD technique are highly sensitive to the processing parameters. The physical processes behind the film properties such as surface roughness, cracking and macroscopic inhomogenity are not well understood and the parameters for controlled sub-100 nm growth rate required for precise layering have not been identified [24, 127, 162]. The fundamental studies characterising the target ablation threshold (chapter 5) and the plume species in dependence of laser fluence (chapter 6) for the first time enable such an investigation. The importance of exceeding a certain temperature during processing has been identified in previous research [127, 162, 163]. It has however not been investigated as to whether this temperature may be applied after depositions, which would simplify and speed up the fabrication process. Hybrid tellurite-silica film formation in a two step process of deposition and heating is investigated first. Following this, thin film formation on silica, silicon and silica-on-silicon substrates is carried out at varying laser fluences to identify the optimal regime for photonic applications and provide insight into the physical processes. The films fabricated here are the first to be achieved in a vacuum using the ULPD technique as previous research uses an oxygen atmosphere. Finally, having identified a suitable fluence regime, oxygen is introduced into the atmosphere and the interplay with deposition temperature is investigated.

7.2 Theoretical background

7.2.1 Cracking of thin films

Cracking of hybrid tellurite-silica thin films fabricated via the ULPD technique is known (primarily from experience as it is rarely reported) to occur once a certain threshold film thickness is surpassed [25]. In these cases, even if the optical properties of the film or coating are adequate, the mechanical stability and integrity are inadequate for use. Understanding the stress-induced failure is therefore of great importance and the

various origins and theoretical models of residual stress for physical vapour deposited (PVD) coatings have been analysed in [213].

Thermal residual stress arises when the film-substrate is cooled down to room temperature after processing and a thermal expansion/contraction mismatch occurs [213]. The larger the mismatch in the film and substrate Coefficient of Thermal Expansion (CTE), the greater the residual stress and if the breaking point is exceeded microcracking in plane to the interfaces occurs [214].

The stress σ induced to the film away from the edges can be described by [215–217]

$$\sigma_C = \frac{1}{\delta_C}\left(\frac{1-v_C}{\delta_C E_C} + \frac{1-v_S}{\delta_S E_S}\right)^{-1} \cdot \int_{T_0}^{T_1} \left(\alpha_S(T) - \alpha_C(T)\right)\delta T, \tag{7.1}$$

where α is the CTE, E is Young's modulus, v is Poisson's ratio, T is the ambient temperature and the subscripts C and S refer to the film/coating and the substrate, respectively. Under the assumption that the CTE's are linear and the substrate is much thicker than the film, the equi-biaxial stress state of the interior of the film is given by [215, 216]

$$\Delta\sigma_C = \frac{E_C \Delta T(\alpha_S - \alpha_C)}{(1-v_C)}, \tag{7.2}$$

which shows that the strain is proportional to the mismatch in CTE coefficients. The CTE for 80TeO_2-10ZnO-10Na_2O glass is 19.8$\times 10^{-6}$/K [208], SiO_2 glass is 0.54 $\times 10^{-6}$/K [218] and 4 $\times 10^{-6}$/K for Si [219]. Multicomponent silicate glasses typically have a higher CTE compared to pure silica [220]. For example, the borosilicate Borofloat 33 has 3.25$\times 10^{-6}$/K [221] and the sodalime glass Unicrown has 9.3$\times 10^{-6}$/K [222].

As a result of the very large CTE of tellurite glass in comparison to the silica substrate cracking occurs during post processing cooling. For TeO_2 E = 50.7 GPa and v = 0.233 [223]. The residual strain in a pure tellurite film on a silica substrate when cooled to room temperature from 600 degrees will therefore be approximately 764 MPa compared to 627 MPa on Si. The CTE of hybrid tellurite-silica films fabricated by the ULPD technique will therefore lie in between that of silica and the tellurite target glass and depend on relative density determined by the dissolution during fabrication and rate of Te evaporation. Additionally, the films fabricated with the ULPD technique have a grading due to the dissolution process in film formation. The transition from film to

substrate reduces the stress considerably [213, 224]. Thicker films produced by the use of higher laser fluences, higher repetition rates or ablation periods are typically denser and have a sharper index grading as the dissolution is lower [128, 162, 163]. This will give rise to increased strain and ultimately lead to cracking in the thin film. Increasing the dissolution rate by increasing the substrate temperature therefore appears to be the only viable route to avoid cracking for thicker films on silica substrates. There is merit for future investigations into silicate substrates, which have a higher CTE and lower softening temperature.

7.3 Experimental setup

7.3.1 Fabrication

The ULPD system used to fabricate the samples is described in chapter 4. Each substrate was cleaned for 5 minutes in an ultrasonic bath with acetone and then iso-propanol. Four 10 by 10 mm substrates were mounted in a 2 by 2 stainless steel holder 70 mm above and parallel to the target surface. The increase in distance between target and substrate compared to chapter 6 was to reduce heating effects on the target from the IR heater. The holder was rotated at 10 RPM around its centre.

At the start of each run, the chamber was pumped down to a vacuum ($< 1 \times 10^{-4}$ mTorr). For samples that required it, an oxygen atmosphere (100 mTorr, 15 sccm) was introduced at this point. The system was then heated to the set processing temperature T required for the run. The target was an erbium doped zinc-sodium tellurite glass of composition $79TeO_2$-$10ZnO$-$10Na_2O$-$1Er_2O_3$ mol.% (1ErTZN). A high doping concentration target was used to maximise the photoluminescence (PL) signal from for ease of characterisation, as it was anticipated that the fabricated films would be thin due to the short deposition time and laser repetition rate set to 1 kHz. The target was wet polished with P320 grit silicon carbide (SiC) sandpaper to the dimensions of ~40 (laser raster axis) × 20 (target raster axis) × 4 (thickness) mm. The elliptical laser spot on the target surface had an area of $A \approx 6.24 \times 10^{-5}$ cm^2 (Gaussian beam waists of $\sim$ 65.0 and 31.6 μm) for all depositions bar the highest laser energy processed sample, which had $A \approx 5.04 \times 10^{-5}$ cm^2 (Gaussian beam waists of $\sim$ 60.52 and 26.48 μm). The target was first prepared so that a steady state ablation threshold (surface roughness and incubation) was achieved by irradiating with the set laser fluence several times over

the target surface. Each sample was processed with 1.2×10^6 pulses per cm^2 applied to the target surface directly below the substrate, taking 1 hour and 44 minutes. More concretely, the laser rastering involved scanning 150 lines at a speed of 10 mm/s over a length wider than the substrates (35 mm) and moving the target in 0.1 mm steps perpendicular to the laser raster axis after each line. This constituted a single pass over the target and 8 passes in total were performed for each experiment.

Several experiments were performed to investigate and optimise the film formation. Firstly, samples were fabricated via room temperature depositions followed by post heating with the goal of forming either tellurite or metastable hybrid tellurite-silica layers in a two step process. Depositions were performed on silicon (P<100>B doped, resistivity of 1-30 ohm·cm, nominal thickness 675 μm), Si, and synthetic fused silica (Heraeus Spectrosil 2000, thickness 1.1 mm), SiO_2, substrates at room temperature, T = 22°C, in a vacuum at a laser fluence F of 1.04 J/cm^2 and 2.08 J/cm^2. Each of the substrates was then placed, deposition side up, in a furnace set to 750°C for 6 hours and then taken out of the furnace to cool in air to room temperature, which took approximately 7 minutes ($\sim$ 100°C per minute cooling rate).

Next, the laser fluence F was optimised for substrate heated depositions. Samples were processed in a vacuum at T = 600°C with F varying from 1.04 to 4.27 J/cm^2. This corresponded to pulse energies E_p of 65 to 215 μJ. This was the highest T that could be used without causing the targets to melt. The substrates included for each run were Si, thermally grown silica on silicon (SOS) (1 or 10 μm: N<100>As doped, resistivity of 0.001-0.005 ohm·cm nominal thickness of 675 μm) and SiO_2. The SOS substrates were chosen such that the silica layer was much thicker than the predicted hybrid tellurite-silica film.

Lastly, investigations into improving the film properties by using higher T (600 to 700 °C) to increase the dissolution rate were performed at a F = 1.76 J/cm^2 (E_p = 98 μJ) in an oxygen atmosphere[1]. The purpose of oxygen flow (70 mTorr) was to cool the target and surrounding chamber metal housing to avoiding target melting and reacting with the metal holder at the elevated temperatures. The substrates used for these experiments were 1 μm SOS and SiO_2.

[1] Oxygen was chosen as this was used in previous research using the ULPD technique. The use of an inert gas, such as nitrogen, may have been more suitable here to avoid complications in interpreting the results.

Table 7.1: Table showing the processing parameters of all samples.

Section†	F [J/cm^2]	E_p [μJ]	T [°C]	Atm.	Substrate (number)
7.4.1	1.04	65	22	Vac	Si (2), SiO_2 (2)
	2.08	130	22	Vac	Si (2), SiO_2 (2)
7.4.2	1.04	65	600	Vac	Si (2), SiO_2 (2)
	1.56	98	600	Vac	Si (1), 10um SOS (1), SiO_2 (2)
	2.08	130	600	Vac	Si (1), 1um SOS (1), SiO_2 (2)
	4.27	215	600	Vac	Si (1), 10 um SOS (1), SiO_2 (2)
7.4.3	1.56	98	600	O_2	1um SOS (2), SiO_2 (2)
	1.56	98	650	O_2	1um SOS (2), SiO_2 (2)
	1.56	98	700	O_2	1um SOS (2), SiO_2 (2)

† The results section in which the samples are analysed

A summary of the processing parameters for all samples in this chapter is given in Table 7.1.

7.3.2 Characterisation

A limitation of many previous studies is that the macroscopic properties of the film, which are relevant for optical devices, are not observed under high resolution imaging techniques. Therefore characterisation is best performed at both the macroscopic and microscopic scales. Initial inspection of all the samples was performed visually and photographs were taken (iPhone 8, Apple). Key film properties, such as roughness, cracking, uniformity and thickness (from the colour and birefringence), are easily observed with the eye to give a qualitative assessment.

Surface morphology was characterised via optical microscopy (Olympus BX51 with Zeiss AxioCam MRc5 camera) at varying magnifications for all samples. More detailed characterisation, when required, was preformed using high resolution scanning electron microscopy (SEM, Hitachi SU8230). Elemental mapping was performed using energy-dispersive X-ray spectroscopy (EDX) coupled to the SEM (80mm^2 X-Max detector, Oxford Instruments). The film thickness d of the samples measured via SEM were performed using a backscattered detector on 125 μm thick transmission-electron microscopy (TEM) prepared cross-sections coated in 1 nm graphite to avoid surface

charging.

Characterisation of surface topography was achieved via atomic force microscopy (AFM) operating in tapping mode (Innova Atomic Force Microscope, Bruker with a μmasch AFM probe of 8 nm nominal tip radius). The average surface roughness R_a and root mean squared surface roughness R_{RMS} were evaluated by averaging over areas at least several times larger than the largest features. The data was analysed with the open source software Gwyddion [186, 187].

The optical transmission spectra of the room temperature deposited films were acquired by using a double beam spectrophotometer (Perkin-Elmer Lambda 950) in the UV-vis-NIR regions (250 - 2000 nm).

The film thickness and refractive index (n and k) of the thin film on SiO_2 substrate at the optimal fluence was determined using variable angle spectroscopic ellipsometry (M-2000 Spectroscopic ellipsometer, JA Wollam) (VASE) over the wavelength range from 245 to 1650 nm and at multiple angles of incidence (60° to 75° by 5°). The spot diameter on the film was ∼3 mm. All analysis was performed with CompleteEASE version 6.43. n and k of the target and substrate were first measured so that a suitable model for the film on substrate could be derived. Backside reflection was taken into account during the fitting procedure.

PL measurements were performed using a fluorescence spectrometer (FLS 920, Edinburgh Instruments) at room temperature (∼20°C). A 976 nm excitation laser source (BL976-PAG500976, Thorlabs), which resonates with the $^4I_{15/2} \rightarrow ^4 I_{11/2}$ transition of Er^{3+}, with a power of 375 mW was focused to a spot size of approximately 1 mm at an angle of 45° to the sample normal. For the bulk target, in order to reduce radiation trapping effects, the laser was focused on the edge at 90° to the surface normal to minimise the number of Er^{3+} ions between the illuminated area and the collection slit. The 1.54 μm centred PL, corresponding to the $^4I_{13/2} \rightarrow ^4 I_{15/2}$ transition of Er^{3+} was collected at 45° for the samples or 0° for the target and initially spectrally analysed with a single grating monochromator, detected with a liquid-nitrogen cooled photomultiplier tube (Hamamatsu) and then analysed with a photon counting multichannel scaler (PMS-400A, Becker and Hickl) with an overall time resolution of 10 μs. The steady state emission PL spectra of the samples was acquired in nm steps from 1400 to 1700 nm with a 0.2 ms dwell time. For the time-resolved PL measurement a 0.1 ms excitation pulse, modulated electronically at a frequency of 10 Hz, was accumulated

over 250 sweeps. The data was first fitted with a single exponential model and then increasing numbers of exponential were added until the residuals appeared flat and fits had a chi-squared value of less than 1.1, indicating a good fit.

7.4 Results and Discussion

7.4.1 RT deposition followed by post heating

Photographs of the room temperature deposited films pre- and post-heat treatment are shown in fig. 7.1. The room temperature depositions on silica, (a) and (e) in fig. 7.1, had a homogeneous brown appearance. This brown appearance was not visible on the Si substrates as Si is not transparent in the visible spectrum. For Si substrates the film is only visible by observing the reflection at the edge shadow masks from the substrate holder. The UV-vis-NIR transmission spectra of the depositions on silica substrates are shown in fig. 7.2. The decrease in transmittance at shorter wavelengths is due to Rayleigh scattering as the size of tellurite NPs, ∼10 nm radius (characterised in chapter 6), is much smaller than the wavelength of radiation. The higher fluence deposition had a much lower transmission due to an increase in scattering resulting from a greater number and larger average size of deposited NPs (see chapter 6). The variation in spectral shape seen between the two depositions is also a result of this.

A significant change is observed in all the films after heat treatment, shown by the photographs (e - h) in fig. 7.1, in which the films are no longer homogeneous. The films on silica substrates both loose their brown appearance with the low fluence deposition appearing cloudy in patches and the high fluence deposition being covered in white spots. The high fluence deposition on the Si substrate developed a completely matt white appearance while the low fluence deposition has a complex inhomogeneous surface that varies from left to right.

Silicon substrate

Further insight into the changes in film properties before and after heat treatment are gained from optical microscopy images, shown in fig. 7.3. Only sparse sub-micron particulates can be observed for the 1.04 J/cm^2 room temperature deposition. As reported previously in chapter 6, the ablation plume at this fluence is composed primarily of ∼10 nm radius NPs and a small proportion of ∼200 nm diameter droplets. It is only the

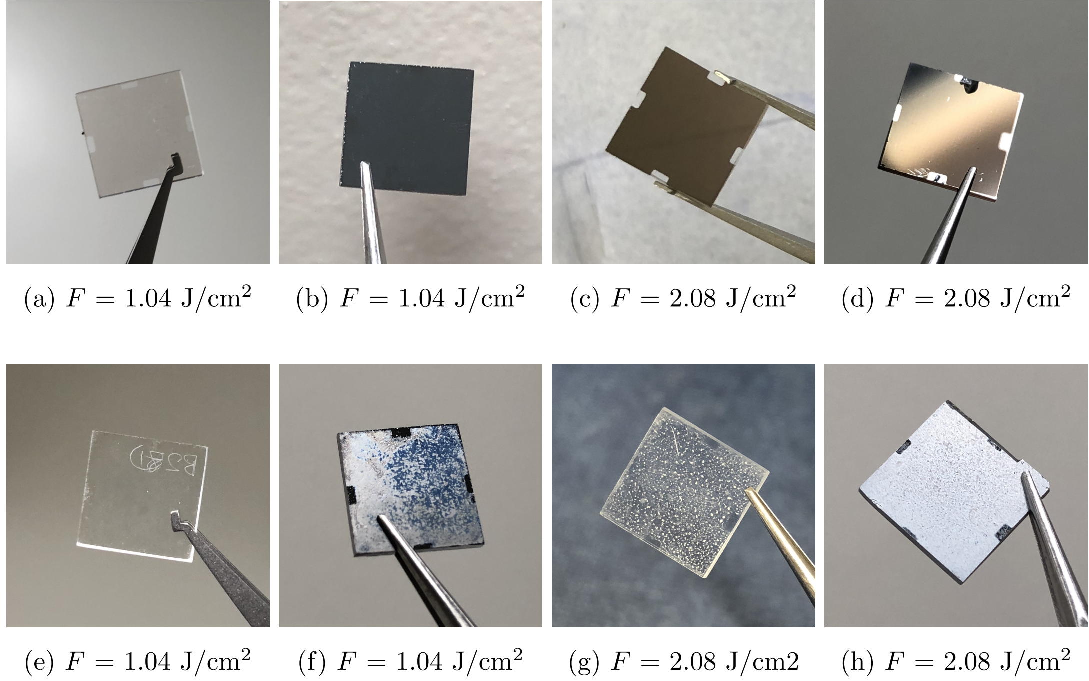

(a) $F = 1.04$ J/cm^2 (b) $F = 1.04$ J/cm^2 (c) $F = 2.08$ J/cm^2 (d) $F = 2.08$ J/cm^2

(e) $F = 1.04$ J/cm^2 (f) $F = 1.04$ J/cm^2 (g) $F = 2.08$ J/cm2 (h) $F = 2.08$ J/cm^2

Figure 7.1: Photographs of room temperature depositions (a, b, c, d) and post heat treatment (e, f, g, h) on silica (a, c, e, g) and silicon (b, f, d, h) substrates.

larger droplets that are visible in optical microscopy images and the substrate appears pristine due to the very low film thickness of the randomly stacked NPs. The increase in deposited material (NPs and droplets) at 2.08 J/cm^2 results in an opaque film when viewed under the optical microscope.

The post heat treated films exhibit very different surface morphologies. At 1.04 J/cm^2, fig. 7.3(c), there is an incomplete surface coverage of the film, resulting in islands. The SEM image of the film surface is shown in fig. 7.4a shows a similar profile. EDX spectra of the film only identified fluorine. Flourine contamination was not present in any of the other films and may have come from the electric furnace. The film deposited at 2.08 J/cm^2, shown in fig. 7.3(d), was characterised by large scale $\sim$20 μm diameter circular features dispersed throughout the surface. The surrounding regions have a much larger 50 - 100 μm diffused region. Further inspection via SEM revealed the exotic three dimensional shapes of these features, as shown in fig. 7.4. The typical features were elevated rims with crater like centres, usually extending from a central point, and varied slightly with size of the feature. Elemental mapping of the region is

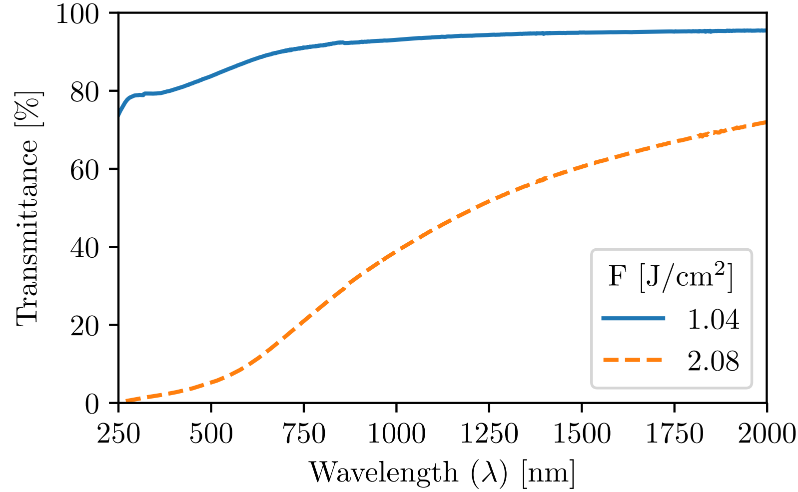

Figure 7.2: UV-VIS transmission measurement of deposited nanoparticle films on silica at two fluences. Measurements performed using a pristine silica substrate in reference beam path. Rayleigh scattering by the nanoparticle depositions results in the reduction in transmittance.

shown in fig. 7.5. The elements Te, Zn, Na and and Er were highly concentrated in these regions while O was well dispersed throughout the entire surface. The large features are crystalline phases, that have either grown from the room temperature deposited films (see chapter 6) or formed during the heat treatment [130, 163]. The regions outside the crystals are predominantly composed of Si and O, which suggests that the Te corroded the Si substrate before evaporating leaving an Er^{3+}-doped silica/silicate surface layer.

The PL spectra of the $F = 2.08$ J/cm^2 deposited film prior and post heat treatment is shown in fig. 7.6a. The PL intensity of the $F = 1.04$ J/cm^2 deposited film was too weak to measure. The spectra of the RT deposition is similar to what was measured in chapter 6. The film had a slightly narrower (39 nm) full width half maximum (FWHM) compared to the target (68 nm) due to the slight loss of Te during plume transport. The PL peak was at 1534 nm for both the target and the deposited film as the Er^{3+} ions are in a tellurite environment. The side-bands of the film at 1555 nm and 1499 nm were also reduced compared to the target due to the compositional changes. Post heating, the spectra FWHM narrowed to 25 nm and two peaks at 1536 nm and 1545 nm were observed. The tellurite shoulders to the spectra were also reduced in intensity due to Te evaporation during heating. The spectra is similar for that of Er^{3+} in a

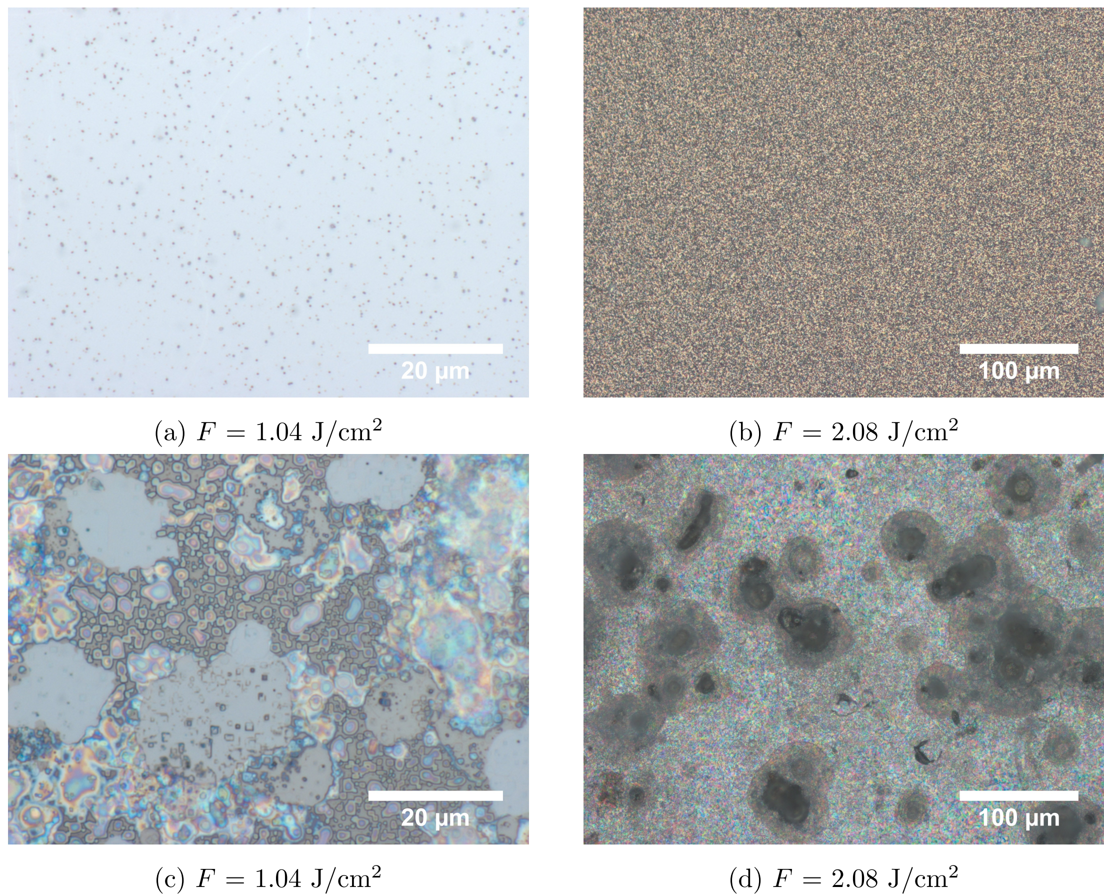

(a) F = 1.04 J/cm^2 (b) F = 2.08 J/cm^2

(c) F = 1.04 J/cm^2 (d) F = 2.08 J/cm^2

Figure 7.3: Optical microscopy of room temperature depositions on silicon pre (a, b) and post heat treatment (c, d).

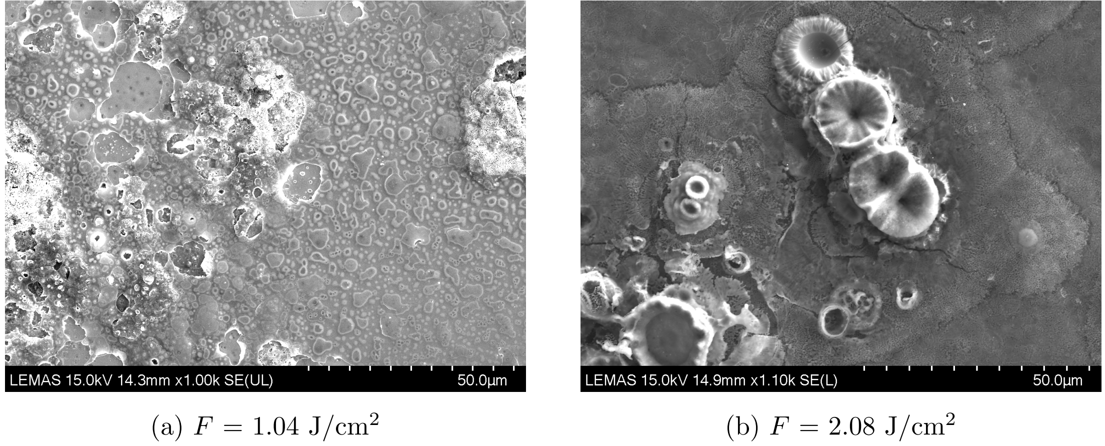

(a) $F = 1.04$ J/cm^2

(b) $F = 2.08$ J/cm^2

Figure 7.4: SEM images of room temperature depositions on silicon post heat treatment at two different laser fluences. The features in (a) were measured by EDX and identified as fluorine contamination. The crystalline features seen in (b) grew with heating.

silicate, confirming the conclusions from the EDX measurements, and indicates that the ions within the crystalline structures are not optically active.

The PL decay, shown in fig. 7.6b, shows that the deposited film had a single exponential decay with a lifetime of 3.76 ± 0.04 ms. This was the same for the deposited films in chapter 6. After heat treatment, the decay was a double exponential with lifetimes of 3.57 ± 0.06 ms (73 %) and 0.49 ± 0.01 ms (27 %). The appearance of a shorter sub-millisecond lifetime is indicative of clustering of Er^{3+} ions, which results in pair induced quenching. Again, it is unlikely that the Er^{3+} ions in the crystals are optically active as a double exponential decay would be in the deposited films that are known to have crystal structures. Furthermore, Er^{3+} ions precipitates are usually assumed to not be optically active and are therefore not probed by PL measurements [5].

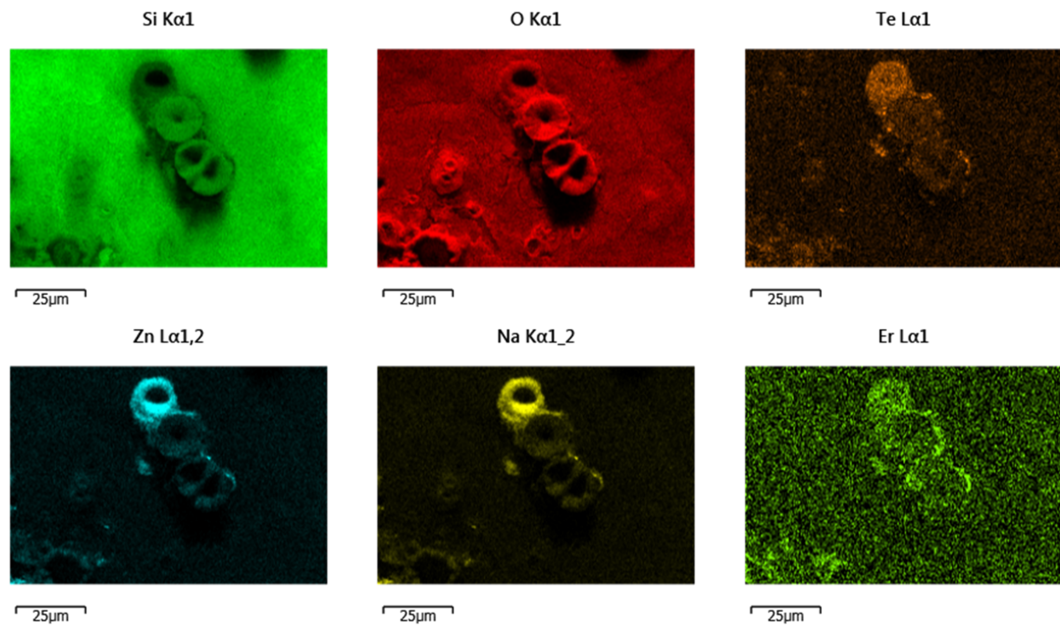

Figure 7.5: EDX images of room temperature depositions at $F = 2.08$ J/cm^2 on Si post heat treatment, fig. 7.4(b). The large crystalline features are composed of elements in the erbium doped TZN target glass. Oxygen appears over the entire surface and indicates that a it has formed a silica with the silicon substrate while the remainder of the target glass elements have evaporated off.

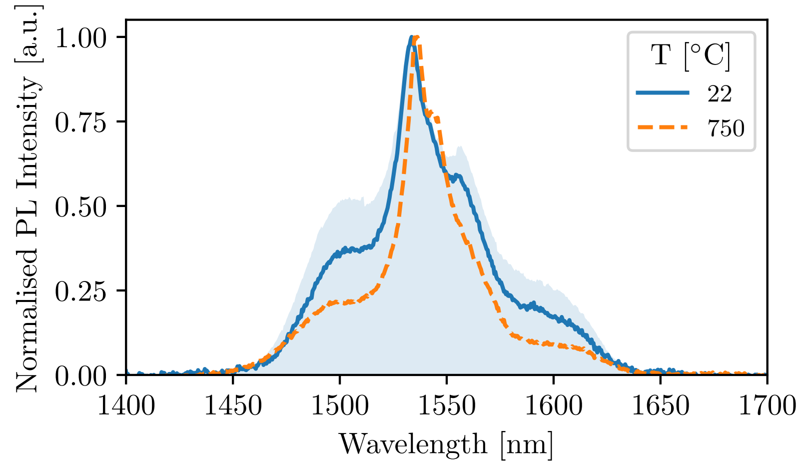

(a)

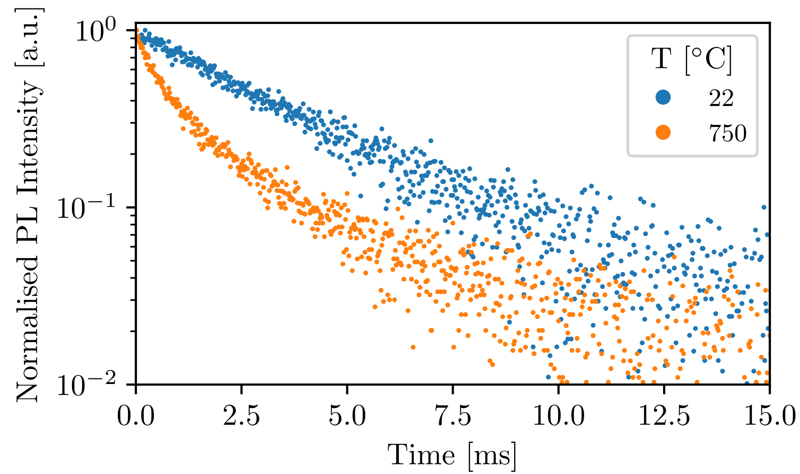

(b)

Figure 7.6: Photoluminescence (a) spectra and (b) decay of $F = 2.08$ J/cm^2 depositions on Si substrates. Light blue shaded region in (a) shows the spectra of the 1ErTZN target glass for reference. The narrowing in spectra and shift in peak wavelength upon heat treatment indicates that the Er^{3+} ions transition from a tellurite to a silica environment.

Silica substrate

Optical microscopy of the depositions on silica substrate samples pre- and post-heat treatment are shown in fig. 7.7. The room temperature depositions show features identical to those observed on silicon substrates. This is expected as the NPs and droplets that make up the majority of the ablation plume undergo rapid freezing upon impact and therefore do not react with the substrate.

The white features visible by eye in the post-heat treatment depositions, (a) and (e) in fig. 7.1, are revealed in the optical microscopy images. At 1.04 J/cm^2, fig. 7.7a, ring structures with an approximate diameter of 2.5 μm are scattered over the, apparently pristine, silica surface. SEM of the ring structures in fig. 7.8a reveals their crystalline nature. The EDX spectra only showed the elements Si and O, i.e. the substrate, indicating that all the deposited material has evaporated like for the equivalent Si substrate samples. It is concluded that these structures are microcrystallites of cristobalite formed by defects created by the impact of high energy ions and electrons in the ablation plume. Strained Si-O-Si bonds due to irradiation with 0 - 20 eV electrons is known to occur and the precipitation in the amorphous SiO_2 of microcrystallites due to a strain-releasing mechanism has been suggested to explain experimental observations [225].

The higher fluence 2.08 J/cm^2 deposition has features on a much larger scale. Similar to the silicon substrate, circular structures tens of micron in size are surrounded by a diffused region in the optical microscopy image in fig. 7.7b. Higher resolution SEM imaging, fig. 7.8b, shows the three dimensional crystalline structures. In the regions of diffusion surrounding the features, a leaf-like reticulate venation pattern is observed. EDX mapping, shown in fig. 7.9, reveals that the Te is primarily found in these crystals. The other elements Si, O, Zn, Na, Er appear well dispersed. The three dimensional structure from shadowing is not seen in the Te map as it has an emission spectra at high >3 keV where the other elements (bar the low concentration Er) do not absorb. The increased penetration of the higher radiation results in signals from deeper into the structure (i.e. not just superficial material) being detected. It is also notable that at the bottom of the image, were a feature has not developed a 3D profile, that these elements are also in higher concentrations.

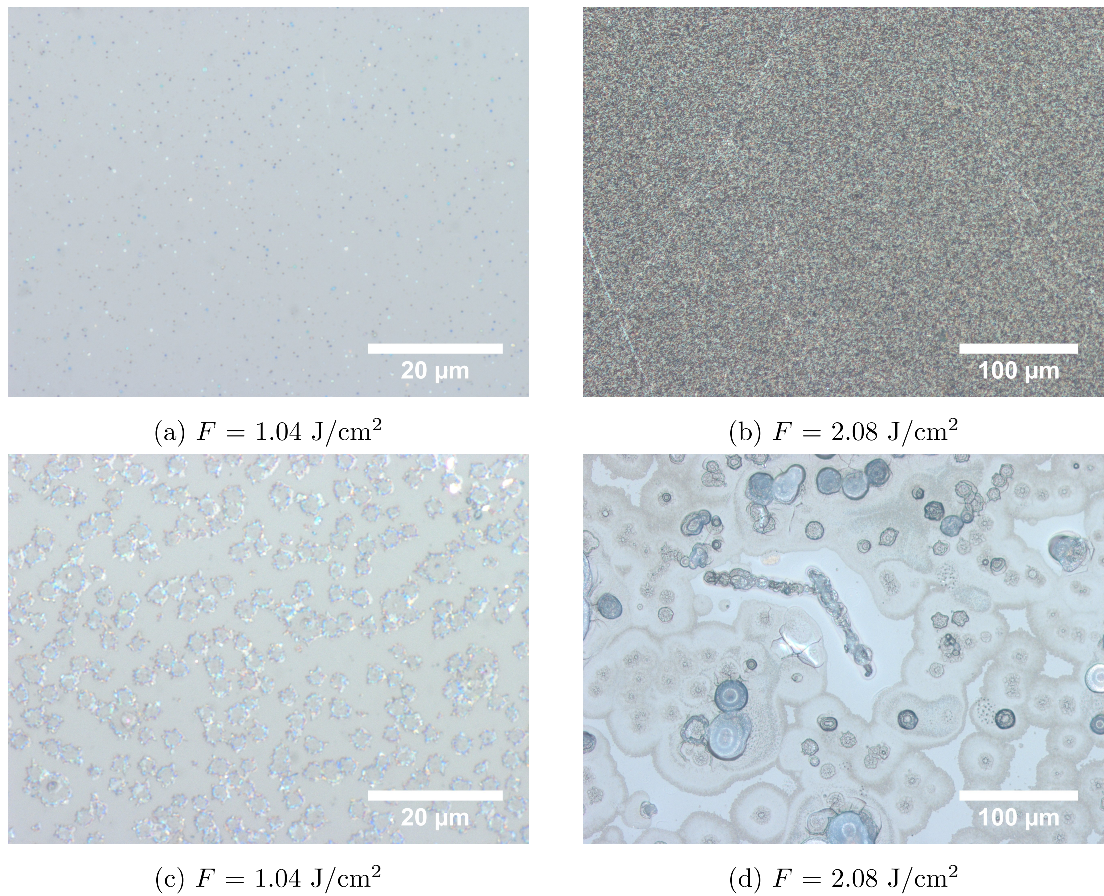

(a) F = 1.04 J/cm^2 (b) F = 2.08 J/cm^2

(c) F = 1.04 J/cm^2 (d) F = 2.08 J/cm^2

Figure 7.7: Optical microscopy of room temperature depositions on silica pre (a, b) and post heat treatment (c, d).

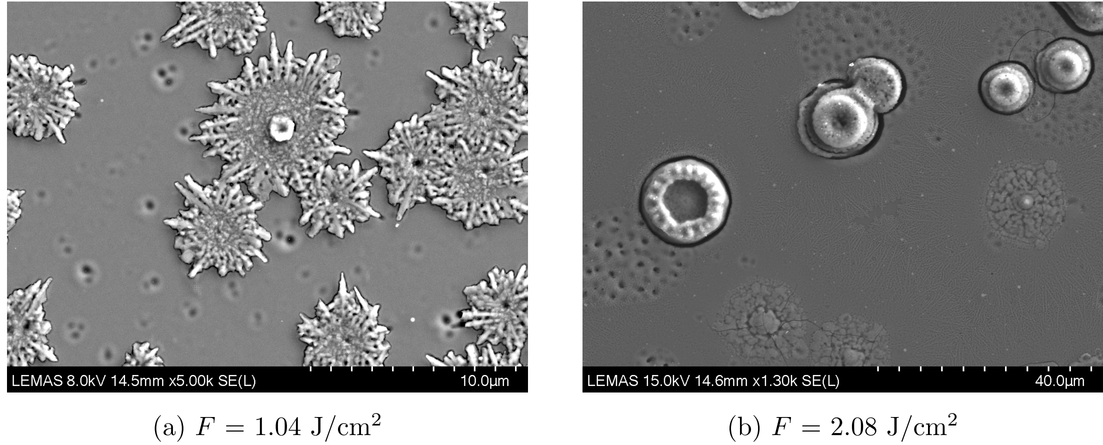

(a) $F = 1.04$ J/cm^2 (b) $F = 2.08$ J/cm^2

Figure 7.8: SEM images of room temperature depositions on silica post heat treatment at two laser fluences. The crystalline features in (a) were crystabolites as EDX only detected the elements Si and O and result from stress induced in the substrate by the high energy electrons and ions in the plume.

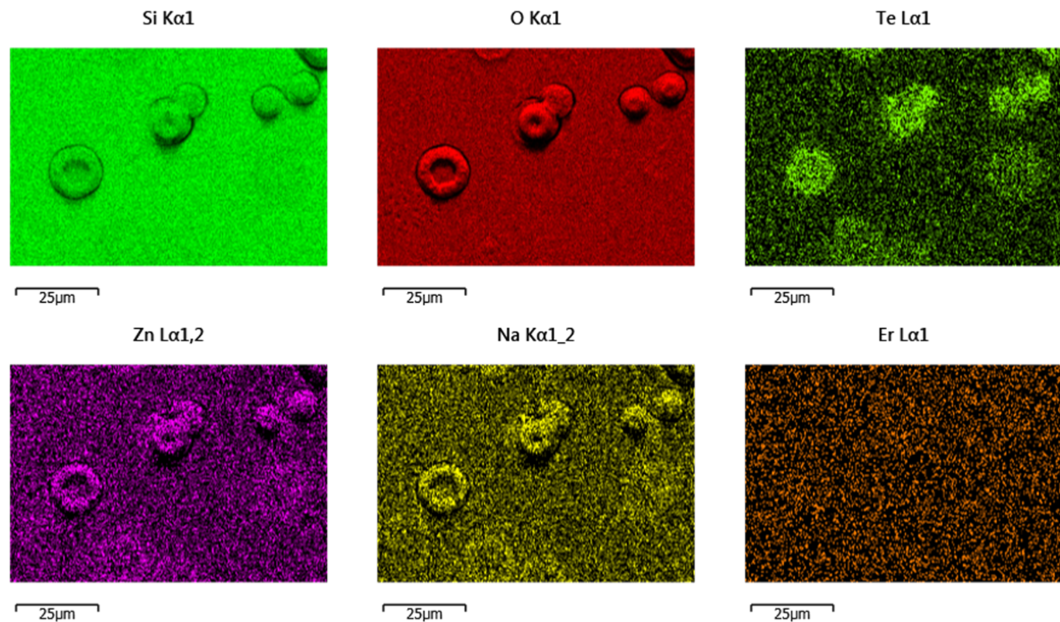

Figure 7.9: EDX images of room temperature depositions at $F = 2.08$ J/cm^2 on silica post heat treatment, fig. 7.8(b). The crystalline features correspond to the regions concentrated in Te.

The PL spectra of the $F = 2.08$ J/cm^2 deposited film prior and post heat treatment is shown in fig. 7.10a. The spectra of the RT deposition was identical to the Si substrate and the deposited films in chapter 6. The full width half maximum (FWHM) was 39 nm (target FWHM was 68 nm) and the PL peak was at 1534 nm. Post heat treatment, the spectra FWHM narrowed to 36 nm due to the slight reduction in the tellurite sidebands and the main peak was red shifted by only 0.5 nm. Nonetheless, the Er^{3+} ions still appear to be in a tellurite environment unlike for the Si substrate sample. The PL decay, shown in fig. 7.10b, had a single exponential decay with a lifetime of 3.72 $\pm$ 0.04 ms for the room temperature deposited film. The PL spectra and decay was identical to the Si substrate and the deposited films in chapter 6. After heat treatment, the decay transitioned to a double exponential with lifetimes of 4.52 $\pm$ 0.06 ms (76 %) and 0.96 $\pm$ 0.01 ms (24 %). The appearance of the shorter lifetime is again attributed to the clustering of Er^{3+} ions. The increase in the long lifetime component may be due to the formation of a silicate in the regions away from the crystals. The lower decay rate of the long lifetime component for the silica substrates compared to the silicon substrate is because the non-radiative deexcitation mechanisms (energy backtransfer and Auger quenching) between the Er^{3+} ions and silicon do not occur (see section 6.2) and the lower density of states due to the decreased refractive index of silica compared to silicon.

Conclusion

Er^{3+}-doped tellurite glass films were deposited on silicon and silica glass substrates at room temperature and then heated at 750°C (1023 K), which is above the melting temperature $T_m \approx 850$ K (measured for $75TeO_2$-20ZnO-2.25Na_2O-2.25Li_2O-0.5NaF (mol%) glass [207]), crystallisation temperature $T_x = 694$ K and transition temperature $T_g = 565$ K (measured for $80TeO_2$-10ZnO-10Na_2O (mol%) glass [208]). For both of the low laser fluence depositions at 1.04 J/cm^2, most (if not all) of the material that was deposited evaporated off the surface and could not be detected with EDX or PL spectroscopy. It is also worth noting that since no PL signal was detected after the deposited nanoparticles and droplets evaporated, the contribution of implanted ions to the PL signal is negligible in the ULPD technique. This may be expected considering the small fraction of total matter that they make up in the femtosecond laser ablation plume (see section 4.2). In the case of SiO_2 substrates, the formation of microcrystallites

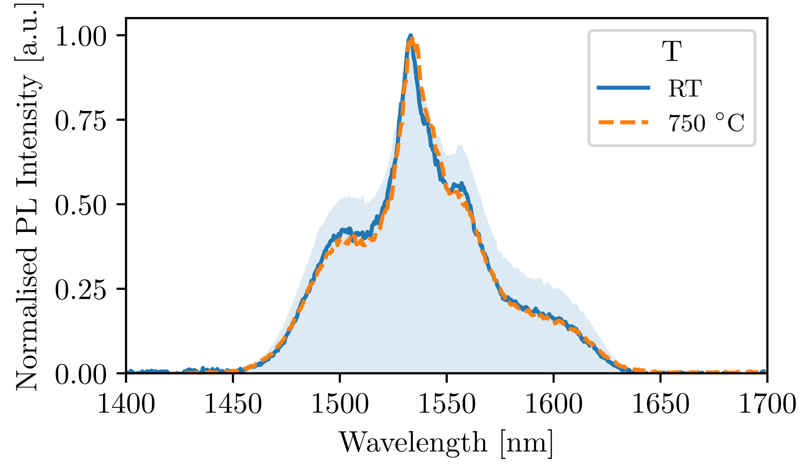

(a)

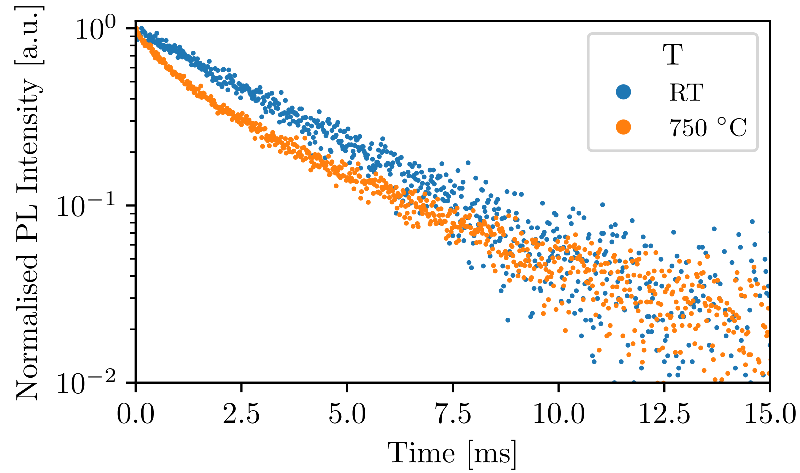

(b)

Figure 7.10: Photoluminescence (a) spectra and (b) decay of $F = 2.08$ J/cm^2 depositions on silica substrates. Light blue shaded region in (a) shows the spectra of the 1ErTZN target glass for reference. The decrease in lifetime after annealing, due to the appearance of a second shorter exponential component is due to the Er^{3+} ions forming clusters.

of cristobalite was observed due to strain induced by the high eV electrons in the ablation plume.

The depositions at the higher laser fluence of 2.08 J/cm^2 showed highly inhomogenous surfaces after heat treatment. Large crystalline structures primarily composed of Te, Zn, Na and O were observed on the surface. The room temperature depositions are known to contain numerous crystalline phases (chapter 6) and their progressive growth or development of new phases is enabled by heating [130]. For the Si substrate, the corrosion by the tellurium resulted in the formation of a hybrid tellurite-silica layer in which the PL spectra was similar to that of Er^{3+} in silicate. Despite this, the PL lifetime did not increase as the ions were not well dispersed and deexcitation energy transfer processes between the Er^{3+} ions and Si occur. Slight dissolution between the SiO_2 substrate and the deposited material occurred, resulting in an increase in the long lifetime component. For both substrates the PL decays became double exponential with a second sub-millisecond decay rate appearing. The growth of crystalline structures most likely promoted ion clustering, leading to an overall shortening in the PL decay rate.

Due to the inadequate film properties (inhomogeneous surface and undesirable shortening of the PL lifetime) in this two step deposition then heating process, no more characterisation or investigations were performed. The important conclusion can be made in regards to the ULPD technique that the formation of amorphous hybrid tellurite-silica films occurs through a heat activated dynamical dissolution process in which the continual deposition of material prevents the development and formation of crystalline phases.

7.4.2 Laser fluence optimisation

Photographs of the samples fabricated at a processing temperature of 600°C with varying laser fluences are shown in fig. 7.11. At the lowest laser fluence of 1.04 J/cm^2, which is $\sim 5 \times F_{th}(\infty)$ of the target glass (chapter 5), no film can be seen on either of the substrates indicating that either the film was very thin or, more likely based on the results of the previous section, the deposition rate was lower than the evaporation rate and so no film was formed. At 1.56 J/cm^2 a film is observed by the substrate holder shadow mask and birefringence is visible on the transparent SiO_2 substrate. Birefringence is a result of the interference of light and therefore indicates a low surface

roughness and scattering of the films. At 2.08 J/cm^2 the films appeared rougher and no birefringince was observed. The roughening is expected as the average particle size and droplet frequency in the ablation plume increases with laser fluence (chapter 6).

The SiO_2 substrate sample in fig. 7.11(e) showed high scattering predominantly in the central region of the sample resulting from undissolved material. This may be explained by realising that the dissolution rate is a function of temperature. Heating of the substrates occurs through direct absorption of radiation from the quartz infrared heating lamps and conductive heating from the metallic holder to the substrate. The observation of a central undissolved region suggests that conductive heating to the SiO_2 substrate is less efficient. Direct radiative absorption is also much lower compared to Si (above 500°C Si has an emissivity of approximately 0.64), which increases the dependence on conductive heating. The temperature gradient across the SiO_2 sample surface, which has the lowest temperature in the central region of the substrate, results in the dissolution rate being insufficient to accommodate the volume of material deposition at the laser fluence. The efficiency of substrate heating due to thermal conduction with the metallic substrate holder is described by the thermal conductivity of the substrate. The B-doped ($\sim 1\times10^{16}$ cm^{-3}) Si wafer has a thermal conductivity of approximately 30 - 100 W/(m·K) at 27°C [226] whereas SiO_2 has a thermal conductivity of 1.38 W/(m·K) at 27°C and $\sim$ 2 W/(m·K) at 600°C [218]. This large difference combined with the lower mass of the thinner Si substrate relative to the thicker SiO_2 substrate accounts for the temperature gradient.

Finally, at the highest processing fluence of 4.27 J/cm^2 all samples surfaces are visibly rough and, for the Si and SOS substrates, highly inhomogeneous. The entire surface of the SiO_2 substrate has a frosted appearance. As a side note, the white plume extending away from the target at a laser fluence of 4.27 J/cm^2 was large and visible over several centimetres, whereas the plume at 1.56 J/cm^2 was at most one millimetre long and barely visible. The individual substrate materials processed at the varying laser fluences will be analysed in the following after which, the optimal fluence is chosen and a more detailed characterisation is performed.

Si Substrates

Optical microscopy images of the sample surfaces are given in fig. 7.12. At the lowest fluence, 1.04 J/cm^2, disperse black spots are present upon an apparently unmodified

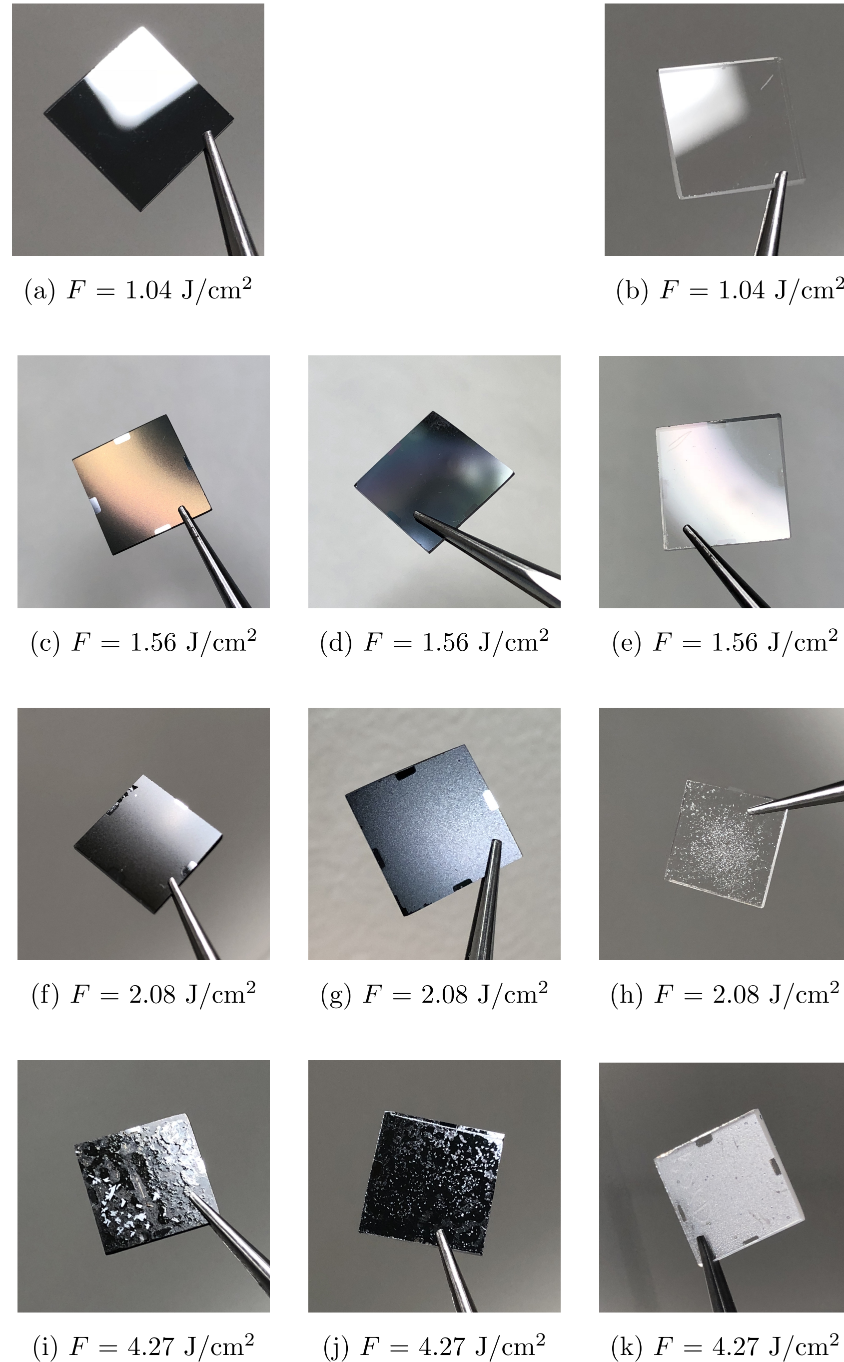

(a) $F = 1.04$ J/cm^2 (b) $F = 1.04$ J/cm^2

(c) $F = 1.56$ J/cm^2 (d) $F = 1.56$ J/cm^2 (e) $F = 1.56$ J/cm^2

(f) $F = 2.08$ J/cm^2 (g) $F = 2.08$ J/cm^2 (h) $F = 2.08$ J/cm^2

(i) $F = 4.27$ J/cm^2 (j) $F = 4.27$ J/cm^2 (k) $F = 4.27$ J/cm^2

Figure 7.11: Photographs of heated depositions at varying fluences on different substrates. Left column (a, c, f, i) Si substrate, middle column (d, g, j) SOS, right column (b, e, h, k) SiO_2 substrate.

substrate. An SEM image of one of these spots is shown in fig. 7.13(a), where it appears that the surface has been slightly corroded. An EDX map of the same region, in fig. 7.14 reveals that the composition matches that of the target glass (Te, Zn, Na, O). Erbium was not observed as the signal was too weak due to it being the lowest concentration element in the target glass. The large size of the spot can only be the result of a droplet, which has a larger volume than the NPs and therefore did not fully evaporate off the surface. A second feature that was observed under SEM, see the inset in fig. 7.13(a), is dispersed islands of clusters. EDX point spectra at these points confirmed that they were gold. A log-normal distribution fit to the 23 Au clusters gave a mean radius of 13.6 nm and standard deviation of 4.3 nm, as shown in fig. 7.15. In ion irradiated SiO_2 it has been observed that a microscopic redistribution of impurity Au and Ag occurs resulting in metallic nanometer sized clusters [91, 227]. In this case the Au is from the crucible which is slightly corroded by the molten Te during the target glass melting.

The intermediate fluence regimes have homogeneous surfaces and, at $F = 2.08$ J/cm^2, a rippled surface profile was seen (clearer under DIC microscopy). This featureless surface is expected from the corresponding photographs (f) and (h) in fig. 7.11. At $F = 2.08$ J/cm^2, crystals were not visible unlike for the room temperature deposited and post heat treated films in fig. 7.4(b). At $F = 4.27$ J/cm^2, a sudden change in the surface properties is observed. Large ∼50 μm diameter features are surrounded by clear but cracked regions of film. Other regions in the films are composed of smaller ringed structures. A higher resolution SEM image is shown in fig. 7.13(b). An EDX elemental map of a region where the ringed structure transitions to the smooth area is shown in fig. 7.16. Notably, O, Zn and Na are relatively homogeneously dispersed. The ring features are exposed Si with little Te in these regions. Instead Te is homogeneously dispersed in the smooth upper region. An EDX map of the crystalline structure in fig. 7.13(b) is shown in fig. 7.17. The central region shows the clustering of Er inside a crystal composed of Zn, Na and O. Circular regions of Te appear around the edge. The corrosive nature of Te combined with the high deposition rate is responsible for the complex surface stoichiometry.

Photoluminescence was collected for all bar the lowest fluence sample, which had a signal too weak for an accurate characterisation. The low PL signal is a result of only the deposited droplets remaining on the film due to evaporation of the nanoparticles. In addition to this, Auger quenching and energy backtransfer at the Si interface acts to

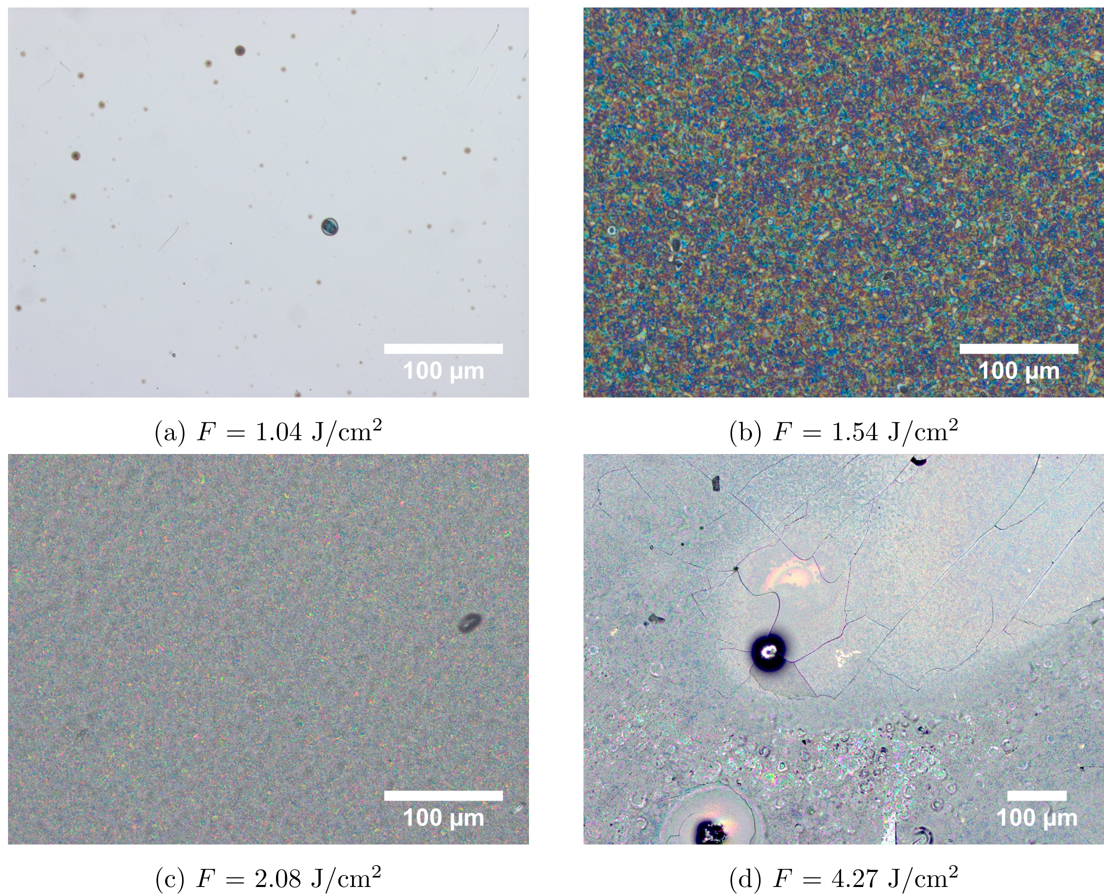

(a) $F = 1.04$ J/cm^2

(b) $F = 1.54$ J/cm^2

(c) $F = 2.08$ J/cm^2

(d) $F = 4.27$ J/cm^2

Figure 7.12: Optical microscopy images of heated depositions on Si substrates. Note (d) has a different scale bar to the other images.

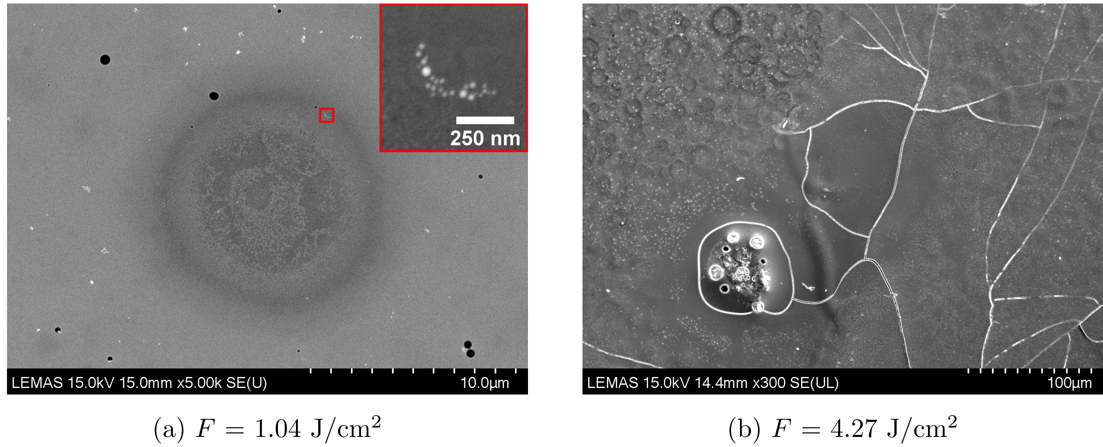

(a) $F = 1.04$ J/cm^2 (b) $F = 4.27$ J/cm^2

Figure 7.13: SEM images of heated depositions at two laser fluences on Si substrates. Inset in (a) shows a higher magnification image of gold nanoparticle clusters. Note that the black spots seen in (a) are not physical and are due to charging effects.

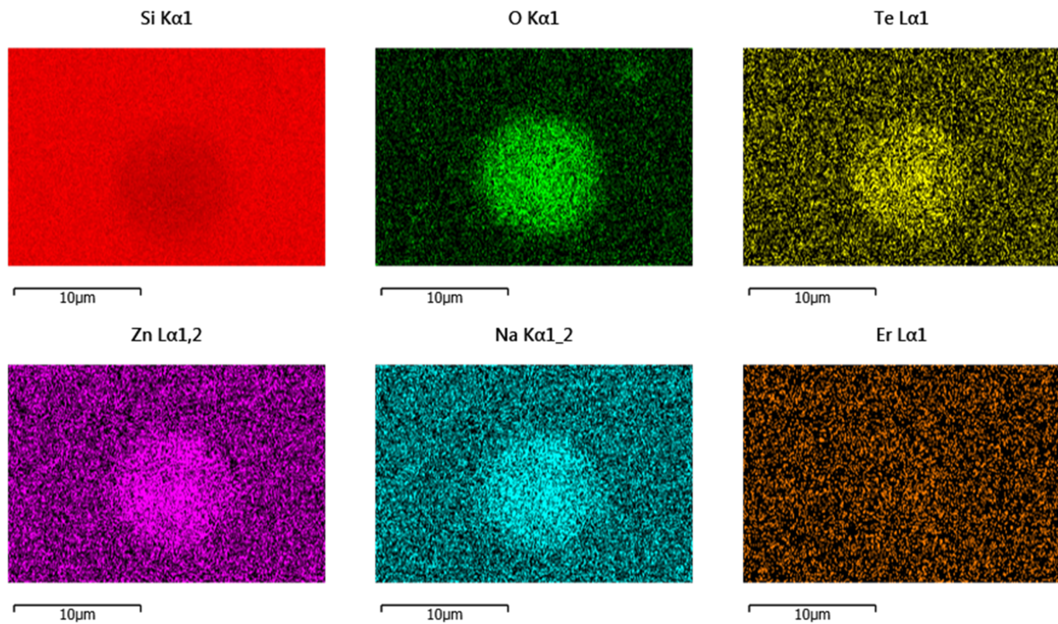

Figure 7.14: EDX images of heated depositions at $F = 1.04$ J/cm^2 on Si substrate corresponding to the SEM image in fig. 7.13(a). The spots on the target surface are droplets of target glass that have not evaporated.

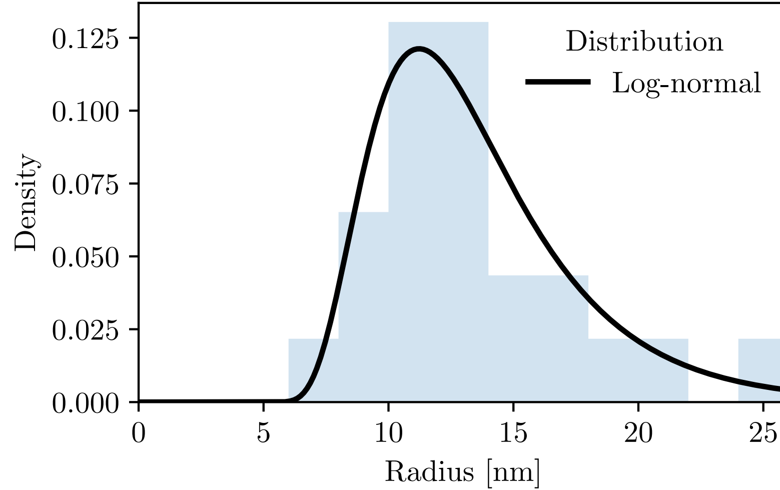

Figure 7.15: The size distribution of the 23 Au clusters shown in the inset of fig. 7.13(a) fitted with a log-normal distribution of mean 13.6 nm and standard deviation of 4.3 nm.

reduce to quantum efficiency of the Er^{3+} ions further reducing the collected intensity (see chapter 6). PL spectra shown in fig. 7.18(a) was similar for all of the samples and the room temperature post heat treated samples in section 7.4.1. The main peak was at 1536 nm for all the samples and the second lower intensity peak at 1543 nm decreased from 84 % to 75 % with an increase in laser fluence of 1.56 to 4.27 J/cm^2. The spectra FWHM is given in table 7.2. The F = 4.27 J/cm^2 sample had the narrowest FWHM of 21.2 nm. With a decreasing F, the FWHM increased slightly to 23.4 nm at 1.56 J/cm^2.

The average PL lifetime of the samples increases with laser fluence, as shown in fig. 7.18(b) and reported in table 7.2. The decays are composed of up to three lifetimes; a short sub-microsecond lifetime attributed to ion clustering, an intermediate ∼3 ms lifetime attributed to ions in a tellurite host and a long ∼7.5 ms lifetime that is attributed to ions in a silicate. The F = 2.08 J/cm^2 sample contained all three lifetimes, while the F = 1.56 J/cm^2 sample did not have the silicate lifetime and the F = 4.27 J/cm^2 sample did not have the shortest component. The lack of sub-microsecond lifetime in the high fluence sample is likely due it's relative intensity being very low. A decrease in intensity of the peak in the PL spectra at 1543 nm may therefore be

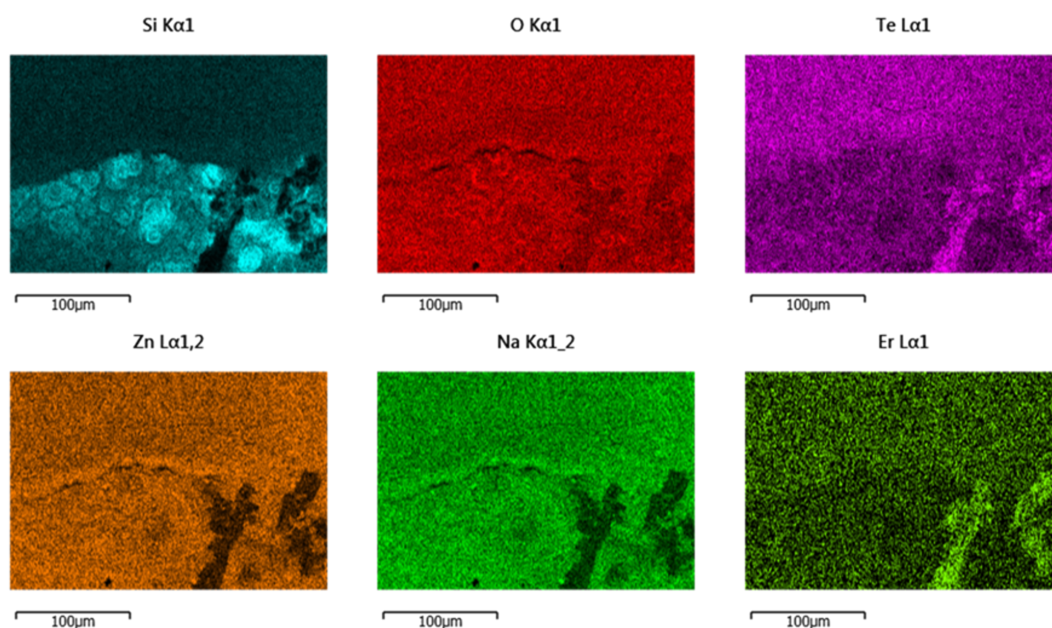

Figure 7.16: EDX images of the transition between the ring structured and the smooth cracked film in the heated deposition at $F = 4.27$ J/cm^2 on Si substrate in fig. 7.13(b).

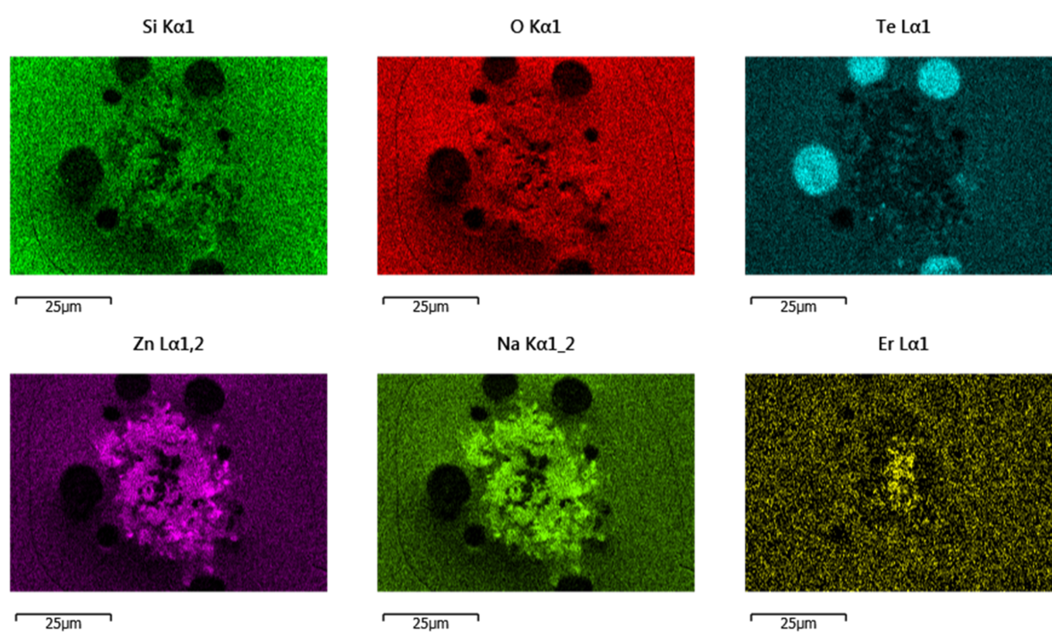

Figure 7.17: EDX images of the feature surrounded by a circular crack in the heated deposition at $F = 4.27$ J/cm^2 on Si substrate in fig. 7.13(b).

attributed Stark level shifts from a tellurite to a silicate environment and is therefore a better indicator of the Er^{3+} ion environment than the intensity of the tellurite sidebands.

Table 7.2: Photoluminescence properties of the films on Si substrates.

F [J/cm^2]	$\tau^{\dagger}$[ms]	FWHM [nm]
1.56	2.91 ± 0.04 (79 %), 0.59 ± 0.23 (21 %)	23.4
2.08	7.45 ± 0.30 (67 %), 3.23 ± 0.28 (31 %), 0.52 ± 0.08 (2 %)	22.1
4.27	7.48 ± 0.66 (89 %), 2.24 ± 0.10 (11 %)	21.2

† PL decays with multiple lifetimes have the relative intensity in brackets for each lifetime

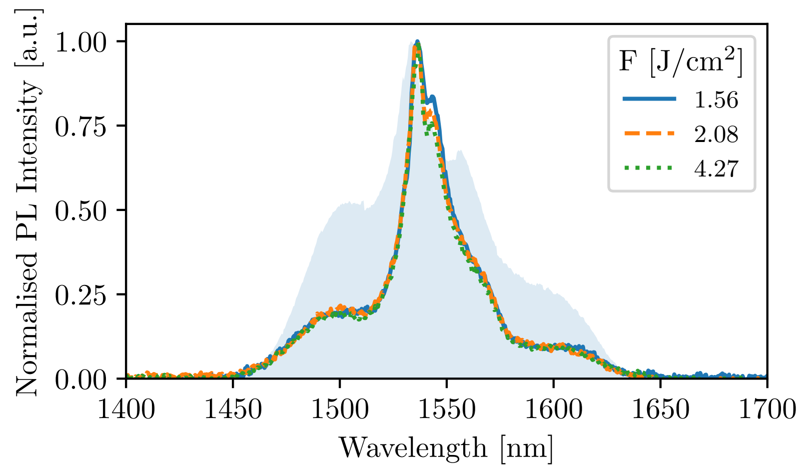

(a)

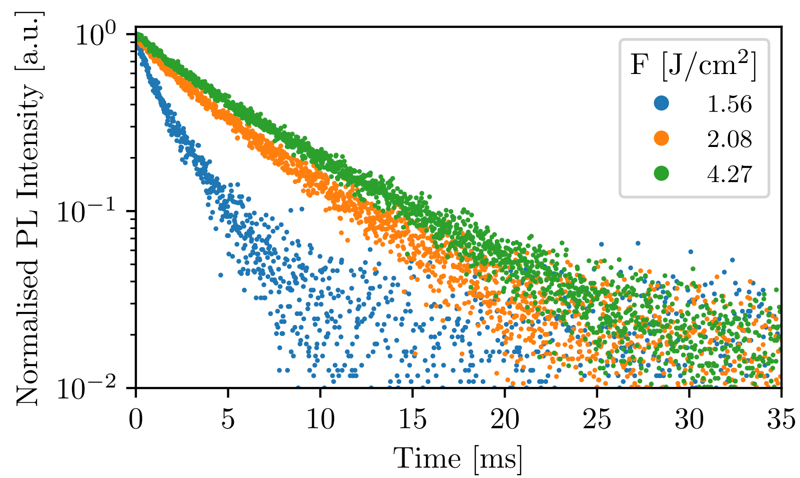

(b)

Figure 7.18: Photoluminescence (a) spectra and (b) decay of the films on Si substrates. Light blue shaded region in (a) shows the spectra of the 1ErTZN target glass, which had a FWHM of 68.0 nm, for reference.

SOS Substrates

Optical microscopy images of the samples are presented in fig. 7.19. The $F = 1.54$ J/cm^2 sample had a smooth mottled surface. The 2.08 J/cm^2 sample had a profile composed of ~ 10 μm diameter mounds, while the $F = 4.27$ J/cm^2 sample had numerous cracks and had regions that had a similar mound-like profile but also regions that were relatively smooth. At the origin of the cracks, the peeling of the top layer of glass can be seen. Cracks did not pass through these mounded regions and were only present in the smooth regions. As the tensile stress, caused by the mismatch in coefficient of thermal expansion between the film and the substrate, builds, the surface gains a mound-like surface profile and upon release of this tension through cracking during the cooling, the surface assumes a smooth profile once again. As the film is the thickest and densest at a deposition of 4.27 J/cm^2, the tensile stresses are expected to be the greatest, which is why cracking is only seen for this film.

Figure 7.20 shows SEM images at two magnifications of a crack origin on the $F =$ 4.27 J/cm^2 sample. The inset in fig. 7.20(a) identifies an island of Au clusters, as was also observed for the Si substrate. The size distribution of the 4800 clusters in this image was well described by a log-normal distribution with a mean of 72.4 nm and a standard deviation of 31.1 nm, as shown in fig. 7.21. The increase in cluster size is due to the greater volume of material that was deposited and hence a greater number of impurity atoms. Apart from the Au islands, large $\sim$10 μm diameter hemispheres are observed on the film surface, which may be due to droplets at this laser fluence. An EDX map of the crack origin in fig. 7.20(b) is shown in fig. 7.22. Firstly, another Au island is observed near the crack. The elements Zn, Na and O appeared to be well dispersed and the weak signal from Er (not shown) was featureless. Surrounding the defect, Te clusters or crystals can be observed and inside the crack the Si signal was strong. The latter may be a result of the entire 10 μm silica layer peeling off in the cracking process. It seems likely that the Te crystals provided the defect origin for the crack to initiate.

PL measurements are shown in fig. 7.23 and presented in table 7.3. The two lowest fluence samples had mono-exponential decays of $\sim$9 ms and narrow FWHMs of $\sim$21 nm. This indicates a good dissolution between the silica layer and the deposited material. The highest fluence sample had a double exponential decay, with a shorter lifetime

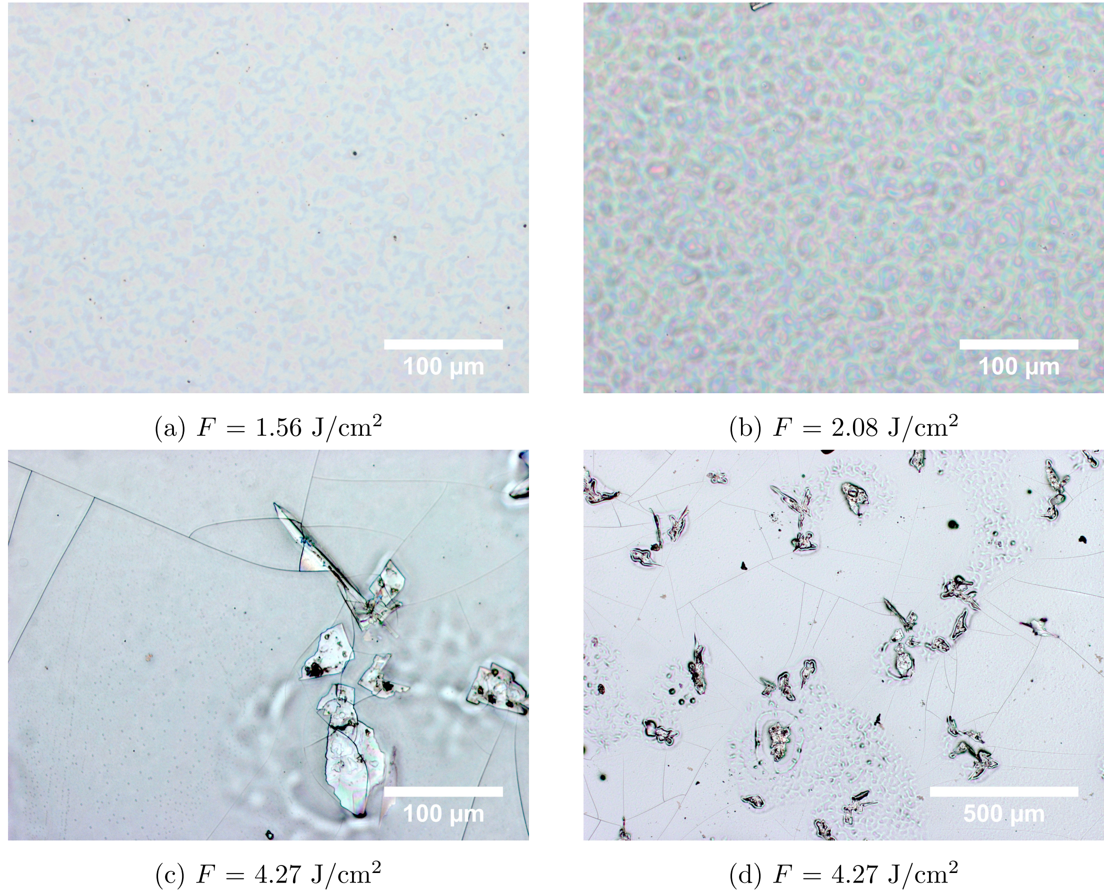

(a) $F = 1.56$ J/cm^2 (b) $F = 2.08$ J/cm^2

(c) $F = 4.27$ J/cm^2 (d) $F = 4.27$ J/cm^2

Figure 7.19: Optical microscopy images of films on SOS substrates. Cracking occurs only for the highest fluence due to the increase in film thickness and density. Images (c) and (d) are the same sample but at different magnifications.

component of 2.6 ms. The decrease in the long lifetime with laser fluence is a result of an increase in volume of deposited material giving a higher density film. Thus, the closer average Er-Er distance increases concentration quenching effects and acts to reduce the measured lifetime [163]. The shorter second lifetime for the high fluence sample is expected for Er^{3+} in tellurite host and is due to an incomplete dissolution of the large volume of deposited material and the silica layer. The PL spectra also shows an increase in the tellurite side bands of the ablated target glass resulting in the larger FWHM and confirms this conclusion.

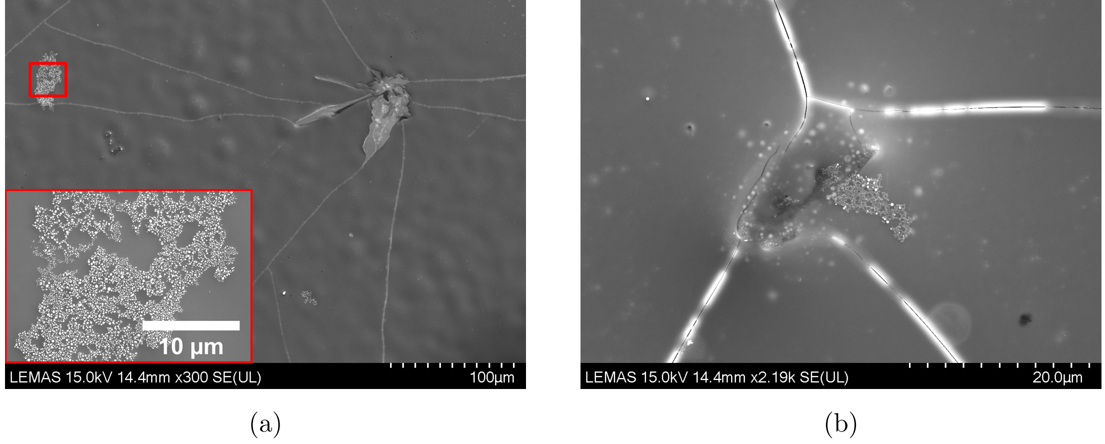

(a) (b)

Figure 7.20: SEM images of films fabricated at $F = 4.27$ J/cm^2 on SOS substrates. Inset in (a) shows a higher magnification of one of the islands of Au clusters. The cracking occurred upon cooling due to the the high thickness of the film an the mismatch in CTE and the substrate.

Table 7.3: Photoluminescence properties of films fabricated on SOS substrates.

F [J/cm^2]	$\tau^\dagger$ [ms]	FWHM [nm]
1.56	9.41 ± 0.02	20.7
2.08	8.63 ± 0.01	21.2
4.27	7.28 ± 0.02 (94 %), 2.60 ± 0.10 (6 %)	29.7

† PL decays with multiple lifetimes have the relative intensity in brackets for each lifetime

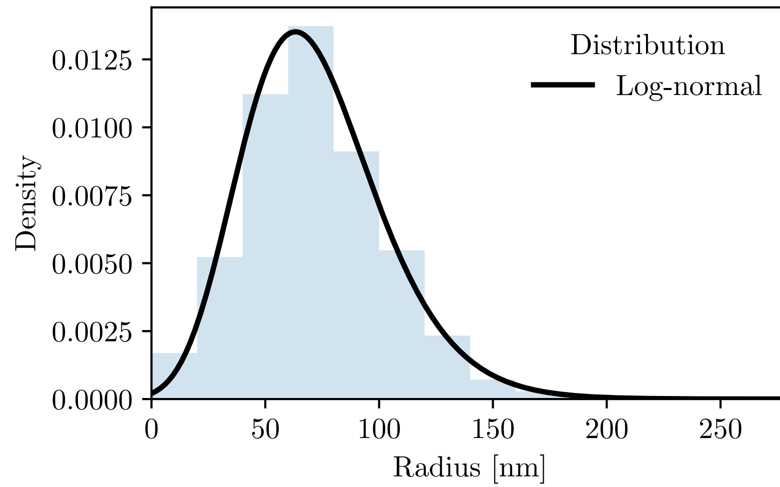

Figure 7.21: The size distribution of the Au clusters shown in the inset of fig. 7.20(a) fitted with a log-normal distribution of mean 72.4 nm and standard deviation of 31.1 nm.

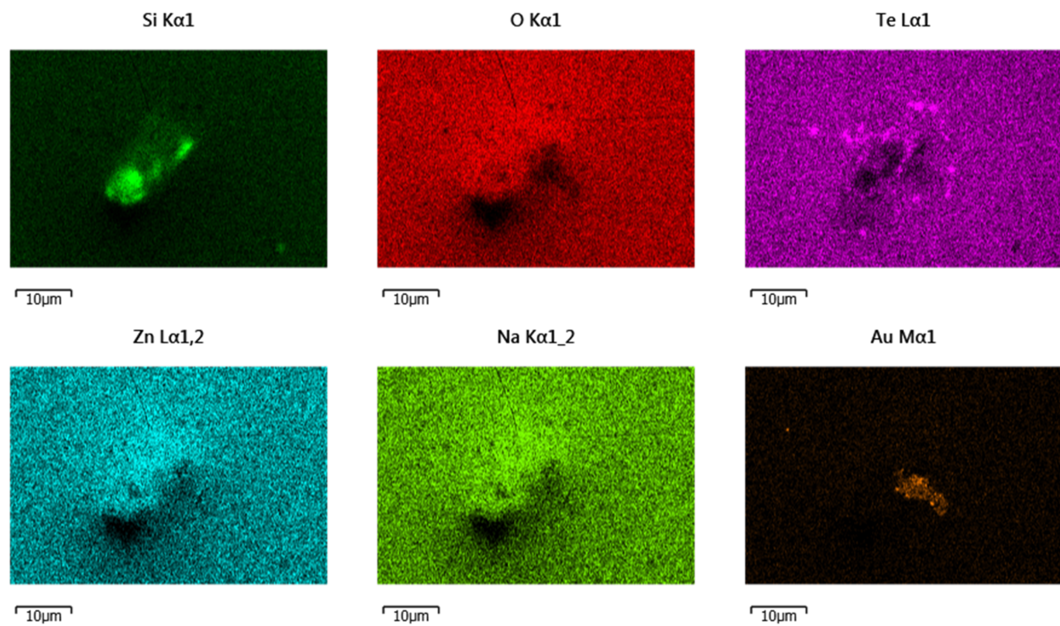

Figure 7.22: EDX images of a film fabricated at F = 4.27 J/cm^2 on SOS substrates, corresponding to the SEM image in fig. 7.20(b). Note that the Er signal is not shown due to low signal to noise.

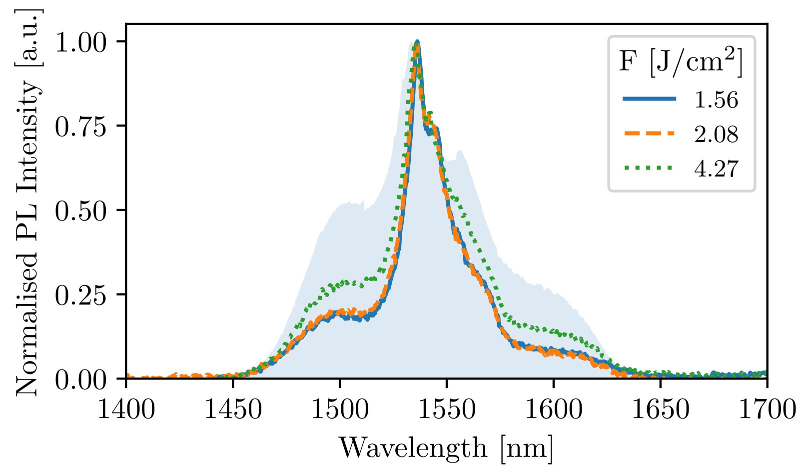

(a)

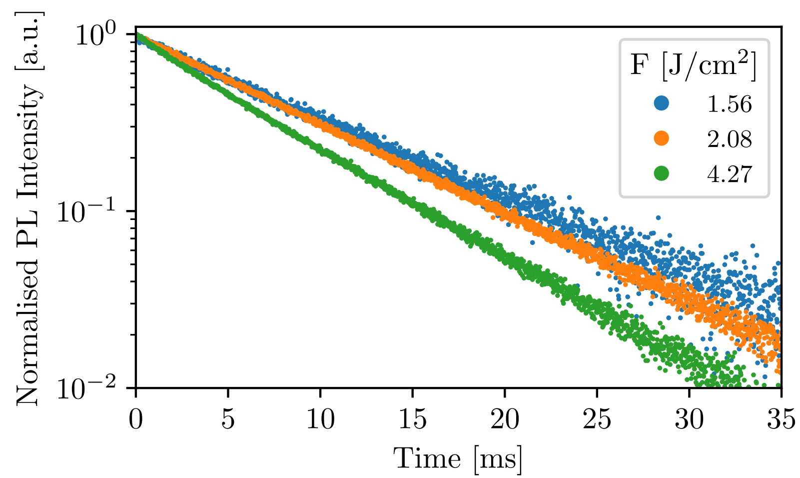

(b)

Figure 7.23: Photoluminescence (a) spectra and (b) decay of films fabricated on SOS substrates. Light blue shaded region in (a) shows the spectra of the 1ErTZN target glass, which had a FWHM of 68.0 nm, for reference.

SiO_2 Substrates

The surface of the SiO_2 substrate samples was highly dependent on the laser fluence, as shown in the optical microscopy images in fig. 7.24. At 1.04 J/cm^2, black spots were observed on what appears to be a pristine silica substrate. This is similar to what was observed for the Si substrate in fig. 7.12(a). An SEM image of one of the spots is shown in fig. 7.25 and the corresponding EDX map for the region is shown in fig. 7.26. As was the case with the Si substrate, the spot is composed of Te, Zn and Na and again likely results from the deposition of a droplet.

With a slight increase in fluence to 1.56 J/cm^2, a reduction in black spot density and a mottled interference pattern due to variations in density and film thickness was observed. Despite this, the surface appeared smooth. Cracks were first observed for the sample fabricated at 2.08 J/cm^2 and interference patterns can be seen from under the crack where the thin film has peeled off the substrate. Cracking occurred at a lower fluence compared with the Si and SOS substrates in fig. 7.19 and is due to the reduced dissolution rate resulting in a higher density film and the lower CTE for SiO_2. At the highest fluence of 4.27 J/cm^2 the surface was rough, corresponding to the cloudy undissolved tellurite glass deposited film observed in fig. 7.11(k).

The PL spectra and lifetime is shown in fig. 7.27 and reported in table 7.4. The PL intensity from the lowest $F = 1.04$ J/cm^2 sample was too low to be characterised. An increase in laser fluence resulted in a broadened spectra accompanied by a blue-shift in peak wavelength from 1.536 μm to 1.533 μm to 1.532 μm. This indicates that dissolution with the SiO_2 did not occur for the majority of deposited material for laser fluences above 1.56 J/cm^2.

The PL lifetime confirmed this conclusion as a long lifetime characteristic of Er^{3+} in a silicate was only observed for the 1.56 J/cm^2 sample. Thus a mixing between the deposited tellurite glass and the silica substrate only occurred for this sample. A complete mixing is not achieved as evidenced by the shorter $\sim$3.5 ms tellurite lifetime component in the double exponential decay. As noted in table 7.4, the edge of the 2.08 J/cm^2 sample that appeared partially clear in fig. 7.11(h) had a longer component lifetime. The hotter temperatures at the edges of the film due to conductive heating from the substrate holder result in an improved dissolution rate.

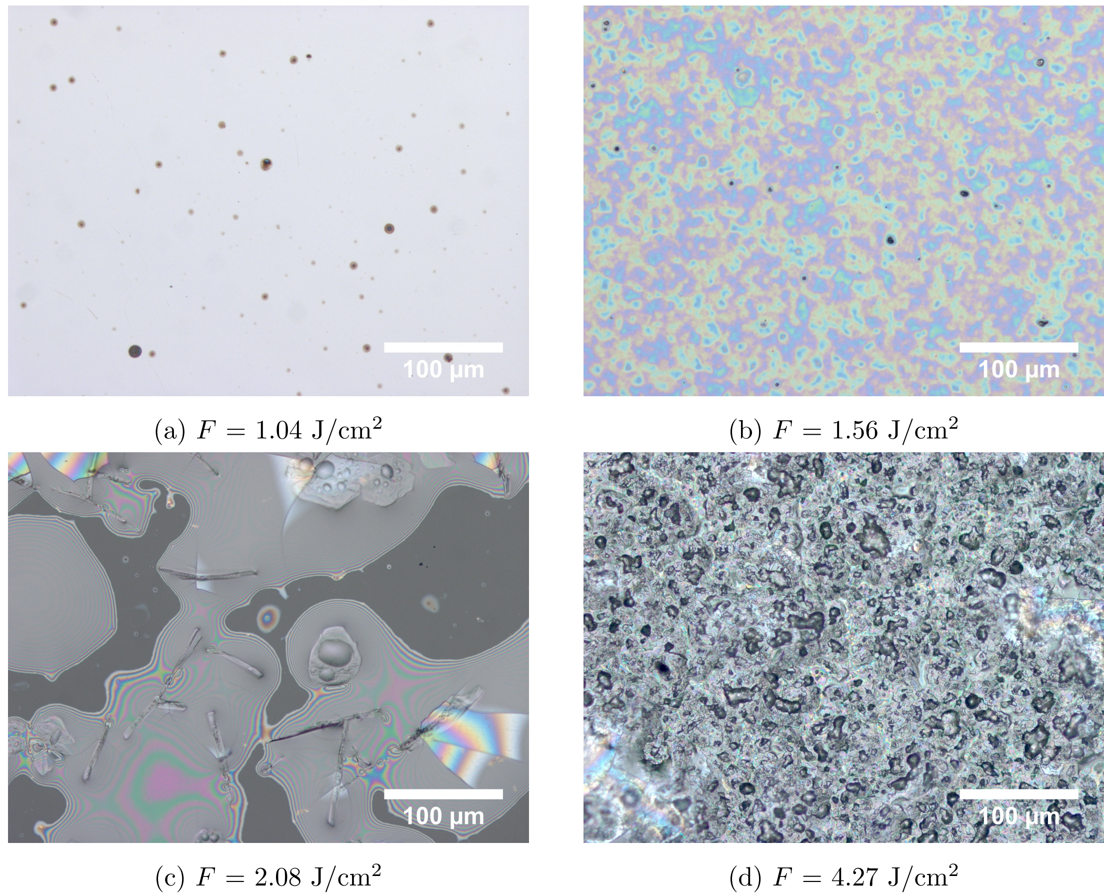

(a) F = 1.04 J/cm^2 (b) F = 1.56 J/cm^2

(c) F = 2.08 J/cm^2 (d) F = 4.27 J/cm^2

Figure 7.24: Optical microscopy images of films fabricated on SiO_2 substrates at different laser fluences.

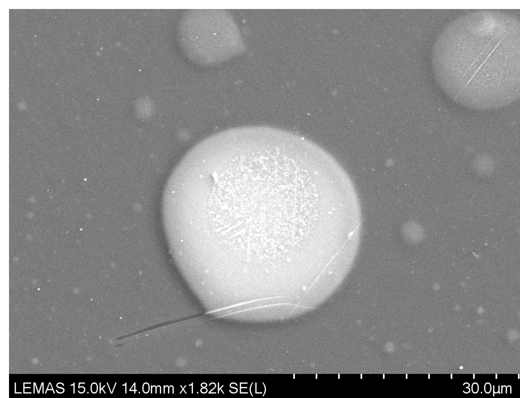

Figure 7.25: SEM image of a droplet on a film fabricated at F = 1.04 J/cm^2 on SiO_2 substrate. Droplets appear as dark spots in the optical microscopy images in fig. 7.24(a).

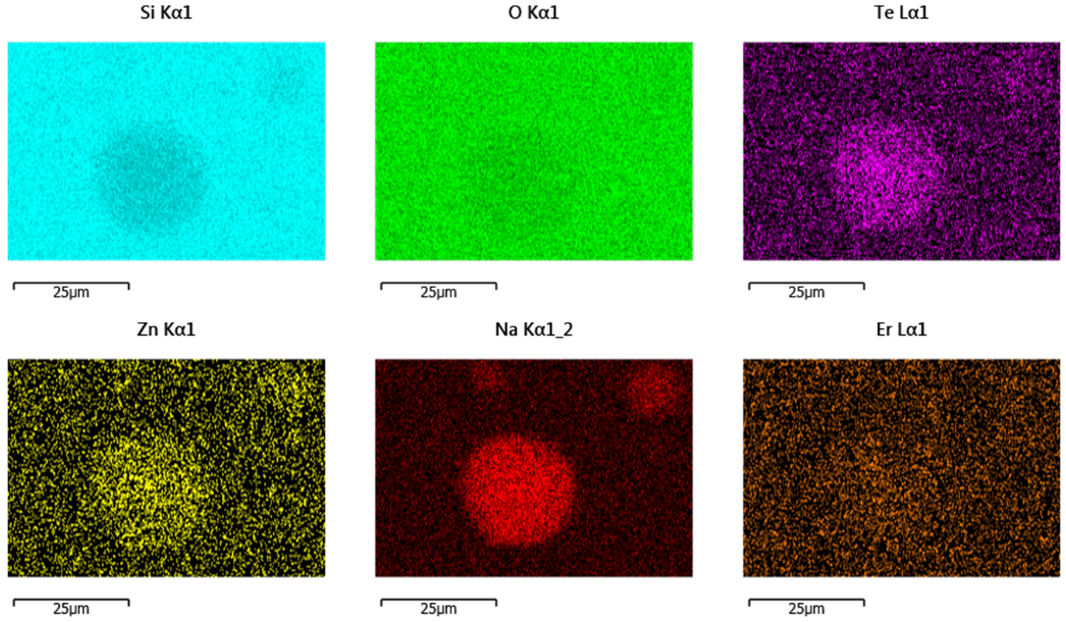

Figure 7.26: EDX images of a droplet on a film fabricated at $F = 1.04$ J/cm^2 on a SiO_2 substrate. The region corresponds to the SEM image in fig. 7.25.

Table 7.4: Photoluminescence properties of films fabricated on SiO_2 substrates at different laser fluences.

F [J/cm^2]	$\tau^{\dagger}$ [ms]	FWHM [nm]
1.56	7.37 ± 0.63 (66 %), 3.43 ± 0.39 (34 %)	23.9
2.08	3.91 ± 0.02*	33.3
4.27	4.90 ± 0.02	36.0

† PL decays with multiple lifetimes have the relative intensity in brackets for each lifetime

* Measurement taken from centre of the sample. The edge of the sample, which appeared clearer, had a longer ∼ 6.60 ms lifetime decay

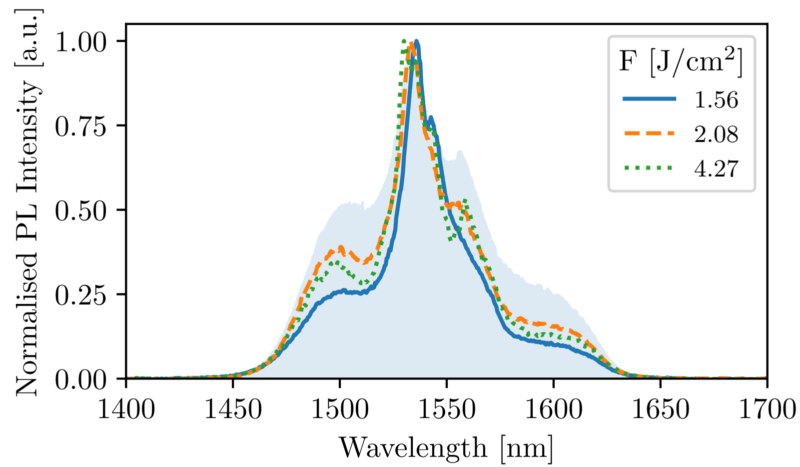

(a)

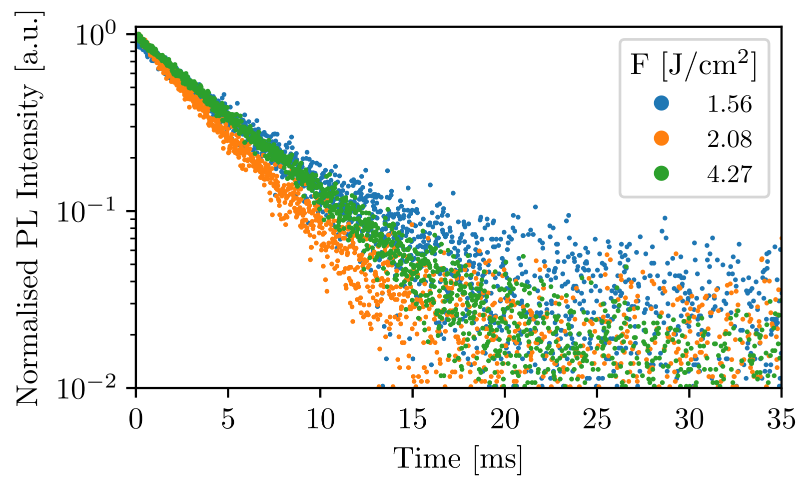

(b)

Figure 7.27: Photoluminescence (a) spectra and (b) decay of films fabricated on SiO_2 substrates at different laser fluences. Light blue shaded region in (a) shows the spectra of the 1ErTZN target glass for reference.

Optimum fluence

The results presented so far have shown that thin films fabricated with lower laser fluences in general produced a better film quality (smooth surface, homogeneity, transparent, no cracking). The frequency of droplets can be eliminated at low laser fluences (see chapter 6), which is desired for thin film homogeneity and critical for films on the 100 nm scale. During the dynamic process of film formation through dissolution with the ULPD technique, a competition between material deposition and evaporation occurs at the substrate. This is evidenced by a very low Te content in the hybrid tellurite-silica films relative to the target [6]. Practically, this means that a minimum threshold rate for material deposition must be surpassed before any film formation can occur. Samples fabricated at $F = 1.04$ J/cm^2 were spotted and did not have a film on the surface. The deposition rate was too low such that nanoparticles evaporated off the substrate surface and only the disperse droplets remained. It was shown in chapter 6 that material deposition at low fluences occurs primarily in the form of nanoparticles and therefore the ideal solution would be to ablate with a laser fluence just above threshold and increase the laser repetition rate until a suitable volume of material is ablated. Increasing the laser repetition rate to the maximum (manufacturer specified) 10 kHz was not possible during the work in this thesis due to insufficient cooling in the laser cryostat. For the SOS and SiO_2 substrates, improved PL properties (narrow PL spectra, long PL lifetime with minimal numbers of decays) were also shown at lower laser fluences owing to the lower volume of deposited material per unit time which ensures that the dissolution rate with the silica in the substrate is not surpassed. Taking all of these factors into account, it was therefore decided that the optimum laser fluence for hybrid tellurite-silica thin film formation at a fixed laser repetition of 1 kHz was the second highest laser fluence tested, $F = 1.56$ J/cm^2 ($E_\mathrm{p} = 98$ μJ).

AFM measurements on 100 by 100 μm squares for each of the samples are shown in fig. 7.28 and reported in table 7.5. The surface morphology of each substrate is quite different. The film on the Si substrate was cauliflower-like and the roughest of the three with $R_a = 38.7$ nm. The SOS substrate was the smoothest with $R_a = 16.1$ nm and consisted of numerous ring-like structures. The SiO_2 substrate had a web-like surface profile and a slightly higher surface roughness of $R_a = 22$ nm. The lower surface

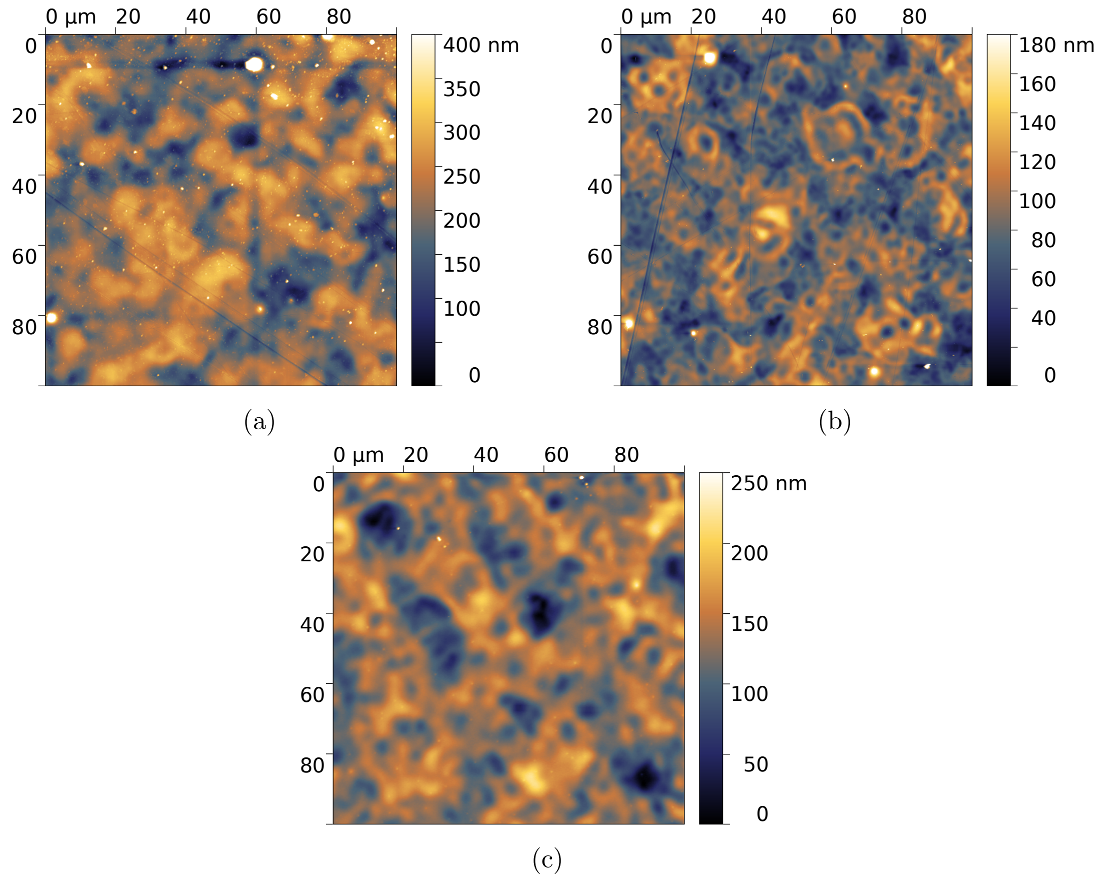

Figure 7.28: AFM images of films fabricated at $F = 1.56$ J/cm^2 on (a) Si, (b) SOS and (c) SiO_2 substrates.

roughness of the SOS substrate compared to the SiO_2 substrate is due to an improved dissolution of deposited material.

Figure 7.29 shows a backscattered electron (BSE) cross-section SEM image for each of the substrates. Heavier elements have an increased chance of scattering electrons causing an increase in average backscattered electron flux and thus an intensity contrast on the image. Differences in contrast of each layer resulting from a variation in material densities are clearly seen in each micrograph. The increased density of the film is a result of the target glass having heavier elements, such as Te and Er. The slight variation in intensity seen on the substrates below the films are a result of the plasma ion beam polishing and was confirmed through EDX mapping. Clustering of heavy elements is only observed in the film on the Si substrate. It is likely that these

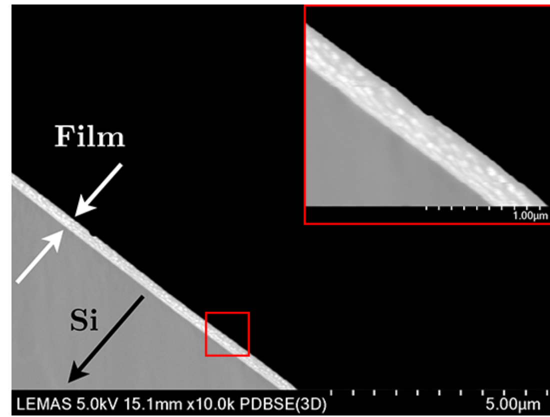

(a)

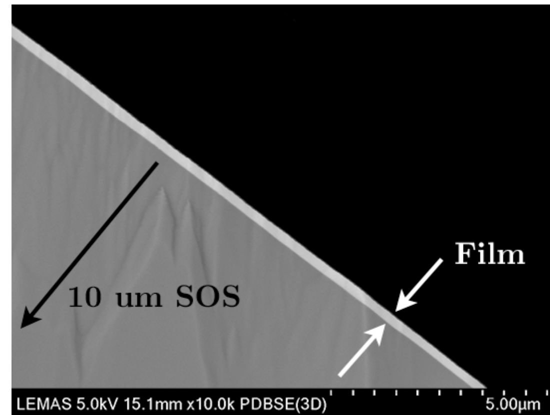

(b)

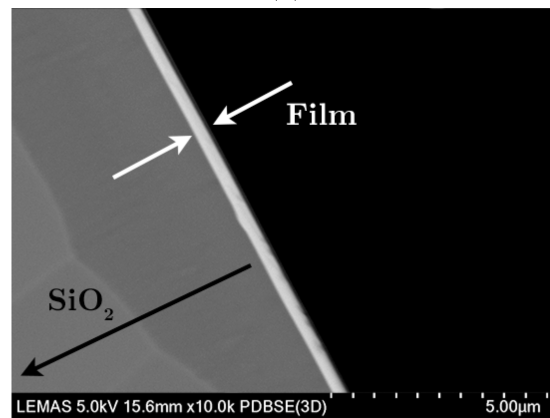

(c)

Figure 7.29: Backscattered electron SEM cross-sectional images of films fabricated at $F = 1.56$ J/cm^2 on Si, SOS and SiO_2 substrates. The features seen in the substrates are due to slight variations in the polish. Inset in (a) shows a higher resolution image of the crystalline structures.

Table 7.5: Physical and optical properties for thin films fabricated at $F = 1.56$ J/cm^2 on Si, SOS and SiO_2 substrates.

	Substrate		
	Si	SOS	SiO_2
$d^{\ddagger}$ [nm]	258 ± 26	243 ± 51	298 ± 38
$R_a{}^*$ [nm]	38.7 (2.0)	16.1 (3.7)	22.1 (6.9)
$R_{\mathrm{RMS}}{}^*$ [nm]	55.5 (4.8)	21.3 (10.5)	29.1 (15.4)
$\tau^{\dagger}$ [ms]	2.91 ± 0.04 (79 %), 0.59 ± 0.23 (21 %)	9.41 ± 0.02	7.37 ± 0.63 (66 %), 3.43 ± 0.39 (34 %)
FWHM [nm]	23.4	20.7	23.9

‡ Cross-sectonal backscattered electron detector SEM measurements. Error represents the 99 % confidence interval

* Measured on a 100 by 100 μm square. Bracketed values are for the pristine substrate.

† PL decays with multiple lifetimes have the relative intensity in brackets for each lifetime

are crystalline Te, which has been observed at the interface of SOS films processed at 570°C when the silica layer becomes saturated with the deposited material by [163]. The crystalline structures act to increase the surface roughness of the film. Due to the focal volume of EDX (typically a 1 μm spot) and the small thickness (~250 nm) of the films, an accurate line scan or spot identification was not possible to identify the film composition. Transmission electron microscopy or Rutherford backscattering spectrometry would be required for an accurate film compositional analysis. The thickness of each film for the three substrates is reported in table 7.5. The thicknesses of the Si based substrates were around 250 nm and lower than the SiO_2 substrate which was 298 nm. The increase in thickness for the SiO_2 is explained by the lower surface temperature, which results in a reduced evaporation of deposited material.

The film thickness and refractive index was measured with ellipsometry. An acceptable model could only be achieved for the SiO_2 as the Si substrate had crystalline structures and the SOS substrate had a silica layer much larger than the film resulting in high uncertainties. A detailed description of the fitting procedure, optical model and fit to the raw data is found in appendix E.3.1. The optically transparent layer

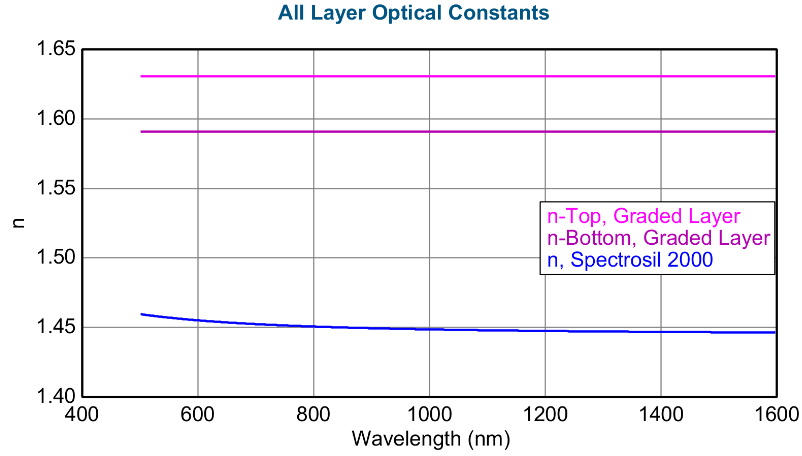

Figure 7.30: Optical model fitted to the ellipsometry data for the thin film fabricated at $F = 1.56$ J/cm^2 on SiO_2 (Spectrosil 2000). The transparent film has a slight linear index grading resulting from the dissolution process during film formation. The raw data is given in appendix E.3.1.

had a wavelength independent refractive index of 1.611 and an index grading of 8.02 % (between 500 nm and 1600 nm), as shown in fig. 7.30 and reported in table 7.6. The film thickness and surface roughness was 297 nm and 13 nm, respectively, which are both in excellent agreement with the cross-sectional SEM and AFM measurements. The low index grading of the film shows that there is a sharp interface between the modified layer and the pristine substrate. The higher refractive index of the hybrid tellurite-silica film compared to the pristine silica substrate (11% or a step in index of 0.137) is due to the heavier elements from the ablated target and results in a well defined layer.

In chapter 6 it was shown that a 500 ± 200 nm thickness film was deposited after the application of 180 k pulses/cm^2 at $F = 1.25$ J/cm^2. An estimation of the film thickness deposited here, where 1,200 k pulses were applied at 1.56 J/cm^2, gives ∼3.3 μm. At most, the film thickness at the elevated processing temperature of 600°C was 10 % of this value (300 nm). Evaporation of the deposited material at the film surface after heating was shown earlier in this chapter and must account for this difference. The entire deposition took 104 minutes and an extra 30 minutes of post stabilisation time. It is therefore concluded that around 20 nm/minute is evaporated off the surface during processing and this therefore represents the minimum deposition rate for film

Table 7.6: Physical and optical properties of the $F = 1.56$ J/cm^2 film on Spectrosil 2000 measured via ellipsometry. MSE is the mean square error of the fit, % Inhomogeneity is the linear refractive index grading from top to bottom of the film assuming a mixing with the substrate index $n_{\text{substrate}}$, n is the average film refractive index, the difference in refractive index from top to bottom of the film $\Delta n = n_{\text{top}} - n_{\text{bottom}}$ and the roughness assumes a 50% volume fraction.

Parameter	Value
MSE	4.935
Roughness [nm]	13.1
d [nm]	297
A	1.611
% Inhomogeneity	8.02
n_{top}	1.631
n_{bottom}	1.591
$n_{\text{substrate}}$ @ 633 nm	1.454
Δn	0.04

formation. Such a large evaporation rate is not surprising as the Te concentration is typically 26 % in the target (chapter 6) and typically <3 at.% in the hybrid tellurite-silica film [6]. A 90% reduction in Te content is ocnsistent with the reduction in film through the application of heat during the deposition (3.3 μm to 300 nm). The film growth rate on Si based substrates was ~2.48 nm/minute and for SiO_2 substrates was ~2.87 nm/minute. A definition of the dissolution rate as the upper rate of film growth before the PL lifetime becomes a double exponential (i.e. the ions in the film are no longer homogeneously dispersed) with explicit temperature dependence should be evaluated in future work.

The PL spectra and lifetime of the different substrates are shown in fig. 7.31 and reported in table 7.5. The main peak for all the samples was at 1.536 μm. The lower tellurite side-band was higher in intensity for the SiO_2 substrate compared to the other substrates (26 % compared to 19 %), while the 1.543 μm peak was stronger in the Si substrate compared to the other substrates (84 % compared to 78 % in SiO_2 and 73 % in SOS) and is attributed to the unresolved emission line of crystalline Te. The lifetime of the Si substrate was the shortest reflecting that of the tellurite target, as the tellurite

corrosion of the Si substrate was not sufficient to form a hybrid tellurite-silica. The SOS substrate had the longest lifetime at 9.41 ms and was the only sample that had a single exponential decay. The reduced lifetime of the SiO_2 and second shorter exponential, giving an average lifetime of 6.03 ms, is due to the reduced dissolution enhancing the concentration quenching effects, similar to the observations in PL lifetime with increasing laser fluence in SOS substrate.

The thin nature of the films results in enhancement of the local density of states (LDoS) and the spontaneous emission rate. Simulations were performed using a quantum-electrodynamical formalism suited to the analysis of the radiative SE rate in multilayer dielectric structures (model is described in chapter 2) [36]. Using the physical and (average no index grading) optical parameters measured for the film formed on the silica substrate in table 7.6, the radiative SE rates normalised to the free space value (Purcell factor F_p) for a dipole emitting at $\lambda = 1.54$ μm as a function of position is shown in fig. 7.32. The film structure did not support any guiding modes. The decay rates for dipoles orientated perpendicular $\perp$, parallel $\parallel$ and randomly Avg $= (2/3) \parallel + (1/3) \perp$ are shown. For Er^{3+} ions the randomly orientated dipole decay rate is relevant. The average $F_p = 1.31$ corresponds to the experimentally measured decay lifetime of the ensemble average of ions approximated at all positions within the film. While the SE emission of within the film is enhanced relative to the free space value, i.e. $F_p > 1$, the SE rate is suppressed compared to a homogeneous dielectric media, i.e. $F_p = n = 1.611$. For thicker films that support waveguiding modes, the SE rate would be even higher than for a bulk media.

As a final point of note, improvements to the optical properties of the film can not be achieved through post heat treatment of the meta-stable film as the growth of crystalline phases occurs when there is no driving to the mixing by the deposition of new material [130]. The results of a high temperature post-fabrication anneal is shown in appendix F and improvements to the film quality may only be achieved through heating the substrate to higher temperatures during processing to improve the dissolution rate.

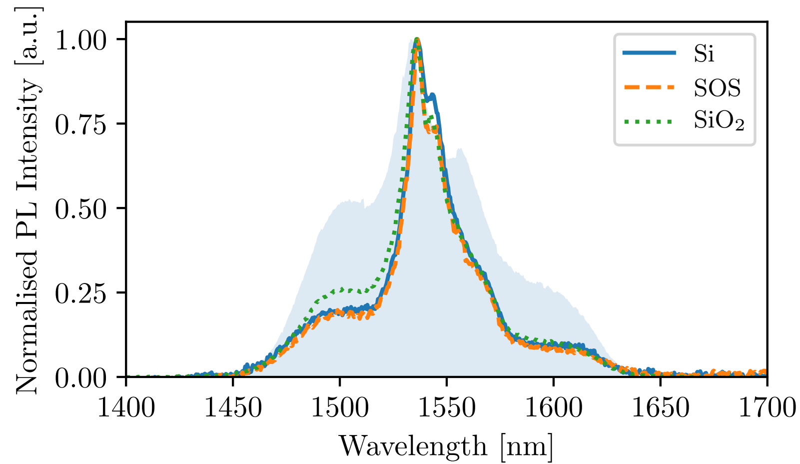

(a)

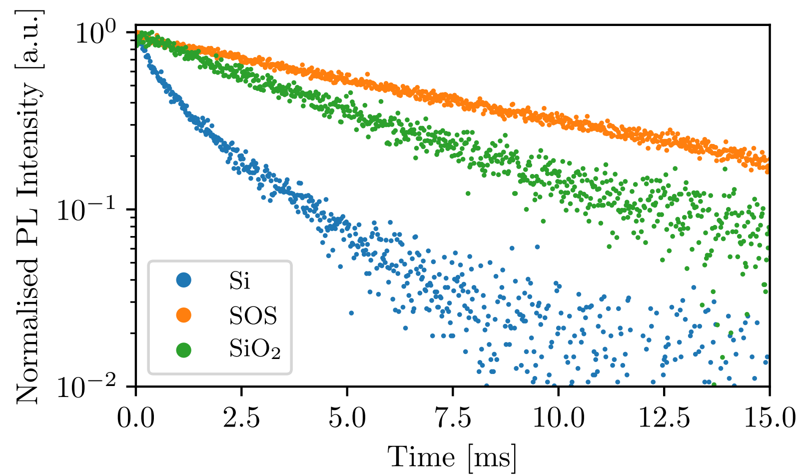

(b)

Figure 7.31: Photoluminescence (a) spectra and (b) decay of films fabricated at 1.56 J/cm^2 on various substrates; Silicon (Si), fused silica (SiO_2) and 10 μm silica-on-silicon. Light blue shaded region in (a) shows the spectra of the 1ErTZN target glass for reference.

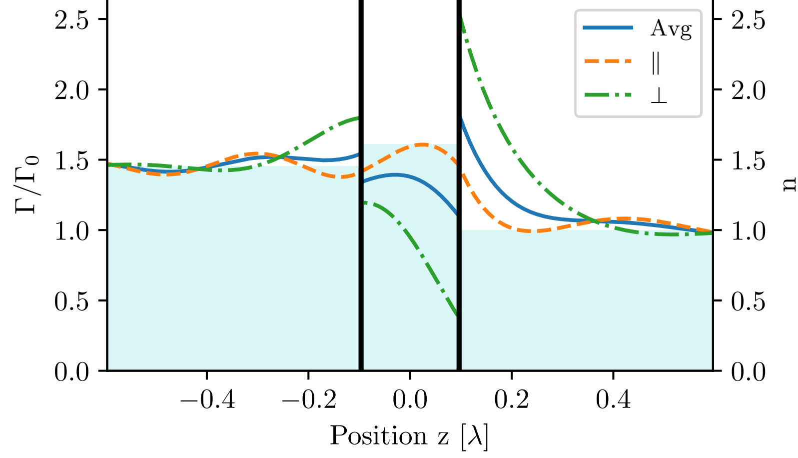

Figure 7.32: The radiative decay rate of perpendicular $\perp$, parallel $\parallel$ and randomly Avg $= (2/3) \parallel + (1/3) \perp$ orientated dipole compared to the free space decay rate at $\lambda =$ 1540 nm as a function of position in a multilayer structure; SiO_2 substrate at $z \to -\infty$, hybrid tellurite-silica film of ($n = 1.611$, $d = 297$ nm), air superstrate at $z \to \infty$. The parameters are the same as measured in table 7.6. Light blue shaded regions indicate the refractive index of each layer and vertical black lines indicate the boundaries of the layers. The average purcell factor $F_p = \Gamma/\Gamma_0$ within the film was 1.31.

7.4.3 Oxygen atmosphere depositions

Oxygen was introduced into the atmosphere and the processing temperature T was increased from 600°C to 700°C. The aim was to increase T while avoiding melting of the target, which would lead to non-steady state ablation due to surface modification (amongst other undesirable effects such as reaction with the metal holder, the formation of bubbles that rise from under the glass to the top, the potential evaporation of Te and warping of the surfaces at the edge). Photographs of the target surface after the standard preparation with SiC 320P grit sandpaper prior to processing and after the fabrication of a thin film at 600°C in vacuum are shown in fig. 7.33(a) and (b), respectively. After processing the samples at 600 and 650°C in the oxygen atmosphere, the target surface had the similar matt appearance as in fig. 7.33(b). About an hour into processing of the 700°C sample the surface could be seen to slowly start melting and the ablation plume decreased from being barely visible to invisible. A photograph of the target post processing is shown in fig. 7.33(c), in which it can be seen that the

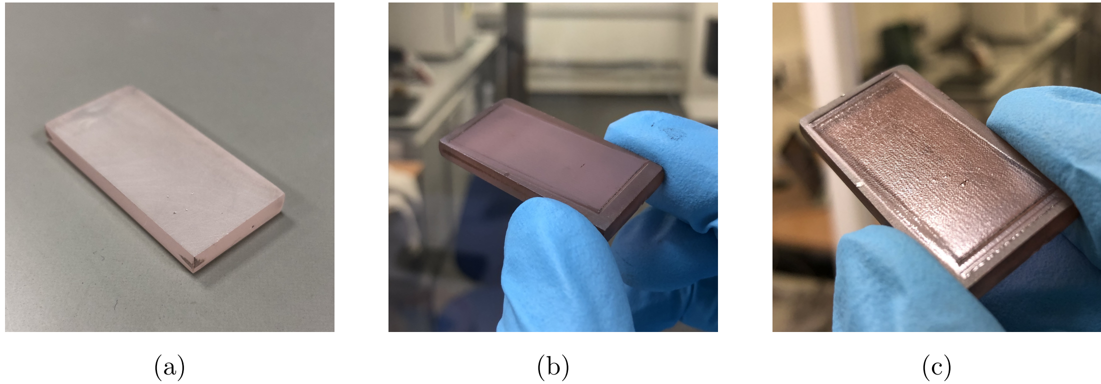

(a) (b) (c)

Figure 7.33: Photographs of the Er^{3+}-doped target at various stages of processing; (a) Polished with P320 SiC paper prior to processing, (b) post processing with F = 1.56 J/cm^2 at 600°C in vacuum and (c) post processing with F = 1.56 J/cm^2 at 700°C in an O_2 atmosphere of 100 mTorr. In (b) and (c), the laser raster area on the target can be seen, however the increased heating in (c) causes the target surface to melt and become shiny (i.e. smoother).

melting has caused the surface to gain some reflectively resulting in the increase in ablation threshold. The addition of the oxygen atmosphere therefore only allowed an additional 50°C of temperature to be used. Furthermore, with the oxygen flow rate in the chamber it is reasonable to expect a drop in the substrate surface temperature that will likely counteract the increase in set processing temperature. After processing, all samples appeared transparent with a faint outline of the film from the shadow mask from the substrate holder, like in fig. 7.11(e).

SOS

Optical microscopy images of the SOS sample surfaces are shown in fig. 7.34. All surfaces had a mottled pattern, similar to the vacuum atmosphere fabricated sample in fig. 7.19(a), that did not vary significantly with temperature. The PL spectra and decays are shown in fig. 7.35 and reported in table 7.7. The peak of all the samples was at 1.536 nm. Increasing the temperature from 600°C to 650°C caused a reduction in the tellurite sidebands and a narrowing of the FWHM from 22.1 nm to 20.3 nm, respectively. The FWHM for the sample fabricated in a vacuum at 600°C in section 7.4.2 was 20.7 nm and so it can be expected that the temperature drop at the substrate surface due to the oxygen flow is approximately 50°C. At 750°C, the spectra was much

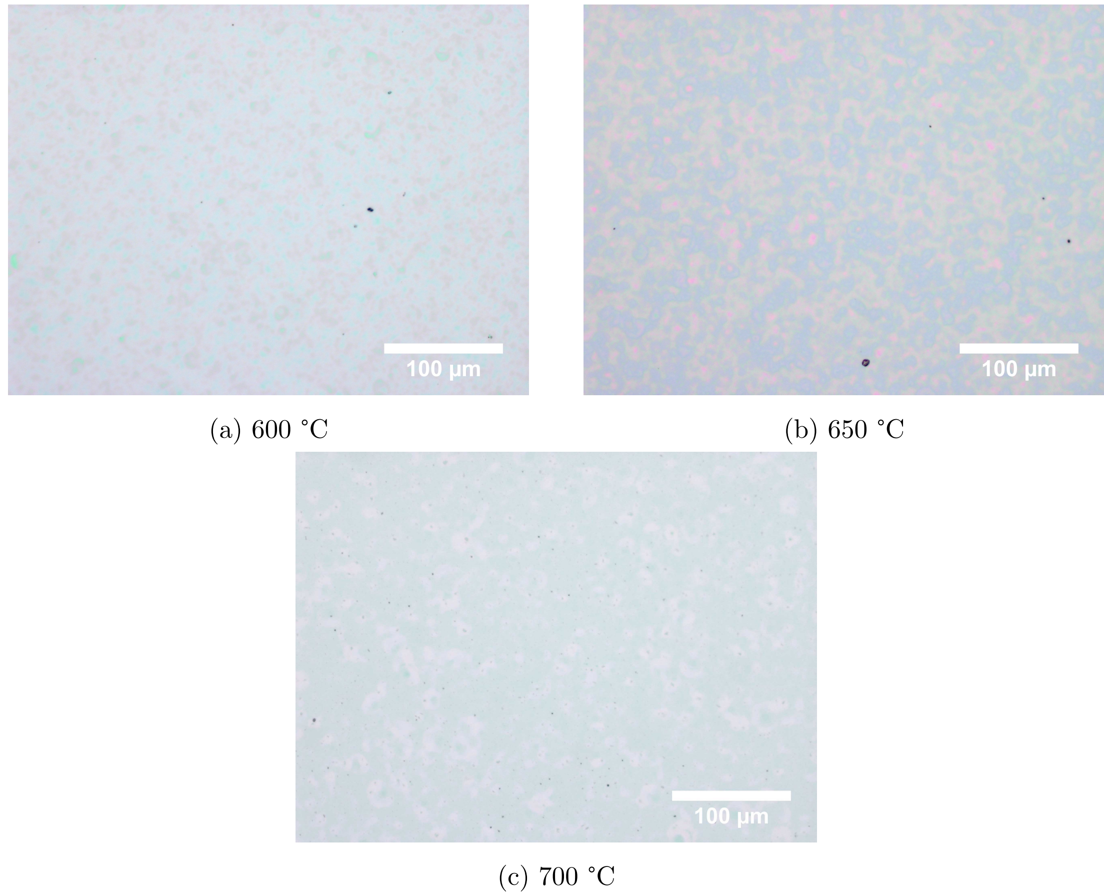

(a) 600 °C (b) 650 °C

(c) 700 °C

Figure 7.34: Optical microscopy images of films fabricated at different temperatures in an oxygen atmosphere on SOS substrates.

sharper and the peak at 1.543 μm was enhanced. As for the vacuum depositions on silicon substrates in section 7.4.2, this is attributed to unresolved crystalline phases. The devitrification of the amorphous metastable film likely formed when the target glass began to melt such that there was no more deposition and the sample was therefore effectively annealed at high temperature [130]. The PL lifetime in of the films fabricated in the oxygen atmosphere are shorter than those fabricated in the vacuum atmosphere and is likely a result of enhanced cooling during plume transport and film formation. It can be concluded that these studies did not improve the thin film properties compared to the films fabricated in a vacuum in section 7.4.2.

Table 7.7: Photoluminescence properties of films fabricated on SOS substrates at different deposition temperatures in an oxygen atmosphere.

T [°C]	$\tau^{\dagger}$[ms]	FWHM [nm]
600	5.03 ± 0.06 (92 %), 1.65 ± 0.10 (8 %)	22.1
650	7.44 ± 0.06 (97 %), 2.83 ± 0.49 (3 %)	20.3
700	7.61 ± 0.07	18.5

† Decays with multiple lifetimes have the relative intensity in brackets for each lifetime

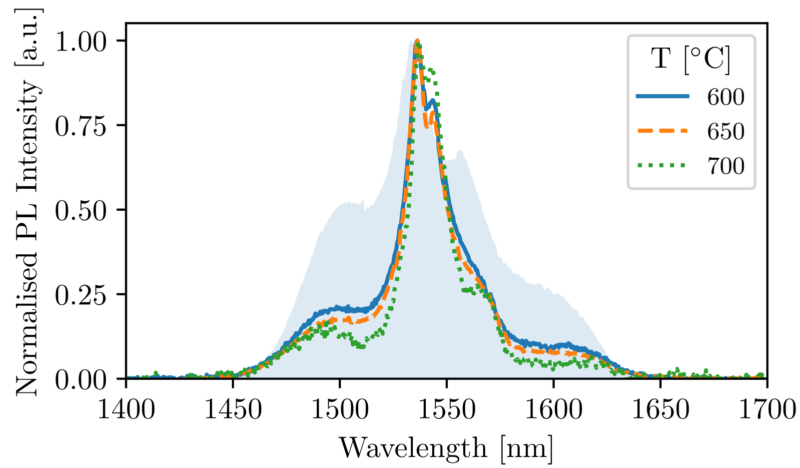

(a)

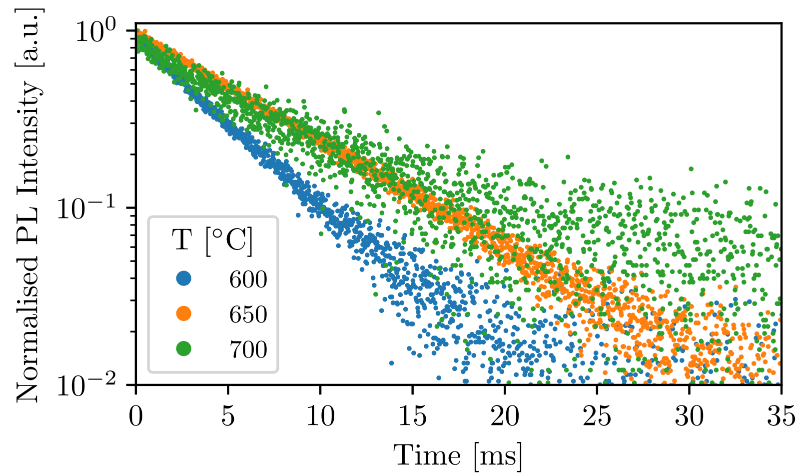

(b)

Figure 7.35: Photoluminescence (a) spectra and (b) lifetime of SOS substrates at varying deposition temperatures in an oxygen atmosphere.

Silica

Optical microscopy images of the film surfaces on SiO_2 in fig. 7.36 show that there is a clear variation with processing temperature. The film fabricated at 600°C, fig. 7.36(a), had numerous black craters all over the surface. The origin of these is similar to what was observed in section 7.4.1. In this case the large droplets of the tellurite target glass are not hot enough to form a melt with the surrounding nanoparticles. As a result their droplet shape remains and, due to the large volume, they do not completely dissolve into the silica. At 650°C, fig. 7.36(b), the surface appeared similar to the vacuum deposition in section 7.4.2 again confirming the conclusion for SOS samples that the oxygen flow in the chamber reduces the substrate temperature by approximately 50°C.

The PL spectra and decays are shown in fig. 7.35 and reported in table 7.8. The peak positions varied with temperature; 1.535 μm at 600°C, 1.536 μm at 650°C and 1.534 μm at 700°C. The PL spectra of the sample fabricated at 650°C had lower side-bands compared to the other two samples. The PL lifetime shows a similar trend. The 650°C sample had a similar decay compared to the vacuum depositions in section 7.4.2, i.e. predominantly a long 7.78 ms decay with a weaker intensity shorter 2.75 ms decay. The other two samples had similar double exponential decay rates, but the intensity of the shorter decay was stronger ($\sim$25 % compared to 7%) indicating a reduction in dissolution. The melting of the target after an hour into processing at 700°C resulted in no more ablation and deposition and so the phase separation and devitrification mechanisms were able to take place [130]. The inhomogeneous films therefore showed a broader PL spectra and shorter PL lifetime despite the increase in processing temperature.

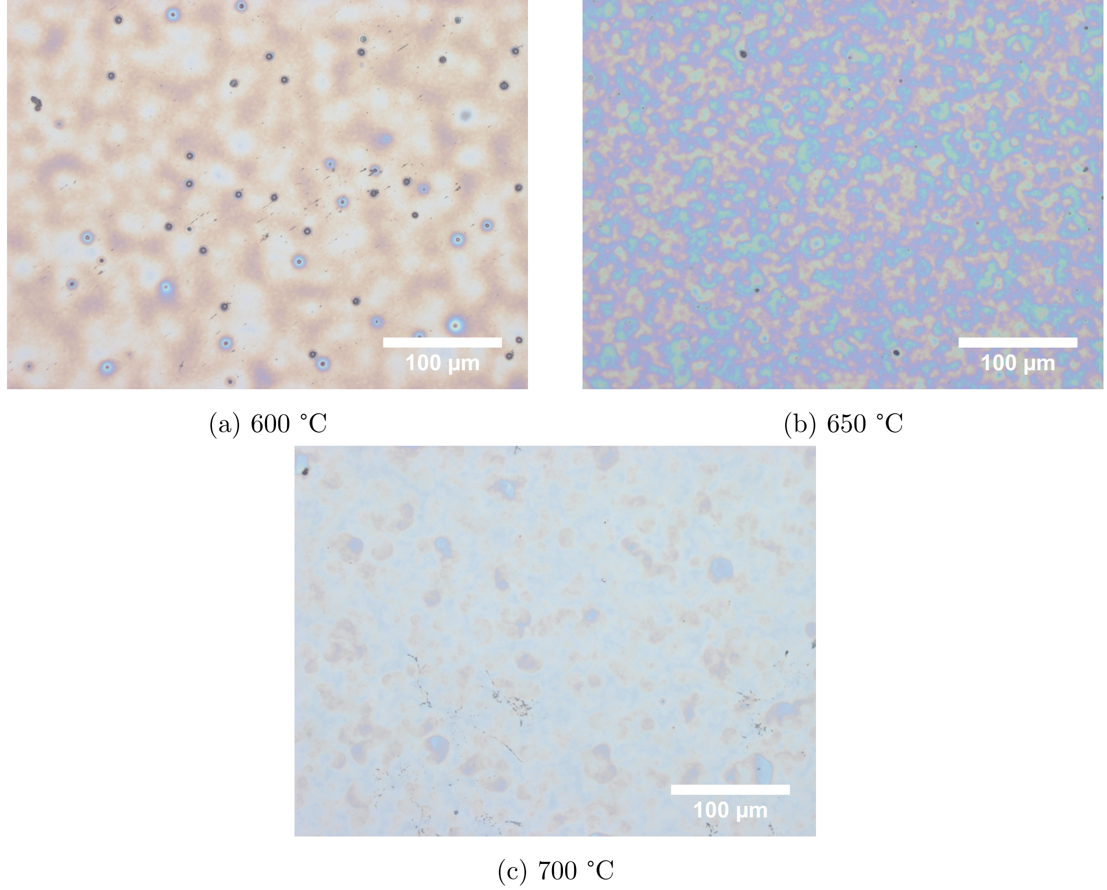

(a) 600 °C (b) 650 °C

(c) 700 °C

Figure 7.36: Optical microscopy images of films fabricated on SiO_2 substrates at different temperatures in an oxygen atmosphere.

Table 7.8: Photoluminescence properties of films on SiO_2 substrates fabricated at varying deposition temperatures in an oxygen atmosphere.

T [°C]	$\tau^{\dagger}$[ms]	FWHM [nm]
600	7.25 ± 0.09 (73 %), 2.96 ± 0.07 (27 %)	24.3
650	7.78 ± 0.03 (97 %), 2.75 ± 0.11 (7 %)	22.1
700	7.76 ± 0.07 (76 %), 2.73 ± 0.06 (24 %)	24.3

† Decays with multiple lifetimes have the relative intensity in brackets for each lifetime

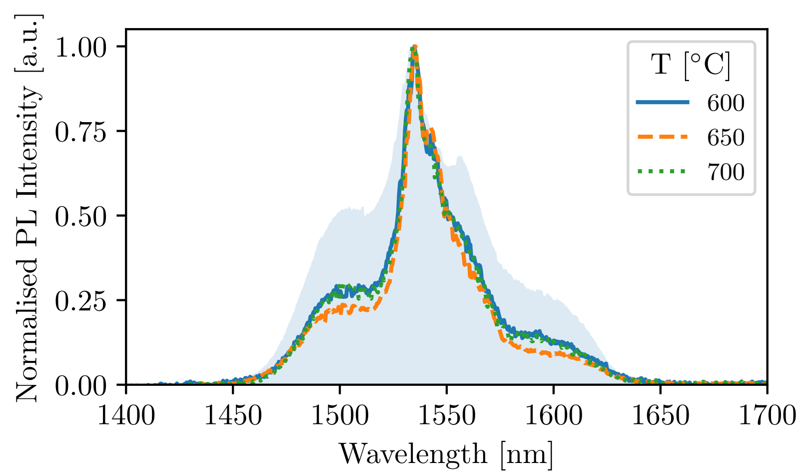

(a)

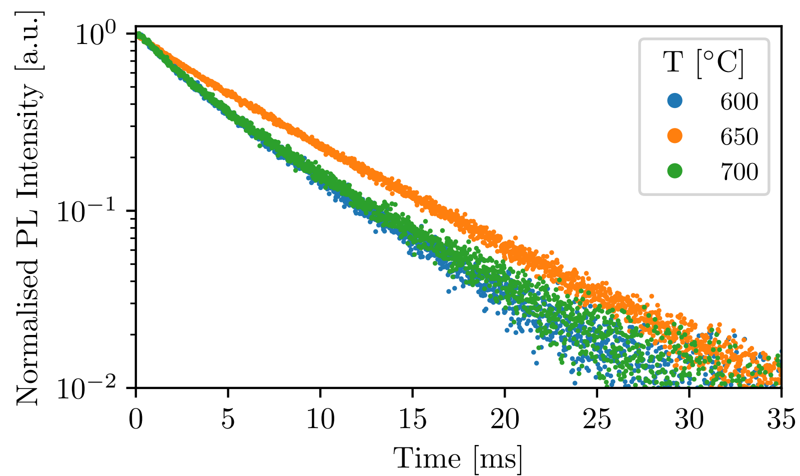

(b)

Figure 7.37: Photoluminescence (a) spectra and (b) lifetime of films on silica substrates fabricated at varying deposition temperatures in an oxygen atmosphere.

7.5 Conclusion

It is not possible to form a tellurite or hybrid tellurite-silica glass thin film in a two step fabrication of depositing followed by heat treatment. This is because the room temperature tellurite glass depositions contain crystalline phases that form upon cooling either during plume transport or substrate impact. The application of heat above T_x and below T_m only serves to grow the crystals and higher temperatures enable the formation of new crystalline phases. The unique feature of the ULPD technique is that while the substrate is heated to a similar temperature regime to weaken the Si-O bonds, the disruption caused by the continual impact of deposited material does not allow crystalline phases to form (even if they form in the plume transport).

The optimum laser fluence for vacuum depositions at 600°C at a laser repetition rate of 1 kHz was $F = 1.56$ J/cm^2. The film thicknesses of Si/SOS and SiO_2 was ~ 250 nm and ~300 nm, respectively. The formation of tellurite glass films on silicon contained crystals that were likely Te. Crystalline structures would cause unwanted scattering losses for optical wave-guiding applications. The dissolution rate of the Si-based substrates was higher than the SiO_2 substrates due to the improved efficiency of conductive heating from the holder and radiative absorption. This resulted in better physical and optical properties of the hybrid tellurite-silica thin films. Cracking was observed for higher fluence depositions due to an increase in thickness and density of the thin film and the mismatch in the CTE with the substrate. Mono-exponential PL decays were only achieved for the SOS substrate and it was found that the lower the deposition rate, the longer the PL decay lifetime due to an increase in dissolution. Incomplete dissolution resulted in a top tellurite surface layer to the film and therefore a double exponential decay. For the SOS substrate, this was only observed at the highest laser fluence. It is critical to improve the heating of the SiO_2 substrate for future work so that complete dissolution can occur providing optimum PL properties.

The introduction of a flowing oxygen atmosphere into the chamber had the effect of cooling the substrate surface by around 50°C and did not change the optical properties of the thin films significantly. It can therefore be concluded that the role of oxygen in the atmosphere is not critical and that this chapter presents results of the first thin films fabricated via the ULPD technique in a vacuum.

Chapter 8

Surface dehydroxylation during the ultrafast laser plasma doping technique

This chapter compares the properties of Er^{3+}-doped hybrid tellurite-silica thin films fabricated on silica and borosilicate glass substrates using the ultrafast laser plasma doping technique. It is found that the high temperature processing results in surface dehydroxylation, which eliminates concentration quenching by energy migration and plays a role in defining the film profile. An introduction to the chapter is given first in section 8.1. Following this, the theoretical background behind the measurement of the free OH content in glass and the surface dehydroxylation during heating of silica is presented in section 8.2. The experimental procedure is described in section 8.3. The results in section 8.4 compare the film structural and optical properties for the different substrates and the photoluminescent lifetime in dependence of substrate OH concentration. A conclusion to the chapter is given in section 8.5.

8.1 Introduction

The ultrafast laser plasma doping (ULPD) technique is capable of incorporating Er^{3+} ions into amorphous hybrid tellurite-silica thin films at high concentrations ($10^{21} - 10^{22}$ cm^{-3}) required for Er^{3+}-doped waveguide amplifiers [6, 23, 69]. A long metastable lifetime between the first excited state and the ground state is required to achieve popula-

tion inversion in such devices. At high doping concentrations conventional techniques such as ion implantation [5], ion-exchange [111–113], sputtering [114, 115] and sol-gel [110] all suffer from concentration quenching effects (energy migration and cooperative upconversion) that are enhanced due to inhomogeneous Er^{3+} ion distributions (clustering and crystallisation) and act to shorten the photoluminescence (PL) lifetime [7, 91]. Precipitation can also occur, which reduces the fraction of optically active ions [5]. Importantly, Er^{3+}-doped films fabricated via the ULPD technique do not suffer such undesirable effects at these doping concentrations, as evidenced by a record-high lifetime-density product of 0.96×10^{19} s·cm^{-3} [6].

In an amorphous media, the efficiency of non-radiative Förster type dipole-dipole interactions increase strongly with the inverse of the sixth power of the ion-ion separation, determined by the doping concentration, and leads to the concentration quenching mechanisms cooperative upconversion and energy migration [69, 89, 91]. Cooperative upconversion occurs between two excited ions and is therefore also dependent on the pump power or population inversion. Energy migration involves a transfer of the excitation from an excited ion to a neighbouring ion in the ground state. The sequential transfer of energy between ions (migration) may occur until an ion coupled to a non-radiative quenching site is met, resulting in the loss of an excitation. Energy migration therefore depends on the concentration of dopant ions, the host-dependent ion-ion interaction strength and the concentration of quenching centres coupled to the optically active ions [91].

OH-groups ('hydroxyl groups') are known quenching centres in glasses and are incorporated into the silica network during melting through interaction with water vapour according to [228, 229]

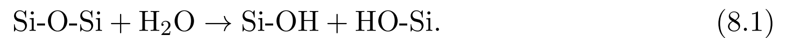

$$\text{Si-O-Si} + H_2O \rightarrow \text{Si-OH} + \text{HO-Si}. \tag{8.1}$$

Silanol hydroxyl groups are responsible for strong absorption between 3800 - 3200 cm^{-1} (2630 - 3125 nm) and exist in two forms; 'physically bonded Silanol' and 'free Silanol'. The former is not present after heating the glass above 200°C, which occurs during melting, and the remaining chemically bonded or free Silanol has a stretching vibration at ∼3670 cm^{-1} (2725 nm) [228]. Commercially available silica glasses are categorised into four types and have varying OH contents depending on the manufacturing method

and raw materials used [230]. Type I silica, such as Infrasil, is produced from natural quartz under electrical fusion in either a vacuum or an inert gas atmosphere and contains the fewest OH-groups (typically $<$5 ppm) [230]. Due to complexity of the manufacturing technology, the cost of such high-purity glasses is high. A lower cost alternative is type III silica, such as Spectrosil, that have high concentrations of OH-groups ($\sim$1000 ppm) but also fewer metallic impurities. These widely used synthetic fused silicas are produced by pyrolysis reaction of $SiCl_4$ in a hydrogen-oxygen flame [230, 231].

As a result of the large variation in OH content, the choice of glass substrate is known to have a large effect on the PL properties of rare earth doped ions [5, 7, 91]. Previous research with the ULPD technique routinely uses type III fused silica as a substrate, despite the relatively high OH concentration [6, 23, 127, 128]. Recently a comparison between Spectrosil 2000 and Infrasil 301 in the fabrication of Tm^{3+}-doped hybrid tellurite-silica films showed a longer PL lifetime in the lower OH content quartz glass, suggesting that this was due to a reduced concentration quenching and highlighting the possibility of further improving the thin film material spectroscopic properties simply through choice of glass substrate [25]. However, the differences in processing parameters (laser fluence and processing time) between the two films result in variable thicknesses and refractive index. Such effects lead to a modification in the average spontaneous emission rate of ions within the film (see chapter 2 and chapter 3) and lead to complications in the interpretation. Cracking of thick films may also be reduced by using silicates, which have a higher Coefficient of Thermal Expansion (CTE) and softening temperature, but this has not been previously investigated.

In this chapter, four different Er^{3+}-doped films were fabricated on three silica substrates with different OH contents and a borosilicate glass substrate. The film structure and optical properties are measured using variable angle spectroscopic ellipsometry and the concentration quenching by energy migration is investigated by comparing the different substrate OH contents with the PL decay rates.

8.2 Theoretical background

8.2.1 Measuring the OH content in silicate glass

The calculation of the OH content in a glass can be estimated from FT-IR transmittance data using the procedure described in [228]. This method was chosen as it accounts for the shift in OH absorption peaks, which depend on OH concentration and glass composition. Furthermore, the method is appropriate for measuring very low OH concentrations in quartz glass.

The peak height of the OH absorption at $\sim$3670 cm^{-1} (2725 nm) is estimated by fitting a third order B-spline to the data surrounding the peak to give a baseline for the spectra. The location of the peak T_{min} is found by evaluating where the maximum difference between the spectra and the baseline occurs. The baseline is then normalised at 100% and the peak height is calculated. Locating the peak through fitting is more accurate than choosing a specific absorption wavelength and using the OH absorption cross section [232], which other researchers have used [91], as it can change position with composition.

The maximum transmission T_{max} is calculated according to $T_{\text{max}} = T_{\text{min}} +$ peak height and using Beer-Lambert law, which states that the optical density β [mm^{-1}] at the peak wavelength is given by

$$\beta = \frac{1}{d} \log \left(\frac{T_{\text{max}}}{T_{\text{min}}} \right), \tag{8.2}$$

where d is the sample thickness in mm. The OH content is then calculated according to

$$\text{OH [ppm]} = \beta \times \frac{M_{\text{OH}} \times 10,000}{e_{\text{OH}} \times \rho_{\text{glass}}}, \tag{8.3}$$

where M_{OH} is the molar weight of OH^- (17.008 g/mol), ρ_{glass} is the density of the glass (2.21 g cm^{-3}) and e_{OH} (77.5 L mol^{-1} cm $^{-1}$)[1] is the absorption coefficient of OH at the peak wavelength. The concentration is converted to the density by

$$N_{\text{OH}} \; [\text{OH}^-/\text{cm}^3] = \frac{\text{OH [ppm]}}{1 \times 10^6} \cdot \frac{\rho_{\text{glass}} N_A}{M_{\text{OH}}}, \tag{8.4}$$

[1] This is the ‘Stephenson’ value. A wide range of absorption coefficients are reported in the literature and the reader is referred to [228] for more information in the differences between the values.

where N_A [mol^{-1}] is the Avogadro constant.

8.2.2 Surface dehydroxylation by annealing in silica glass

Silica glass has hydroxyl groups built in to the network during and depending on the manufacturing technique [233]. In a water containing environment, such as air, exposed glass surfaces are known to hydrate [234]. Similarly, prolonged heating (annealing) results in the dehydroxylation of the surface layer [231]. Both can lead to changes in the mechanical properties and the formation of stress related defects in the glass surface layer [233, 234]. During the ULPD technique, glass substrates are typically heated to > 600°C for several hours, which results in a significant dehydrated surface layer where the film is formed.

The relative OH concentration at a depth H into the surface of a glass plate with total thickness h after annealing for set period of time t_0 is given by [231, 235]

$$\frac{N_{\mathrm{OH}}}{N^0_{\mathrm{OH}}} = \frac{4}{\pi}\sum_{n=0}^{\infty}\frac{(-1)^n}{(2n+1)}\cdot e^{\frac{-D(2n+1)^2\pi^2 t_0}{h^2}}\cdot \cos\frac{\pi(2n+1)(h-2H)}{2h}), \tag{8.5}$$

where D is the temperature dependent diffusion coefficient of OH and is determined by measuring the OH concentration with infrared spectroscopy after annealing for a time t according to [233, 236]

$$D = \frac{\pi h^2}{16t}\left(1 - \frac{N_{\mathrm{OH}}}{N^0_{\mathrm{OH}}}\right)^2. \tag{8.6}$$

For a type III silica glass, KU-1, with an OH content ~1300 ppm, the diffusion coefficient had an exponential dependence on the annealing temperature T [k] between 800 - 980°C, given by $D = 8.83 \times 10^{-9}\exp(-15,537/T)$ [m^2/s] [233]. The depth dependent relative OH concentration for three different annealing temperatures (similar to processing temperatures used in the ULPD technique) after 1.5 hours is plotted in fig. 8.1. The dehydroxylated layer shows a large difference between 500°C and 600°C due to the exponential dependence of temperature of D. At 600°C the depth of dehydroxylation, defined as where $N_{\mathrm{OH}}/N^0_{\mathrm{OH}} < 0.1$, is < 200 nm, whereas the higher temperatures have depths much larger than the typical thickness of films fabricated with the ULPD technique after this length of processing time.

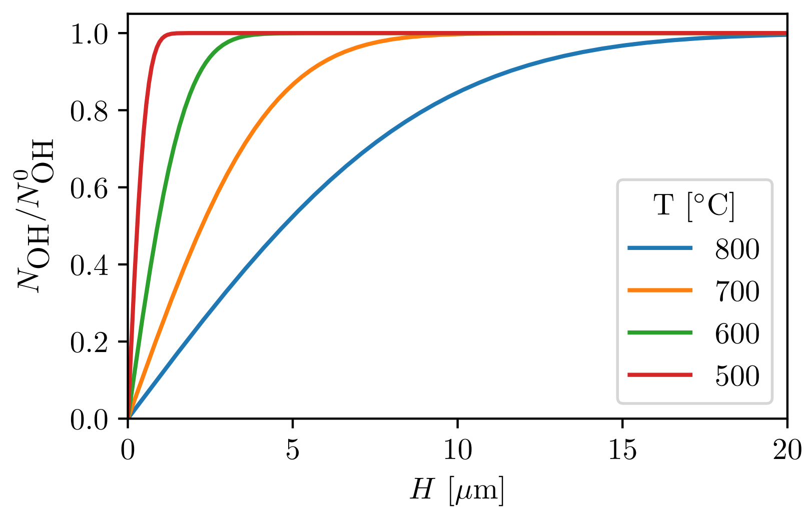

(a)

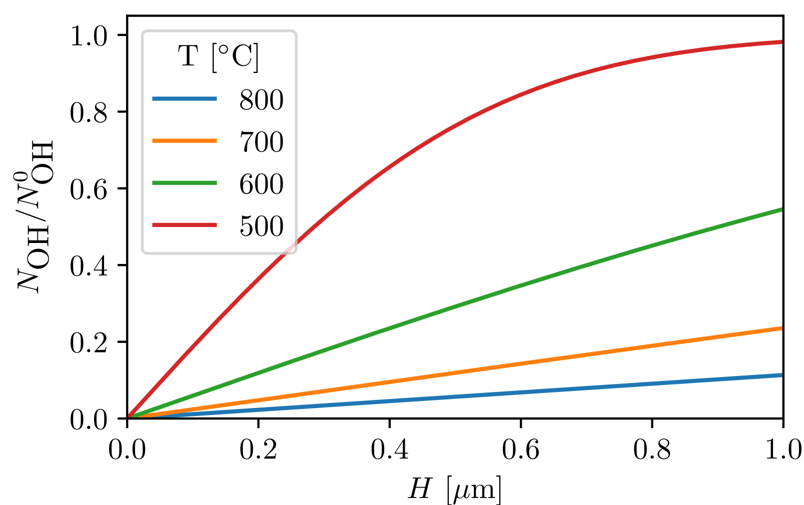

(b)

Figure 8.1: Relative concentration of OH-groups at a depth H from the surface of a KU-1 (type III silica) glass plate after annealing for 1.5 hours at varying temperatures T. The entire modified surface layer is shown in (a) and the region 1 μm below the surface is shown in (b).

Table 8.1: Mechanical and thermal properties of the different glass substrates as specified by the manufacturer [218, 221, 237]. CTE is the Coefficient of Thermal Expansion and c is the specific heat capacity.

Property	Glass			
	Infrasil 301	Borofloat 33	Spectrosil 2000	Corning 7980
Density [gcm^{-3}]	2.2	2.2	2.2	2.2
Knoop hardness [kg/mm^2]	600	480	600	522
Softening temperature [°C]	1730	820	1600	1585
Heat conductivity [W/m·K]	2	1.2	2	1.38
CTE [$10\times^{-7}$/K]	5.3	32.5	5.3	5.7
c [kJ/kg·K]	0.77	0.83	0.77	0.77

8.3 Experimental setup

Four commercially available glasses were used as substrates in this study: two different type III fused silica glasses (Heraeus Spectrosil 2000 and Corning 7980), a type I quartz glass (Heraeus Infrasil 301) and a low alkali content borosilicate glass (Schott Borofloat 33). The composition of the quartz and silica glasses was SiO_2 (100%) and the borosilicate composition, according to the manufacturer, was SiO_2 (81%), B_2O_3 (13%), Na_2O/K_2O (4%), Al_2O_3 (2%). Some of the mechanical and thermal properties for the different glasses given by the manufacturers are compared in table 8.1. The quartz and silica glasses were investigated as they have different concentrations of OH impurities. The borosilicate glass was investigated for it's lower softening point and higher CTE.

The optical transmission spectra of the substrates were acquired in the UV-vis-NIR regions (250 - 2500 nm) by using a double beam spectrophotometer (Perkin-Elmer Lambda 950) and between 2.5 - 5.0 μm (2000 - 4000 cm^{-1}) using Fourier-transform infrared spectroscopy (FT-IR). The quantification of the OH content was carried out using the method detailed in section 8.2.1.

Er^{3+}-doped hybrid tellurite-silica thin films were formed on the glass substrates with the ULPD technique in one run at a laser fluence $F = 1.76$ J/cm^2 (pulse energy $E_p = 110$ μJ) at 600°C and in a vacuum. The target was a highly Er^{3+}-doped zinc-sodium tellurite glass of composition $79TeO_2$-$10ZnO$-$10Na_2O$-$1Er_2O_3$ mol.% (1ErTZN) and chosen so

that ion-ion concentration quenching interactions in the film would be efficient. The Er^{3+}-doping concentration of the ablated nanoparticles from the 1ErTZN target was $\sim 8.78 \times 10^{20}$cm^{-3}, based on the measurements in chapter 6, and the Er^{3+}-doping concentration in the final hybrid tellurite-silica films is estimated to be $10^{21} - 10^{22}$ cm^{-3} [6]. The samples were processed with 1.2×10^{6} pulses per cm^{2} applied to the target surface directly below the substrate, taking 1 hour and 44 minutes. The target to substrate distance was 70 mm and the procedure identical to that detailed in section 7.3.

Surface inspection was carried out via optical microscopy (Olympus BX51 with Zeiss AxioCam MRc5 camera) at varying magnifications for all samples. Ellipsometry measurements were performed using the same setup and fitted model (that was verified with cross-sectional scanning electron microscopy) as in chapter 7. PL measurements were also performed using the setup described in chapter 7. The steady-state spectra was measured with a pump power of 375 mW, as in chapter 7, and a lower pump power of 330 mW was used for the time-resolved decay measurements to minimise cooperative upconversion.

8.4 Results and discussion

8.4.1 Substrate hydroxyl impurities

The transmittance in the visible spectrum was high and relatively featureless for all the glasses, as shown in fig. 8.2. The slight differences in the transmission between the glasses are due to Fresnel losses and small variations in the refractive index. The strong absorption below 2400 cm^{-1} is attributed to the excitation of Si-O vibrations [91, 238]. Borofloat 33 had absorption bands at 2520, 2760, 3620, 4520 and 7140 cm^{-1}. The silica glasses had absorption bands at 2260, 2670 and 3670 cm^{-1} and two additional absorption bands at 4250 and 7220 cm^{-1} are on seen in the type III fused silica glasses. The absorption band at 3660 cm^{-1} is very weak in Infrasil 301 and can not be seen in the figure. All of these absorption bands are attributed to hydroxyl groups in the glass network and in particular the band at $\sim$3670 cm^{-1} is due to free (chemical bonded Silanol) OH-groups [91, 228, 238, 239].

The concentration of free OH-groups ρ_{OH} was calculated from the $\sim$3670 cm^{-1} band using the procedure described in section 8.2.1. The baseline normalised data and fitted peaks are shown in fig. 8.3. The position of the OH peak is shifted significantly for the

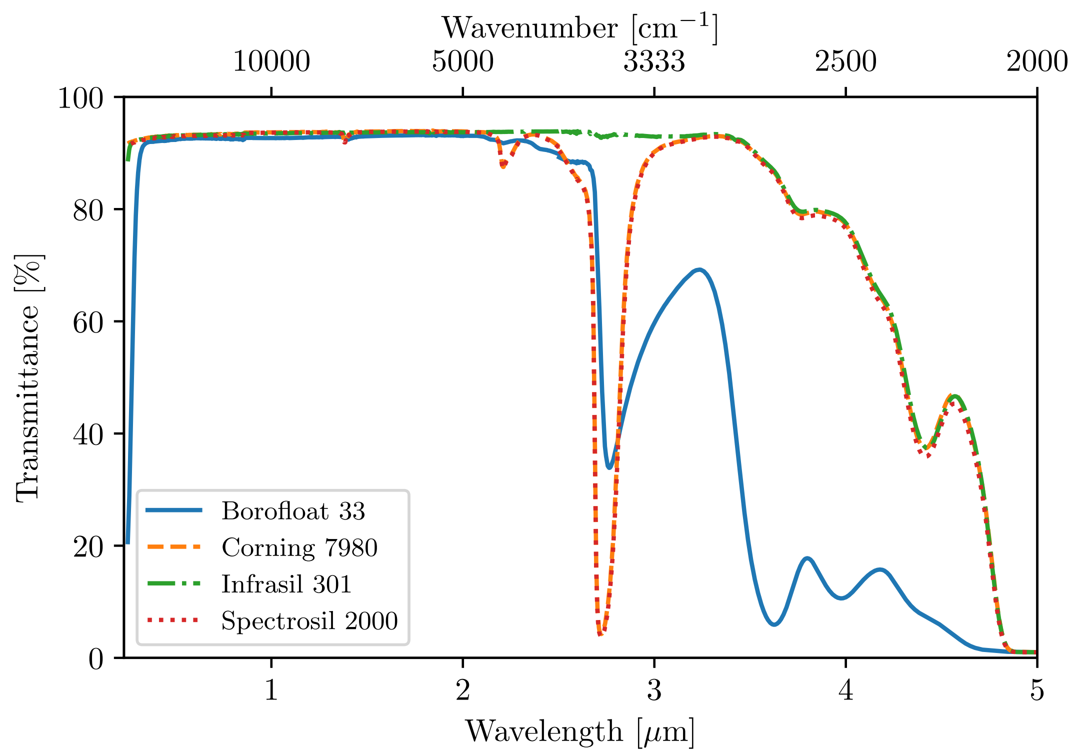

Figure 8.2: Transmission measurements of 1.1 mm thick glass substrates. Data from UV-vis-NIR and FT-IR is joined at 2.5 μm. The strong absorption below 2400 cm^{-1} is attributed to the excitation of Si-O vibrations.

borosilicate glass due to the network formers and modifiers. The ρ_{OH} in the glasses was 4 ppm in Infrasil 301, 369 ppm in Borofloat 33, 1329 ppm in Spectrosil 2000 and 1283 ppm in Corning 7980. The corresponding densities, which span over two orders of magnitude, were 8.27×10^{16} cm^{-3} for Infrasil 301, 8.13×10^{18} cm^{-3} for Borofloat 33, 2.93×10^{19} cm^{-3} for Spectrosil 2000 and 2.83×10^{19} cm^{-3} for Corning 7980. The values are reported in table 8.3 and agree with the manufacturer specifications [218, 221, 237].

8.4.2 Film characterisation

Birefringince could be seen on all the films and the appearance was visually similar to fig. 7.11e. This was to be expected as the processing parameters were almost identical. Figure 8.4 shows optical microscopy of the film surfaces. The surfaces had a mottled interference pattern due to thickness and refractive index variations across the film surface, which modifies the path length of the light. The interference patterns for Infrasil 301 had the largest features (>100 μm), while the other glasses had features smaller (<20 μm) features. Overall the profiles of the samples were very smooth (verified in differential interference contrast microscopy).

The physical and optical properties of the films, measured via ellipsometry, are shown in table 8.2. The optical model was a one term transparent Cauchy layer (i.e. wavelength independent refractive index) with a linear index grading. The mean square error (MSE) was acceptable for all of the fits and full details of the fitting procedure and raw data are given in appendix E. The refractive index at the top and bottom of the film and the substrate are shown in fig. 8.5. The ∼365 nm thick films on Spectrosil 2000 and Corning 7980 were the most well defined as they had a difference in refractive index between the bottom of the film and the substrate of >5 %. The index difference for Infrasil 301 and Borofloat 33 were much lower at 2.4% and 1.3%, respectively. As a result of this more gradual transition, these substrates had thicker films measuring 437 nm and 531 nm, respectively, and a lower average refractive index. The differences in the film properties between the glass substrates will be revisited at the end of this section.

The PL spectra and lifetime is shown in fig. 8.6 and summarised in table 8.3. The tellurite target had a main peak at 1.533 μm, sidebands at 1.504 μm, 1.555 μm and 1.598 μm, and a full-width half maximum (FWHM) of 68 nm. All samples showed a

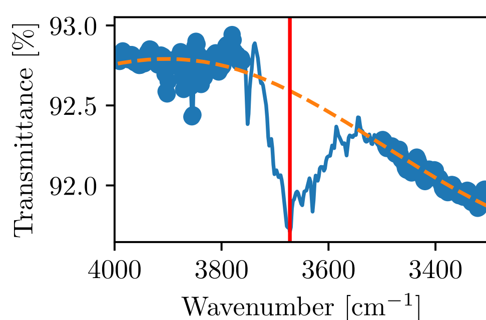

(a) Infrasil 301, 3672 cm^{-1} peak height 0.88%.

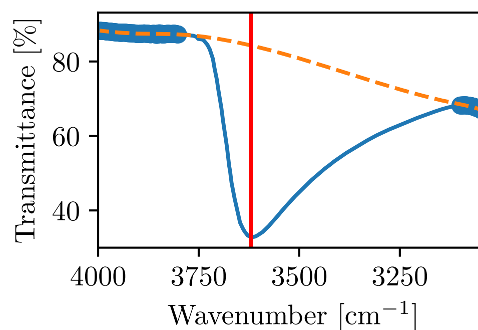

(b) Borofloat 33, 3620 cm^{-1} peak height 51.40%.

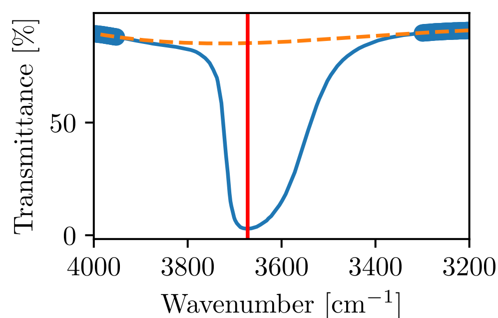

(c) Spectrosil 2000, 3672 cm^{-1} peak height 82.38%.

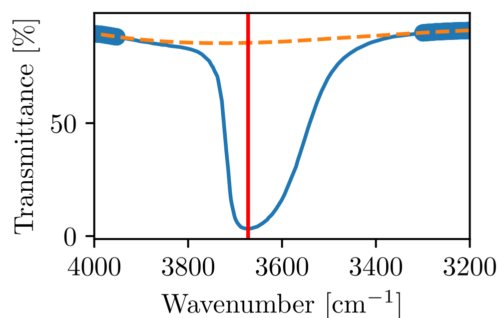

(d) Corning 7980, 3672 cm^{-1} peak height 82.29%.

Figure 8.3: Transmission spectra near the free OH absorption peak at ∼3670 cm^{-1} with cubic spline baseline (dashed) evaluated from the points marked with filled circles. The peak location is denoted with a vertical red line and the height from the baseline is evaluated at this location.

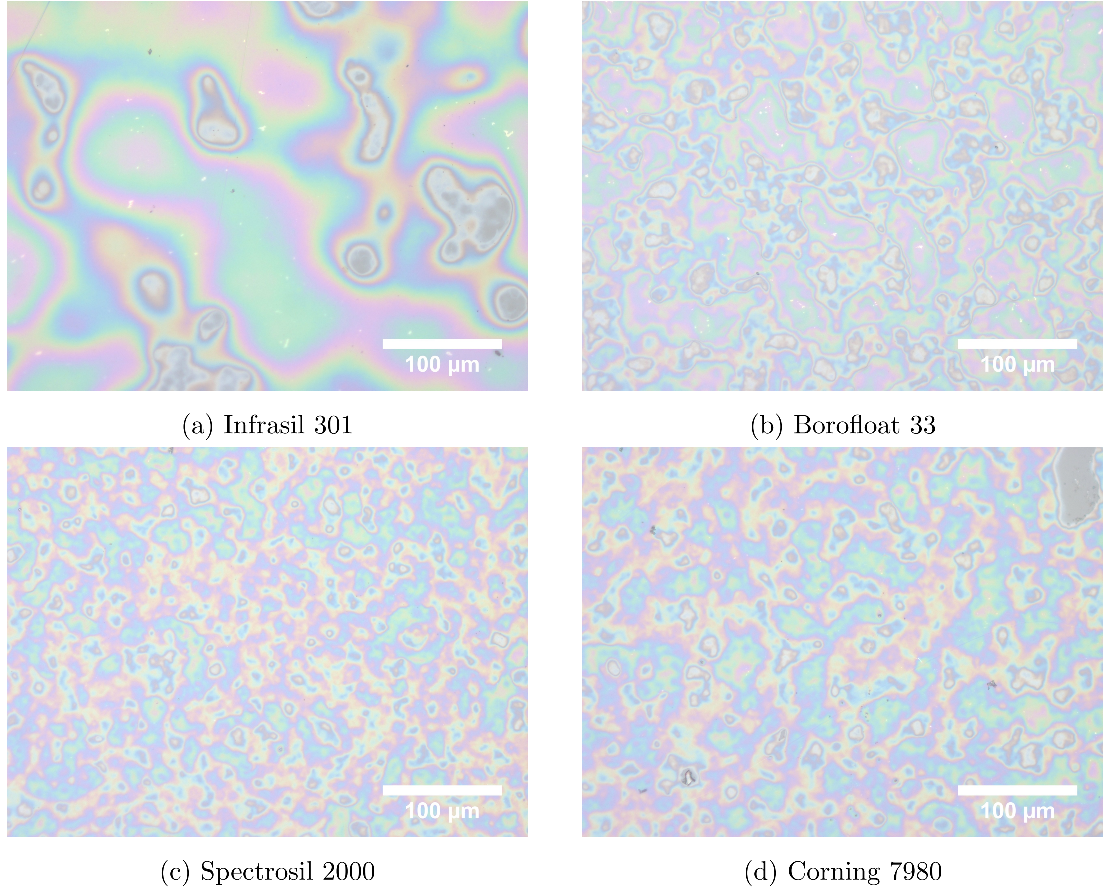

(a) Infrasil 301 (b) Borofloat 33

(c) Spectrosil 2000 (d) Corning 7980

Figure 8.4: Optical microscopy of the thin films on different glass substrates.

PL spectra around 1.54 μm (main peak at 1.536 μm and second peak at 1.543 μm) and FWHM of $\sim$ 22 nm. The tellurite shoulders were much reduced in intensity for all samples and characteristic of that for Er^{3+} ions in a hybrid tellurite-silica host [6, 23]. The FWHM of the Infrasil 301 and Borofloat 33 substrates were slightly wider at 22.5 nm and 23.4 nm, respectively, compared to that of the fused silica substrates at 21.6 nm and is a result of the increased intensity of the tellurite sidebands. Infrasil had the highest intensity 1.504 μm sideband of 25%, followed by Borofloat 33 with 23 % and then Spectrosil 2000 and Corning 7980 with 20%. A similar trend in the 1.598 μm sideband was observed. In ion implanted borosilicate glasses, the low concentration of the network former B and network modifiers (Na, K, Al) in the glass lead to a more inhomogeneous distribution of Er^{3+} ion sites and increases the FWHM to over 100 nm [91]. It is surprising that this does not occur for films fabricated with the ULPD

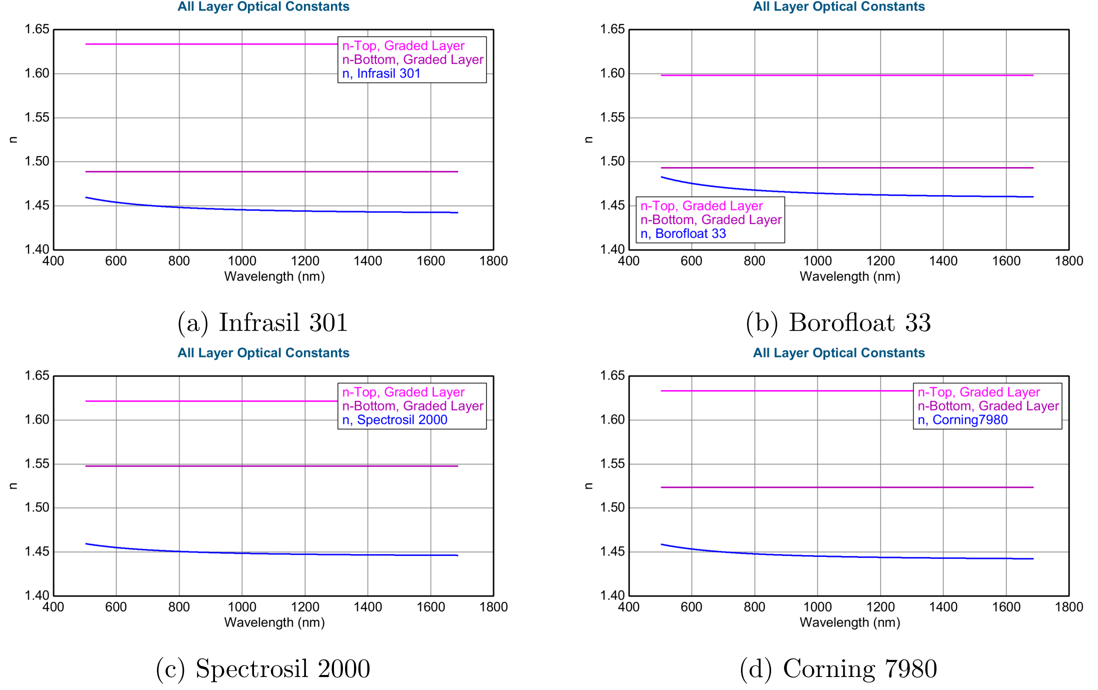

Figure 8.5: Ellipsometry fits of a graded wavelength independent refractive index thin film on different glass substrates.

technique and indicates that the network formers and modifiers are not present in the surface film layer of the glass.

The PL lifetime had a double exponential decay for all the samples. A short lifetime component of around 1.5 ms, attributed to ions in a tellurite environment, made up $<10\%$ of the intensity. The longer lifetime, attributed to ions in a silicate environment, was around 8 ms for the silica and quartz substrates and 3.9 ms for the borosilicate substrates. This indicates that the substrate temperature was not high enough to either evaporate a sufficient amount of tellurium or weaken the Si-O bonds for complete dissolution. The average lifetime was calculated according to $\bar{\tau} = \sum_i \tau_i w_i$, where the summation is over all of the components in the lifetime and w_i is the fractional intensity (i.e. the weight) of the ith lifetime component τ_i. Spectrosil 2000 had the longest average lifetime of 8.60 ms. The measured decay rate (inverse of the lifetime) is composed of radiative and non-radiative components. The differences between PL lifetimes for the different substrates are attributed to changes in the non-radiative decay rates and will be discussed in the next section.

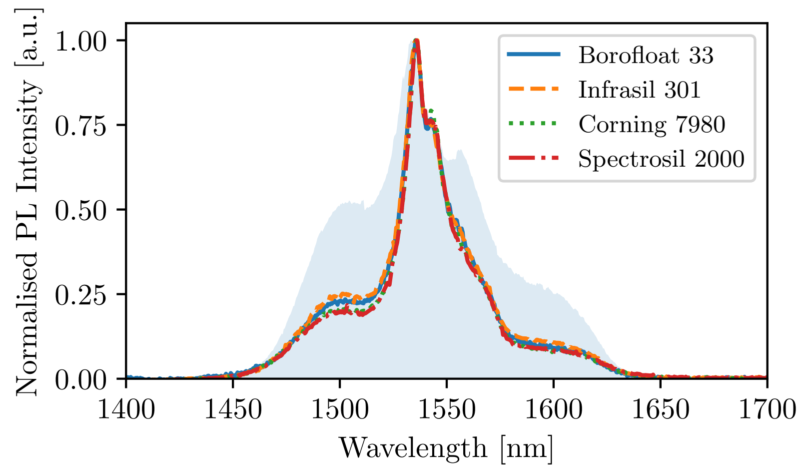

(a)

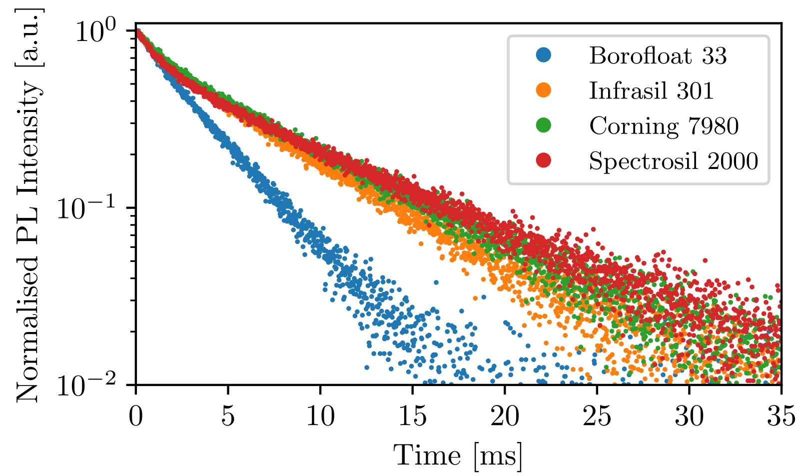

(b)

Figure 8.6: Photoluminescence (a) spectra and (b) lifetime of different glass substrates. Shadowed fill plot in (a) shows the spectra of the 1ErTZN target glass for reference.

Table 8.2: Physical and optical properties of the films measured via ellipsometry. MSE is the mean square error of the fit, % Inhomogeneity is the linear refractive index grading from top to bottom of the film assuming a mixing with the substrate index $n_{\text{substrate}}$, n is the average film refractive index, the difference in refractive index from top to bottom of the film $\Delta n = n_{\text{top}} - n_{\text{bottom}}$ and the roughness assumes a 50% volume fraction.

	Infrasil 301	Borofloat 33	Spectrosil 2000	Corning 7980
MSE	12.61	10.97	12.80	13.10
Roughness [nm]	9.2	6.5	9.0	9.6
d [nm]	437	531	358	371
n	1.563	1.546	1.587	1.579
% Inhomogeneity	31.3	23.3	15.8	23.2
n_{top}	1.643	1.598	1.624	1.633
n_{bottom}	1.489	1.493	1.549	1.523
$n_{\text{substrate}}$ @ 633 nm	1.453	1.474	1.454	1.452
Δn	0.145	0.105	0.075	0.110

8.4.3 Concentration quenching

Dipole-dipole interactions in doped media are responsible for the migration of excitation energy between ions. If an ion coupled to a quenching centre is reached, non-radiative recombination occurs resulting in the loss of the excitation. The efficiency of dipole-dipole interactions increases with ion doping concentration and results in a detrimental reduction of the metastable PL lifetime at high ion doping concentrations. OH-groups ('hydroxyl groups') are known to be quenching centres in Er^{3+}-doped glasses [91, 92]. The energy of the $^4I_{13/2} \rightarrow ^4I_{15/2}$ transition in Er^{3+} ($\sim$ 6500 cm^{-1}) matches the energy of the second harmonic of the OH-group stretching vibration. As a result an excited Er^{3+} ion can non-radiatively relax by excitation of two OH vibrational quanta.

For a homogeneous distribution of Er^{3+} ions and a low density of quenching sites, the decay rate Γ as a function of optically active Er^{3+} ion concentration N_{Er} resulting from energy migration is given by (eq. (3.8)) [5, 91]

$$\Gamma = \Gamma_{\text{rad}} + \Gamma_{\text{int}} + 8\pi C_{\text{Er-Er}} N_{\text{Er}} N_{\text{Q}}, \tag{8.7}$$

Table 8.3: Physical and optical properties of thin films on different glass substrates.

Substrate	N_{OH} [cm^{-3}]	τ^{*}[ms]	$\bar{\tau}$ [ms]	FWHM [nm]
Infrasil 301	8.27 $\times 10^{16}$	7.38 $\pm$ 0.03 (92 %), 1.48 $\pm$ 0.04 (8 %)	6.91	22.5
Borofloat 33	8.13 $\times 10^{18}$	3.89 $\pm$ 0.04 (93 %) 1.26 $\pm$ 0.11 (7 %)	3.71	23.4
Spectrosil 2000	2.93 $\times 10^{19}$	9.31 $\pm$ 0.04 (91 %), 1.45 $\pm$ 0.03 (9 %)	8.60	21.6
Corning 7980	2.82 $\times 10^{19}$	8.41 $\pm$ 0.05 (91 %), 1.71 $\pm$ 0.05 (9 %)	7.81	21.6

* Decays with multiple lifetimes have the relative intensity in brackets for each lifetime.

where Γ_{rad} is the radiative decay rate, Γ_{int} is the internal non-radiative recombination rate (due to the emission of phonons), N_{Q} the density of quenching centres and $C_{\text{Er-Er}}$ the interaction constant between ions. Derivation of the equation approximates that the overlap between the absorption spectra of the quenching sites and the Er^{3+} are equal as the OH-groups that are closely bound to a few of the Er^{3+} quench via excitation of vibrations [91].

The decay rate in the absence of migration is given by $\Gamma_{\text{rad}} + \Gamma_{\text{int}}$. The 6500 cm^{-1} gap below the $^4I_{13/2}$ level of Er^{3+} is large enough such that multiphonon relaxation can be considered negligible in both tellurite (700 cm^{-1}) and silicate (1100 cm^{-1}) glasses as $\Gamma_{\text{int}} < 1\text{s}^{-1} \approx 0$ [64]. The radiative decay rate Γ_{rad} does not vary significantly in similar multicomponent silica-based hosts as the $4f$ electrons, involved in the transition, are shielded from the host by the outer lying $5s^25p^6$ shells [64, 65]. Evaluation of the radiative decay in hybrid tellurite-silica films fabricated with the ULPD technique has not been reported in the literature, however in ion implanted sodalime glass, the radiative decay rate is $\Gamma_{\text{rad}} \approx 45\ \text{s}^{-1}$ (22 ms) [45, 240]. The slight variations in the film thickness and refractive index of the substrate and film result in small changes to the spontaneous emission rate due to changes in the position dependent local density of states [36]. The Purcell factor $F_{\text{p}} = \Gamma/\Gamma_0$ of the four samples is simulated in fig. 8.7. While the trends in decay rates agree with the observed results, the absolute values were not large enough to explain the changes. For example, Borofloat 33 substrate had the highest average decay rate but comparing with Infrasil 301 the simulations predict an enhancement of $1.406/1.372 = 1.025$ when the experimental data predicts an enhancement of $6.91/3.71 = 1.863$. Alternatively, comparing Infrasil 301 with Spectrosil 2000 the decay rate enhancement predicted by the simulations is $1.372/1.346 = 1.019$ while the experimental measurements show $7.81/6.91 = 1.130$.

Approximating that $C_{\text{Er-Er}}$ and N_{Er} are invariant between samples, the changes to decay rate are therefore dependent on the fraction of Er^{3+} ions coupled to quenching sites N_{Q}. This is justified as the variation in OH concentration in the substrates is over three orders of magnitude, which is much larger than the variation in film properties previously measured via ellipsometry. It is typically assumed (for ion implanted glass) that all the free OH-groups contribute to quenching, i.e. $N_{\text{Q}} = N_{\text{OH}}$ [91]. Figure 8.8 shows the PL decay rate ($1/\tau$) as a function of the density of free OH-groups in the glass substrates. The decay rate of Borofloat 33 is 270 s^{-1} and the highest of all

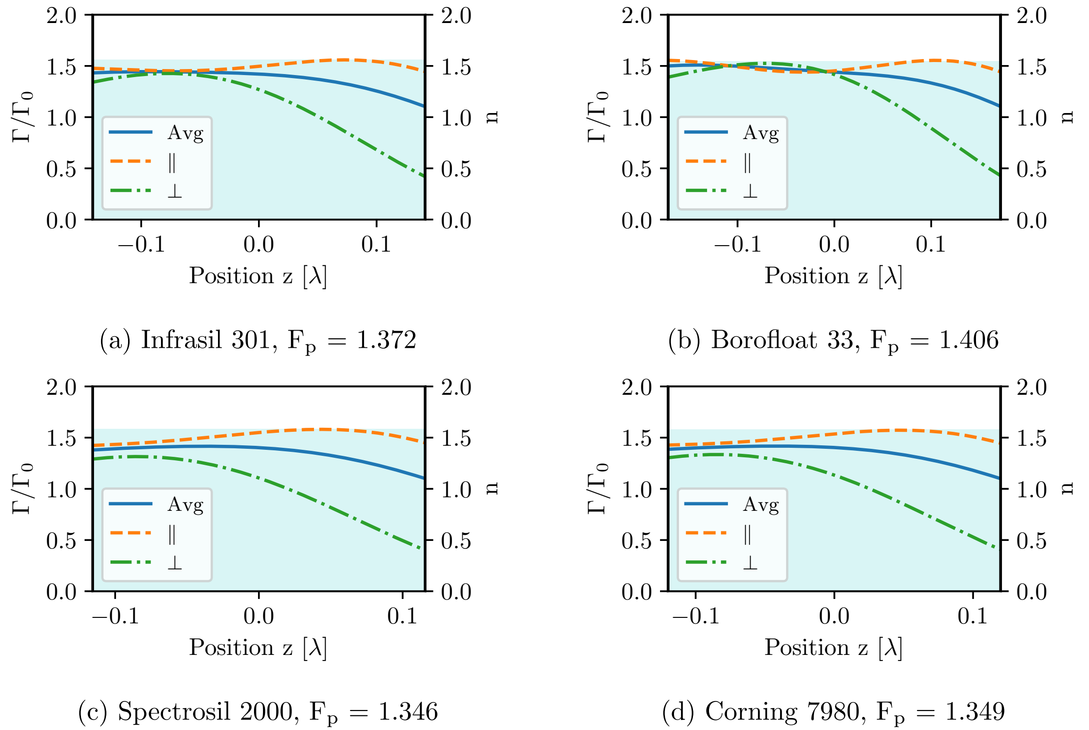

(a) Infrasil 301, $\mathrm{F_p} = 1.372$

(b) Borofloat 33, $\mathrm{F_p} = 1.406$

(c) Spectrosil 2000, $\mathrm{F_p} = 1.346$

(d) Corning 7980, $\mathrm{F_p} = 1.349$

Figure 8.7: The radiative decay rate of perpendicular $\perp$, parallel $\parallel$ and randomly Avg $= (2/3) \parallel + (1/3) \perp$ orientated dipole compared to the free space decay rate at $\lambda = 1540$ nm as a function of position in the film; Glass substrate is at $z \to -\infty$ and the air superstrate is at $z \to \infty$ and the film in between is plotted. The values for the film thickness, (average) film and substrate refractive index are given in table 8.3. Shaded light blue region indicates the refractive index of the layer. $\mathrm{F_p}$ gives the average Purcell factor (Γ/Γ_0) for randomly orientated dipoles at all locations within the film.

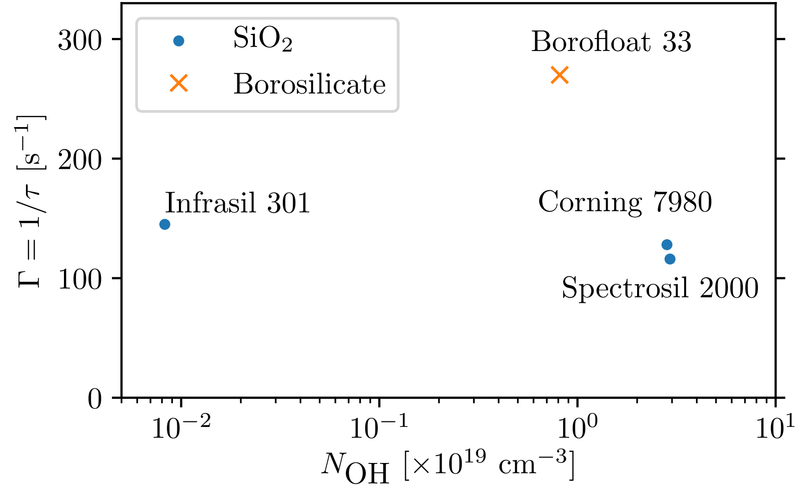

Figure 8.8: PL decay rate for thin films fabricated on four different glasses as a function of OH concentration in the bulk glass. The borosilicate glass has a PL higher decay rate to the silica glasses due to boron related defects caused by the high energy ions and electrons in the plume. The PL decay rates of the silica glasses show no/slight decreasing dependence with an increase in OH content, which is because the surface layer is dehydroxylated during processing.

the glasses. Electron-spin-resonance studies have shown that the presence of boron increases the sensitivity of silica glass to ionisation damage by orders of magnitude [241]. The formation of B-related point defects that result in significant internal non-radiative quenching for each Er^{3+} ion was shown by Snoeks, Kik, and Polman [91] through observations of an enhanced PL decay rate in ion implanted borosilicate glasses compared with sodalime glasses. The high energy ions in the ablation plume due to Coulomb explosion (see chapter 4) may therefore contribute to this non-radiative loss pathway. Surprisingly the decay rate for the silica and quartz glasses shows no/slight decreasing trend with OH density contradicting eq. (8.7). Infrasil 301 has the greatest decay rate at 145 s^{-1} despite having very little OH. Corning 7980 has the a decay rate of 128 s^{-1} and Spectrosil 2000 has the lowest decay rate of 116 s^{-1}, despite having the highest density of free OH-groups. To put these results into perspective, Fisher Premium sodalime glass with $N_{\mathrm{OH}} = 0.8 \times 10^{19}$ cm^{-3} and alkali-borosilicate BG33 with $N_{\mathrm{OH}} = 2.6 \times 10^{19}$ cm^{-3} both ion implanted with an Er^{3+} density of 1×10^{20} cm^{-3} had decay rates of $\sim$500 s^{-1} and 1250 s^{-1}, respectively [91].

The low decay rate despite the high substrate OH-group concentration and high Er^{3+}-doping concentrations combined with the decrease in decay rate with increasing OH concentration shows that energy migration does not occur in thin films fabricated with the ULPD technique. Either the doped ions do not couple to the free OH-groups or the free OH groups are not present within the film. Realising that the high temperature processing (600°C for 1 hour 44 minutes) induces a dehydroxylation process in the surface layer, described in section 8.2.2, it can be concluded that OH-group quenching by energy migration is negligible for thin films [231, 233]. The trend of slightly decreasing decay rate with increasing substrate N_{OH} is understood by considering that the emission spectra of the infrared heating lamp overlaps with the absorption peaks from OH and so substrates with higher N_{OH} (in the bulk, which does not change with dehydroxylation of the surface) are heated more efficiently and to higher temperatures. This is consistent with the trend of an increased refractive index at the top of the film for silica substrates with higher N_{OH}, which signifies a reduction in evaporation of Te. Furthermore the % inhomogeneity follows this trend, suggesting that the OH diffusion force out of the substrate counteracts the Fickian diffusion of deposited elements into the substrate resulting in the sharp transition region from film to substrate that is characteristic of the ULPD technique. The turbulence caused by the competing processes results in improved mixing, as evidenced by the smaller features in the mottling pattern for the high N_{OH} substrates in fig. 8.4. Note that the gradual transition in Borofloat 33 despite the relatively high OH content is due to low softening temperature that will increase the diffusion depth as the bonds in the glass network will be weakened.

The decay rates for the silica glasses in dependence of the film % inhomogenity, which characterises the differences in film thickness, grading and refractive index are shown in fig. 8.9. There is a strong linear dependence showing that with a more homogeneous environment and improved mixing, the average decay rate of the ions is improved. This is to be expected as a greater ion-ion separation is achieved through improved mixing, which reduces concentration quenching through cooperative upconversion and pair induced quenching. Furthermore, the cooperative upconversion is more efficient in tellurites due to the broader spectra and so the greater presence of Er^{3+} ions in a tellurite environment due to poorer dissolution further increases the decay rate.

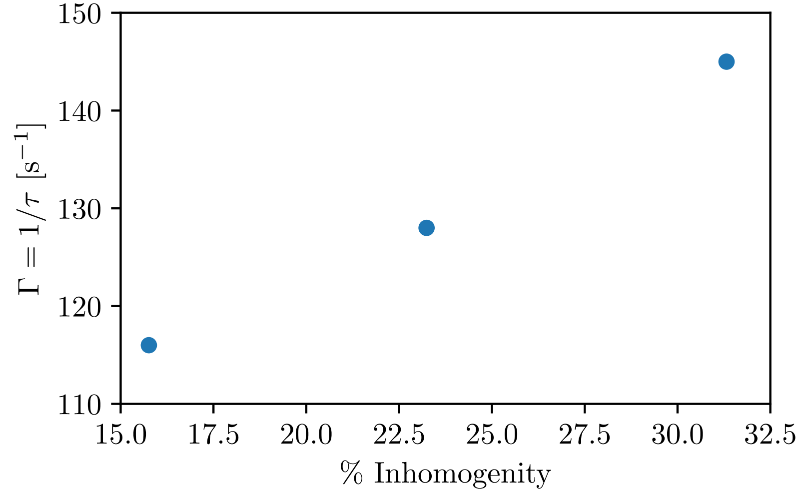

Figure 8.9: PL decay rate for films fabricated on SiO_2 glass substrates (Infrasil 301, Corning 7980 and Spectrosil 2000) as a function of the film inhomogenity (index grading from top to bottom of the film). The films with lower inhomogenity have improved dissolution and surface dissolution, due to increased radiative heating, and therefore have lower PL decay rates. Radiative heating of the bulk in these substrates was determined by the impurity OH content.

8.5 Conclusion

Er^{3+}-doped hybrid tellurite-silica thin films were fabricated using the ULPD technique using four different substrates; three silica glasses with varying OH contents and one borosilicate glass. The concentration of OH-groups was measured in the substrates prior to processing.

The refractive index and film thicknesses were measured using ellipsometry and depended strongly on the type of glass substrate. The fused silica glasses Spectrosil 2000 and Corning 7980 had thin and well defined films that had an index much higher than the substrate. Borofloat 33 and Infrasil 301 glasses had a higher index grading inhomogenity due to the more gradual transition from film to substrate. The differences are attributed to the dissolution which depends on a combination of the substrate OH content (determines the radiative absorption and resistive force due to dehydroxylation) and glass softening temperature (determines the weakening of the Si-O bonds).

The 1.54μm centred PL spectrum and lifetime were measured and it was found

that the fused silica substrates had the narrowest spectra with a FWHM of 21.6 nm. The broader spectra in Borofloat 33 and Infrasil 301 glass was partly attributed to the network-modifiers and a lower surface temperature due to reduced radiative heating efficiency, respectively. The PL lifetime differed between the borosilicate and the silica glasses but did not depend on the substrate OH-group impurity, a known non-radiative quenching site for Er^{3+}, as a dehydroxylation process was induced in the surface layer by the high temperature processing. This unique feature of the ULPD technique means that expensive high purity glasses are not required. Instead, concentration quenching in films primarily occurs through cooperative upconversion and future research should focus on characterising this. The high decay rate for Borofloat 33 was attributed to defects created by high energy ions. Reduction in energy of the ions and electrons in the ablation plume during processing, possibly through the use of an atmosphere, would result in an improved PL decay rate in this case. The results indicate that other silicate glasses would be suitable for use with the ULPD technique and may be preferable as their lower softening points will allow for lower processing temperatures and thicker films to be formed due to the higher CTE compared to silica.

Chapter 9

Conclusion and outlook

This thesis describes the physical processes behind film formation and Er^{3+} ion photoluminescence in hybrid tellurite-silica glass thin films fabricated with the ultrafast laser plasma doping (ULPD) technique. It documents the sequential steps from femtosecond laser ablation to plume expansion to film dissolution and comes at an ideal time as it coincides with the instalment of an upgraded ULPD system. While previous research has shown the superior spectroscopic properties of thin films fabricated with the ULPD technique compared to other conventional techniques, a lack of understanding in the processing parameters has hindered the fabrication of high quality thin films required for optical applications (i.e. low scattering losses, uniform thicknesses and controlled film growth rate). This is achieved through the sequential characterisation and optimisation of each parameters. The key findings of this research are summarised in section 9.1 and the further developments required, in both understanding of the underlying physical processes and technology implementation, for the ULPD technique are listed in section 9.2.

9.1 Key findings

Chapter 4 The first milestone was to identify the physical processes responsible for film formation in the ULPD technique and how these depend on the processing parameters. It was found that an oxygen atmosphere, which was used by previous research, was not necessary for film formation as nanoparticles are formed by the hydrodynamic expansion of the femtosecond laser irradiated material. Elimination of this parameter

greatly simplifies the process and can in future be used to modulate kinetic energy of electrons and ions in the plume. The optimisation methodology is outlined for the remaining processing parameters and can, in future research, be applied for new target glass compositions.

Chapter 5 Femtosecond laser ablation of the target only occurs above a certain threshold fluence. The single and multipulse values for tellurite glass were characterised at two laser spot sizes. At a Gaussian beam waist of 32.0 μm, the single pulse ablation threshold $F_{\mathrm{th}}(1) = 0.51$ J/cm^2 dropped to a multipulse value of $F_{\mathrm{th}}(\infty) = 0.18$ J/cm^2 due to material incubation. The ablation threshold was found to decrease with an increase in the laser spot size at the surface due to an increase in the probability of the laser beam striking a defect in the glass. It was also shown that the addition of a rare-earth dopant, which introduces linear absorption at the laser wavelength, had no effect on the ablation threshold. This is due to the fact that femtosecond light-matter interaction occurs through non-linear processes (multiphoton, tunneling and avalanche ionisation).

Chapter 6 The deposition of ablated material is primarily responsible for film formation in the ULPD technique. The laser fluence controls the constituents of the ablation plume (electrons, ions, nanoparticles and droplets). Large droplets are undesirable for thin film formation and only form if the laser fluence is sufficiently high. This fluence regime was found through room temperature depositions at different laser fluences to be $\gtrapprox 1$ J/cm^2 for a target with high surface roughness. The average radius of the nanoparticles in the plume was 12 nm. Furthermore, the target surface quality was found to affect the ablation threshold and particle size. Crystalline phases of $\gamma-TeO_2$ and $Zn_2Te_3O_8$ were present in the deposited material and it was reasoned that these may occur in the droplets, which travel the slowest in the plume and therefore undergo a longer period of slow radiative cooling.

Chapter 7 The fabrication of hybrid tellurite-silica films using the ULPD technique in a vacuum for the first time is presented. Film formation of the deposited material with the substrate silica glass is shown to occur through dissolution and evaporation. At a processing temperature of 600°C approximately 90% of the deposited tellurite

glass evaporated. The optimal laser fluence at a laser repetition of 1 kHz was $F = 1.56$ J/cm^2. Below this the material evaporation rate was higher than the deposition rate and so no film was formed. At higher fluences, the material deposition rate was above the dissolution rate resulting in multi-exponential photoluminescence decays. Furthermore, the droplet presence and size in the ablation plume increases with laser fluence and resulted in rougher film surfaces.

Chapter 8 OH-groups are known quenching centres for Er^{3+} ions and act to decrease the photoluminescence lifetime through energy migration. This effect becomes much more efficient at high doping concentrations. Processing during the ULPD technique occurs at high temperature and is shown to cause the surface of silica glass to to dehydroxylate. As a result, the non-radiative losses in the highly doped films are primarily attributed to the cooperative upconversion process and do not depend on the bulk substrate OH content. Instead the substrate OH content improves the radiative heating efficiency by the infrared lamps leading to higher quality films. The thin films fabricated with on a borosilicate substrate had a reduced photoluminescence lifetime due the high energy electrons in the plume creating boron related defects.

9.2 Further investigations

Laser repetition rate For optimal film surface quality, i.e. low surface roughness, the laser fluence is ideally tuned just above the target ablation threshold so that the ablation plume is free of droplets. The laser repetition rate must therefore be increased significantly from the 1 kHz used in this research to provide a suitable material deposition rate on the substrate that overcomes the evaporation rate and gives a suitable film growth rate. In addition to this, increasing the throughput of film production with the ULPD technique in the future will likely require megahertz repetition rate lasers. Increasing the laser repetition rate to this regime must take into account two key effects. Firstly, the laser pulse must not interact with the ablation plume from the previous pulse as this may ionise the ablation plume, when the process requires the deposition of nanoparticles. Secondly, the coupling of successive pulses on the target can lead to an accumulation of heat in the fluence region below ablation threshold of

the Gaussian pulse, leading to differences in the ablation.

Substrate heating The upper limit to the processing temperature of the upgraded ULPD system was 600°C as the increased radiation emitted by the bank of quartz infrared heating lamps reaching the target caused it to melt above this point. This was a key limitations for silica substrates as a high enough temperature for optimal film dissolution could not be achieved. Previous studies have shown that temperatures above 700°C are optimal. Silica-on-silicon substrates did not have this issue due to increased radiative absorption and conductive heating form the substrate holder. The OH-group content in silica, which are also a quenching site for Er^{3+} ions, is primarily responsible for radiative absorption and so, somewhat counter intuitively, the lower purity silica glasses had improved thin film physical and optical properties. The improved heating also increases the surface dehydroxylation and so quenching sites do not exist in the film region despite being present in the bulk. A resistive pressure due to dehydroxylation also appears to affect the tellurite-silica dissolution process and requires further investigation. Ideally the glass OH-content should be decoupled from the heating efficiency. A possibility is to back the silica substrates with an absorbing coating or material to enhance the heating efficiency and reduce the intensity of radiation reaching the target. Alternatively the heating elements could be changed to SiC elements (used in the previous system) with a flatter emission spectrum. Another more radical solution would be to use a CO_2 laser to directly heat the substrate surface layer from below.

High energy ions and electrons High energy ions and electrons in the plume arise due to Coulomb explosion when ablating the dielectric target glass. Their role in film formation was not specifically investigated as part of this research as it was not deemed critical due to the relatively small contribution to the total ablated mass. Nonetheless, the impact on the substrate is known to possibly cause detrimental effects such as sputtering, crystallisation and compositional changes. Furthermore the sensitivity of borosilicate glass to ion related defects is believed to result in high photoluminescence decay rates. It has been suggested that the energy of the ions and electrons may be modulated with the introduction of an atmosphere into the chamber. While it is not deemed critical to film fabrication with the ULPD technique, as evidenced by the comparable results for films fabricated in vacuum here to previous films fabricated in an

oxygen atmosphere, Langmuir probe studies will be able to quantify their energy and possible dependence on processing parameters.

Plume species The temperature, velocity and ratio of constituents (ions, nanoparticles, droplets) in the ablation plume can be quantified with time-resolved optical emission spectroscopy. Characterisation of these characteristics will provide an insight into the dynamics of plume transport. Furthermore, the introduction of a gas atmosphere will act to reduce the plume energy through collisions, and so quantification is required to understand the observed differences in the film properties.

Target and substrate glass The use of zinc-sodium tellurite target glasses is standard in the ULPD technique. It was shown that the majority of tellurium evaporates at the substrate surface during dissolution and so the use of tellurium may not be critical. The zinc and sodium remains in the film surface and so the use of a sodalime substrate may eliminate the need for sodium in the target glass. Furthermore, the use of lower processing temperatures may be possible due to the lower softening temperature and the higher coefficient of thermal expansion will allow for thicker films without cracking. Other compositions of target glasses should be investigated using a similar characterisation procedure as presented in this thesis as new compositions will enable further tuning of the spectroscopic and physical properties of the thin glass films.

Radiative decay rate The radiative decay rate of the $4f$ rare-earth ion transitions are only weakly dependent on the host. The work in this thesis has assumed a similar radiative decay rate of 42 s^{-1} that is found for Er^{3+} ions implanted in silica. While acceptable, an accurate determination is not a major task and should be undertaken for a more rigorous characterisation of the photoluminescence properties in the hybrid tellurite-silica material fabricated with the ULPD technique. A simple measurement technique is to vary the refractive index of the superstrate on a film and compare theoretical simulations for the decay rate inside the film with the experimentally measured ones [28, 45].

Cooperative upconversion Concentration quenching reduces the photoluminescence lifetime at high doping concentrations due to the reduced ion separation distances.

Energy migration to OH-group quenching points is not significant in Er^{3+}-doped thin films fabricated with the ULPD technique due to surface dehydroxylation at the high processing temperatures. Non-radiative decay through cooperative upconversion dominates and should therefore be characterised. The interaction is typically characterised by the pump dependent lifetime in waveguiding films and should be the focus of the next investigation into the optical properties of the films. A quantification of cooperative upconversion will allow for numerical modelling to guide the experimental sample fabrication for optical devices, especially waveguide amplifiers.

Photonic applications Most importantly, the realisation of an Er^{3+}-doped waveguide amplifier should be the next step. Previous research has proven the suitable material properties of the films and the processing parameters required for a suitable film quality have been identified in this research. The fabrication of a strip loaded waveguide from a planar film is relatively straightforward and will be a true demonstration for the capability of this technique. Further down the line, optical devices such as lasers, ring resonators and sensors are all feasible with little modification required to the processing parameters.

References

[1] P Balling and J Schou. “Femtosecond-laser ablation dynamics of dielectrics: basics and applications for thin films”. *Reports on Progress in Physics* 76.3 (2013), p. 036502.

[2] P.G. Kik and A Polman. “Erbium-Doped Optical-Waveguide Amplifiers on Silicon”. *MRS Bulletin* 23.04 (1998), pp. 48–54.

[3] Jia-Ming Liu. *Photonic devices.* Cambridge University Press, 2009.

[4] E. Desurvire. “Erbium-doped fiber amplifiers”. *in Principle and applications* (1992).

[5] Appl Polman. “Erbium implanted thin film photonic materials”. *Journal of Applied Physics* 82.1 (1997), pp. 1–39.

[6] Jayakrishnan Chandrappan et al. “Target dependent femtosecond laser plasma implantation dynamics in enabling silica for high density erbium doping”. *Scientific reports* 5.February (2015), p. 14037.

[7] F. Auzel and P. Goldner. “Towards rare-earth clustering control in doped glasses”. *Optical Materials* 16.1-2 (2001), pp. 93–103.

[8] Kazuo Arai et al. “Aluminum or phosphorus co-doping effects on the fluorescence and structural properties of neodymium-doped silica glass”. *Journal of Applied Physics* 59.10 (1986), pp. 3430–3436.

[9] Tao Pan et al. “Gain flattened, high index contrast planar Er3+-doped waveguide amplifier with an integrated mode size converter” (2002).

[10] K Shuto et al. “Erbium-doped phosphosilicate glass waveguide amplifier fabricated by PECVD”. *Electronics Letters* 29.2 (1993), pp. 139–141.

[11] Ruby N Ghosh et al. “8-mV threshold Er3+-doped planar waveguide amplifier”. *IEEE Photonics Technology Letters* 8.4 (1996), pp. 518–520.

[12] M Nakazawa and Y Kimura. "Electron-beam vapour-deposited erbium-doped glass waveguide laser at 1.53 μm". *Electronics Letters* 28.22 (1992), pp. 2054–2056.

[13] Robert R Thomson et al. "Internal gain from an erbium-doped oxyfluoride-silicate glass waveguide fabricated using femtosecond waveguide inscription". *IEEE Photonics Technology Letters* 18.14 (2006), pp. 1515–1517.

[14] A Bouajaj, R R Gonçalves, and M Ferrari. "Sol-Gel-Derived Erbium-Activated Silica-Titania and Silica-Hafnia Planar Waveguides for 1.5 μm Application in C Band of Telecommunication". *Spectroscopy Letters* 47.5 (2014), pp. 381–386.

[15] Khu Vu and Steve Madden. "Tellurium dioxide Erbium doped planar rib waveguide amplifiers with net gain and 2.8 dB/cm internal gain". *Optics express* 18.18 (2010), pp. 19192–19200.

[16] Y C Yan et al. "Erbium-doped phosphate glass waveguide on silicon with 4.1 dB/cm gain at 1.535 µm". *Applied Physics Letters* 2922 (1997), pp. 1–4.

[17] Motoshi Ono et al. "Fabrication of ultra-compact Er-doped waveguide amplifier based on bismuthate glass". *Journal of the Ceramic Society of Japan* 116.1358 (2008), pp. 1134–1138.

[18] Yuki Kondo et al. "Fabrication of Bi2O3-based Er-doped waveguide for integrated optical amplifiers". *Optical Fiber Communication Conference*. Optical Society of America. 2002, TuB4.

[19] J D B Bradley et al. "Gain bandwidth of 80 nm and 2 dB/cm peak gain in Al 2 O 3: Er 3+ optical amplifiers on silicon". *JOSA B* 27.2 (2010), pp. 187–196.

[20] Ross Schermer et al. "Optical amplification at 1534 nm in erbium-doped zirconia waveguides". *IEEE journal of quantum electronics* 39.1 (2003), pp. 154–159.

[21] Anh Quoc Le Quang et al. "Demonstration of net gain at 1550 nm in an erbium-doped polymersingle mode rib waveguide". *Applied physics letters* 89.14 (2006), p. 141124.

[22] R E N Fang et al. "Thermal stability and Judd-Ofelt analysis of optical properties of Er3+-doped tellurite glasses". *Transactions of Nonferrous Metals Society of China* 22.8 (2012), pp. 2021–2026.

[23] Jayakrishnan Chandrappan et al. "Doping silica beyond limits with laser plasma for active photonic materials". *Optical Materials Express* 5.12 (Dec. 2015), p. 2849.

[24] Suraya Ahmad Kamil et al. "Ultrafast laser plasma doping of Erˆ3+ ions in silica-on-silicon for optical waveguiding applications". *Optics Letters* 41.20 (Oct. 2016), p. 4684.

[25] Billy D.O. O. Richards et al. "Tm3+ Tellurite-Modified-Silica Glass Thin Films Fabricated Using Ultrafast Laser Plasma Doping". *IEEE Journal of Selected Topics in Quantum Electronics* 25.4 (2019), pp. 1–8.

[26] Thomas Mann et al. "Femtosecond laser ablation properties of Er3+ ion doped zinc-sodium tellurite glass". *Journal of Applied Physics* 124.4 (2018), p. 044903.

[27] Christian Cortes and Zubin Jacob. "Fundamental figures of merit for engineering Forster resonance energy transfer". *arXiv Optics* 26.15 (2018), pp. 19371–19387.

[28] Celestino Creatore et al. "Modification of erbium radiative lifetime in planar silicon slot waveguides". *Applied Physics Letters* 94.10 (2009), p. 103112.

[29] A J Kenyon. "Erbium in silicon". *Semiconductor Science and Technology* 20.12 (2005), R65.

[30] Robert J. Moerland and Jacob P. Hoogenboom. "Subnanometer-accuracy optical distance ruler based on fluorescence quenching by transparent conductors". *Optica* 3.2 (2016), p. 112.

[31] Pablo Solano et al. "Super- and sub-radiance reveal infinite-range interactions through a nanofiber". *Nature* 8.1 (2017), pp. 1–19.

[32] Joseph R Lakowicz. *Principles of fluorescence spectroscopy.* 2nd ed. Springer, 1999.

[33] P G Wu and Ludwig Brand. "Resonance energy transfer: methods and applications". *Analytical biochemistry* 218.1 (1994), pp. 1–13.

[34] Feng Wang and Xiaogang Liu. "Recent advances in the chemistry of lanthanide-doped upconversion nanocrystals". *Chemical Society Reviews* 38.4 (2009), p. 976.

[35] George W Ford and Willes H Weber. "Electromagnetic interactions of molecules with metal surfaces". *Physics Reports* 113.4 (1984), pp. 195–287.

[36] Celestino Creatore and Lucio Claudio Andreani. "Quantum theory of spontaneous emission in multilayer dielectric structures". *Physical Review A* 78.6 (2008), p. 63825.

[37] Jun John Sakurai. *Advanced quantum mechanics.* Pearson Education India, 1967.

[38] Rodney Loudon. *The quantum theory of light.* OUP Oxford, 2000.

[39] H. Khosravi and R. Loudon. "Vacuum Field Fluctuations and Spontaneous Emission in the Vicinity of a Dielectric Surface". *Proceedings of the Royal Society A: Mathematical, Physical and Engineering Sciences* 433.1888 (1991), pp. 337–352.

[40] Maciej Janowicz et al. "Quantum radiation of a harmonic oscillator near the planar dielectric-vacuum interface". *Physical Review A* 50.5 (1994), p. 4350.

[41] Roy J. Glauber and M. Lewenstein. "Quantum optics of dielectric media". *Physical Review A* 43.1 (1991), pp. 467–491.

[42] E Yablonovitch, T J Gmitter, and R Bhat. "Inhibited and enhanced spontaneous emission from optically thin AlGaAs/GaAs double heterostructures". *Physical review letters* 61.22 (1988), p. 2546.

[43] Edward Mills Purcell. "Spontaneous emission probabilities at radio frequencies". *Physical Review* 69 (1946), p. 681.

[44] Daniel Kleppner. "Inhibited spontaneous emission". *Physical Review Letters* 47.4 (1981), pp. 233–236.

[45] E. Snoeks, A. Lagendijk, and A. Polman. "Measuring and modifying the spontaneous emission rate of erbium near an interface". *Physical review letters* 74.13 (1995), p. 2459.

[46] R Sprik, B A Van Tiggelen, and A Lagendijk. "Optical emission in periodic dielectrics". *EPL (Europhysics Letters)* 35.4 (1996), p. 265.

[47] Evangelos Almpanis et al. "Tuning the spontaneous light emission in phoxonic cavities". *JOSA B* 29.9 (2012), pp. 2567–2574.

[48] Vilson R Almeida et al. "Guiding and confining light in void nanostructure". *Optics letters* 29.11 (2004), pp. 1209–1211.

[49] Qianfan Xu et al. "Experimental demonstration of guiding and confining light in nanometer-size low-refractive-index material". *Optics letters* 29.14 (2004), pp. 1626–1628.

[50] Władysław Żakowicz and Maciej Janowicz. "Spontaneous emission in the presence of a dielectric cylinder". *Physical Review A - Atomic, Molecular, and Optical Physics* 62.1 (2000), p. 17.

[51] Ali M. Adawi et al. "Spontaneous emission control in micropillar cavities containing a fluorescent molecular dye". *Advanced Materials* 18.6 (2006), pp. 742–747.

[52] Jung-Hwan Song et al. "Fast and bright spontaneous emission of Er3+ ions in metallic nanocavity". *Nature Communications* 6.May (2015), p. 7080.

[53] M. D. Birowosuto et al. "Observation of spatial fluctuations of the local density of states in random photonic media". *Physical Review Letters* 105.1 (2010), pp. 20–23.

[54] Peter Lodahl et al. "Controlling the dynamics of spontaneous emission from quantum dots by photonic crystals". *Nature* 430.7000 (2004), p. 654.

[55] R Lo Savio et al. "Room-temperature emission at telecom wavelengths from silicon photonic crystal nanocavities". *Applied Physics Letters* 98.20 (2011), p. 201106.

[56] R Lo Savio et al. "Photonic crystal light emitting diode based on Er and Si nanoclusters co-doped slot waveguide". *Applied Physics Letters* 104.12 (2014), p. 121107.

[57] C. K. Carniglia and L. Mandel. "Quantization of Evanescent Electromagnetic Waves". *Physical Review D* 3.2 (Jan. 1971), pp. 280–296.

[58] David L Dexter. "A theory of sensitized luminescence in solids". *The Journal of Chemical Physics* 21.5 (1953), pp. 836–850.

[59] David Andrews. "Resonance Energy Transfer: Theoretical Foundations and Developing Applications". *Tutorials in Complex Photonic Media* 46 (2009), pp. 439–478.

[60] Th Förster. "Zwischenmolekulare energiewanderung und fluoreszenz". *Annalen der physik* 437.1-2 (1948), pp. 55–75.

[61] Gregory D. Scholes. "Long-range resonance energy transfer in molecular systems". *Annual Review of Physical Chemistry* 54.1 (2003), pp. 57–87.

[62] Baldassare Di Bartolo and Xuesheng Chen. *Advances in energy transfer processes: proceedings of the 16th course of the International School of Atomic and Molecular Spectroscopy: Erice, Sicily, Italy, 17 June-1 July, 1999.* World Scientific, 2001.

[63] Pradyot Patnaik. *Handbook of inorganic chemicals.* Vol. 529. McGraw-Hill New York, 2003.

[64] William Miniscalco. "Optical and Electronic Properties of Rare Earth Ions in Glasses". *Rare earth doped fiber lasers and amplifiers.* Marcel Dekker, Inc., 1993. Chap. 2.

[65] S Hufner. *Optical Spectra of Transparent Rare Earth Compounds*. Academic press, 1978.

[66] I. Hemmilä and V. Laitala. "Progress in lanthanides as luminescent probes". *Journal of Fluorescence* 15.4 (2005), pp. 529–542.

[67] C.R. Giles and E. Desurvire. "Modeling erbium-doped fiber amplifiers". *Journal of Lightwave Technology* 9.2 (1991), pp. 271–283.

[68] A.J Kenyon. "Recent developments in rare-earth doped materials for optoelectronics". *Progress in Quantum Electronics* 26.4 (2002), pp. 225–284.

[69] William J. Miniscalco. "Erbium-Doped Glasses for Fiber Amplifiers at 1500 nm". *Journal of Lightwave Technology* 9.2 (1991), pp. 234–250.

[70] D. L. Sidebottom et al. "Structure and optical properties of rare earth-doped zinc oxyhalide tellurite glasses". *Journal of non-crystalline solids* 222 (1997), pp. 282–289.

[71] Brian R. Judd. "Optical Absorption Intensities of Rare-Earth Ions". *Physical Review* 197.3 (1962).

[72] G. S. Ofelt. "Intensities of Crystal Spectra of Rare-Earth Ions". *The Journal of Chemical Physics* 37.3 (1962), pp. 511–520.

[73] C A Morrison, R P Leavitt, and C A Morrison. "Crystal-field analysis of triply ionized rare earth ions in lanthanum trifluoride". *The Journal of Chemical Physics* 71.2 (1979), pp. 749–757.

[74] R P Leavitt and C A Morrison. "Crystal-field analysis of triply ionized rare earth ions in lanthanum trifluoride. II. Intensity calculations". *The Journal of Chemical Physics* 73.2 (1980), pp. 749–757.

[75] G. C. Righini and M. Ferrari. "Photoluminescence of rare-earth-doped glasses". *Rivista del Nuovo Cimento* 28.12 (2005), pp. 1–53.

[76] G. Liu and B. Jacquier. *Spectroscopic Properties of Rare Earths in Optical Materials*. Vol. 83. Springer, 2005, pp. 103–169.

[77] R. S. Quimby, W. J. Miniscalco, and B. Thompson. "Clustering in erbium-doped silica glass fibers analyzed using 980 nm excited-state absorption". *Journal of Applied Physics* 76.8 (1994), pp. 4472–4478.

[78] Vincent Benoit et al. “Optical and spectroscopic properties of erbium-activated modified silica glass with 1.54 μm high quantum efficiency”. Ed. by Shibin Jiang and Michel J. Digonnet. International Society for Optics and Photonics, Apr. 2005, p. 79.

[79] M D Shinn et al. “Optical transitions of Er + ions in fluorozirconate glass”. *Physical Review B* 27.11 (1983).

[80] Toru Miyakawa and D. L. Dexter. “Phonon sidebands, multiphonon relaxation of excited states, and phonon-assisted energy transfer between ions in solids”. *Physical Review B* 1.7 (1970), pp. 2961–2969.

[81] Leslie Allen Riseberg and H-W Moos. “Multiphonon orbit-lattice relaxation of excited states of rare-earth ions in crystals”. *Physical Review* 174.2 (1968), p. 429.

[82] J. M.F. Van Dijk and M. F.H. Schuurmans. “On the nonradiative and radiative decay rates and a modified exponential energy gap law for 4f-4f transitions in rare-earth ions”. *The Journal of Chemical Physics* 78.9 (1983), pp. 5317–5323.

[83] C. B. Layne, W. H. Lowdermilk, and M. J. Weber. “Multiphonon relaxation of rare-earth ions in oxide glasses”. *Physical Review B* 16.1 (1977), pp. 10–20.

[84] R. Reisfeld and Y. Eckstein. “Dependence of spontaneous emission and non-radiative relaxations of Tm3+and Er3+on glass host and temperature”. *The Journal of Chemical Physics* 63.9 (1975), pp. 4001–4012.

[85] J. S. Wang, E. M. Vogel, and E. Snitzer. “Tellurite glass: a new candidate for fiber devices”. *Optical Materials* 3.3 (1994), pp. 187–203.

[86] A Jha et al. “Review on structural, thermal, optical and spectroscopic properties of tellurium oxide based glasses for fibre optic and waveguide applications”. *International Materials Reviews* 57.6 (2012), pp. 357–382.

[87] Thalangunam Krishnaswamy Subramaniam. “Erbium Doped Fiber Lasers for Long Distance Communication Using Network of Fiber Optics”. *American Journal of Optics and Photonics* 3.3 (2015), p. 34.

[88] François Auzel. “Upconversion and Anti-Stokes Processes with f and d Ions in Solids”. *Chemical Reviews* 104.1 (2004), pp. 139–173.

[89] F Auzel. “Multiphonon processes, cross-relaxation and up-conversion in ion-activated solids, exemplified by minilaser materials”. *Radiationless processes.* Springer, 1980, pp. 213–286.

[90] Yingchao Yan, Anne Jans Faber, and Henk de Waal. "Luminescence quenching by OH groups in highly Er-doped phosphate glasses". *Journal of Non-Crystalline Solids* 181.3 (1995), pp. 283–290.

[91] E Snoeks, P G Kik, and A Polman. "Concentration quenching in erbium implanted alkali silicate glasses". *Optical Materials* 5.3 (1996), pp. 159–167.

[92] Shixun Dai et al. "Concentration quenching in erbium-doped tellurite glasses". *Journal of Luminescence* 117.1 (2006), pp. 39–45.

[93] Allan J Bruce et al. "Concentration and Hydroxyl Impurity Quenching of the 4 I 13/2- 4 I 15/2 Luminescence in Er 3+ Doped Sodium Silicate Glasses". *MRS Online Proceedings Library Archive* 244 (1991).

[94] G N den Hoven et al. "Upconversion in Er-implanted Al2O3 waveguides". *Journal of Applied Physics* 79.3 (1996), pp. 1258–1266.

[95] E Snoeks et al. "Cooperative upconversion in erbium-implanted soda-lime silicate glass optical waveguides". *JOSA B* 12.8 (1995), pp. 1468–1474.

[96] David Boivin et al. "Quenching investigation on new erbium doped fibers using MCVD nanoparticle doping process". *SPIE* 7580.February (2010), 75802B.

[97] J Nilsson et al. "Evaluation of Parasitic Upconversion Mechanisms Analysis of Fluorescence at 980 nm". *Lightwave* 13.3 (1995).

[98] Henning Kühn et al. "Model for the calculation of radiation trapping and description of the pinhole method". *Optics Letters* 32.13 (2007), p. 1908.

[99] Cyril Koughia and Safa O Kasap. "Excitation diffusion in GeGaSe and GeGaS glasses heavily doped with Er3+". *Optics express* 16.11 (2008), pp. 7709–7714.

[100] Z. Y. Zhang et al. "Characterization of erbium-doped intrinsic optical fiber sensor probes at high temperatures". *Review of Scientific Instruments* 69.8 (1998), pp. 2924–2929.

[101] Jaehoon Jung, Namkyoo Park, and Byoungho Lee. "Simultaneous measurement of strain and temperature by use of a single fiber Bragg grating written in an erbium:ytterbium-doped fiber". *Applied Optics* 39.7 (2000), p. 1118.

[102] D. N. Messias et al. "All optical integrated upconversion fluorescence-based point temperature sensing system using Er3+-doped silica-on-silicon waveguides". *Review of Scientific Instruments* 73.2 I (2002), pp. 476–479.

[103] E. Maurice et al. "Erbium-doped silica fibers for intrinsic fiber-optic temperature sensors". *Applied Optics* 34.34 (1995), p. 8019.

[104] Peng Chun Peng et al. "Long-distance fiber grating sensor system using a fiber ring laser with EDWA and SOA". *Optics Communications* 252.1-3 (2005), pp. 127–131.

[105] Emmanuel Desurvire, Jay R Simpson, and P C Becker. "High-gain erbium-doped traveling-wave fiber amplifier". *Optics Letters* 12.11 (1987), pp. 888–890.

[106] Emmanuel Desurvire. *Erbium-doped fiber amplifiers: principles and applications.* Wiley New York, 1994.

[107] Robert J Mears et al. "Low-noise erbium-doped fibre amplifier operating at 1.54 μm". *Electronics Letters* 23.19 (1987), pp. 1026–1028.

[108] A Jha, S Shen, and M Naftaly. "Structural origin of spectral broadening of 1.5-μm emission in Er3+-doped tellurite glasses". *Physical Review B - Condensed Matter and Materials Physics* 62.10 (2000), pp. 6215–6227.

[109] Fang Ren et al. "Thermal stability and Judd-Ofelt analysis of optical properties of Er3+-doped tellurite glasses". *Transactions of Nonferrous Metals Society of China (English Edition)* 22.8 (2012), pp. 2021–2026.

[110] L. Weng and S. N.B. Hodgson. "Sol-gel processing of TeO2-TiO2-PbO thin films". *Journal of Non-Crystalline Solids* 297.1 (2002), pp. 18–25.

[111] V. K. Tikhomirov. "Characterization of ion-exchanged waveguides in tungsten tellurite and zinc tellurite Er3+-doped glasses". *Optical Engineering* 42.10 (2003), p. 2805.

[112] V A G Rivera et al. "Planar waveguides by ion exchange in Er3+-doped tellurite glass". *Journal of Non-Crystalline Solids* 352.5 (2006), pp. 363–367.

[113] Shinichi Sakida, Tokuro Nanba, and Yoshinari Miura. "Optical properties of Er3+-doped tungsten tellurite glass waveguides by Ag+–Na+ ion-exchange". *Optical materials* 30.4 (2007), pp. 586–593.

[114] E. B. Intyushin and Yu I. Chigirinskii. "Preparation of amorphous films from tungsten tellurite glasses by radio-frequency magnetron sputtering of an oxide target". *Glass Physics and Chemistry* 31.2 (2005), pp. 162–164.

[115] Ranu Nayak et al. "Optical waveguiding in amorphous tellurium oxide thin films". *Thin Solid Films* 445.1 (2003), pp. 118–126.

[116] A. P. Caricato et al. "Er3+-doped tellurite waveguides deposited by excimer laser ablation". *Materials Science and Engineering B: Solid-State Materials for Advanced Technology* 105.1-3 (2003), pp. 65–69.

[117] M. Bouazaoui et al. "Pulsed laser deposition of Er doped tellurite films on large area". *Journal of Physics: Conference Series* 59.1 (2007), pp. 475–478.

[118] M. Martino et al. "Pulsed laser deposition of active waveguides". *Thin Solid Films* 433.1-2 SPEC. (2003), pp. 39–44.

[119] Robert W Eason et al. "Optical waveguide growth and applications". *Pulsed Laser Deposition of Thin Films: Applications-Led Growth of Functional Materials* (2007), pp. 385–420.

[120] Rajiv K. Singh, D. Bhattacharya, and J. Narayan. "Subsurface heating effects during pulsed laser evaporation of materials". *Applied Physics Letters* 57.19 (1990), pp. 2022–2024.

[121] C. Boulmer-Leborgne et al. "Femtosecond laser beam in interaction with materials for thin film deposition". *Proceedings of SPIE - The International Society for Optical Engineering* 6261 II (2006), pp. 2–10.

[122] O. Albert et al. "Time-resolved spectroscopy measurements of a titanium plasma induced by nanosecond and femtosecond lasers". *Applied Physics A: Materials Science and Processing* 76.3 (2003), pp. 319–323.

[123] Eugene G Gamaly, Andrei V Rode, and Barry Luther-Davies. "Film Deposition". *Pulsed laser deposition of thin films: applications-led growth of functional materials* (2007), p. 99.

[124] J. Perrière et al. "Nanoparticle formation by femtosecond laser ablation". *Journal of Physics D: Applied Physics* 40.22 (2007), pp. 7069–7076.

[125] Mikel Sanz et al. "Ultrafast Laser Ablation and Deposition of Wide Band Gap Semiconductors". *The Journal of Physical Chemistry C* 115.8 (2011), pp. 3203–3211.

[126] Mikel Sanz et al. "Femtosecond pulsed laser deposition of nanostructured TiO2 films". *Applied Surface Science* 255.10 (2009), pp. 5206–5210.

[127] G. Jose et al. "High quality erbium doped tellurite glass films using ultrafast laser deposition". *2009 11th International Conference on Transparent Optical Networks* (2009), pp. 20–23.

[128] G Jose et al. "Multi-ion diffusion in silica glass using femtosecond pulsed laser deposition". *Conference on Lasers and Electro-Optics: Science and Innovations* (2012), pp. 5–6.

[129] M. Sanz et al. "Ultra-fast laser ablation and deposition of TiO2". *Applied Physics A: Materials Science and Processing* 101.4 (2010), pp. 639–644.

[130] Jayakrishnan Chandrappan et al. "Devitrification of ultrafast laser plasma produced metastable glass layer". *Scripta Materialia* 131 (2017), pp. 37–41.

[131] J. Schou. "Physical aspects of the pulsed laser deposition technique: The stoichiometric transfer of material from target to film". *Applied Surface Science* 255.10 (2009), pp. 5191–5198.

[132] Baerbel Rethfeld Anisimov et al. "Modelling ultrafast laser ablation". *Journal of Physics D: Applied Physics* 50.19 (2017), p. 193001.

[133] Adela Ben-Yakar and Robert L. Byer. "Femtosecond laser ablation properties of borosilicate glass". *Journal of Applied Physics* 96.9 (2004), pp. 5316–5323.

[134] L V Keldysh et al. "Ionization in the field of a strong electromagnetic wave". *Sov. Phys. JETP* 20.5 (1965), pp. 1307–1314.

[135] I Introduction and N Bloembergen. "Laser-induced electric breakdown in solids". *IEEE Journal of Quantum Electronics* 10.3 (1974), pp. 375–386.

[136] A Kaiser et al. "Microscopic processes in dielectrics under irradiation by subpicosecond laser pulses". *Phys. Rev. B* 61.17 (May 2000), pp. 11437–11450.

[137] Baerbel Rethfeld. "Free-electron generation in laser-irradiated dielectrics". *Physical Review B* 73.3 (2006), p. 35101.

[138] P C Becker et al. "Femtosecond photon echoes from band-to-band transitions in GaAs". *Physical review letters* 61.14 (1988), p. 1647.

[139] D von der Linde, K Sokolowski-Tinten, and J Bialkowski. "Laser-solid interaction in the femtosecond time regime". *Applied Surface Science* 109-110.March 2016 (1997), pp. 1–10.

[140] R. Stoian et al. "Surface charging and impulsive ion ejection during ultrashort pulsed laser ablation". *Physical Review Letters* 88.9 (2002), pp. 976031–976034.

[141] N M Bulgakova et al. "Electronic transport and consequences for material removal in ultrafast pulsed laser ablation of materials". *Phys. Rev. B* 69.5 (Feb. 2004), p. 54102.

[142] R. Stoian et al. "Coulomb explosion in ultrashort pulsed laser ablation of Al2O3". *Physical Review B - Condensed Matter and Materials Physics* 62.19 (2000), pp. 13167–13173.

[143] Christoph Rose-Petruck et al. "Picosecond-milliångström lattice dynamics measured by ultrafast X-ray diffraction". *Nature* 398 (1999), p. 310.

[144] H J Zeiger et al. "Theory for displacive excitation of coherent phonons". *Phys. Rev. B* 45.2 (Jan. 1992), pp. 768–778.

[145] Dmitriy Ivanov and Leonid Zhigilei. "Combined atomistic-continuum modeling of short-pulse laser melting and disintegration of metal films". *Physical Review B - Condensed Matter and Materials Physics* 68.6 (2003), pp. 1–22.

[146] S Amoruso et al. "Emission of nanoparticles during ultrashort laser irradiation of silicon targets". *Europhysics Letters (EPL)* 67.3 (2004), pp. 404–410.

[147] Thornton Ernest Glover. "Hydrodynamics of particle formation following femtosecond laser ablation". *Journal of the Optical Society of America B* 20.1 (2003), p. 125.

[148] Adela Ben-Yakar et al. "Thermal and fluid processes of a thin melt zone during femtosecond laser ablation of glass: The formation of rims by single laser pulses". *Journal of Physics D: Applied Physics* 40.5 (2007), pp. 1447–1459.

[149] F. Vidal et al. "Critical-point phase separation in laser ablation of conductors". *Physical Review Letters* 86.12 (2001), pp. 2573–2576.

[150] N. A. Inogamov et al. "Nanospallation induced by an ultrashort laser pulse". *Journal of Experimental and Theoretical Physics* 107.1 (2008), pp. 1–19.

[151] E. Millon et al. "Femtosecond pulsed-laser deposition of BaTiO3". *Applied Physics A: Materials Science and Processing* 77.1 (2003), pp. 73–80.

[152] S. Amoruso et al. "Femtosecond laser pulse irradiation of solid targets as a general route to nanoparticle formation in a vacuum". *Physical Review B - Condensed Matter and Materials Physics* 71.3 (2005), pp. 1–4.

[153] S. Amoruso et al. "Generation of silicon nanoparticles via femtosecond laser ablation in vacuum". *Applied Physics Letters* 84.22 (2004), pp. 4502–4504.

[154] Roberto Teghil et al. "Nanoparticles and thin film formation in ultrashort pulsed laser deposition of vanadium oxide". *Journal of Physical Chemistry A* 113.52 (2009), pp. 14969–14974.

[155] P. P. Pronko et al. "Isotope enrichment in laser-ablation plumes and commensurately deposited thin films". *Physical Review Letters* 83.13 (1999), pp. 2596–2599.

[156] P. K. Diwakar et al. "Expansion dynamics of ultrafast laser produced plasmas in the presence of ambient argon". *Journal of Applied Physics* 116.13 (2014).

[157] P. K. Diwakar et al. "Characterization of ultrafast laser-ablation plasma plumes at various Ar ambient pressures". *Journal of Applied Physics* 118.4 (2015).

[158] Salvatore Amoruso, B. Toftmann, and Jørgen Schou. "Thermalization of a UV laser ablation plume in a background gas: From a directed to a diffusionlike flow". *Physical Review E - Statistical Physics, Plasmas, Fluids, and Related Interdisciplinary Topics* 69.5 (2004), p. 6.

[159] E. G. Gamaly et al. "Expansion-limited aggregation of nanoclusters in a single-pulse laser-produced plume". *Physical Review B - Condensed Matter and Materials Physics* 80.18 (2009), pp. 1–12.

[160] J Perriere et al. "Comparison between ZnO films grown by femtosecond and nanosecond laser ablation". *Journal of Applied Physics* 91.2 (2002), pp. 690–696.

[161] Eric. Kumi-Barimah et al. "Erbium-doped glass nanoparticle embedded polymer thin films using femtosecond pulsed laser deposition". *Optical Materials Express* 8.7 (2018), pp. 1997–2007.

[162] Jayakrishnan Chandrappan. "Femtosecond laser plasma assisted rare-earth doping in silica for integrated optics". PhD thesis. University of Leeds, 2015, p. 181.

[163] Suraya Ahmad Kamil. "Ultrafast laser plasma doping of rare earth ions for optical waveguiding applications". PhD thesis. University of Leeds, 2018, p. 220.

[164] Wolfgang Kautek et al. "Laser ablation of dielectrics with pulse durations between 20 fs and 3 ps". *Applied Physics Letters* 69.21 (1996), pp. 3146–3148.

[165] An-Chun Tien et al. "Short-Pulse Laser Damage in Transparent Materials as a Function of Pulse Duration". *Physical Review Letters* 82.19 (1999), pp. 3883–3886.

[166] D Pietroy et al. "Femtosecond laser volume ablation rate and threshold measurements by differential weighing". *Optics Express* 20.28 (2012), p. 29900.

[167] J. M. Liu. "Simple technique for measurements of pulsed Gaussian-beam spot sizes". *Optics Letters* 7.5 (1982), p. 196.

[168] American Institute of Physics. *Blasting tiny craters in glass, creating material to miniaturize telecommunication devices.* 2018.

[169] Giancarlo C. Righini and Andrea Chiappini. "Glass optical waveguides: a review of fabrication techniques". *Optical Engineering* 53.7 (2014), p. 071819.

[170] V A G Rivera, Danilo Manzani, and V A G Rivera. *Technological Advances in Tellurite Glasses*. Springer, 2017.

[171] Shaoxiong Shen et al. "Tellurite glasses for broadband amplifiers and integrated optics". *Journal of the American Ceramic Society* 85.6 (2002), pp. 1391–1395.

[172] Bo Zhou et al. "Superbroadband near-IR photoluminescence from Prˆ3+-doped fluorotellurite glasses". *Optics Express* 20.4 (2012), p. 3803.

[173] Bo Zhou et al. "Superbroadband NIR photoluminescence in Nd 3+/Tm 3+/Er 3+ codoped fluorotellurite glasses". *IEEE Photonics Technology Letters* 24.11 (2012), pp. 924–926.

[174] Lawrene Shah et al. "Waveguide writing in fused silica with a femtosecond fiber laser at 522 nm and 1 MHz repetition rate". *Optics Express* 13.6 (2005), pp. 1999–2006.

[175] Shane Eaton et al. "Heat accumulation effects in femtosecond laser-written waveguides with variable repetition rate." *Optics express* 13.12 (2005), pp. 4708–4716.

[176] Andrés Ferrer et al. "In situ assessment and minimization of nonlinear propagation effects for femtosecond-laser waveguide writing in dielectrics". *Journal of the Optical Society of America B* 27.8 (2010), p. 1688.

[177] V. Diez-Blanco et al. "Deep subsurface waveguides with circular cross section produced by femtosecond laser writing". *Applied Physics Letters* 91.5 (2007), pp. 2005–2008.

[178] P Nandi et al. "Femtosecond laser written channel waveguides in tellurite glass". *Optics Express* 14.25 (2006), pp. 12145–12150.

[179] E. M. Hsu et al. "Microscopic investigation of single-crystal diamond following ultrafast laser irradiation". *Applied Physics A: Materials Science and Processing* 103.1 (2011), pp. 185–192.

[180] D. Puerto et al. "Transient reflectivity and transmission changes during plasma formation and ablation in fused silica induced by femtosecond laser pulses". *Applied Physics A: Materials Science and Processing* 92.4 (2008), pp. 803–808.

[181] Francesca Di Niso et al. "Role of heat accumulation on the incubation effect in multi-shot laser ablation of stainless steel at high repetition rates". *Optics Express* 22.10 (2014), p. 12200.

[182] Shizhou Xiao, Evgeny L. Gurevich, and Andreas Ostendorf. "Incubation effect and its influence on laser patterning of ITO thin film". *Applied Physics A: Materials Science and Processing* 107.2 (2012), pp. 333–338.

[183] R T Williams. "Optically generated lattice defects in halide crystals". *Optical Engineering* 28.10 (1989), p. 281034.

[184] N Itoh and K Tanimura. "Effects of photoexcitation of self trapped excitons in insulators". *Opt. Eng.* 28 (1989), pp. 1034–1038.

[185] D Ashkenasi et al. "Surface damage threshold and sturcturing of dielectrics using femtosecond laser pulses: the role of incubation". *Applied Surface Science* 150 (1999), pp. 101–106.

[186] David Nečas and Petr Klapetek. *Gwyddion*. 2018.

[187] David Nečas and Petr Klapetek. "Gwyddion: an open-source software for SPM data analysis". *Open Physics* 10.1 (2012), pp. 181–188.

[188] E. A. Davis and N. F. Mott. "Conduction in non-crystalline systems V. Conductivity, optical absorption and photoconductivity in amorphous semiconductors". *Philosophical Magazine* 22.179 (1970), pp. 903–922.

[189] Franz Urbach. "The long-wavelength edge of photographic sensitivity and of the electronic Absorption of Solids [8]". *Physical Review* 92.5 (1953), p. 1324.

[190] M. Lenzner et al. "Photoablation with sub-10 fs laser pulses". *Applied Surface Science* 154 (2000), pp. 11–16.

[191] Ričardas Buividas, Mindaugas Mikutis, and Saulius Juodkazis. "Surface and bulk structuring of materials by ripples with long and short laser pulses: Recent advances". *Progress in Quantum Electronics* 38.3 (2014), pp. 119–156.

[192] A. Rosenfeld et al. "Ultrashort-laser-pulse damage threshold of transparent materials and the role of incubation". *Applied Physics A: Materials Science and Processing* 69.7 (1999), pp. 373–376.

[193] M. Lenzner et al. "Incubation of laser ablation in fused silica with 5-fs pulses". *Applied Physics A: Materials Science and Processing* 69.4 (1999), pp. 465–466.

[194] M Lenzner et al. "Precision laser ablation of dielectrics in the 10 - fs regime". *Applied Physics A* 371.1999 (1999), pp. 369–371.

[195] J. Bonse et al. "Ultrashort-pulse laser ablation of indium phosphide in air". *Applied Physics A: Materials Science and Processing* 72.1 (2001), pp. 89–94.

[196] L. G. Deshazer, B. E. Newnam, and K. M. Leung. "Role of coating defects in laser-induced damage to dielectric thin films". *Applied Physics Letters* 23.11 (1973), pp. 607–609.

[197] S. Martin et al. "Spot-size dependence of the ablation threshold in dielectrics for femtosecond laser pulses". *Applied Physics A: Materials Science and Processing* 77.7 (2003), pp. 883–884.

[198] B. Stuart et al. "Nanosecond-to-femtosecond laser-induced breakdown in dielectrics". *Physical Review B - Condensed Matter and Materials Physics* 53.4 (1996), pp. 1749–1761.

[199] M. D. Perry et al. "Ultrashort-pulse laser machining of dielectric materials". *Journal of Applied Physics* 85.9 (1999), pp. 6803–6810.

[200] D H Lowndes et al. "Silicon and zinc telluride nanoparticles synthesized by pulsed laser ablation: size distributions and nanoscale structure". *Applied Surface Science* 129 (1998), pp. 355–361.

[201] Giorgia Franzò, Francesco Priolo, and Salvatore Coffa. "Understanding and control of the erbium non-radiative de-excitation processes in silicon". *Journal of Luminescence* 80.1-4 (1998), pp. 19–28.

[202] N. Hamelin et al. "Energy backtransfer and infrared photoresponse in erbium-doped silicon p-n diodes". *Journal of Applied Physics* 88.9 (2000), pp. 5381–5387.

[203] H Ennen et al. "1.54-μm luminescence of erbium-implanted III-V semiconductors and silicon". *Applied Physics Letters* 43.10 (1983), pp. 943–945.

[204] Johannes Schindelin et al. "Fiji: an open-source platform for biological-image analysis". *Nature methods* 9.7 (2012), p. 676.

[205] Caroline A Schneider, Wayne S Rasband, and Kevin W Eliceiri. "NIH Image to ImageJ: 25 years of image analysis". *Nature methods* 9.7 (2012), p. 671.

[206] Brent Fultz and James M Howe. *Transmission electron microscopy and diffractometry of materials.* Springer Science & Business Media, 2012.

[207] Lydia Le Neindre et al. "Effect of relative alkali content on absorption linewidth in erbium-doped tellurite glasses". *Journal of non-crystalline solids* 255.1 (1999), pp. 97–102.

[208] Sean Manning, Heike Ebendorff-Heidepriem, and Tanya M. Monro. "Ternary tellurite glasses for the fabrication of nonlinear optical fibres". *Optical Materials Express* 2.2 (2012), p. 140.

[209] E. G. Gamaly et al. “Ablation of metals with picosecond laser pulses: Evidence of long-lived non-equilibrium surface states”. *Laser and Particle Beams* 23.2 (2005), pp. 167–176.

[210] L. Zampedri et al. “Evaluation of local field effect on the 4I13/2 lifetimes in Er-doped silica-hafnia planar waveguides”. *Physical Review B* 75.7 (2007), p. 073105.

[211] Gerald M. Miller, Ryan M. Briggs, and Harry A. Atwater. “Achieving optical gain in waveguide-confined nanocluster-sensitized erbium by pulsed excitation”. *Journal of Applied Physics* 108.6 (2010).

[212] Zhiping Zhou, Bing Yin, and Jurgen Michel. “On-chip light sources for silicon photonics”. *Light: Science & Applications* 4.11 (2015), e358.

[213] V. Teixeira. “Mechanical integrity in PVD coatings due to the presence of residual stresses”. *Thin Solid Films* 392.2 (2001), pp. 276–281.

[214] Toshihiko Ono and R. A. Allaire. *Fracture Analysis, A Basic Tool to Solve Breakage Issues.* Tech. rep. November. Corning, 2004, pp. 1–9.

[215] John W Hutchinson. “Stresses and failure modes in thin films and multilayers”. *Notes for a Dcamm Course. Technical University of Denmark, Lyngby* (1996), pp. 1–45.

[216] Vitro. *Glass Breakage - Failure Mode and Stress Estimation.* Tech. rep. Vitro, 2016, pp. 1–12.

[217] George D Quinn and George D Quinn. *Fractography of ceramics and glasses.* National Institute of Standards and Technology Washington, DC, 2007.

[218] Heraeus. *Quartz Glass for Optics Data and Properties.* Tech. rep. Heraeus, 2005.

[219] Alexander V. Mazur and Michael M. Gasik. “Thermal expansion of silicon at temperatures up to 1100 °C”. *Journal of Materials Processing Technology* 209.2 (2009), pp. 723–727.

[220] Alexander Fluegel. “Thermal expansion calculation for silicate glasses at 210 C based on a systematic analysis of global databases”. *Glass Technology-European Journal of Glass Science and Technology Part A* 51.5 (2010), pp. 191–201.

[221] Schott. *Schott Borofloat 33.* Tech. rep. Schott, 2009, pp. 1–32.

[222] Corning. *Unicrown technical specification sheet.* Tech. rep. Corning, 2006.

[223] Raouf El-Mallawany. “Tellurite glasses part 1. Elastic properties”. *Materials Chemistry and Physics* 53.2 (1998), pp. 93–120.

[224] K S Ravichandran. "Thermal residual stresses in a functionally graded material system". *Materials Science and Engineering: A* 201.1-2 (1995), pp. 269–276.

[225] F J Grunthaner, P J Grunthaner, and J Maserjian. "Radiation-induced defects in SiO2 as determined with XPS". *IEEE Transactions on Nuclear Science* 29.6 (1982), pp. 1462–1466.

[226] M. Asheghi et al. "Thermal conduction in doped single-crystal silicon films". *Journal of Applied Physics* 91.8 (2002), pp. 5079–5088.

[227] R. H. Magruder et al. "Optical properties of gold nanocluster composites formed by deep ion implantation in silica". *Applied Physics Letters* 62.15 (1993), pp. 1730–1732.

[228] Bert Sloots. "Measuring the low OH content in quartz glass". *Vibrational Spectroscopy* 48.1 (2008), pp. 158–161.

[229] I M Levin, V S Khotimchenko, and G M Sochivkin. "Concentration of hydrogen and water in fused silica blanks". *Glass and Ceramics* 42.8 (1985), pp. 359–361.

[230] Rolf Brückner. "Properties and structure of vitreous silica. I". *Journal of non-crystalline solids* 5.2 (1970), pp. 123–175.

[231] Boris S. Lunin and Kirill V. Tokmakov. "Reduction in internal friction in silica glass with high OH content". *Journal of the American Ceramic Society* April (2018), pp. 1–12.

[232] Horst Scholze. "Der einbau des wassers in glasern". *Glastech. Ber.* 32 (1959), pp. 142–152.

[233] B.S. Lunin, A.N. Kharlanov, and S.E. Kozlov. "Dehydroxylation and formation of KU-1 silica glass surface defects during annealing". *Moscow University Chemistry Bulletin* 65.1 (2010), pp. 34–37.

[234] Damir R Tadjiev and Russell J Hand. "Surface hydration and nanoindentation of silicate glasses". *Journal of Non-Crystalline Solids* 356.2 (2010), pp. 102–108.

[235] John Crank et al. *The mathematics of diffusion.* Oxford university press, 1979.

[236] K.M., Davis and Tomozawa M. "Water diffusion into silica glass : structural changes in silica glass and their effect on water solubility and diffusivity". *Journal of Non-Crystalline Solids* 185 (1995), pp. 203–220.

[237] Corning. *Corning HPFS 7979, 7980, 8655 Fused Silica.* Tech. rep. Corning, 2014.

[238] Horst Scholze. *Glass: nature, structure, and properties.* Springer Science & Business Media, 1991.

[239] Edward Stolper. "Water in Silicate Glasses: An Infrared Spectroscopic Study". *Contrib Mineral Petrol* 81 (1982), pp. 1–17.

[240] E Snoeks, G N Van den Hoven, and A Polman. "Optical doping of soda-lime-silicate glass with erbium by ion implantation". *Journal of Applied Physics* 73.12 (1993), pp. 8179–8183.

[241] D L Griscom, G H Sigel Jr, and Robert J Ginther. "Defect centers in a pure-silica-core borosilicate-clad optical fiber: ESR studies". *Journal of Applied Physics* 47.3 (1976), pp. 960–967.

[242] Amnon Yariv. *Quantum Electronics*. 1975.

[243] Oliver S Heavens. *Optical properties of thin solid films*. Courier Corporation, 1991.

[244] Zdenek Knittl. *Optics of thin films: an optical multilayer theory*. Vol. 1. Wiley London: 1976.

[245] Leif A A Pettersson, Lucimara S Roman, and Olle Inganäs. "Modeling photocurrent action spectra of photovoltaic devices based on organic thin films". *Journal of Applied Physics* 86.1 (1999), p. 487.

[246] David J Griffiths. *Introduction to electrodynamics*. 2005.

[247] Steven Jenkins. "On The Pole Structure of the S-Matrix for a Square Potential-Well" (2019).

[248] Kunststoff-Schweiz. *Infrarot-Wärme für die Kunststoffverarbeitung*. 2018.

[249] J.E. Stewart and J.C. Richmond. "Infrared emission spectrum of silicon carbide heating elements". *Journal of Research of the National Bureau of Standards* 59.6 (1957), p. 405.

[250] D. Ashkenasi et al. "Laser processing of sapphire with picosecond and sub-picosecond pulses". *Applied Surface Science* 120.1-2 (1997), pp. 65–80.

[251] Jeppe Byskov-Nielsen et al. "Ultra-short pulse laser ablation of metals: Threshold fluence, incubation coefficient and ablation rates". *Applied Physics A: Materials Science and Processing* 101.1 (2010), pp. 97–101.

Appendix A

Field amplitudes

The equations presented here are summarised from [36].

A.1 Radiative modes

The radiative modes constitute a superposition of two modes propagating in opposite z-axis directions in each of the inner M layers and a single outgoing mode with two incomming modes in either cladding layers. They are indexed by the propagation wavevector $\mathbf{k} = (\mathbf{k}_\parallel, q)$, where the z-component q in each of the M+2 layers is given by

$$q_j = \sqrt{\varepsilon_j \frac{\omega^2}{c^2} - k_\parallel^2}, \qquad j = 0, \ldots, \mathrm{M}+1. \tag{A.1}$$

For TE-polarized radiative modes with implicit time dependence $e^{-i\omega t}$ the field amplitudes are given by

$$E_\parallel^{\mathrm{TE}}(k_\parallel, z) = \begin{cases} W_{\mathrm{M}+1} e^{iq_{\mathrm{M}+1}(z-z_{\mathrm{M}+1})} + X_{\mathrm{M}+1} e^{-iq_{\mathrm{M}+1}(z-z_{\mathrm{M}+1})}, & z > z_{\mathrm{M}+1} \\ W_j e^{iq_j(z-z_j-d_j/2)} + X_j e^{-iq_j(z-z_j-d_j/2)}, & z_j < z < z_{j+1} \\ W_0 e^{iq_0(z-z_1)} + X_0 e^{-iq_0(z-z_1)}, & z < z_1 \end{cases} \tag{A.2}$$

$$H_\perp^{\mathrm{TE}}(k_\parallel, z) = \begin{cases} k_\parallel \left[W_{\mathrm{M}+1} e^{iq_{\mathrm{M}+1}(z-z_{\mathrm{M}+1})} + X_{\mathrm{M}+1} e^{-iq_{\mathrm{M}+1}(z-z_{\mathrm{M}+1})} \right], & z > z_{\mathrm{M}+1} \\ k_\parallel \left[W_j e^{iq_j(z-z_j-d_j/2)} + X_j e^{-iq_j(z-z_j-d_j/2)} \right], & z_j < z < z_{j+1} \\ k_\parallel \left[W_0 e^{iq_0(z-z_1)} + X_0 e^{-iq_0(z-z_1)} \right], & z < z_1 \end{cases} \tag{A.3}$$

$$H_{\parallel}^{\mathrm{TE}}(k_{\parallel}, z) = \begin{cases} q_{\mathrm{M}+1}\left[X_{\mathrm{M}+1}e^{-iq_{\mathrm{M}+1}(z-z_{\mathrm{M}+1})} - W_{\mathrm{M}+1}e^{iq_{\mathrm{M}+1}(z-z_{\mathrm{M}+1})}\right], & z > z_{\mathrm{M}+1} \\ q_j\left[X_j e^{-iq_j(z-z_j-d_j/2)} - W_j e^{iq_j(z-z_j-d_j/2)}\right], & z_j < z < z_{j+1} \\ q_0\left[X_0 e^{-iq_0(z-z_1)} - W_0 e^{iq_0(z-z_1)}\right], & z < z_1 \end{cases} \tag{A.4}$$

where W and X represent the amplitudes of the incoming and outgoing mode amplitudes, respectively. The radiative modes are divided into fully and partially radiative modes. For fully radiative modes outgoing in the substrate $W_{\mathrm{M}+1} = 0$ and from the normalisation of the modes eq. (2.14) it is found that $X_0 = 1/\sqrt{\varepsilon_0}$. Similarly, for fully radiative modes outgoing in the superstrate $X_0 = 0$ and eq. (2.14) gives $W_{\mathrm{M}+1} = 1/\sqrt{\varepsilon_{\mathrm{M}+1}}$. I.e. the normalisation of the modes is determined by the semi-infinite cladding in which the mode is outgoing as the contributions from the semi-infinite multilayer are negligable. Partially radiative modes on the other hand are evanescent in the superstrate ($q_{\mathrm{M}+1}$ is imaginary), assuming that $\varepsilon_0 > \varepsilon_{\mathrm{M}+1}$, and occur when the conditions for total internal reflection are met $\omega\frac{\sqrt{\varepsilon_{\mathrm{M}+1}}}{c} \leq k_{\parallel} \leq \omega\frac{\sqrt{\varepsilon_0}}{c}$. The field amplitudes in this case are found again from eq. (2.14) after applying the time reversal operator such that $W_{\mathrm{M}+1} = 0$ and $q_{\mathrm{M}+1} \to q_{\mathrm{M}+1}^*$. The rest of the coefficients are found from standard transfer matrix theory (see appendix B).

For TM-polarized radiative modes the field amplitudes are

$$H_{\parallel}^{\mathrm{TM}}(k_{\parallel}, z) = \begin{cases} Y_{\mathrm{M}+1}e^{iq_{\mathrm{M}+1}(z-z_{\mathrm{M}+1})} + Z_{\mathrm{M}+1}e^{-iq_{\mathrm{M}+1}(z-z_{\mathrm{M}+1})}, & z > z_{\mathrm{M}+1} \\ Y_j e^{iq_j(z-z_j-d_j/2)} + Z_j e^{-iq_j(z-z_j-d_j/2)}, & z_j < z < z_{j+1} \\ Y_0 e^{iq_0(z-z_1)} + Z_0 e^{-iq_0(z-z_1)}, & z < z_1 \end{cases} \tag{A.5}$$

$$E_{\perp}^{\mathrm{TM}}(k_{\parallel}, z) = \begin{cases} k_{\parallel}\left[Y_{\mathrm{M}+1}e^{iq_{\mathrm{M}+1}(z-z_{\mathrm{M}+1})} + Z_{\mathrm{M}+1}e^{-iq_{\mathrm{M}+1}(z-z_{\mathrm{M}+1})}\right], & z > z_{\mathrm{M}+1} \\ k_{\parallel}\left[Y_j e^{iq_j(z-z_j-d_j/2)} + Z_j e^{-iq_j(z-z_j-d_j/2)}\right], & z_j < z < z_j \\ k_{\parallel}\left[Y_0 e^{iq_0(z-z_1)} + Z_0 e^{-iq_0(z-z_1)}\right], & z < z_1 \end{cases} \tag{A.6}$$

$$E_{\parallel}^{\mathrm{TM}}(k_{\parallel},z)=\begin{cases} q_{\mathrm{M}+1}\left[Z_{\mathrm{M}+1}e^{-iq_{\mathrm{M}+1}(z-z_{\mathrm{M}+1})}-Y_{\mathrm{M}+1}e^{iq_{\mathrm{M}+1}(z-z_{\mathrm{M}+1})}\right], & z>z_{\mathrm{M}+1}\\ q_j\left[Z_je^{-iq_j(z-z_j-d_j/2)}-Y_je^{iq_j(z-z_j-d_j/2)}\right], & z_j<z<z_{j+1}\\ q_0\left[Z_0e^{-iq_0(z-z_1)}-[Y_0e^{iq_0(z-z_1)}\right], & z<z_1\end{cases} \tag{A.7}$$

where Y and Z represent the amplitudes of the incoming and outgoing mode amplitudes, respectively. For fully radiative modes outgoing in the substrate $Y_{\mathrm{M}+1}=0$ and eq. (2.14) gives $Z_0=1$. Similarly for fully radiative modes outgoing in the superstrate $Z_0=0$ and, by eq. (2.14), $Y_{\mathrm{M}+1}=1$. For partially radiative modes travelling in the substrate and evanescent in the superstrate, the application of the time reversal operator gives $Y_{\mathrm{M}+1}=0$ and $q_{\mathrm{M}+1}\to q^*_{\mathrm{M}+1}$. As for the TE modes, the rest of the coefficients are found from standard transfer matrix theory (see appendix B).

A.2 Guided modes

Guided modes propagate in the xy plane inside the highest index internal layer and are evanescent along z in the claddings. They are labelled by a joint single index $\mu=(\mathbf{k}_{\parallel},\alpha)$, where $\mathbf{k}_{\parallel}$ is the in-plane wavevector and α is the mode index. The z-component of the guided mode wavevector $q_{j,\mu}$ in the internal layers is given by

$$q_{j\mu}=\sqrt{\varepsilon_j\frac{\omega_\mu^2}{c^2}-k_{\parallel}^2}\qquad j=1,\ldots,\mathrm{M}, \tag{A.8}$$

where ω_μ is the frequency of the α-th guided mode. In the upper and lower cladding layers $q_{j\mu}$ is purely imaginary and so $q_{j\mu}=i\chi_{j\mu}=i\sqrt{k_{\parallel}^2-\varepsilon_j\frac{\omega_\mu^2}{c^2}}$. As a result, the mode field which is proportional to $\exp(\pm iq_{j\mu}z)$ decays exponentially in the z-axis increasing in distance away from the multilayer structure [242].

The field amplitudes for the TE-polarized guided modes are given by

$$E_{\parallel}^{\mathrm{TE}}(k_{\parallel},z)=\begin{cases} A_{\mathrm{M}+1}e^{-\chi_{\mathrm{M}+1,\mu}(z-z_{\mathrm{M}+1})}, & z>z_{\mathrm{M}+1}\\ A_{j\mu}e^{iq_{j\mu}(z-z_j-d_j/2)}+B_{j\mu}e^{-iq_{j\mu}(z-z_j-d_j/2)}, & z_j<z<z_{j+1}\\ B_{0\mu}e^{\chi_{0\mu}(z-z_1)}, & z<z_1\end{cases} \tag{A.9}$$

$$H_{\perp}^{\mathrm{TE}}(k_{\parallel},z)=\begin{cases} ik_{\parallel}A_{\mathrm{M}+1,\mu}e^{-\chi_{\mathrm{M}+1,\mu}(z-z_{\mathrm{M}+1})}, & z>z_{\mathrm{M}+1}\\ ik_{\parallel}\left[A_{j\mu}e^{iq_{j\mu}(z-z_j-d_j/2)}+B_{j\mu}e^{-iq_{j\mu}(z-z_j-d_j/2)}\right], & z_j<z<z_{j+1}\\ ik_{\parallel}B_{0,\mu}e^{\chi_{0,\mu}(z-z_1)}, & z<z_1 \end{cases} \tag{A.10}$$

$$H_{\parallel}^{\mathrm{TE}}(k_{\parallel},z)=\begin{cases} \chi_{\mathrm{M}+1\mu}A_{\mathrm{M}+1\mu}e^{-\chi_{\mathrm{M}+1\mu}(z-z_{\mathrm{M}+1})}, & z>z_{\mathrm{M}+1}\\ iq_{j\mu}\left[B_{j\mu}e^{-iq_{j\mu}(z-z_j-d_j/2)}-A_{j\mu}e^{iq_{j\mu}(z-z_j-d_j/2)}\right], & z_j<z<z_{j+1}\\ -\chi_0B_{0\mu}e^{\chi_{0\mu}(z-z_1)}, & z<z_1 \end{cases} \tag{A.11}$$

where the magnetic field is derived with the Maxwell equation eq. (2.15). The M+2 coefficients are found through application of transfer matrix theory (that provides M+1 relations) together with the orthonormality condition eq. (2.14) for the modes that gives

$$\begin{aligned}\int|\mathbf{H}(\boldsymbol{\rho},z)|^2\mathrm{d}\boldsymbol{\rho}\mathrm{d}z=1=&\frac{\chi_0^2+k_{\parallel}^2}{2\chi_0}|B_0|^2+\frac{\chi_{\mathrm{M}+1}^2+k_{\parallel}^2}{2\chi_{\mathrm{M}+1}}|A_{\mathrm{M}+1}|^2\\ &+\sum_{j=1}^{\mathrm{M}}d_j\left[(k_{\parallel}^2+q_jq_j^*)(|A_j|^2+|B_j|^2)\mathrm{sinc}\left(\frac{(q_j-q_j^*)d_j}{2}\right)\right.\\ &\left.+(k_{\parallel}^2-q_jq_j^*)(A_j^*B_j+B_j^*A_j)\mathrm{sinc}\left(\frac{(q_j+q_j^*)d_j}{2}\right)\right],\end{aligned} \tag{A.12}$$

where $\mathrm{sinc}=\sin(x)/x$. For TM-polarized guided modes the field amplitudes are given by

$$H_{\parallel}^{\mathrm{TM}}(k_{\parallel},z)=\begin{cases} C_{\mathrm{M}+1}e^{-\chi_{\mathrm{M}+1,\mu}(z-z_{\mathrm{M}+1})}, & z>z_{\mathrm{M}+1}\\ C_{j\mu}e^{iq_{j\mu}(z-z_j-d_j/2)}+D_{j\mu}e^{-iq_{j\mu}(z-z_j-d_j/2)}, & z_j<z<z_{j+1}\\ D_{0\mu}e^{\chi_{0\mu}(z-z_1)}, & z<z_1 \end{cases} \tag{A.13}$$

$$E_{\perp}^{\mathrm{TM}}(k_{\parallel},z)=\begin{cases} \dfrac{ik_{\parallel}}{\varepsilon_{\mathrm{M}+1}}C_{\mathrm{M}+1,\mu}e^{-\chi_{\mathrm{M}+1,\mu}(z-z_{\mathrm{M}+1})}, & z>z_{\mathrm{M}+1}\\ \dfrac{ik_{\parallel}}{\varepsilon_j}\left[C_{j\mu}e^{iq_{j\mu}(z-z_j-d_j/2)}+D_{j\mu}e^{-iq_{j\mu}(z-z_j-d_j/2)}\right], & z_j<z<z_{j+1}\\ \dfrac{ik_{\parallel}}{\varepsilon_0}D_{0,\mu}e^{\chi_{0,\mu}(z-z_1)}, & z<z_1 \end{cases} \tag{A.14}$$

$$E_{\parallel}^{\mathrm{TM}}(k_{\parallel}, z) = \begin{cases} \frac{\chi_{\mathrm{M}+1\mu}}{\varepsilon_{\mathrm{M}+1}} C_{\mathrm{M}+1\mu} e^{-\chi_{\mathrm{M}+1\mu}(z-z_{\mathrm{M}+1})}, & z > z_{\mathrm{M}+1} \\ \frac{iq_{j\mu}}{\varepsilon_j}\left[D_{j\mu} e^{-iq_{j\mu}(z-z_j-d_j/2)} - C_{j\mu} e^{iq_{j\mu}(z-z_j-d_j/2)}\right], & z_j < z < z_{j+1} \\ -\frac{\chi_0}{\varepsilon_0} D_{0\mu} e^{\chi_{0\mu}(z-z_1)}, & z < z_1 \end{cases} \tag{A.15}$$

where the M+2 coefficients found as before through application of transfer matrix theory together with the normalisation integral eq. (2.14) that states

$$\begin{aligned} \int |\mathbf{H}(\boldsymbol{\rho}, z)|^2 \mathrm{d}\boldsymbol{\rho}\mathrm{d}z = 1 = & \frac{|D_0|^2}{2\chi_0} + \frac{|C_{\mathrm{M}+1}|^2}{2\chi_{\mathrm{M}+1}} \\ & + \sum_{j=1}^{\mathrm{M}} d_j \left[(|C_j|^2 + |D_j|^2)\mathrm{sinc}\left(\frac{(q_j - q_j^*)d_j}{2}\right)\right. \\ & \left. + (C_j^* D_j + D_j^* C_j)\mathrm{sinc}\left(\frac{(q_j + q_j^*)d_j}{2}\right)\right], \end{aligned} \tag{A.16}$$

and sinc $= \sin(x)/x$.

Appendix B

Transfer matrix method

The transfer matrix method is a way to describe the electric or magnetic fields within a multilayer structure using a 2×2 matrix by making use of the fact that the tangential component of the electric field across dielectric interfaces is continuous [243–245]. Reflection and transmission rates of the entire structure are also easily found once the 2×2 transfer matrix of the entire multilayer structure is found.

The system under consideration is illustrated in fig. B.1: it consists of M dielectric layers that are parallel to the xy plane and infinite along the x and y directions. Each layer is d_j thick and the cladding layers (the substrate is j = M+1 and the ambient/superstrate is $j = 0$) are taken to be semi-infinite. Each of the M + 2 dielectric media is non-magnetic ($\mu = \mu_0$), linear, isotropic and homogeneous and characterised by a (wavelength dependent) complex refractive index $n_j = \eta_j + i\kappa_j$ ($j = 1, \ldots,$ M) and thickness d_j. It is also imposed that the claddings are transparent (i.e. $\kappa_j = 0$ for $j = 0$ or M+1). This is a requirement as all fields will be defined in units of the field amplitude of the incoming light at the superstrate-layer interface.

The theory presented here is derived within the framework of classical electromagnetism by first considering the wave solutions to Maxwell's equations in appendix B.1, then deriving the Fresnel reflection and transmission coefficients at a dielectric interface appendix B.2 and finally the transfer matrix (composed of interference and wave propagation matrices) is defined by considering an electric field incident on the multilayer structure appendix B.3. Note that while the transfer matrix formalism is widely reported in the literature (e.g. [243–245]), the derivation presented here specifically defines it in terms of the electric **E** and magnetic **H** fields, which are directly imple-

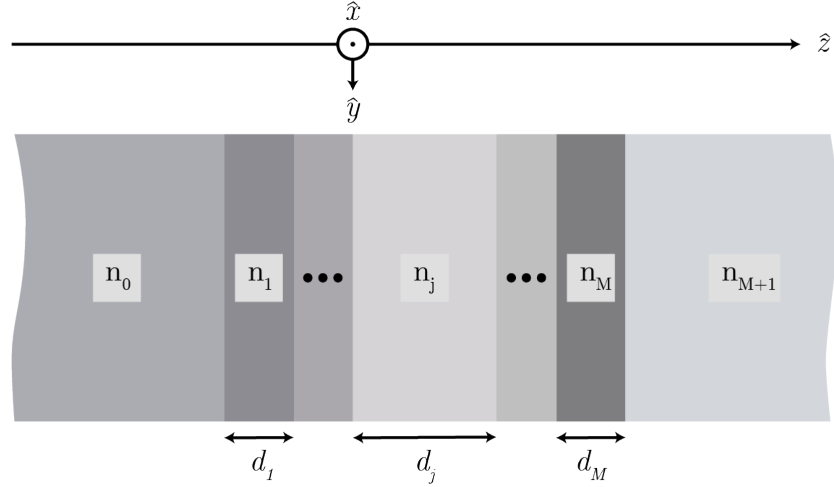

Figure B.1: Schematic of a multilayered structure consisting of M layers between a semi-infinite transparent ambient medium ($j = 0$) and a semi-infinite substrate ($j = \mathrm{M}{+}1$). Each layer j ($j = 1, 2, ..., \mathrm{M}$) has a thickness d_j and is described by its complex index of refraction n_j.

mented for the calculation of the spontaneous emission rate inside multilayer structures in chapter 2 and appendix A.

B.1 Maxwell's equations

Maxwell's equations describe how electric **E** (displacement **D**) and magnetic **B** (magnetising **H**) fields are generated by charges, currents and changes of each other. Inside matter and in the absence of free charges and currents Maxwell's (macroscopic) equations are given by

$$\nabla \cdot \mathbf{E} = 0\,, \tag{B.1a}$$

$$\nabla \cdot \mathbf{B} = 0\,, \tag{B.1b}$$

$$\nabla \times \mathbf{E} = -\frac{\partial \mathbf{B}}{\partial t}\,, \tag{B.1c}$$

$$\nabla \times \mathbf{B} = \frac{\partial \mathbf{D}}{\partial t}\,, \tag{B.1d}$$

where the position $\mathbf{r}$ and time t dependence of the fields is implicit. If the medium is linear,

$$\mathbf{D} = \epsilon(\mathbf{r})\mathbf{E}\,, \quad \mathbf{H} = \frac{1}{\mu(\mathbf{r})}\mathbf{B}, \tag{B.2}$$

and homogeneous, the permittivity $\epsilon(\mathbf{r}) = \epsilon$ and permeability $\mu(\mathbf{r}) = \mu$, then the equations reduce to

$$\nabla \cdot \mathbf{E} = 0\,, \tag{B.3a}$$

$$\nabla \cdot \mathbf{H} = 0\,, \tag{B.3b}$$

$$\nabla \times \mathbf{E} = -\mu\frac{\partial \mathbf{H}}{\partial t}\,, \tag{B.3c}$$

$$\nabla \times \mathbf{H} = \epsilon\frac{\partial \mathbf{E}}{\partial t}\,. \tag{B.3d}$$

The solution for the electromagnetic field is found after applying the curl to eq. (B.3c):

$$\nabla \times (\nabla \times \mathbf{E}) = \nabla(\nabla \cdot \mathbf{E}) - \nabla^2\mathbf{E} = -\mu\frac{\partial}{\partial t}(\nabla \times \mathbf{H}). \tag{B.4}$$

Inserting eq. (B.3a) into the left hand side and eq. (B.3d) into the right hand side gives the second order differential equation

$$\nabla^2\mathbf{E} = \mu\epsilon\frac{\partial^2 \mathbf{E}}{\partial t^2}, \tag{B.5}$$

which is simply the three-dimensional wave equation with velocity $v = 1/\sqrt{\epsilon\mu}$ [246]. The solutions are monochromatic plane waves of the form

$$\mathbf{E}(\mathbf{r}, t) = Ee^{i(\mathbf{k}\cdot\mathbf{r} - \omega t)}, \tag{B.6}$$

where E is the complex amplitude and the dispersion formula $\omega = ck$ gives the the magnitude of the wave-vector $\mathbf{k}$. The solutions of eq. (B.3d) for the $\mathbf{H}$ field may be found in a similar fashion

$$\mathbf{H}(\mathbf{r}, t) = He^{i(\mathbf{k}\cdot\mathbf{r} - \omega t)}. \tag{B.7}$$

In a vacuum $\epsilon = \epsilon_0$ and $\mu = \mu_0$ and the speed of the waves is given by

$$c = \frac{1}{\sqrt{\epsilon_0 \mu_0}}, \tag{B.8}$$

and so we can write

$$v = \frac{1}{\sqrt{\epsilon\mu}} = \frac{c}{n} \tag{B.9}$$

where

$$n \equiv \sqrt{\frac{\epsilon\mu}{\epsilon_0\mu_0}} = \sqrt{\epsilon_r\mu_r} \tag{B.10}$$

is the complex index of refraction of the medium. In a non-magnetic medium $\mu_r \approx 1$ (typical for most materials), giving

$$n \approx \sqrt{\epsilon_r}, \tag{B.11}$$

where ϵ_r is the (complex) dielectric constant.

Having found the wave solutions to Maxwell's equations for the system, it is now possible to rewrite them in complex form. Applying the nabla and time derivative operators to the plane-wave solutions for the **E** or **H** fields (eq. (B.6) and eq. (B.7)) it is easily seen that the operators may be replaced by

$$\frac{\partial}{\partial t} \rightarrow -i\omega\,, \quad \nabla \rightarrow i\,\mathbf{k} \tag{B.12}$$

and so Maxwell's equations (eq. (B.3)) may be written in the complex form

$$\mathbf{k} \cdot \mathbf{E} = 0\,, \tag{B.13a}$$

$$\mathbf{k} \cdot \mathbf{H} = 0\,, \tag{B.13b}$$

$$\mathbf{k} \times \mathbf{E} = \mu\omega\mathbf{H}\,, \tag{B.13c}$$

$$\mathbf{k} \times \mathbf{H} = -\epsilon\omega\mathbf{E}\,. \tag{B.13d}$$

From eq. (B.13a) and eq. (B.13b) we can see that the the **E** and **H** vector fields have no component parallel to the **k** wave vector. Thus electromagnetic waves are transverse. Additionally eq. (B.13c) (eq. (B.13d)) shows that the **E** field is perpendicular to the **H** field and so the **k**, **E** and **H** vectors form a right handed tetrahedral. The amplitudes between the waves at a certain position in time is therefore

$$|\mathbf{k} \times \mathbf{E}| = kE = \mu\omega H \tag{B.14}$$

where k, H and E are the complex amplitudes of the corresponding (bold) vectors. Therefore

$$E = \frac{\mu\omega}{k}H = \frac{\mu c}{n}H = ZH, \tag{B.15}$$

where the relation $k = \omega c/n$ has been used and the optical impedance is defined as

$$Z \equiv \frac{\mu c}{n} = \sqrt{\frac{\mu}{\epsilon}}. \tag{B.16}$$

B.2 Reflection and transmission at an interface

At a single interface between two semi-infinite media with differing dielectric constants, a fraction of a monochromatic plane electromagnetic wave incident at an oblique angle of incidence will be reflected and a fraction will be transmitted. The medium from which the light is incident from (transmitted to) is characterised by a refractive index n_j (n_k).

Using the superposition principle[1] the fields are decomposed at a position z into forward and backward travelling waves defined by their wavevector $\mathbf{k}$. There is no backwards travelling wave in the second medium, n_k, for the case of a single interface. All three waves have the same frequency ω [246].

The origin is defined such that light incident on the interface has it's wave-vector in the xz-plane (the plane of incidence). There exists two possible orientations of incident the $\mathbf{E}$ field, called polarisations. Transverse electric (TE) or s-polarised waves correspond to waves where the incident and reflected fields have their electric field perpendicular to the plane of incidence (defined as the plane formed by the incident, reflected and transmitted wave-vectors). Transverse magnetic (TM) or p-polarised waves have their magnetic field perpendicular to the plane of incidence. Figure B.2a and fig. B.2b illustrate the case for TE and TM waves, respectively. The fields are labelled with a subscript i to indicate the medium, of refractive index n_i, that the wave is travelling in and a superscript + (-) for forwards (backward) waves travelling

[1]This applies as Maxwell's equations are linear.

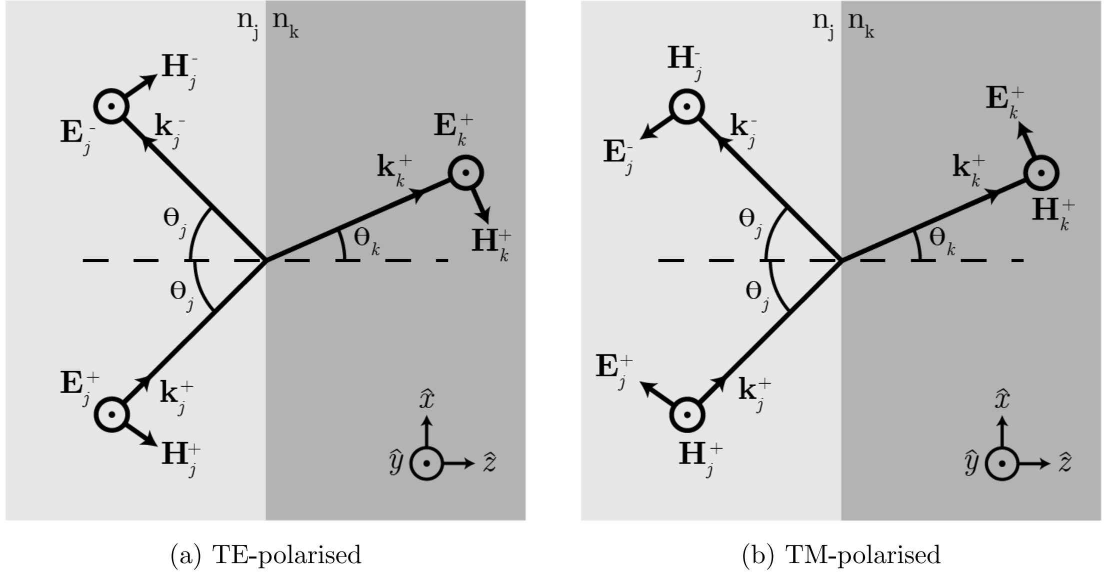

Figure B.2: Monochromatic electromagnetic plane wave incident on an dielectric interface.

in $+z$ $(-z)$ direction. For TM polarised waves, we have used the convention that the reflected wave has it's magnetic field in the same direction as the incident wave and the tangential component of the electric field flips from the positive to negative $\hat{x}$ direction[1]. The law of reflection has already been used to equate the angle of incidence with the angle of reflection and the angle of the transmitted wave is given by Snell's law $n_j \sin(\theta_j) = n_k \sin(\theta_k)$, which both arise by matching the boundary conditions of the three fields with equal frequency in space and time [246].

Start with the boundary conditions for electromagnetic fields, which may be derived from the integral form of Maxwell's equations, the tangential components of the **E** and **H** fields are continuous and the perpendicular components of the **D** and **B** fields are continuous across the interface [246]. It suffices to work solely with the tangential

[1]We use this convention for consistency when evaluating the fields inside multilayered structures. The alternative convention where the magnetic field flips upon reflection and the tangential component of the electric field remains in the positive $\hat{x}$ direction is often used so that for the case of normal incidence the TE and TM Fresnel coefficients are the same. Switching conventions will give rise to an additional - sign in the Fresnel reflection coefficients. As long as only a single convention is employed, both yield identical results for a single interface as the measurable quantities, reflection and transmission, take the square of the absolute magnitude of the fields.

components to derive the Fresnel relations[1]. Equating the tangential field components at the interface and taking the point of incidence as the origin ($\mathbf{r} = 0$) and time $t = 0$, causes the exponential parts of the plane-wave solutions (eq. (B.6) and eq. (B.7)) to drop out. Therefore equating the tangential components of the complex amplitudes is the task at hand, which will give the relations between the incident, reflected and transmitted plane-wave amplitudes.

B.2.1 Transverse Electric Waves (TE or s-polarised)

Figure B.2a depicts the situation for transverse electric polarised waves (TE or s-polarised), where the **E** field is perpendicular to the plane of incidence. The convention used is that the reflected **E** field is positive 'upward', matching the incident field as is standard. The **k** and **E** field amplitudes are easily attained and the **H** field amplitude may be evaluated with eq. (B.13c):

Incident

$$\mathbf{k}_j^+ = \frac{\omega n_j}{c}\left[\sin(\theta_j)\hat{x} + \cos(\theta_j)\hat{z}\right] , \tag{B.17a}$$

$$\mathbf{E}_j^+ = E_j^+ \hat{y} , \tag{B.17b}$$

$$\mathbf{H}_j^+ = \frac{1}{\mu\omega}\mathbf{k}_j^+ \times \mathbf{E}_j^+ = \frac{n_j}{c\mu}E_j^+\left[-\cos(\theta_j)\hat{x} + \sin(\theta_j)\hat{z}\right] . \tag{B.17c}$$

Reflected

$$\mathbf{k}_j^- = \frac{\omega n_j}{c}\left[\sin(\theta_j)\hat{x} - \cos(\theta_j)\hat{z}\right] , \tag{B.18a}$$

$$\mathbf{E}_j^- = E_j^- \hat{y} , \tag{B.18b}$$

$$\mathbf{H}_j^- = \frac{1}{\mu\omega}\mathbf{k}_j^- \times \mathbf{E}_j^- = \frac{n_j}{c\mu}E_j^-\left[\cos(\theta_j)\hat{x} + \sin(\theta_j)\hat{z}\right] . \tag{B.18c}$$

Transmitted

$$\mathbf{k}_k^+ = \frac{\omega n_k}{c}\left[\sin(\theta_k)\hat{x} + \cos(\theta_k)\hat{z}\right] , \tag{B.19a}$$

$$\mathbf{E}_k^+ = E_k^+ \hat{y} , \tag{B.19b}$$

$$\mathbf{H}_k^+ = \frac{1}{\mu\omega}\mathbf{k}_k^+ \times \mathbf{E}_k^+ = \frac{n_k}{c\mu}E_k^+\left[-\cos(\theta_k)\hat{x} + \sin(\theta_k)\hat{z}\right] . \tag{B.19c}$$

[1]This is an advantage of working with with the **E** and **H** fields.

The boundary conditions for continuity of the tangential components of the **E** and **H** fields to the interface gives

$$E_j^+ + E_j^- = E_k^+ \,, \tag{B.20a}$$
$$n_j \cos(\theta_j) \left[E_j^+ - E_j^-\right] = n_k \cos(\theta_k) E_k^+ \,, \tag{B.20b}$$

which may be solved to give the reflection and transmission coefficients for the electric field

$$r_{jk} = \frac{E_j^-}{E_j^+} = \frac{n_j \cos(\theta_j) - n_k \cos(\theta_k)}{n_j \cos(\theta_j) + n_k \cos(\theta_k)} = \frac{\xi_j - \xi_k}{\xi_j + \xi_k} \,, \tag{B.21a}$$
$$t_{jk} = \frac{E_k^+}{E_j^+} = \frac{2 n_j \cos(\theta_j)}{n_j \cos(\theta_j) + n_k \cos(\theta_k)} = \frac{2\xi_j}{\xi_j + \xi_k} \,. \tag{B.21b}$$

which we have simplified using

$$\xi_j = n_j \cos\theta_j = [n_j^2 - \eta_0^2 \sin^2\theta_0]^{\frac{1}{2}} \tag{B.22}$$

where θ_j is the angle of refraction in layer j and the second equality is derived by considering that the incoming wave is incident from a transparent ambient with a (real) refractive index $n_0 = \eta_0$ at an angle θ_0 and realising that the parallel wavevector component to the interface is continuous and equal for linear media where the wave frequency ω is fixed [246].

B.2.2 Transverse Magnetic Waves (TM or p-polarised)

Figure B.2b depicts the situation for transverse magnetic polarised waves (TM or p-polarised), where the **H** field is perpendicular to the plane of incidence. The convention we use is that the incident and reflected **H** fields are parallel. From the schematic the **k** and **H** field amplitudes may be seen and the **E** field amplitude may be evaluated with eq. (B.13d):

Incident

$$\mathbf{k}_j^+ = \frac{\omega n_j}{c}\left[\sin(\theta_j)\hat{x} + \cos(\theta_j)\hat{z}\right] , \tag{B.23a}$$
$$\mathbf{H}_j^+ = H_j^+ \hat{y} , \tag{B.23b}$$
$$\mathbf{E}_j^+ = -\frac{1}{\epsilon_j \omega}\mathbf{k}_j^+ \times \mathbf{H}_j^+ = \frac{1}{c n_j} H_j^+ \left[\cos(\theta_j)\hat{x} - \sin(\theta_j)\hat{z}\right] . \tag{B.23c}$$

Reflected

$$\mathbf{k}_j^- = \frac{\omega n_j}{c}\left[\sin(\theta_j)\hat{x} - \cos(\theta_j)\hat{z}\right] , \tag{B.24a}$$
$$\mathbf{H}_j^- = H_j^- \hat{y} , \tag{B.24b}$$
$$\mathbf{E}_j^- = -\frac{1}{\epsilon_j \omega}\mathbf{k}_j^- \times \mathbf{H}_j^- = \frac{1}{c n_j} H_j^- \left[-\cos(\theta_j)\hat{x} + \sin(\theta_j)\hat{z}\right] . \tag{B.24c}$$

Transmitted

$$\mathbf{k}_k^+ = \frac{\omega n_k}{c}\left[\sin(\theta_k)\hat{x} + \cos(\theta_k)\hat{z}\right] , \tag{B.25a}$$
$$\mathbf{H}_k^+ = H_k^+ \hat{y} , \tag{B.25b}$$
$$\mathbf{E}_k^+ = -\frac{1}{\epsilon_k \omega}\mathbf{k}_k^+ \times \mathbf{H}_k^+ = \frac{1}{c n_k} H_k^+ \left[\cos(\theta_k)\hat{x} - \sin(\theta_k)\hat{z}\right] . \tag{B.25c}$$

The boundary conditions for continuity of the tangential components of the **E** and **H** fields to the interface gives

$$H_j^+ + H_j^- = H_k^+ , \tag{B.26a}$$
$$\frac{1}{n_j}\cos(\theta_j)\left[H_j^+ - H_j^-\right] = \frac{1}{n_k}\cos(\theta_k) H_k^+ , \tag{B.26b}$$

which may be solved, using the relation from before $H = \frac{n}{\mu c}E$ (eq. (B.15)), to give the reflection and transmission coefficients for the electric field

$$r_{jk} = \frac{E_j^-}{E_j^+} = \frac{n_k \cos(\theta_j) - n_j \cos(\theta_k)}{n_k \cos(\theta_j) + n_j \cos(\theta_k)} = \frac{n_k^2 \xi_j - n_j^2 \xi_k}{n_k^2 \xi_j + n_j^2 \xi_k} , \tag{B.27a}$$
$$t_{jk} = \frac{E_k^+}{E_j^+} = \frac{2 n_j \cos(\theta_j)}{n_j \cos(\theta_k) + n_k \cos(\theta_j)} = \frac{2 n_j n_k \xi_j}{n_k^2 \xi_j + n_j^2 \xi_k} . \tag{B.27b}$$

which we have simplified using

$$\xi_j = n_j \cos\theta_j = [n_j^2 - \eta_0^2 \sin^2\theta_0]^{\frac{1}{2}} \tag{B.28}$$

where η_0 is the refractive index of the transparent ambient, θ_0 is the angle of incidence and θ_j is the angle of refraction in layer j, as with for the TE-polarised waves.

B.2.3 Summary

We have derived the Fresnel complex reflection and transmission equations for the electric field at an interface jk. For TE polarised light the Fresnel complex reflection and transmission coefficients are defined by

$$r_{jk} = \frac{\xi_j - \xi_k}{\xi_j + \xi_k} \tag{B.29a}$$

$$t_{jk} = \frac{2\xi_j}{\xi_j + \xi_k} \tag{B.29b}$$

and for TM polarised light by

$$r_{jk} = \frac{n_k^2\xi_j - n_j^2\xi_k}{n_k^2\xi_j + n_j^2\xi_k}\,, \tag{B.30a}$$

$$t_{jk} = \frac{2n_j n_k \xi_j}{n_k\xi_j + n_j\xi_k}\,. \tag{B.30b}$$

where

$$\xi_j = \tilde{n}_j \cos\theta_j = [n_j^2 - \eta_0^2 \sin^2\theta_0]^{\frac{1}{2}} \tag{B.31}$$

and η_0 is the refractive index of the transparent ambient from which the wave is incident, θ_0 is the angle of incidence, and θ_j is the angle of refraction in layer j.

The corresponding reflection and transmission coefficients for the H field, which we now denote with a H superscript, field may be easily found from the using the relationship between the magnetic and electric field amplitudes, eq. (B.15), ($H \propto nE$) as follows

$$r_{jk}^H = \frac{H_j^-}{H_j^+} = \frac{n_j E_j^-}{n_j E_j^+} = r_{jk}\,, \tag{B.32a}$$

$$t_{jk}^H = \frac{H_k^+}{H_j^+} = \frac{n_k E_k^+}{n_j E_j^+} = \frac{n_k}{n_j} t_{jk}\,. \tag{B.32b}$$

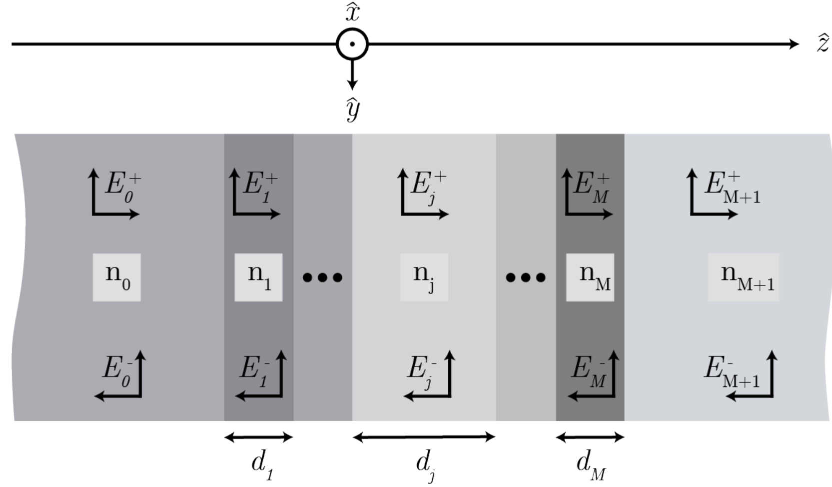

Figure B.3: Schematic of a multilayered structure consisting of M layers between a semi-infinite transparent ambient medium ($j = 0$) and a semi-infinite substrate ($j =$ M+1). Each layer j ($j = 1, 2, ..., \text{M}$) has a thickness d_j and is described by its complex index of refraction n_j. The electric (shown) and magnetic field within each layer is described by the superposition of a forward and a backward propagating field.

The reflection coefficient does not change as the incident and reflected waves travel in the same medium and hence the optical impedance of the medium does not change.

B.3 Transfer Matrix Method

Recalling that, for the multilayer dielectric medium under consideration, the equations governing electric **E** and magnetic **H** field propagation are linear and their tangential component across the interface is continuous. A 2 × 2 matrix is sufficient to describe the fields within a given layer and by multiplying several of such matrices, the entire multilayer structure may be described [243–245].

A plane wave propagating in an ambient medium and incident onto a such a multilayer structure is shown schematically in fig. B.3. The superposition principle holds for the electric field and the electric field at a position z in layer j can be resolved into components propagating in the positive and negative z direction, denoted $\mathbf{E}_j^+(z)$ and $\mathbf{E}_j^-(z)$, respectively.

B.3.1 Interference Matrix

A single interface between two dielectric layers within the multilayer structure is considered. In this case there may be backwards travelling waves in the second medium, $E_k^- \neq 0$, due to reflections from deeper lying layers (the transmitted medium is no longer semi-infinite as when deriving the Fresnel coefficients). For TE waves, the boundary conditions for the electric **E** and magnetic **H** tangential components gives

$$E_j^+ + E_j^- = E_k^+ + E_k^- \,, \tag{B.33a}$$

$$\xi_j \left[E_j^+ - E_j^- \right] = \xi_j \left[E_k^+ - E_k^- \right] \,, \tag{B.33b}$$

$$\tag{B.33c}$$

which can be written in matrix form as

$$\begin{bmatrix} 1 & 1 \\ \xi_j & -\xi_j \end{bmatrix} \begin{bmatrix} E_j^+ \\ E_j^- \end{bmatrix} = \begin{bmatrix} 1 & 1 \\ \xi_j & -\xi_j \end{bmatrix} \begin{bmatrix} E_k^+ \\ E_k^- \end{bmatrix} . \tag{B.34}$$

Solving this for the electric field components in layer j gives

$$\begin{bmatrix} E_j^+ \\ E_j^- \end{bmatrix} = \begin{bmatrix} 1 & 1 \\ \xi_j & -\xi_j \end{bmatrix}^{-1} \begin{bmatrix} 1 & 1 \\ \xi_j & -\xi_j \end{bmatrix} \begin{bmatrix} E_k^+ \\ E_k^- \end{bmatrix} . \tag{B.35}$$

The interference matrix that relates the amplitudes of waves either side of the interface can now be defined as

$$\mathbf{I}_{jk} = \begin{bmatrix} 1 & 1 \\ \xi_j & -\xi_j \end{bmatrix}^{-1} \begin{bmatrix} 1 & 1 \\ \xi_j & -\xi_j \end{bmatrix} \tag{B.36a}$$

$$= \frac{1}{-2\xi_j} \begin{bmatrix} -\xi_j & -1 \\ -\xi_j & 1 \end{bmatrix} \begin{bmatrix} 1 & 1 \\ \xi_j & \xi_j \end{bmatrix} \tag{B.36b}$$

$$= \frac{1}{2\xi_j} \begin{bmatrix} \xi_j + \xi_j & \xi_j - \xi_j \\ \xi_j - \xi_j & \xi_j + \xi_j \end{bmatrix} \tag{B.36c}$$

$$= \frac{1}{t_{jk}} \begin{bmatrix} 1 & r_{jk} \\ r_{jk} & 1 \end{bmatrix} , \tag{B.36d}$$

$$\tag{B.36e}$$

where the TE reflection and transmission Fresnel coefficients, given in eq. (B.29), have been used. The same relation is found for the **H** field of TM polarised modes

using the TM reflection and transmission Fresnel coefficients, given in eq. (B.30). To summarise, at an interface jk between two dielectric media, n_j and n_k, the electric field components are related by

$$\begin{bmatrix} E_j^+ \\ E_j^- \end{bmatrix} = \mathbf{I}_{jk} \begin{bmatrix} E_k^+ \\ E_k^- \end{bmatrix}, \tag{B.37}$$

where

$$\mathbf{I}_{jk} = \frac{1}{t_{jk}} \begin{bmatrix} 1 & r_{jk} \\ r_{jk} & 1 \end{bmatrix} \tag{B.38}$$

and r_{jk} t_{jk} refer to the corresponding Fresnel coefficients for the incident wave polarisation. Analogously, the interference matrix for the magnetic H field components is easily obtained in the same form by substituting in the magnetic Fresnel coefficients, given in eq. (B.32).

B.3.2 Layer matrix

A layer matrix (phase matrix) describes the propagation in z of the field through layer j and is easily found from the plane wave solutions as

$$L_j = \begin{bmatrix} e^{-iq_j d_j} & 0 \\ 0 & e^{iq_j d_j} \end{bmatrix} \tag{B.39}$$

where the component of the wavevector in the z direction is given in terms of the ambient incident wavelength as

$$q_j = \frac{2\pi}{\lambda_0} \xi_j \tag{B.40}$$

and $q_j d_j$ is the layer phase thickness corresponding to the phase change the wave experiences as it traverses layer j.

B.3.3 System transfer matrix

Combining the interface matrix and the layer matrix, the total system transfer matrix, $\mathbf{S}$, which relates the electric field at the ambient side and substrate side by

$$\begin{bmatrix} E_0^+ \\ E_0^- \end{bmatrix} = \mathbf{S} \begin{bmatrix} E_{\mathrm{M}+1}^+ \\ E_{\mathrm{M}+1}^- \end{bmatrix} \tag{B.41}$$

and can be written as

$$\mathbf{S} = \begin{bmatrix} S_{11} & S_{12} \\ S_{21} & S_{22} \end{bmatrix} = \left(\prod_{\nu=1}^{m} \mathbf{I}_{(\nu-1)\nu} \mathbf{L}_{\nu} \right) \cdot \mathbf{I}_{\mathrm{M(M+1)}}. \tag{B.42}$$

When light is incident from the ambient side in the positive x direction there is no wave propagating in the negative x direction inside the substrate and so $E^{-}_{\mathrm{M+1}} = 0$. For the total structure the complex reflection and transmission coefficients can be expressed in terms of the total system transfer matrix of equation (B.42) as

$$r = \frac{E_0^-}{E_0^+} = \frac{S_{21}}{S_{11}} \tag{B.43}$$

$$t = \frac{E^{+}_{\mathrm{M+1}}}{E_0^+} = \frac{1}{S_{11}}. \tag{B.44}$$

Recall that evaluation of the magnetic H field is simply a case of using the magnetic Fresnel coefficients when evaluating the interference matrix.

B.3.4 Internal Layer Field

To find the field in layer j, the total system transfer matrix may be divided into two subsets representing two layered systems separated by layer j

$$\mathbf{S} = \mathbf{S}'_j \mathbf{L}_j \mathbf{S}''_j \tag{B.45}$$

where $\mathbf{S}'_j$ represents the part of the total transfer matrix for all the layers left (superstrate side) of the layer j and $\mathbf{S}''_j$ the part to the right (substrate side) of the layer j. The partial system transfer matrices for layer j are defined

$$\begin{bmatrix} E_0^+ \\ E_0^- \end{bmatrix} = \mathbf{S}'_j \begin{bmatrix} E_j^+ \\ E_j^- \end{bmatrix},$$
$$\mathbf{S}'_j = \begin{bmatrix} S'_{11} & S'_{12} \\ S'_{21} & S'_{22} \end{bmatrix} = \left(\prod_{\nu=1}^{j-1} \mathbf{I}_{(\nu-1)\nu} \mathbf{L}_{\nu} \right) \cdot \mathbf{I}_{(j-1)j}, \tag{B.46}$$

where E_j^+ and E_j^- correspond to the left boundary $(j-1)j$ of layer j and

$$\begin{bmatrix} E_j''^+ \\ E_j''^- \end{bmatrix} = \mathbf{S}''_j \begin{bmatrix} E^{+}_{\mathrm{M+1}} \\ E^{-}_{\mathrm{M+1}} \end{bmatrix},$$
$$\mathbf{S}''_j = \begin{bmatrix} S''_{11} & S''_{12} \\ S''_{21} & S''_{22} \end{bmatrix} = \left(\prod_{\nu=j+1}^{\mathrm{M}} \mathbf{I}_{(\nu-1)\nu} \mathbf{L}_{\nu} \right) \cdot \mathbf{I}_{\mathrm{M(M+1)}}, \tag{B.47}$$

where $E_j''^{+}$ and $E_j''^{-}$ correspond to the right boundary $j(j+1)$ of layer j. The total electric field in layer j at position z is given by

$$E_j(z) = E_j^+(z) + E_j^-(z) \tag{B.48}$$

which can be solved simply from eq. (B.46) in terms of the field amplitude incident on the multilayer structure to give

$$E_j^+ = \frac{S'_{22} - rS'_{12}}{\det\{S'\}} E_0^+ \tag{B.49a}$$

$$E_j^- = \frac{rS'_{11} - S'_{21}}{\det\{S'\}} E_0^+ \,. \tag{B.49b}$$

where eq. (B.43) has been used to eliminate E_0^-, thus reducing the number of unknowns from four to three. Alternatively it may be expressed in terms of the incident plane wave E_0^+ and partial system transfer matrices as [245]

$$E_j(z) = \frac{S''_{j11} \cdot e^{-iq_j(d_j - z)} + S''_{j21} \cdot e^{iq_j(d_j - z)}}{S'_{j11}S''_{j11} \cdot e^{-iq_j(d_j)} + S'_{j21} \cdot e^{iq_j(d_j)}} E_0^+ . \tag{B.50}$$

B.3.5 Guided Modes

When one of the inner layers, j has a higher refractive index than the both of the claddings, such that $n_j > n_0, n_{\mathrm{M}+1}$, the structure may support a finite and discrete number of guided (or bound) modes in this layer. For guided modes, there are no incoming waves either side of the multilayer structure. There are still outgoing waves, however they are characterised by a complex wavevector and are therefore evanescent and decaying as they propagate.

To solve for the wavevectors of the guided modes we use the poles of the system transfer matrix. Reformulating eq. (B.41) in terms of a scattering (M-) matrix, relating the incoming electric field amplitudes to the outgoing electric field amplitudes gives

$$\begin{bmatrix} E_{\mathrm{M}+1}^+ \\ E_0^- \end{bmatrix} = \mathbf{M} \begin{bmatrix} E_{\mathrm{M}+1}^- \\ E_0^+ \end{bmatrix} \tag{B.51}$$

where the M-matrix is, again a 2×2 matrix, given in terms of the transfer matrix elements as

$$\mathbf{M} = \frac{1}{S_{11}} \begin{bmatrix} 1 & -S_{12} \\ S_{21} & \det \mathbf{T} \end{bmatrix} . \tag{B.52}$$

The poles on the M-matrix are clearly determined when $S_{11} = 0$ as it appears in the denominator for each element [247]. Now, going back to the transfer matrix relation (eq. (B.41)), we know that for guided modes there are no incoming waves to the structure and so we have the boundary conditions $E_0^+ = E_{\text{M}+1}^- = 0$. eq. (B.42) is therefore

$$\begin{bmatrix} 0 \\ E_0^- \end{bmatrix} = \mathbf{S} \begin{bmatrix} E_{\text{M}+1}^+ \\ 0 \end{bmatrix} \tag{B.53}$$

and hence

$$0 = S_{11} E_{\text{M}+1}^+ . \tag{B.54}$$

The equation is trivial for $E_{\text{M}+1}^+ = 0$ as all field amplitudes inside the structure will be zero. We therefore look for the poles of the transfer matrix ($S_{11} = 0$), which occur as functions of the wavevector parallel to the interfaces $k_\parallel$ for wavevector magnitudes in the range $\max\{n_0, n_{\text{M}+1}\}k_0 < k_\parallel < \max\{n_j : j = 1, \ldots, \text{M}\}k_0$, where k_0 is the free space wavevector [242]. Note also that radiative/partially radiative modes lie in the range $0 < k_\parallel < \max\{n_0, n_{\text{M}+1}\}k_0$.

As the transmission $S_{11} = 0$ for guided modes, eq. (B.53) only gives the one relation between the two coefficients

$$E_{\text{M}+1}^+ = \frac{1}{S_{21}} E_0^- . \tag{B.55}$$

For internal fields we use the same method as for radiative modes (found by inputting light wave from an ambient), however as there is no incoming wave we begin with the relation

$$\begin{bmatrix} 0 \\ E_0^- \end{bmatrix} = \mathbf{S}' \begin{bmatrix} E_j^+ \\ E_j^- \end{bmatrix} , \tag{B.56}$$

which can be solved for the field components in layer j in terms of the outgoing field in layer 0 (superstrate) to give

$$E_j^+ = -\frac{S'_{12}}{\det\{S'\}} E_0^- \tag{B.57a}$$

$$E_j^- = \frac{S'_{11}}{\det\{S'\}} E_0^- \; . \tag{B.57b}$$

Appendix C

Emission spectrum of heating elements

The typical spectral emission of quartz infrared heating lamps used in the upgraded ultrafast plasma doping system detailed in section 4.3 is shown in fig. C.1(a). The older system shown in fig. 4.1 used silicon carbide (SiC) heating elements, which have a typical emission spectra that is shown in fig. C.1(b).

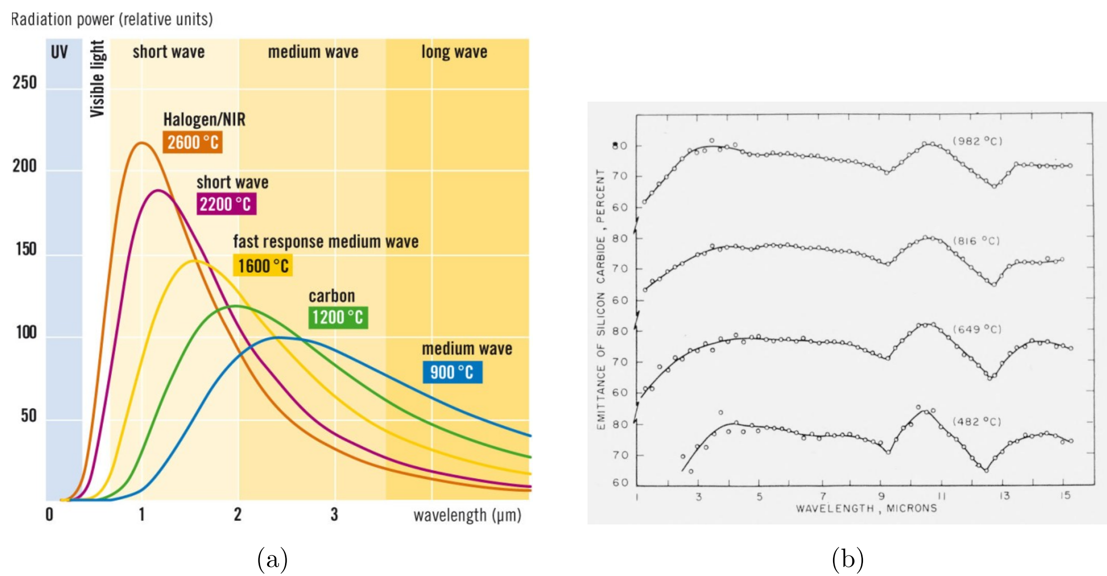

(a) (b)

Figure C.1: Typical emission spectra of (a) an infrared heating lamp [248] and (b) a SiC heating element [249]. The quartz infrared heating lamps in the system described in section 4.3 correspond to the medium wave spectra in section 4.3(a).

Appendix D

Tellurite glass polishing procedure

Achieving a high quality surface polish is critical for D2-LnF measurements. Pits and scratches modify the material ablation threshold and surface reflectivity resulting in a change in shape of the ablation crater, which can lead to erroneous results. Furthermore, for characterisation of the ablation crater sizes, it is required that the surrounding region is smooth (low surface roughness) so that the crater edge is clearly identifiable[1]. Highly parallel faces are also preferable so that the laser is incident normal to the material surface and the focal spot has a circular shape. Nonetheless, in the case of an elliptical focal spot the original D2-LnF method by Liu [167] can be modified to hold for each ellipse axis as described by Byskov-Nielsen et al. [251]. Other optical applications for rare-earth doped tellurite glasses, such as lasers, also require an optical polish.

Tellurite glasses have low thermal and mechanical stability and are relatively soft. It took numerous trials until a suitable polishing procedure using an automated precision lapping and polishing machine (PM5, Logitech Ltd.) was arrived at. Cracking resulting from thermal shocks was particularly problematic resulting in wasted glass samples. It is for this reason that the polishing procedure is given in detail here. Figure D.1 shows optical microscopy images of the glass surface at each stage of the polishing process for reference and the steps are described in the following.

[1] Determination of the ablation threshold of a rough surface can not made via D2-LnF measurements due to ambiguity in the crater edge. Another approach used is to identify the onset of surface damage rely through light scattering of a cw-HeNE laser [250], however this would also not be suitable as rough surfaces already scatter light.

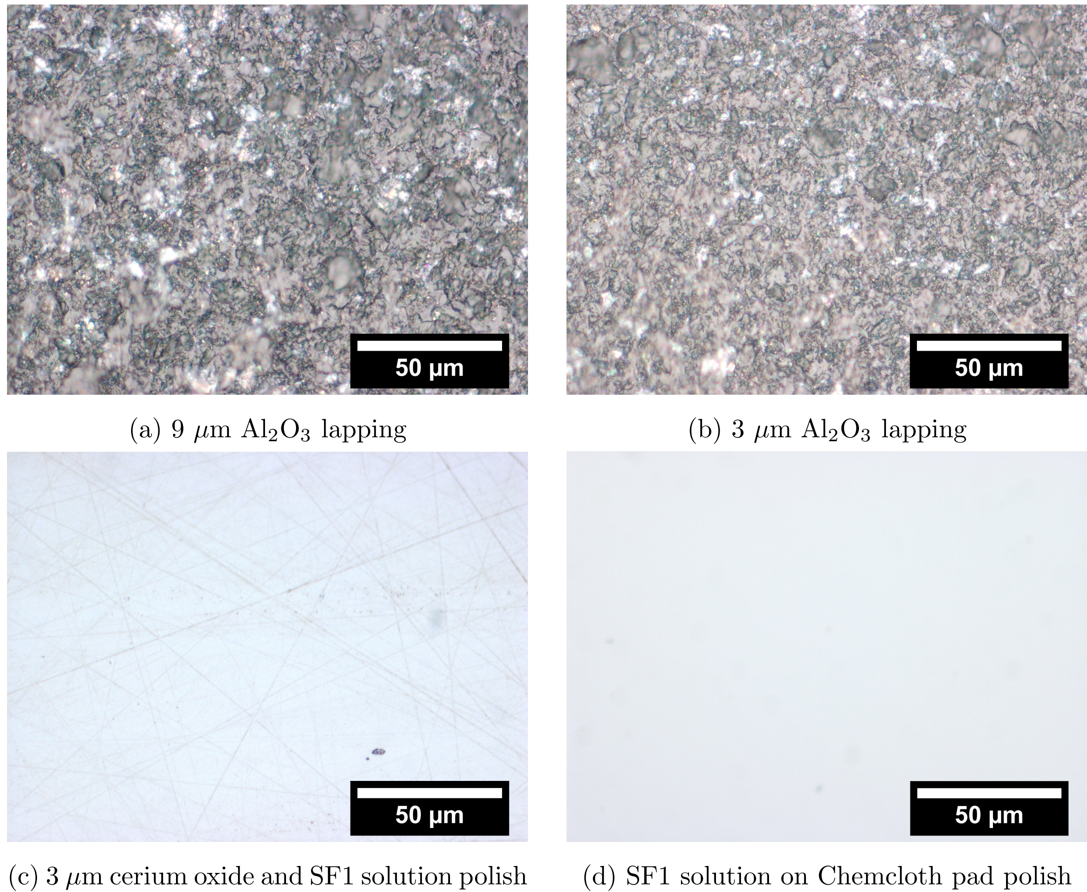

(a) 9 μm Al_2O_3 lapping

(b) 3 μm Al_2O_3 lapping

(c) 3 μm cerium oxide and SF1 solution polish

(d) SF1 solution on Chemcloth pad polish

Figure D.1: Optical microscopy images of the various stages of lapping and polishing the zinc-sodium tellurite glass.

Mounting

The glass is held into the sample jig by using wax to bond it onto the metal holder. The wax melting temperature was 100°C. The metal holder and the glass, placed on a second metal holder, were heated simultaneously on a hotplate. The glass must also be heated to the same temperature as the holder to avoid thermal shocks when mounting. Having mounted the glass onto the holder, a process that must be performed quickly, the setup is cooled to room temperature. Note that this can take several hours as the centre of the glass takes longer to cool.

D. TELLURITE GLASS POLISHING PROCEDURE

Lapping

The lapping stage (to prepare the surface for polishing) is performed with a cast iron plate, rotating at a low speed of 20 RPM and an applied weight of 20-30 g/cm^2. The low plate rotation speed is to avoid the glass bouncing on the lapping plate, which can cause damage. The applied weight is kept low as tellurite glasses are relatively soft.

The first stage of lapping is performed with a 9 μm Al_2O_3 solution until the entire surface is flat (visible by eye) or the glass has the desired thickness (taking into account the material removal in later stages). Optical microscopy of the glass surface after this stage is shown in fig. D.1a.

The second stage of lapping is performed with a 3 μm Al_2O_3 solution until 27 μm (3 times the previous grain size) is removed. This stage typically takes 10 minutes and target surface is shown in fig. D.1b.

Polishing

The first stage of polishing is performed with a ceramic polishing plate. A 3 μm cerium oxide solution and a SF1 (320 nm colloidal silica) solution are used. The plate speed and weight parameters from the lapping stage are unchanged. After polishing for 30 minutes the target surface should appear as shown in fig. D.1c.

To remove scratches the final polishing uses a stainless steel plate with a Chemcloth pad. Following plate preparation (use deionised water to avoid wastage of the SF1 solution) the glass is polished using SF1 solution. The glass surface is inspected under an optical microscope every 30 minutes until a satisfactory polish has been achieved free of pits and scratches, as shown in fig. D.1d.

Unmounting

Unmounting the glass from the holder is the reverse of the mounting process. To dissolve and remove the remaining wax from the surface, the glass is placed in a beaker filled with acetone overnight. Replacing the acetone may be required if there is a lot of wax remaining.

Other considerations

Small thermal shocks from cold liquid may cause the tellurite glass to crack and so it should be ensured that all liquids are at room temperature prior to polishing. This includes water used to clean the glass before inspection with optical microscopy.

To polish the faces of the glass so that they are parallel an autocollimator (LG1, Logitech Ltd.) is used to align the sample holder jig after one face has been optically polished.

Appendix E

VASE measurements and fitting procedure

Variable angle spectroscopic ellipsometry (VASE) was used to measure the optical properties of Er^{3+}-doped zinc-sodium tellurite target glasses, glass substrates and films fabricated on the glass substrates using the ultrafast laser plasma doping technique (ULPD). The procedure was to first characterise the refractive index ($\tilde{n} = n + ik$, where the real part n is the index and the imaginary part k is the extinction coefficient) of the target and substrate bulk glasses. Following this, the optical properties of the thin film could be determined in a wavelength range where the films are expected to be transparent. Measurements of Psi (Ψ) and Delta (Δ) were performed using a JA Wollam M-2000 rotating compensator spectroscopic ellipsometer over the wavelength range from 245 to 1650 nm and at multiple angles of incidence (60° to 75° by 5°). Vaiable angles improves confidence of the fitted model as light travels different paths through the sample. The spot diameter on the sample was ~3 mm and measurements were taken from the centre of the sample. All analysis was performed with CompleteEASE version 6.43.

The optical constants of the transparent and partially transparent dielectric films and bulk glasses in dependence of wavelength were determined with Cauchy's equation. The model assumes an index that varies slowly as a function of wavelength and an exponential absorption tail. The three term Cauchy equation gives the refractive index n in dependence of wavelength λ [μm] in terms of a power series containing only even terms

$$n(\lambda) = A + \frac{B}{\lambda^2} + \frac{C}{\lambda^4}, \tag{E.1}$$

where A, B and C are the fitted coefficients. Where necessary, an exponential absorption tail was included

$$k = k_{amp} \cdot e^{(E-B_g)}, \tag{E.2}$$

where the k amplitude k_{amp} and exponent E are fit parameters determining the shape of the extinction coefficient dispersion. The band edge B_g is set manually. A surface roughness layer assumes a 50:50 mixture of the material above (air) and below the interface and accounts for scattering and depolarisation of the reflected light. The fitting of the Er^{3+}-doped zinc-sodium tellurite target glasses, the glass substrates and the thin films fabricated with the ultrafast laser plasma doping technique (ULPD) are described in the following. The figure of merit for the fits are each described by the mean square error (MSE), which describes the difference between experimental data and model predicted data.

E.1 Target glass

The optical properties of three target glasses with compositions of (80-x)TeO_2-10ZnO-10Na_2O-$x$$Er_2O_3$ (x=0.00, 0.1, 0.5 1.0) mol.%, denoted xErTZN, were measured using VASE. The fabrication procedure of the glasses is presented in chapter 5. The back face was given a rough polish to avoid reflections interfering with the measurement. The two-term form of the Cauchy equation with an exponential absorption tail was sufficient to provide satisfactory fits for the bulk glasses. The fits to the measured data is shown in fig. E.1 and the parameters to the fits are reported in table E.1. The refractive index as a function of wavelength is plotted in fig. E.2.

Table E.1: Parameters to the fits of the optical model for each target glass. MSE is the mean square error. The band edge was set at 390 nm.

	0.1ErTZN	0.5ErTZN	1.0ErTZN
MSE	5.614	5.268	4.945
Roughness [nm]	4.24	5.95	8.46
A	1.987	1.987	1.982
B	0.01612	0.013	0.01241
C	0.00202	0.00214	0.00205
k Amplitude	0.00724	0.00486	0.00501
Exponent	2.478	2.651	2.633
n @ 632.8 nm	2.03985	2.03288	2.02543

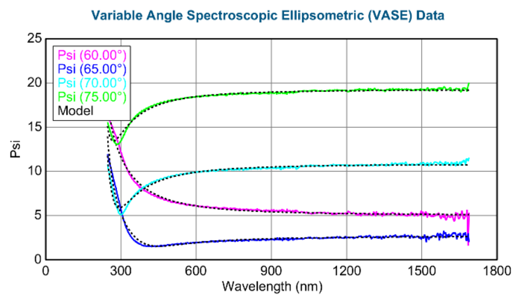

(a) 0.1ErTZN Psi

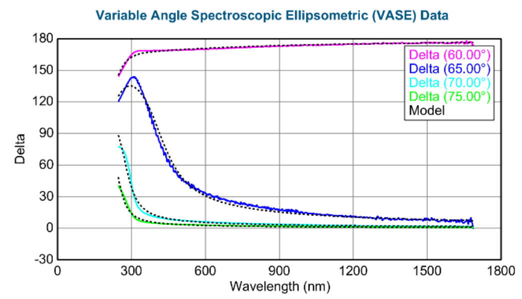

(b) 0.1ErTZN Delta

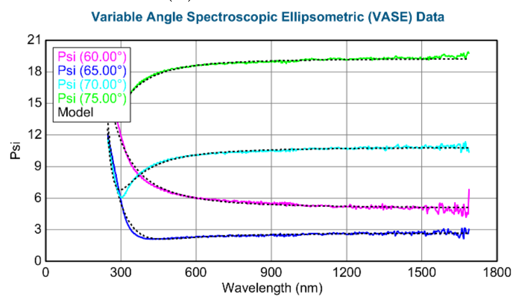

(c) 0.5ErTZN Psi

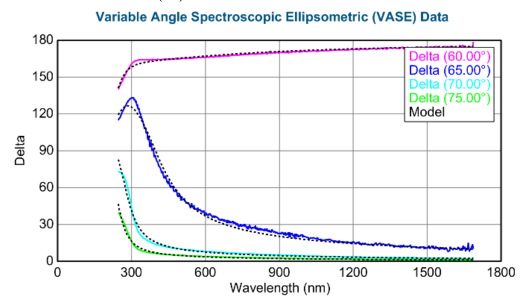

(d) 0.5ErTZN Delta

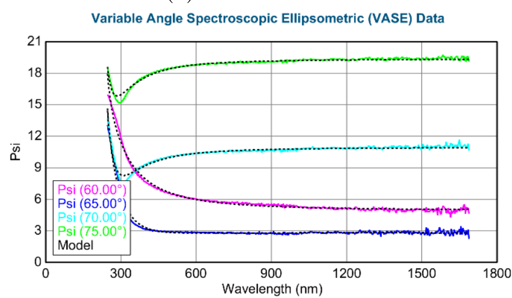

(e) 1.0ErTZN Psi

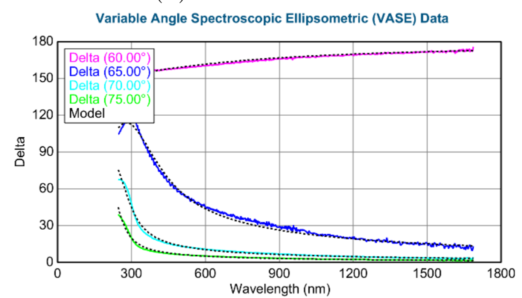

(f) 1.0ErTZN Delta

Figure E.1: VASE measurements of psi and delta with the fitted optical model (black dashed line).

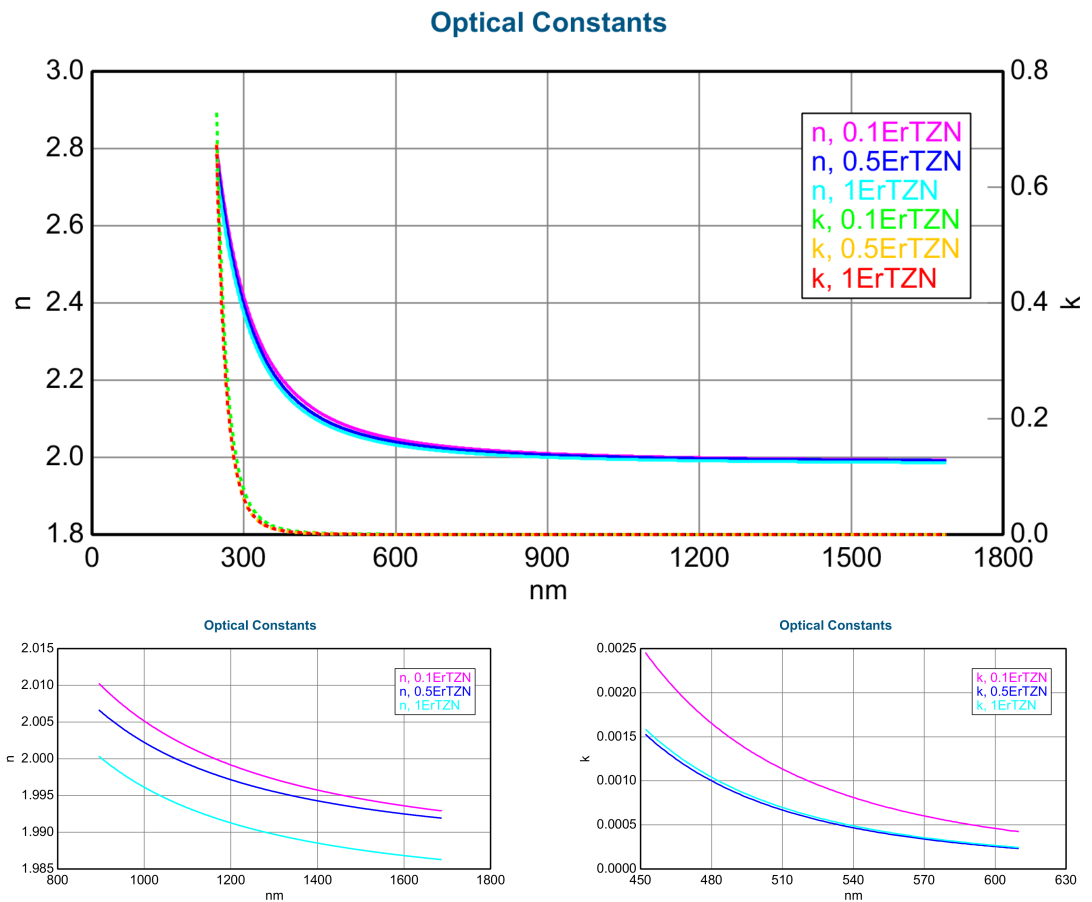

Figure E.2: Refractive index of the targets at a function of wavelength.

E.2 Glass Substrates

The 1.1 mm thick glass substrates were fitted with the two term Cauchy equation. The backside reflection was taken into account. Note that the Spectrosil 2000 substrate was the only sample that was measured with a focused beam of ~150 μm and as a result back reflections did not interfere with the measurement. The fits to the measured data is shown in fig. E.3 and the parameters to the fits are reported in table E.2. The refractive index as a function of wavelength is plotted in fig. E.4.

Table E.2: Parameters to the fits of the optical model for each glass substrate. MSE is the mean square error.

	Infrasil 301	Corning 7980	Borofloat 33	Spectrosil 2000
MSE	3.065	3.268	4.534	4.834
Roughness (nm)	1.59	0.09	0.51	
A	1.441	1.441	1.458	1.445
B	0.00476	0.00452	0.00624	0.00366
# Back Reflections	1.972	1.538	0.659	
% 1st Reflection	100	100	88.58	

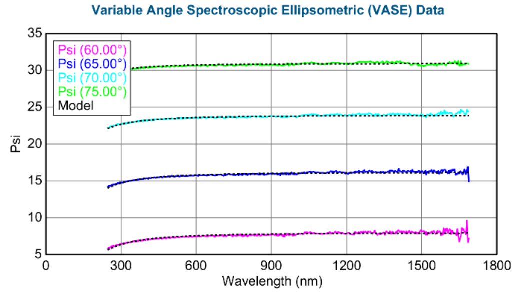

(a) Infrasil 301 Psi

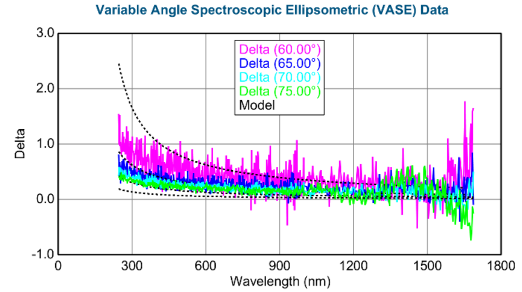

(b) Infrasil 301 Delta

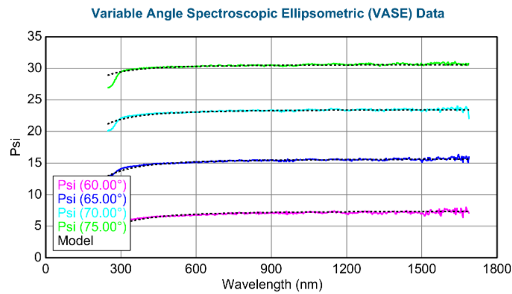

(c) Borofloat 33 Psi

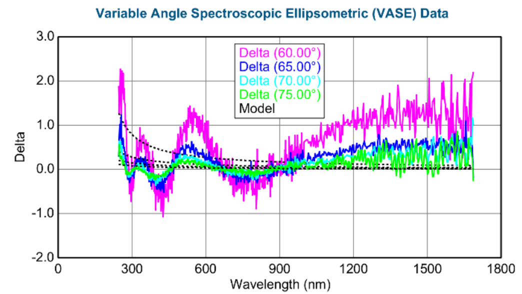

(d) Borofloat 33 Delta

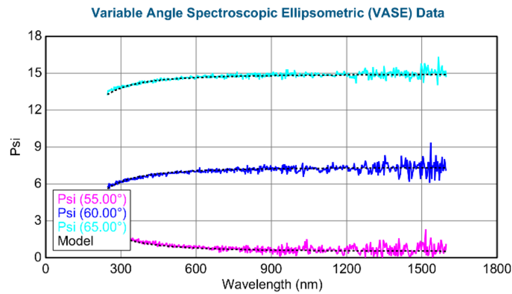

(e) Spectrosil 2000 Psi

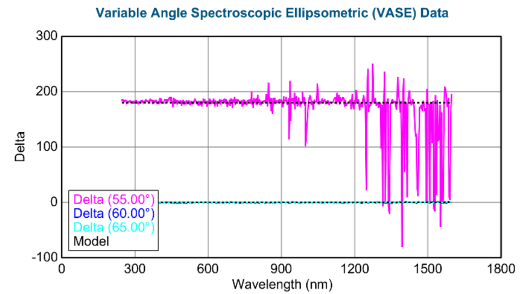

(f) Spectrosil 2000 Delta

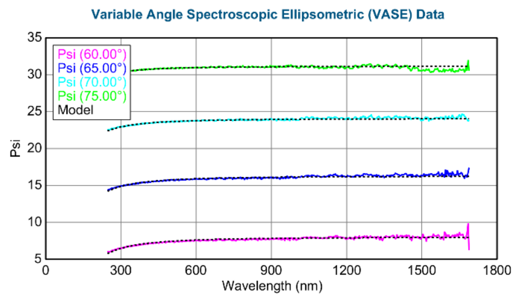

(g) Corning 7980 Psi

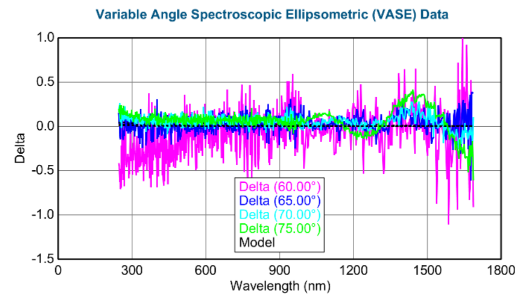

(h) Corning 7980 Delta

Figure E.3: VASE measurements of psi and delta with the fitted optical model (black dashed line).

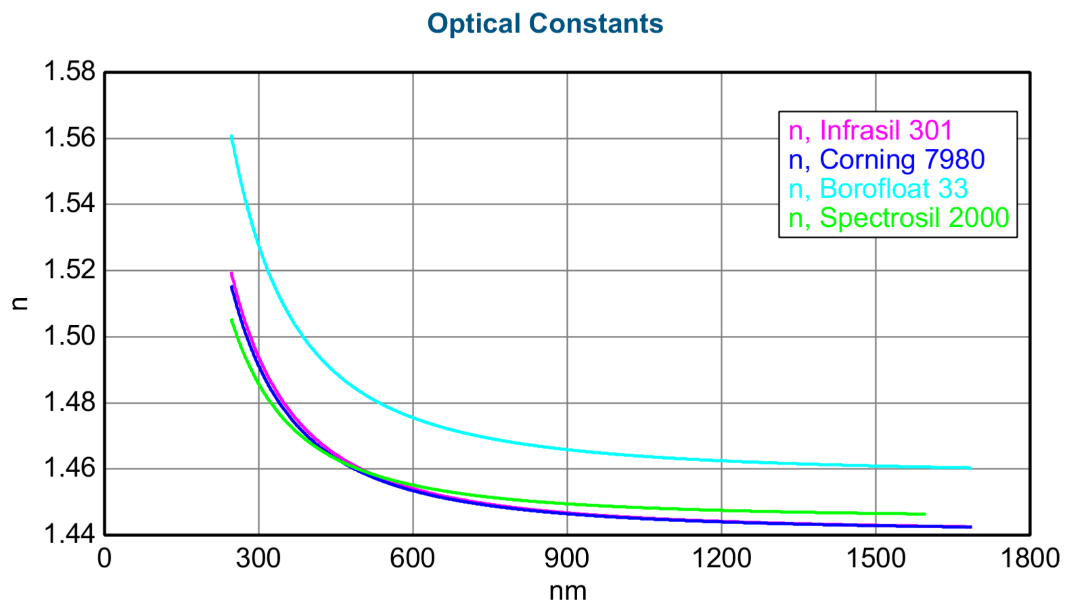

Figure E.4: Refractive index of the glass substrate at a function of wavelength.

E.3 Thin films

When fitting the thin films, a linear grading was applied to the layer to account for the transition region of target ions from the film to the substrate that is known to occur in the ULPD technique. The films were fitted with a transparent optical model in the wavelength region above 500 nm, where the extinction of the target glass became negligible. The optical properties of the glass substrate that were measured previously was used as a layer beneath the film. Initial fitting attempted to use a two term Cauchy equation, however, often this resulted in a negative B coefficient which yields an unphysical refractive index dependence on the wavelength (index must increase toward shorter wavelengths if $k = 0$). To avoid this, a single term Cauchy equation (wavelength independent) was fitted to the films to provide a satisfactory fit. Improvements to the fit may be achieved with a better model for the grading, however, a direct measurement of the elemental profile with depth using an experimental technique such as Rutherford back-scattering would be required first.

E.3.1 Chapter 6 section 4.2

The film fabricated at $F = 1.56$ J/cm^2 on Spectrosil 2000 in section 7.4.2 was fitted with a one term Cauchy equation $n = A$. The fits to the measured data is shown in fig. E.5. The parameters to the fits and refractive index as a function of wavelength are reported in the main text table 7.6 and fig. 7.30, respectively.

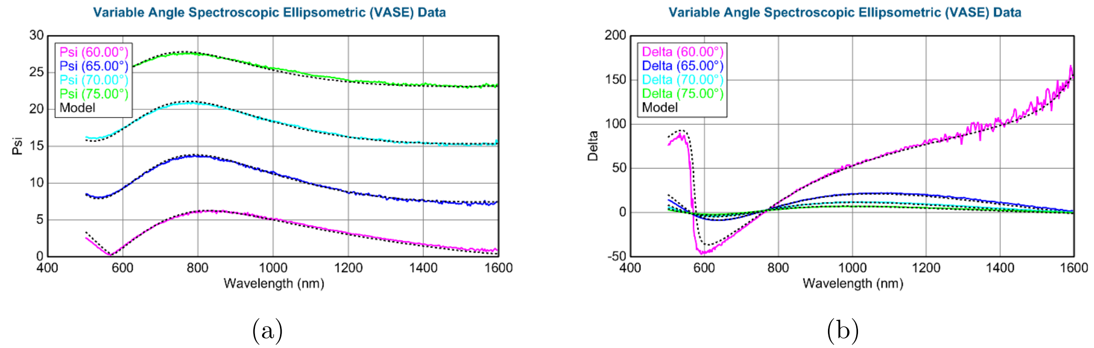

(a) (b)

Figure E.5: VASE measurements of psi and delta for thin film fabricated at $F = 1.56$ J/cm^2 on Spectrosil 2000 with the fitted optical model (black dashed line).

E.3.2 Chapter 7

The samples in chapter 8 were fitted with a one term Cauchy equation $n = A$ and are shown in fig. E.6. The parameters to the fits and refractive index as a function of wavelength are reported in the main text table 8.2 and fig. 8.5, respectively.

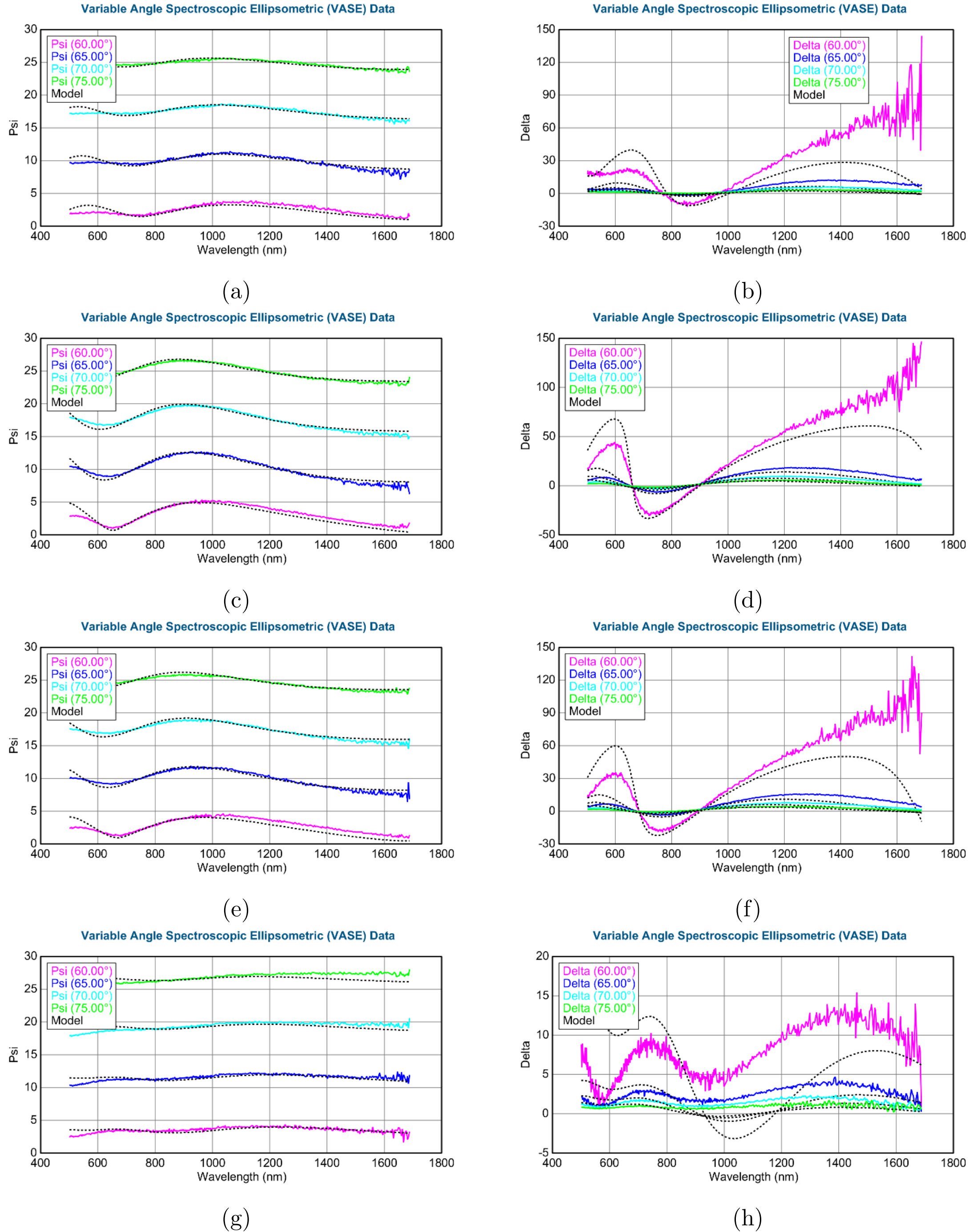

Figure E.6: VASE measurements of psi and delta for thin films fabricated on different glass substrates with the fitted optical model (black dashed line).

Appendix F

Post anneal

It was investigated as to whether a post fabrication high temperature anneal could improve the dissolution in the film for the SiO_2 substrate resulting in a single exponential PL decay. The silica substrate sample from section 7.4.2 was placed film side up in an electric furnace and heated to 750°C (the ideal temperature for fabrication ultrafast laser plasma doping technique) for 6 hours in an air atmosphere. Photographs of the sample before and after heat treatment in fig. F.1 clearly show a degradation in film quality visible to the eye. The birefringince that was originally visible no longer exists and the film appears cloudy. A comparison of the PL lifetime and spectra, presented in fig. F.2 and table F.1, shows that a broadening in spectra and a reduction in lifetime takes place. An increase in the intensity of the spectral side is due to the inhomogeneous environment of the Er^{3+} ions and may also indicate a more tellurite environment due to phase separation. This is in agreement with the increase in the relative intensity of the short lifetime component to the PL decay that occurs when clusters form in the media.

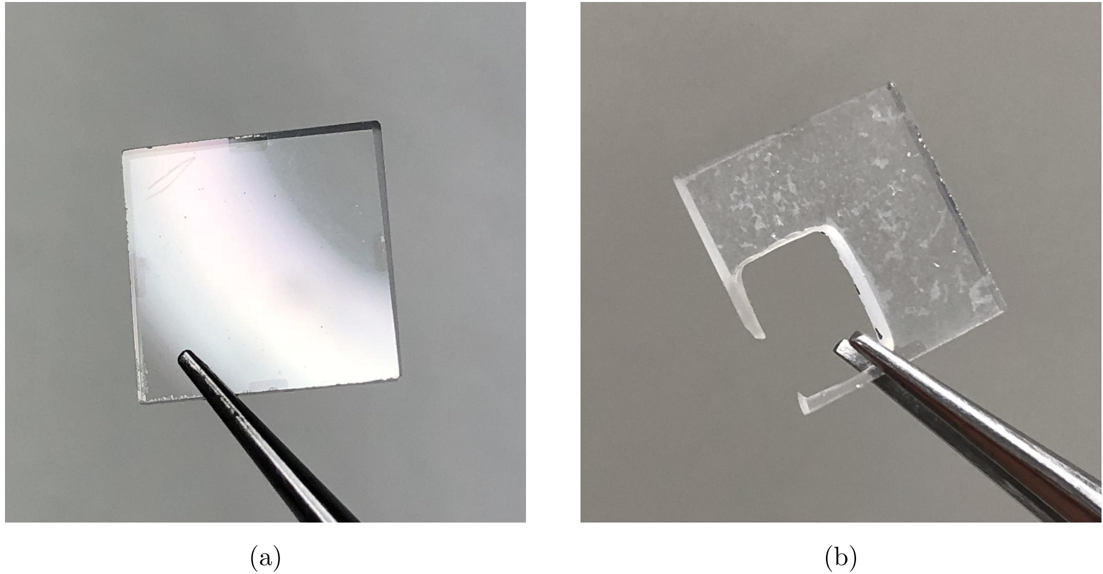

(a) (b)

Figure F.1: SiO_2 substrate sample processed at $F = 1.56$ J/cm^2 (a) pre and (b) post heat treatment. The cutout in the sample in (b) is where a section was taken for cross-sectional SEM analysis.

Table F.1: SiO_2 substrate $F = 1.56$ J/cm^2.

	$\tau^{\dagger}$[ms]	FWHM [nm]
Untreated	7.37 ± 0.63 (66 %), 3.43 ± 0.39 (34 %)	23.9
Heat Treated	4.06 ± 0.30 (45 %), 1.54 ± 0.06 (55 %)	27.5

† Decays with multiple lifetimes have the relative intensity in brackets for each lifetime

* Measurement taken from centre of the sample. The edge sample, which appeared clearer, had a longer ~ 6.60 ms lifetime decay

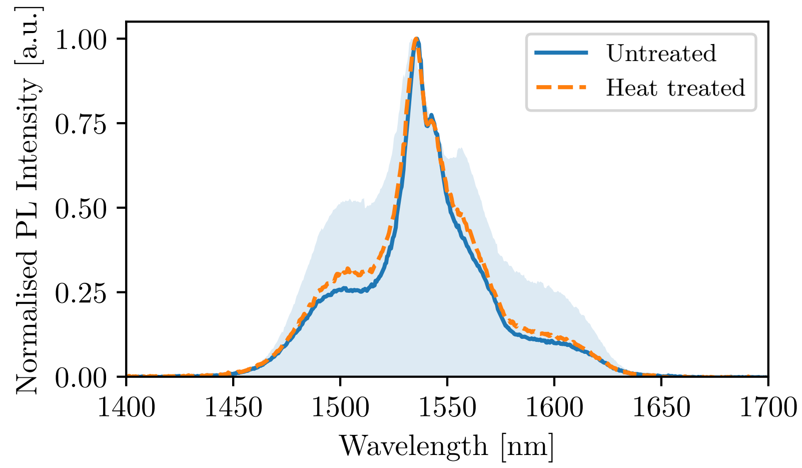

(a)

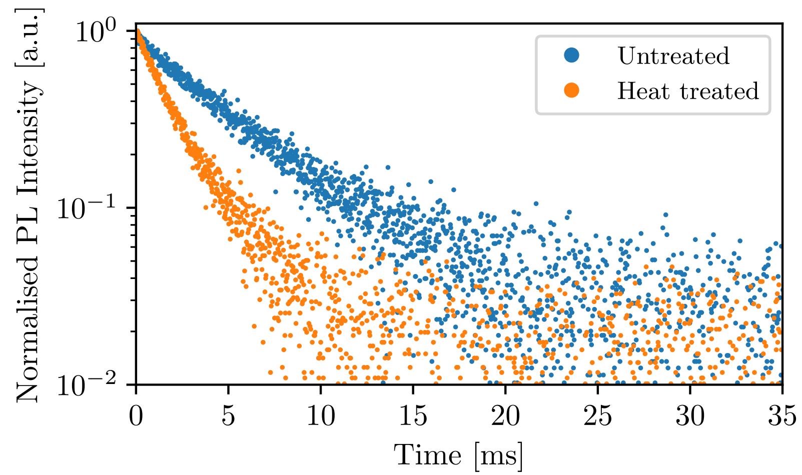

(b)

Figure F.2: Photoluminescence (a) spectra and (b) decay of SiO_2 substrate samples. Shadowed fill plot in (a) shows the spectra of the 1ErTZN target glass for reference.